Institut für Informatik
der Technischen Universität München

Fitting Parametric Curve Models to Images Using Local Self-adapting Separation Criteria

Dissertation

Robert Hanek

Institut für Informatik
der Technischen Universität München

Fitting Parametric Curve Models to Images Using Local Self-adapting Separation Criteria

Robert Hanek

Vollständiger Abdruck der von der Fakultät für Informatik der Technischen Universität München zur Erlangung des akademischen Grades eines

Doktors der Naturwissenschaften (Dr. rer. nat.)

genehmigten Dissertation.

Die Dissertation wurde am 28.11.2003 bei der Technischen Universität München eingereicht und durch die Fakultät für Informatik am 02.07.2004 angenommen.

Abstract

The task of fitting parametric curve models to boundaries of perceptually meaningful image regions is a key problem in computer vision with numerous applications, such as image segmentation, pose estimation, 3-D reconstruction, and object tracking. In this thesis, we propose the *Contracting Curve Density (CCD) algorithm* and the *CCD tracker* as solutions to this problem. The CCD algorithm solves the curve-fitting problem for a single image whereas the CCD tracker solves it for a sequence of images.

The CCD algorithm extends the state-of-the-art in two important ways. First, it applies a novel likelihood function for the assessment of a fit between the curve model and the image data. This likelihood function can cope with highly inhomogeneous image regions because it is formulated in terms of local image statistics that are learned on the fly from the vicinity of the expected curve. Second, the CCD algorithm employs *blurred curve models* as efficient means for iteratively optimizing the posterior density over possible model parameters. Blurred curve models enable the algorithm to trade-off two conflicting objectives, namely a large area of convergence and a high accuracy.

The CCD tracker is a fast variant of the CCD algorithm. It achieves a low runtime, even for high-resolution images, by focusing on a small set of carefully selected pixels. In each iteration step, the tracker takes only such pixels into account that are likely to further reduce the uncertainty of the curve. Moreover, the CCD tracker exploits statistical dependencies between successive images, which also improves its robustness. We show how this can be achieved without substantially increasing the runtime.

In extensive experimental investigations, we demonstrate that the CCD approach outperforms other state-of-the-art methods in terms of accuracy, robustness, and runtime. The CCD algorithm and the CCD tracker achieve sub-pixel accuracy and robustness even in the presence of strong texture, shading, clutter, partial occlusion, poor contrast, and substantial changes of illumination. We present results for different curve-fitting problems such as image segmentation, 3-D pose estimation, and object tracking.

Zusammenfassung

Das Anpassen parametrischer Kurvenmodelle an die Grenzen perzeptuell relevanter Bildregionen ist ein Kernproblem der Bildverarbeitung. Es tritt in zahlreichen wichtigen Anwendungen wie z.B. Bildsegmentierung, Lageschätzung, 3-D Rekonstruktion und Objektverfolgung auf. In dieser Dissertation werden der *Contracting Curve Density (CCD) Algorithmus* und der *CCD Tracker* als Lösungen für dieses Problem vorgeschlagen. Der CCD Algorithmus löst das Anpassungsproblem für ein einzelnes Bild, der CCD Tracker hingegen für eine Bildsequenz.

Der CCD Algorithmus erweitert den derzeitigen Stand der Forschung in zweierlei Hinsicht. Erstens verwendet er eine neuartige Likelihood-Funktion für die Bewertung der Übereinstimmung zwischen dem Kurvenmodell und den Bilddaten. Die Likelihood-Funktion ist selbst für inhomogene Bildregionen geeignet, da sie auf lokalen Statistiken basiert, welche iterativ von der Umgebung der Kurve gelernt werden. Zweitens verwendet der CCD Algorithmus *unscharfe Kurvenmodelle* als effektives Mittel zur iterativen Optimierung der a-posteriori-Dichte. Unscharfe Kurvenmodelle erlauben einen Ausgleich zwischen zwei gegensätzlichen Zielen, nämlich einem großen Konvergenzbereich und einer hohen Genauigkeit.

Der CCD Tracker ist eine schnelle Variante des CCD Algorithmus. Selbst für Bilder mit hoher Auflösung erzielt er eine geringe Rechenzeit, indem er sich auf eine kleine Menge speziell ausgewählter Pixel fokussiert. In jedem Iterationsschritt verwendet er nur solche Pixel, die höchstwahrscheinlich die Unsicherheit der Kurve weiter reduzieren. Darüber hinaus nutzt der Tracker statistische Abhängigkeiten zwischen aufeinanderfolgenden Bildern. Dies führt zu einer zusätzlichen Steigerung der Robustheit, ohne die Rechenzeit substanziell zu erhöhen.

Umfangreiche experimentelle Untersuchungen zeigen, dass der CCD Ansatz anderen Ansätzen sowohl in der Genauigkeit, der Robustheit als auch der Rechenzeit überlegen ist. Der CCD Algorithmus und der CCD Tracker erzielen Subpixel-Genauigkeit und Robustheit selbst bei starken Texturen, Schattierungen, Teilverdeckungen, geringem Kontrast und erheblichen Beleuchtungsänderungen. In dieser Arbeit werden Ergebnisse für verschiedene Anpassungsprobleme vorgestellt, z.B. Bildsegmentierung, 3-D Lageschätzung und Objektverfolgung.

Acknowledgments

This dissertation would not have been possible without the assistance of several people. First of all, I would like to thank my thesis advisor, Prof. Dr. Bernd Radig, for giving me the opportunity to work on this dissertation. I am particularly grateful for his enthusiasm in supporting Thorsten's and my idea of founding our own company.

I would like to express my thanks to Prof. Dr. Nassir Navab, the second reporter on this dissertation. His passion for science was one of the sources of my motivation.

Special thanks go to Michael Beetz. His comments, encouragement, and constructive criticism helped me many times, especially in writing publications and preparing presentations. I would especially like to thank Thorsten Schmitt and Sebastian Buck for being great colleagues and close friends. Working with you and the other members of the AGILO robot soccer team was fun even during stressful periods such as the preparations for World Cups and other events. I would also like to thank my other colleagues at the "Image Understanding and Knowledge-Based Systems Group" at Munich Technical University. Thank you for your assistance and many amazing lunch and coffee breaks. I am indebted to Fabian Schwarzer, Bea Horvath, Andreas Hofhauser, and Gillian McCann for proofreading this thesis.

Thanks go to Michael Isard, Andrew Blake, and the other members of the "Oxford Visual Tracking Group" for providing the code of their tracking library. I am grateful to Juri Platonov for his assistance in conducting the experiments with the condensation and the Kalman tracker.

I would like to thank Carsten Steger for helpful discussions and for providing the DLL of the color edge detector. Jianbo Shi and Jitendra Malik at the University of California at Berkeley provided the executable of their Normalized Cuts algorithm. Thanks go to Lothar Hermes at the University of Bonn for running the PDC algorithm on the test data, see Figure 2.1. Furthermore, I am grateful to Christoph Hansen for providing the PDM depicted in Figure 5.13.

Last, but certainly not least, I would like to thank my girl-friend, Wiebke Bracht, who supported me with her love, encouragement, and assistance in many ways.

Contents

List of Figures

List of Tables

Chapter 1

Introduction

In our daily lives the number of devices equipped with cameras is steadily increasing. PCs are equipped with webcams. Mobile phones and entertainment robots are equipped with small cameras. Even many cars will soon be equipped with imaging devices, such as infrared cameras, in order to amplify the driver's vision at night. Cameras are increasingly being used in different environments, such as conference rooms, shopping malls, train stations, and highways.

The variety of environments and imaging conditions constitute a great challenge for the development of interpretation and image understanding methods. Obviously, methods that can achieve their interpretation task in natural and unmodified environments are becoming particularly important. The mug depicted in Figure 1.1 illustrates the resulting challenge for image understanding, also known as computer vision and scene analysis. Both the mug and its background show a large variety of pixel values, textures, and other image properties. Hence, segmenting the mug, i.e. separating the mug region from the background, is challenging. Several other tasks in computer vision are based on the crucial task of image segmentation.

Many important computer vision problems can only be solved by using a priori knowledge about the scene. In the image formation process the 3-D world is transformed to a 2-D image. Due to the loss of information, the transformation cannot be uniquely inverted. Hence, many computer vision problems are ill-posed[1] (Bertero, Poggio, and Torre, 1988). For example, determining the 3-D location and orientation of an unknown object from a single image is not possible without additional information.

Due to the ill-posedness of many computer vision problems, models specifying a priori knowledge are commonly used. Particularly effective models are parametric curve models, also known as *deformable*[2] *models*, *deformable templates*, *snakes*, or *active contours* (Kass, Witkin,

[1]Ill-posed in the sense of Hadamard (1902) means that the problems have either no solution, no unique solution, or a solution that does not depend continuously on the input.

[2]We prefer the term parametric curve models since in many applications the model is not deformable, but rigid.

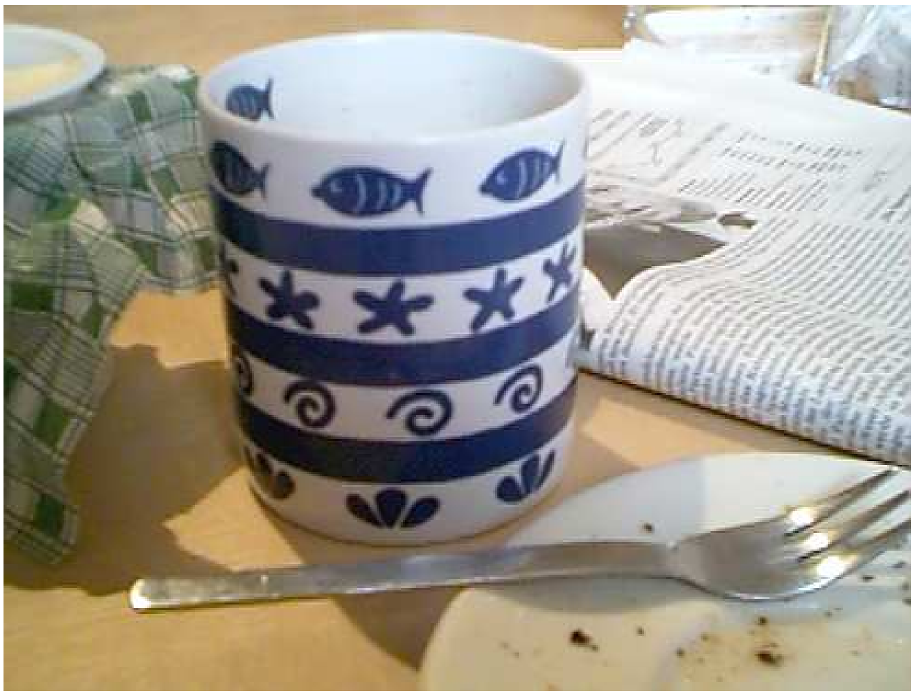

Figure 1.1: A typical computer vision task is to identify the image region corresponding to the mug and to determine the location and orientation of the mug in the 3-D space.

and Terzopoulos, 1988; Yuille, Cohen, and Hallinan, 1992; Blake and Isard, 1998). This class of models defines the set of expected shapes in the image using geometric properties of the curve. The parametric curve model guides the image interpretation process towards particularly likely interpretations.

A number of important and challenging computer vision tasks, including image segmentation, pose estimation, object tracking, and object recognition can be formulated as variants of the curve-fitting problem. This is the problem of fitting a given parametric curve model to sensed image data. In this thesis, we propose robust, accurate, efficient, and versatile methods for fitting parametric curve models to a single image or a sequence of images.

1.1 The Curve-fitting Problem

Let us now introduce the curve-fitting problem by first giving an informal problem description, then listing some of its most important applications, and finally specifying requirements for a method performing curve-fitting.

1.1.1 Problem Description

The **curve-fitting problem** can be described as follows:[3]

Input data: Given are (a) the *image data* (one or multiple images) and (b) a *parametric curve model*. The curve model describes region boundaries, i.e. edges, in the image as a function of a vector of *model parameters*. Such a boundary could be, for example, the contour of an object of interest. The model parameters specify possible variations of the curve. For example, the model parameters could define the 3-D pose (position and orientation), size, and shape of the object of interest. Furthermore, the curve model contains an a priori distribution of the model parameters which represents a priori knowledge about the curve.

Goal (output data): The goal of the curve-fitting process is to estimate the model parameters that best match both the image data *and* the a priori distribution. In the process of curve-fitting, evidence from the image data is combined with the a priori distribution to form a posteriori estimate of the model parameters.

Figure 1.2 depicts a curve-fitting problem. The input image shows the coffee mug in front of an inhomogeneous background. The curve model describes the set of expected contours of the mug. The thick line in Figure 1.2b is the curve corresponding to the mean of the a priori distribution. The a priori distribution probabilistically assigns pixels either to the mug region or to the background region. The pixels having the most uncertain assignments lie between the two thin lines in Figure 1.2b. After the fitting process, the uncertainty is widely reduced and the estimated contour (black curve in Figure 1.2c) accurately matches the contour of the mug.

Based on curve-fitting, different levels of computer vision tasks can be performed:

Image segmentation: Image segmentation can be performed by curve-fitting. Image segmentation is the process of locating regions in an image that correspond to objects in the scene. By curve-fitting, for example the image in Figure 1.2a can be partitioned in a region corresponding to the coffee mug and another region corresponding to the background.

[3] A more formal description of the input and the output data will be given in section 3.1.1.

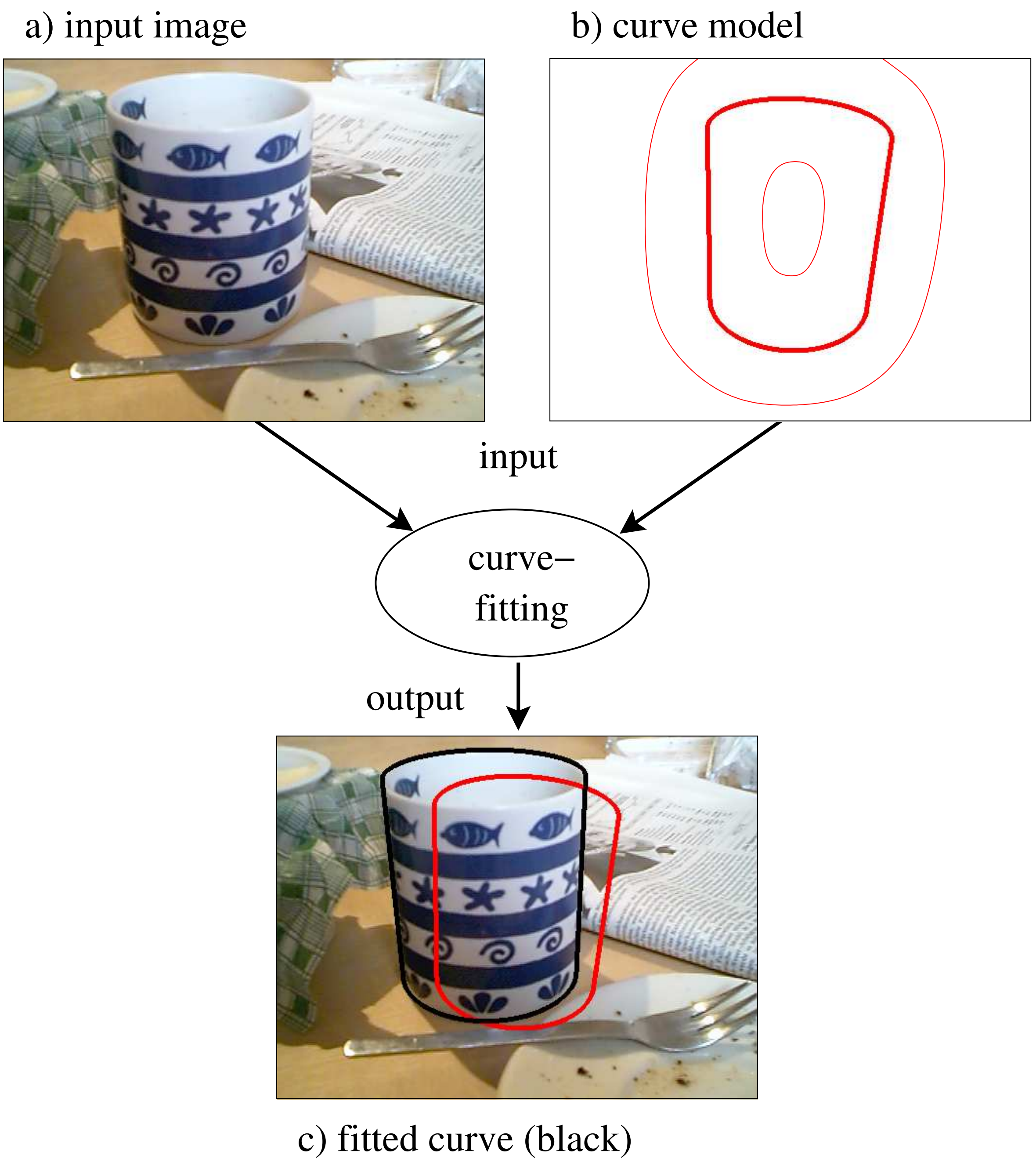

Figure 1.2: The curve-fitting problem: a) The input image. b) A parametric curve model with an a priori distribution of the model parameters. The thick line is the mug contour corresponding to the mean of the a priori distribution. The thin lines illustrate the initial uncertainty of the region boundary. c) The goal is to estimate the model parameters such that the resulting curve (black) fits to the image data and to the a priori distribution. During the fitting process, the uncertainty of the region boundary is widely reduced.

Parameter estimation: By curve-fitting, meaningful properties of the scene can be directly estimated. Depending on the curve model, properties of observed objects (e.g. pose, size, and shape) or properties of the observing camera (internal and external camera parameters) can be estimated. By curve-fitting, e.g. in Figure 1.2a the 3-D pose of the coffee mug can be estimated with respect to the observing camera. Note that this information is of a higher level than the raw image segments are. The obtained 3-D data may, for example, allow a robot to grasp the object, whereas the raw image segments, which contain only 2-D information, are not sufficient for this task. To estimate such higher-level data, a priori knowledge is required. For example, 3-D pose estimation from a single view requires knowledge about the camera (internal parameters) and about the observed object. This knowledge is represented by the curve model.

Why is Curve-fitting Difficult?

Unfortunately, solving image segmentation and the related curve fitting problem is often very difficult, especially in natural and unconstrained scenes. For example, segmenting the coffee mug from the background is difficult because both the mug region and the background region are very inhomogeneous. Both regions exhibit large variations of the pixel values (e.g. RGB values) due to clutter, shading, texture, and highlights, see Figure 1.2a. Furthermore, the sensed image data depend on physical conditions, such as the illumination or surface properties, that are usually unknown. As a consequence, it is often impossible to determine adequate segmentation criteria in advance or even find a single criteria that is applicable for all parts of an object boundary. This is exactly what causes problems for related state-of-the-art methods, which will be discussed in chapter 2.

1.1.2 Applications

Let us now briefly illustrate the wide range of applications of curve-fitting.

Robotics: Many applications of computer vision are in the field of robotics. For example, parametric curves can be used to describe landmarks in the robot's environment. A robot equipped with a camera can localize itself within the environment by fitting the curve models to the sensed image (Aider, Hoppenot, and Colle, 2002; Hanek and Schmitt, 2000). Similarly, it can also localize other objects (Lowe, 1987; Phong et al., 1995; Hanek et al., 2002a). Based on the object's contour, a robot can also establish a set of safe grasps on the observed object (Davidson and Blake, 1998; Rimon and Blake, 1996).

Medical applications: Parametric curve models, i.e. deformable models, have been extensively employed for extracting clinically useful information about anatomic structures imaged through computer tomography (CT), magnetic resonance (MR), and other modalities. McInerney and Terzopoulos (1996) provide a survey on medical applications. For example, parametric curve models are used for measuring the area of leg ulcers (Jones and Plassmann, 2000) or extracting the contour of a cyst from ultrasound breast images (Yezzi et al., 1997). A primary use of parametric models is to measure the dynamic behavior of the human heart, especially the left ventricle (Herlin and Ayache, 1992; Geiger et al., 1995). This allows for isolating the severity and extent of diseases such as ischemia.

User interfaces: A computer equipped with a video camera can provide new perceptual interfaces between humans and machines. The computer can be controlled by gestures and motions captured by a camera (Azarbayejani et al., 1993). Furthermore, the video image can be augmented by artificial elements generated by the computer.

Surveillance and biometrics: In surveillance applications, contour tracking is used to follow and quantify the motions of persons or cars in a video sequence (Siebel, 2003; Sullivan, 1992). Tracking the articulated motion of a human body has several applications in biometrics and clinical gait analysis (Huang, 2001).

1.1.3 Requirements for a Curve-fitting Method

A method for curve-fitting has to meet several requirements in order to be widely applicable to practical computer vision problems:

Robustness: The method should be robust against several variations of the input data. In particular, the method should not fail even in the presence of clutter, texture, changing illumination, highlights, partial occlusion, and shadows. We say a method fails if the distance between the correct solution and the solution returned by the method exceeds a given limit.

Accuracy: In many applications, high sub-pixel accuracy is required. This is especially challenging for textured image regions.

Efficiency / Runtime: In particular, methods for object tracking have to be computationally efficient, i.e. their runtime should be low. The runtime should scale gradually with respect to

1. the resolution of the images. This allows for processing high resolution images within a limited time.
2. the dimension of the parameter vector. This allows for processing complex models, i.e. models with many parameters, within a limited time.

Any-time property: For many time-constrained applications, e.g. in the field of robotics, any-time algorithms are required. These algorithms yield at any time a solution whose quality improves, if more computation time is given (Boddy and Dean, 1994). This allows, for example, a vision-guided robot to react quickly on new image data and to continuously refine its action.

Versatility: The method should be versatile enough to cope with different classes of curve models. In particular, the method should be suitable for *rigid* and *deformable* models, as well as for *linear* and *non-linear* models. For non-linear curve models, the relations between points on the curve and the model parameter vector is non-linear. Relevant classes of curve models will be explained in appendix B.

1.2 The Contracting Curve Density (CCD) Approach

In this section we introduce the Contracting Curve Density (CCD) approach, a novel solution to the curve-fitting problem. We first identify two key questions in the design of curve-fitting methods. Then, in section 1.2.2, we sketch the CCD approach.

1.2.1 Key Questions

The curve-fitting problem that we informally introduced in section 1.1.1 can be formalized as a Bayesian inference problem. The maximum a posteriori (MAP) estimate $\widehat{\mathbf{\Phi}}$ of the model parameters $\mathbf{\Phi}$ is given as

$$\widehat{\mathbf{\Phi}} = \arg\max_{\mathbf{\Phi}} \; p(\mathbf{I}^* \mid \mathbf{\Phi}) \cdot p(\mathbf{\Phi}), \tag{1.1}$$

where $p(\mathbf{\Phi})$ is the a priori probability density of the model parameters and $p(\mathbf{I}^* \mid \mathbf{\Phi})$ is the observation probability density specifying the likely range of images $\mathbf{I}^*$ given the model parameters $\mathbf{\Phi}$. (The superscript $*$ indicates input data.) The conditional probability density $p(\mathbf{I}^* \mid \mathbf{\Phi})$ is also known as the likelihood or fitness function for the model parameters $\mathbf{\Phi}$. It evaluates the fit between the observed image data $\mathbf{I}^*$ and the assumed model parameters $\mathbf{\Phi}$. In order to implement the MAP estimation above, we have to address two *key questions*:

1. How can the likelihood function be approximated appropriately? In general, the actual likelihood function, i.e. the probabilistic relation between the model parameters $\mathbf{\Phi}$ and the image data $\mathbf{I}^*$, is not known. The image data not only depend on the model parameters, but also on other usually unknown properties of the scene, such as the illumination, surface properties, and characteristics of the camera. Approximating the likelihood is especially challenging in the presence of clutter and strong texture.

2. How can the fit be optimized *efficiently*, despite the existence of possibly multiple local optima?

Related curve-fitting methods address the first question by making some assumptions about the image data. For example, edge-based methods assume that the model curve coincides with edges in the image, where edges are usually defined by a maximum image gradient. Region-based methods assume that the image regions defined by the curve are homogeneous. In section 2.1, we will describe such assumptions in more detail. These assumptions are usually not flexible enough to cope with local variations of the image data, e.g. varying texture and clutter. Representative examples will be given in Figure 2.1 (page 15). The second question also poses a challenge for ongoing research. Existing optimization methods are often either inefficient or inaccurate, especially for high dimensional parameter vectors. In section 2.2, we will discuss different optimization methods used for curve-fitting.

1.2.2 Sketch of the CCD Approach

This section sketches two novel methods for curve-fitting, namely the CCD algorithm and the CCD tracker. The CCD algorithm solves the curve-fitting problem for a single image, whereas the CCD tracker solves it for a sequence of images. Let us start with the CCD algorithm. This algorithm iteratively refines the a priori distribution of the model parameters to an a posterior distribution of the parameters. This is achieved by alternately performing two steps until convergence:

1. **Learn local statistics** of the pixel values from the vicinity of the expected curve. In this step, for each pixel v in the vicinity of the expected curve, two sets of local statistics are computed, one set for each side of the curve. The local statistics are obtained from pixels that are close to pixel v and most likely lie on the corresponding side of the curve, according to the current estimate of the model parameters. The resulting local statistics represent an expectation of “what the two sides of the curve look like”.

2. **Refine the estimated model parameters** by assigning the pixels in the vicinity of the expected curve to the side they fit best, according to the local statistics. In this step, a likelihood function is constructed based on the local statistics. By optimizing the resulting MAP criterion, the model parameters are updated, thus changing the expected curve.

In the first step, the estimated model parameters are fixed and based on the fixed model parameters, local statistics of the pixel values are computed. In the second step, the local statistics are fixed and based on the local statistics, the estimated model parameters are updated.

This process is depicted in Figure 1.3. In this example, a radially distorted straight line[4] is being fitted to the image data. Here, the curve has just two parameters, namely the y-coordinates at the left and the right image border.[5] The input image and the estimated curve are depicted in row a) for different iteration steps. The image data expected, according to the learned local statistics, are depicted in row b). During the iteration, the estimated curve converges to the actual image curve, and the expected image data (row b) describe the actual vicinity of the image curve (row a) with increasing accuracy. During the fitting process, the probability density of the curve in the image contracts towards a single curve estimate. Therefore, we call the algorithm Contracting Curve Density (CCD) algorithm.

The CCD tracker is based on the CCD algorithm. It tracks a curve in an image sequence by performing two steps for each image:

1. **Fitting:** In the fitting step, the model curve is fitted to the image using a fast *real-time* variant of the CCD algorithm.

2. **Propagating:** In the propagating step, the parameters of the curve are propagated (predicted) over time, using a dynamical model which describes the set of likely curve motions. In addition, also local statistics of the pixel values can be propagated over time.

Using the propagation, the CCD tracker allows for exploiting two kinds of statistical dependencies between successive images: 1.) dependencies between successive curves (shapes and positions); and 2.) dependencies between successive pixel values.

1.3 Main Contributions of the Thesis

This thesis advances the state-of-the-art in curve-fitting in four important ways:

[4]The line is straight in 3-D coordinates, but due to the radial distortion caused by the lens, it appears curved in the image.

[5]In general, the curve model may have an arbitrary number of parameters.

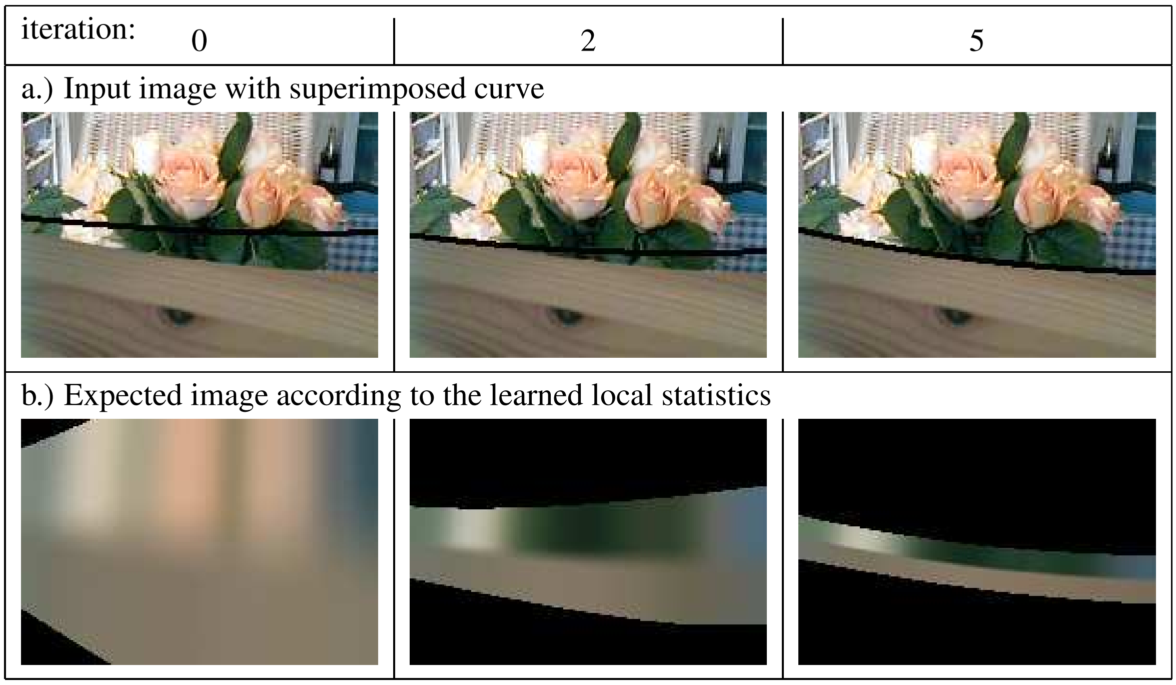
iteration:
0
2
5
a.) Input image with superimposed curve
b.) Expected image according to the learned local statistics

Figure 1.3: The CCD algorithm converges to the corresponding image curve, despite the heavy clutter and texture next to the initialization. During the iteration, the expected image data (row b) describe the actual vicinity of the image curve (row a) with increasing accuracy.

1. **We propose a likelihood function that can cope with highly inhomogeneous image regions:** The likelihood function is based on local image statistics, which are iteratively learned from the vicinity of the expected image curve. The local statistics allow for probabilistically separating adjacent regions even in the presence of spatially changing properties, such as texture, color, shading, or illumination. The resulting locally adapted separation criteria replace predefined fixed criteria (e.g. image gradients or homogeneity criteria). An efficient method is proposed for computing the required local statistics.

2. **We propose a "blurred model" as an efficient and robust means for optimization:** We optimize the MAP criterion, not only for a single vector of model parameters, but for a Gaussian distribution of model parameters. Thus, multiple curves are simultaneously taken into account. This can be seen as fitting a blurred curve model to the image data, where the local scale of blurring depends on the local uncertainty of the curve.

   In order to increase the capture range, other methods typically blur the image first and then fit a single model curve to the blurred image data, e.g. (Kass, Witkin, and Terzopoulos, 1988). We take the opposite approach. We use *non-blurred image data* and a *blurred model*. The advantages are as follows:

   (a) The capture range, i.e. the local scale, is enlarged according to the uncertainty of the model parameters. This yields, for each pixel and each iteration step, an individual compromise between the two conflicting goals, namely a large area of convergence and a high accuracy. Figure 1.3 row b) shows that the blurring in the direction perpendicular to the curve depends on the iteration step and the position along the curve. In the first iteration steps, the blurring is more intense at the right side than at the left side.

   (b) Optimizing the fit between an image and a blurred model is usually computationally cheaper than blurring the image. Especially if the uncertainty of the initialization is small, only a small fraction of the pixels covered by possible curve points is needed in order to refine the fit.

   (c) No high frequency information of the image data is lost. This is particularly important for separating textured regions or for achieving high sub-pixel accuracy.

3. **We propose the CCD algorithm for accurately and robustly fitting a parametric curve model to an image**: The method achieves a high level of accuracy and robustness, even in heavily cluttered and textured scenes. It can cope with partial occlusion, poor contrast, and changing illumination. Moreover, it reliably works also for curves with a relatively high number of parameters.

4. **We propose the CCD tracker, which allows for efficient, accurate, and robust object tracking**: The CCD tracker is based on a fast *real-time* variant of the CCD algorithm. This method achieves a high speed-up by using only a limited number of carefully chosen pixels lying in the vicinity of the expected curve. The algorithm yields, for each iteration step, a runtime complexity that is independent of the image resolution. Hence, even high-resolution images can be processed within limited time. We show that the method achieves sub-pixel accuracy and high robustness even if only a relatively small fraction of the pixels is taken into account. The CCD tracker gains additional robustness and accuracy by exploiting statistical dependencies between pixel values of successive images. The method clearly outperforms other state-of-the-art trackers.

Contribution 1 and 2 give two novel answers to the key questions raised in section 1.2.1. Contributions 3 and 4 are two novel methods for curve-fitting based on these answers.

1.4 Overview of the Thesis

The remainder of this thesis is organized as follows:

Chapter 2. In the next chapter, we classify the body of related work on curve-fitting and image segmentation according to several criteria. In particular, we discuss how related methods address the key questions raised in section 1.2.1.

Chapter 3. In chapter 3, we derive the Contracting Curve Density (CCD) algorithm. First, we give an overview of the method. Then we describe, in detail, the steps and sub-steps performed by the algorithm.

Chapter 4. In chapter 4, we derive an object tracking algorithm called the CCD tracker. To this end, we first propose a fast real-time variant of the CCD algorithm. We then show how two different kinds of statistical dependencies between successive images can be exploited in order to further increase the performance of the tracker.

Chapter 5. In chapter 5, we evaluate the performance of the CCD algorithm and the CCD tracker in terms of robustness, accuracy, and runtime. For the evaluation we use both semi-synthetic images and real images. Furthermore, we compare the CCD tracker with other state-of-the-art trackers.

Chapter 6. Finally, in chapter 6, we conclude this thesis.

Appendix A. Appendix A contains further results of different variants of the CCD algorithm.

Appendix B. In appendix B, we describe different classes of curve models used in this thesis.

Appendix C. Appendix C contains some remarks on our implementation.

Chapter 2

Related Work

In this chapter, we classify the body of related work according to the key questions raised in section 1.2.1. First, in section 2.1, we discuss how related methods construct an objective function that evaluates the quality of the fit. Then, in section 2.2, we describe different methods used for optimizing the fit. Finally, in section 2.3, we classify related work according to alternative dimensions.

2.1 Classification according to the Objective Function

Existing methods for curve-fitting typically optimize, explicitly or implicitly, an objective function that evaluates the quality of the fit. Such an objective function is, for example, the posterior density of the model parameters, see equation (1.1). It usually consists of two parts: The first, the likelihood function, evaluates the fit between the model parameters and the image data. The second part, the a priori distribution, evaluates the fit of the model parameters to the a priori knowledge. Often, the two parts are not expressed in terms of probabilities, but as energies. For example, Kass, Witkin, and Terzopoulos (1988) use the terms “external energy” and “internal energy”. The former corresponds to the likelihood function while the latter corresponds to the a priori distribution.

In order to obtain a likelihood function, curve-fitting methods usually make some assumptions about the image data and the associated curve. These assumptions correspond to image segmentation criteria commonly used in the image segmentation literature. In this section, we first discuss these image segmentation criteria. Then, at the end of this section, we describe how related model-based methods construct an objective function based on the image segmentation criteria. We distinguish four (not disjunct) categories: edge-based, region-based, hybrid, and graph-theoretic segmentation methods.

Edge-based Segmentation

Edge-based segmentation (also referred to as boundary-based segmentation) methods assume that region boundaries coincide with discontinuities of the pixel value or their spatial derivatives. Different edge-profiles, i.e. types of discontinuities, are used: step-edge (Baker, Nayar, and Murase, 1998; Nalwa and Binford, 1986; Canny, 1986), roof-edge (Baker, Nayar, and Murase, 1998; Nalwa and Binford, 1986), and others (Baker, Nayar, and Murase, 1998; Nalwa and Binford, 1986; Cootes et al., 1994). The problem of edge-based segmentation is that usually the edge-profile is not known in practice. Furthermore, in typical images, the profile often varies heavily along the edge caused by, e.g. shading and texture. Due to these difficulties, often a simple step-edge is assumed and edge detection is performed based on a maximum magnitude of image gradient. In Figure 2.1a, the color values on either side of the mug's contour are not constant even within a small vicinity. Hence, methods maximizing the magnitude of the image gradient have difficulties separating the mug and the background. Figure 2.1b shows the result of a typical edge-based segmentation method. Three kinds of difficulties can be observed:

1. Edges not corresponding to the object boundary are detected (false positives).
2. Parts of the object boundary are not detected (false negatives).
3. Some detected edges are very inaccurate due to the inhomogeneities.

These problems may be alleviated by performing edge detection without assuming a particular edge profile. Ruzon and Tomasi (2001) maximize a distance measurement, called the earth mover's distance, between the color distributions of two adjacent windows. However, this approach is computationally expensive.

Region-based Segmentation

Region-based segmentation methods assume that the pixel values within one region satisfy a specific homogeneity criterion. Most of these methods assume that the pixel values of all pixels within one region are statistically independently distributed according to the same probability density function (Zhu and Yuille, 1996; Chesnaud, Refregier, and Boulet, 1999; Mirmehdi and Petrou, 2000). Methods using Markov random fields (MRF) explicitly model the statistical dependency between neighboring pixels which allows for characterizing textures. MRF methods have been proposed for gray value images (Geman and Geman, 1984; Li, 2001) and color images (Bouman and Sauer, 1993; Panjwani and Healey, 1995; Bennett and

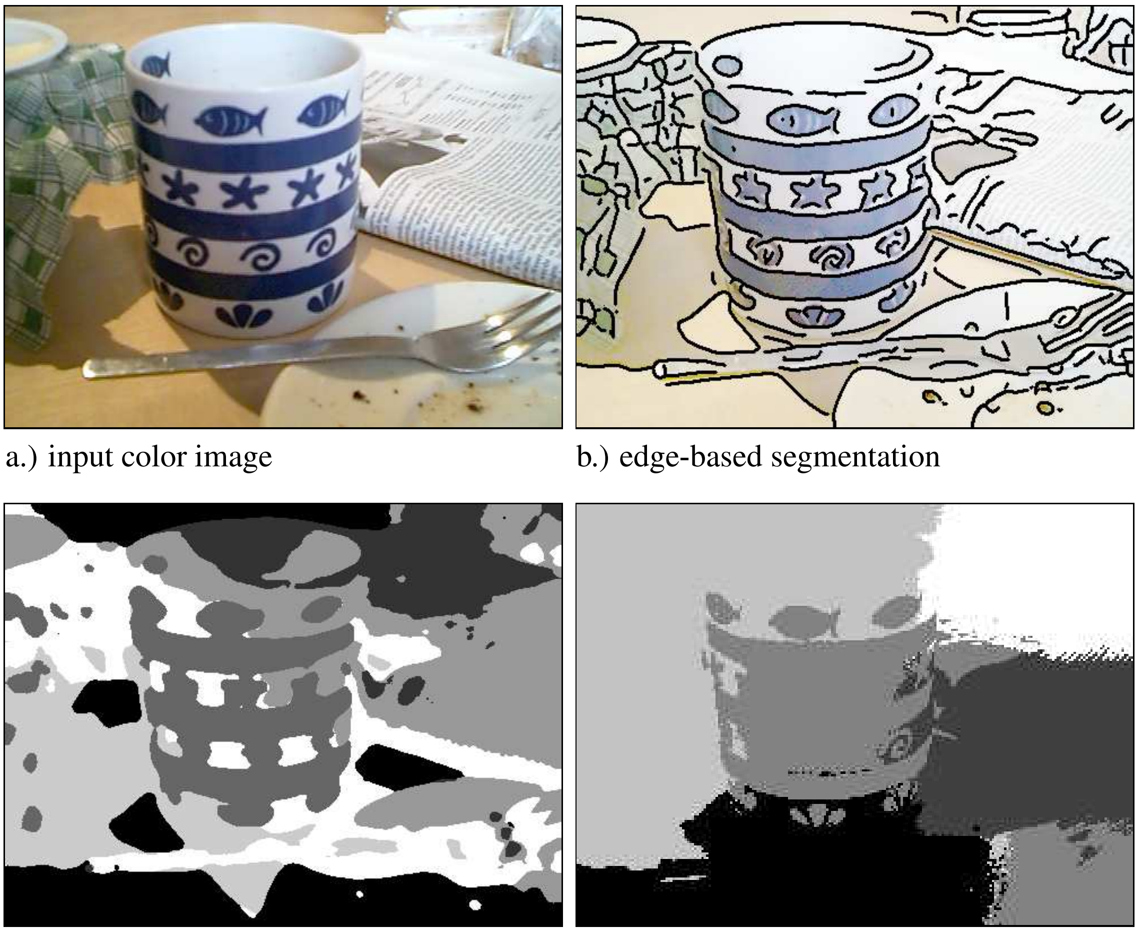
a.) input color image
b.) edge-based segmentation
c.) region-based segmentation
d.) graph-theoretic segmentation

Figure 2.1: Different categories of image segmentation methods: a) Input color image b.) Color edges detected by a gradient-based method (Steger, 2000). c.) Result of a region-based method (Hermes, Zöller, and Buhmann, 2002). d.) Result of a graph-theoretic method called *normalized cuts* (Shi and Malik, 2000) - All three approaches fail to accurately separate the mug and the background region. These methods do not exploit (nor require) model knowledge about the shape of the mug.

Khotanzad, 1998). In section 3.2.2.1, we discuss the similarities and differences between MRF methods and the CCD algorithm proposed in this thesis.

In contrast to edge-based methods, region-based methods do not require an edge-profile. Furthermore, they are able to exploit higher statistical moments of the distributions. For example, two regions which have the same mean pixel value but different covariance matrices (e.g. caused by texture) can be separated. However, often the underlying homogeneity assumption does not hold for the entire region. In Figure 2.1a both the mug region and the background region are inhomogeneous. Hence, the region-based method employed in Figure 2.1c fails to accurately separate the mug and the background region.

Hybrid Segmentation

Hybrid segmentation methods, also known as integrating segmentation methods, try to overcome the individual shortcomings of edge-based and region-based segmentation by integrating both segmentation principles (Thirion et al., 2000; Paragios and Deriche, 2000; Chakraborty and Duncan, 1999; Jones and Metaxas, 1998). Hybrid methods seek a tradeoff between an edge-based criterion, e.g. the magnitude of the image gradient, and a region-based criterion evaluating the homogeneity of the regions. However, it is doubtful whether a tradeoff between the two criteria yields reasonable results when both the homogeneity assumption and the assumption regarding the edge profile do not hold as in Figure 2.1a.

Graph-theoretic Segmentation

Graph-theoretic methods formulate the problem of image segmentation as a graph-theoretic problem (Shi and Malik, 2000; Felzenszwalb and Huttenlocher, 1998; Cox, Zhong, and Rao, 1996; Wu and Leahy, 1993). The image is represented by a weighted undirected graph. The pixels are the nodes of the graph and each pair of neighboring nodes is connected by an edge. The edges are labeled by edge weights quantifying the similarity between the connected pixels. Image segmentation is achieved by removing edges, i.e. cutting the graph into disjoint subgraphs. Suitable cuts are found by minimizing a cost function evaluating the weights of the removed edges. Figure 2.1d depicts the result of the *normalized cuts* algorithm (Shi and Malik, 2000). This method also fails to accurately segment the mug. We suppose that this failure is caused by the predefined similarity function used for computing the weights of the edges. The edge weights only depend on the two pixels connected by the edge. The similarity function does not take the neighborhood of the pixels into account. Hence, the resulting separation criterion does not adapt to the local context of the pixels to be separated.

In order to separate adjacent regions, we do not rely on a predefined fixed edge profile, homogeneity criterion, or similarity measure. Instead, we propose locally adapted separation criteria which are iteratively learned from the vicinity of the curve.

Constructing an Objective Function

Let us now describe how related methods construct an objective function, based on the segmentation criteria discussed above. We distinguish two classes: *feature-extracting* and *non-feature-*

extracting methods.

Feature-extracting methods perform two steps. First salient features, e.g. edge points or region boundaries, are extracted using image segmentation methods as described above. In this step, the image data is substantially reduced to a relatively small set of image features. Then, in the second step, a likelihood function is constructed based on the deviation between the extracted image features and the assumed model curve. In this step, most methods assume that 1.) the errors of extracted features are mutually *statistically independent*, and 2.) the errors are distributed according to the same *constant* and *known* probability density function. Unfortunately, these assumptions do not usually hold, for example, if the illumination is changing. Based on these assumptions, a likelihood function can be obtained quite efficiently. The process of fitting a model to a set of extracted image features is also known as *matching*.

If relevant image features can be extracted reliably, this two-step approach can be very efficient (Blake and Isard, 1998; Lanser, 1997; Xu and Prince, 1998; Luo et al., 2000). In tracking applications, image features can often be found reliably based on background subtraction, if the background, the illumination, and the camera are fixed (Deutscher, Blake, and Reid, 2000; Hansen, 2002). Curve-fitting methods using previously extracted image features have been proposed, e.g. for pose estimation (Lowe, 1991; Hanek, Navab, and Appel, 1999), self-localization (Schmitt et al., 2002), 3-D reconstruction (Sullivan and Ponce, 1998), image segmentation (Cootes et al., 1994), and tracking (Harris., 1992; Koller, Daniilidis, and Nagel, 1993; Blake and Isard, 1998).

Often image features cannot be extracted reliably, see Figure 2.1. The problem caused by missing features and outliers can be alleviated, to some extent, by robust objective functions, i.e. robust estimators (Beck and Arnold, 1977; Huber, 1981; Werman and Keren, 2001; Fitzgibbon, Pilu, and Fisher, 1999; Zhang, 1997; Dierckx, 1993; Blake and Isard, 1998).

Non-feature-extracting methods do not reduce the image data to a relatively small set of image features. They employ a likelihood function based on the dense image data rather than on sparse image features (Kass, Witkin, and Terzopoulos, 1988; Pece and Worrall, 2002; Robert, 1996; Kollnig and Nagel, 1995; Ulrich et al., 2001; Ronfard, 1994). For example Kass, Witkin, and Terzopoulos (1988) obtain the "external energy", which corresponds to the likelihood function, by integrating the spatial derivatives of the pixel values along the assumed curve. Unlike feature-extracting methods, non-feature-extracting methods usually do not make decisions based on local image properties only. Hence, such methods may be applied even if suitable image features cannot be extracted reliably, e.g. in Figure 2.1a. The CCD algorithm proposed here belongs to the class of non-feature-extracting methods.

In order to construct an objective function, evidence from the image data and the a priori knowledge have to be weighted appropriately. Usually a heuristically obtained weighting parameter is applied, e.g. by Kass, Witkin, and Terzopoulos (1988). The CCD algorithm derives the weighting directly from the image statistics. Hence, for example, if a camera with less noise is used or the illumination changes, the CCD algorithm automatically adapts the weighting between the image data and the a priori knowledge.

2.2 Classification according to the Optimization Method

Methods for curve-fitting can be classified according to the optimization technique. Global and local optimization methods are applied.

Global Optimization Methods

Several global optimization methods are employed for curve fitting. These methods can be classified in *deterministic* and *stochastic* methods. Deterministic methods include *dynamic programming* and other *shortest path algorithms* (Amini, Weymouth, and Jain, 1990; Geiger et al., 1995; Mortensen and Barrett, 1998; Dubuisson-Jolly and Gupta, 2001; Coughlan et al., 1998) as well as *Hough transform* (Hough, 1962; Ballard, 1981). These methods require a discretization of the search space, which usually leads to a limited accuracy or to a high computational cost, depending on the number of discretization levels.

Stochastic methods are methods such as *Monte Carlo* optimization or *simulated annealing*. The former is also known as particle filter or the *condensation* algorithm (Isard and Blake, 1996; Li, Zhang, and Pece, 2003). Particle filters have been applied successfully, e.g. for tracking. However, the computational cost of particle filters increases exponentially with respect to the dimension of the search space (the dimension of the parameter vector) (MacCormick and Isard, 2000). Usually, particle filters are fast and accurate only if the search space is of low dimension or sufficiently small. Simulated annealing (Geman and Geman, 1984; Storvik, 1994; Bongiovanni, Crescenzi, and Guerra, 1995) is generally computationally demanding.

Local Optimization Methods

Local optimization methods may achieve a fast, i.e. quadratic, convergence (Press et al., 1996). Approaches aiming to increase the area of convergence such as (Kass, Witkin, and Terzopoulos, 1988; Xu and Prince, 1998; Luo et al., 2000) are edge-based. For methods maximizing the image gradient, the area of convergence depends on the window size used for computing the spatial derivatives. Often a multi-scale description of the image data is used. First, the curve model is fitted to a large scale description yielding a smoothed objective function. Then, the blurring of the image data, i.e. the window size, is gradually reduced. Scale-space theory provides means for automatic scale selection (Lindeberg, 1998). However, blurring the image data eliminates useful high frequency information.

In this thesis, we propose a local optimization method which achieves a large area of convergence and a high accuracy with a relatively small number of iterations (see section 3.3.2).

2.3 Classification according to other Dimensions

Methods for curve-fitting and image segmentation can be further classified according to the used image cues. Several methods integrate different image cues such as texture together with color or brightness (Belongie et al., 1998; Malik et al., 1999; Manduchi, 1999; Thirion et al., 2000; Panjwani and Healey, 1995; Zhong, Jain, and Dubuisson-Jolly, 2000; Zöller, Hermes, and Buhmann, 2002; Mirmehdi and Petrou, 2000; Konishi et al., 2003). We use local statistics which jointly characterize texture, color, and brightness.

Methods for curve-fitting can be further classified according to the types of possible curve models. Some methods, e.g. (Blake and Isard, 1998), require linear curve models; that is, the relation between a point on the curve and the model parameters has to be linear. Our method can cope with both the linear and non-linear cases.

Several methods use a priori knowledge about the pixel values, e.g. intensity or color values (Cootes et al., 1993; Schmitt et al., 2002; Cootes, Edwards, and Taylor, 2001). This has been proven to be very helpful in applications where such a priori knowledge is given with sufficient accuracy. However, in this thesis we address problems where such a priori knowledge is not given. Our method iteratively learns a local model of the pixel values from the pixels in the vicinity of the expected image curve.

Chapter 3

The CCD Algorithm

In this chapter we describe the Contracting Curve Density (CCD) algorithm, a novel curve-fitting algorithm that has been successfully applied to different challenging problems, e.g. model-based image segmentation and object localization (Hanek, 2001b; Hanek, 2001a; Hanek et al., 2002b; Hanek and Beetz, 2004). First, in section 3.1, we give a brief overview of the algorithm. Sections 3.2 and 3.3 then describe, in detail, the two main steps of the algorithm. Finally, we summarize the algorithm in section 3.4.

3.1 Overview

The CCD algorithm fits a parametric curve model to an image. The algorithm determines the vector of model parameters that best match the image data and a given a priori distribution of model parameters.

3.1.1 Input and Output Data

The input of the CCD algorithm consists of the image data and the curve model.

Image data: The image, denoted by $\mathbf{I}^*$, is a matrix of *pixel values*. The superscript $*$ indicates input data. The pixel value $\mathbf{I}^*_p$ is a vector of local single- or multi-channel image data associated with pixel p. In this thesis we use raw RGB values. However, other types of local features computed in a pre-processing step may also be used, e.g. texture descriptors (Portilla and Simoncelli, 2000; Clausi and Jernigan, 2000) or color values in a different color space (Luong, 1993).

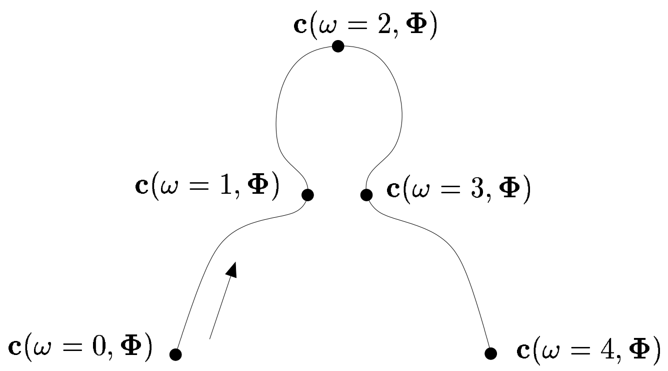
$\mathbf{c}(\omega = 2, \mathbf{\Phi})$
$\mathbf{c}(\omega = 1, \mathbf{\Phi})$
$\mathbf{c}(\omega = 3, \mathbf{\Phi})$
$\mathbf{c}(\omega = 0, \mathbf{\Phi})$
$\mathbf{c}(\omega = 4, \mathbf{\Phi})$

Figure 3.1: Curve defined by a curve function $\mathbf{c}$: The vector of model parameters $\mathbf{\Phi}$ specifies the shape of a particular curve. The scalar ω specifies an individual point on this curve.

Curve model: The curve model is composed of two parts:

1. A *curve function* $\mathbf{c}(\omega, \mathbf{\Phi})$ describing a set of possible model curves in pixel coordinates. The vector of model parameters $\mathbf{\Phi}$ specifies a particular curve, i.e. a particular shape, of the set of possible curves. The scalar ω specifies an individual point on the curve defined by $\mathbf{\Phi}$. The scalar ω monotonically increases as the curve $\mathbf{c}(\cdot, \mathbf{\Phi})$ is traversed, see Figure 3.1. For example, ω could correspond to the arc length of the curve between a starting point $\mathbf{c}(0, \mathbf{\Phi})$ and the point $\mathbf{c}(\omega, \mathbf{\Phi})$. Such curve functions are often used in computer vision (Kass, Witkin, and Terzopoulos, 1988; Blake and Isard, 1998). Models with multiple curve segments, as in Figure 5.12 on page 94, can be described using multiple curve functions. Appendix B gives more details about the curve functions used in this thesis.

2. A Gaussian *a priori distribution* $p(\mathbf{\Phi}) = p(\mathbf{\Phi} \mid \mathbf{m}^*_{\mathbf{\Phi}}, \mathbf{\Sigma}^*_{\mathbf{\Phi}})$ of the model parameters $\mathbf{\Phi}$, defined by the mean vector $\mathbf{m}^*_{\mathbf{\Phi}}$ and the covariance matrix $\mathbf{\Sigma}^*_{\mathbf{\Phi}}$. Depending on the application, the quantities $\mathbf{m}^*_{\mathbf{\Phi}}$ and $\mathbf{\Sigma}^*_{\mathbf{\Phi}}$ may, for example, be supplied by an user or obtained from a prediction over time. Sclaroff and Liu (2001) obtain object hypotheses from an over-segmented image. Object hypotheses can also be generated by global optimization methods, e.g. Monte Carlo methods (Blake and Isard, 1998) or Hough transform (Hough, 1962).

The output of the algorithm consists of the maximum a posteriori (MAP) estimate $\mathbf{m}_{\mathbf{\Phi}}$ of the model parameter vector $\mathbf{\Phi}$ and the corresponding covariance matrix $\mathbf{\Sigma}_{\mathbf{\Phi}}$. The estimate $\mathbf{m}_{\mathbf{\Phi}}$ specifies the best fit of the curve to the image data $\mathbf{I}^*$ and the a priori distribution $p(\mathbf{\Phi})$. The covariance matrix $\mathbf{\Sigma}_{\mathbf{\Phi}}$ defines the expected uncertainty of the estimate. The estimate $\mathbf{m}_{\mathbf{\Phi}}$ and the covariance $\mathbf{\Sigma_\Phi}$ describe a Gaussian approximation $p(\mathbf{\Phi} \mid \mathbf{m_\Phi}, \mathbf{\Sigma_\Phi})$ of the posterior density $p(\mathbf{\Phi} \mid \mathbf{I}^*)$.

3.1.2 Steps of the CCD Algorithm

The CCD algorithm represents its belief of the model parameter vector by a Gaussian distribution. We denote the mean vector, the current estimate of the model parameters, by $\mathbf{m_\Phi}$, and the corresponding covariance matrix by $\mathbf{\Sigma_\Phi}$. The quantities $\mathbf{m_\Phi}$ and $\mathbf{\Sigma_\Phi}$ are initialized using the mean $\mathbf{m}^*_\mathbf{\Phi}$ and covariance $\mathbf{\Sigma}^*_\mathbf{\Phi}$ of the a priori distribution:

$$\mathbf{m_\Phi} = \mathbf{m}^*_\mathbf{\Phi} \tag{3.1}$$

$$\mathbf{\Sigma_\Phi} = c_1 \cdot \mathbf{\Sigma}^*_\mathbf{\Phi}. \tag{3.2}$$

Here, the scaling factor $c_1 > 1$ can be used to increase the initial uncertainty of the curve and thereby it further enlarges the capture range of the CCD algorithm. For the moment, assume that $c_1 = 1$.

The CCD algorithm refines its belief of the model parameters, i.e. the mean vector $\mathbf{m_\Phi}$ and the covariance matrix $\mathbf{\Sigma_\Phi}$, by iterating two steps as shown in Figure 3.2. In the first step, the mean vector $\mathbf{m_\Phi}$ and the covariance matrix $\mathbf{\Sigma_\Phi}$ are fixed. Based on the fixed $\mathbf{m_\Phi}$ and $\mathbf{\Sigma_\Phi}$, local statistics of the pixel values are learned from the vicinity of the expected curve. In the second step, the local statistics are fixed. The mean vector $\mathbf{m_\Phi}$ and the covariance matrix $\mathbf{\Sigma_\Phi}$ are updated by assigning the pixels in the curve's vicinity to the side they fit best according to the local statistics.

At the beginning, usually the uncertainty about the location and shape of the curve is high. Due to this high uncertainty, the windows used for computing the local statistics are relatively large and not close to the actual image curve. Hence, the resulting statistics describe the vicinity of the image curve only roughly, see Figure 1.3 on page 10. As a consequence, after the first iteration step the uncertainty is only partially reduced.

Due to the partial reduction of uncertainty, in the next iteration step, the windows used for computing the local statistics are less wide and closer to the actual image curve. The resulting statistics, thus, describe the vicinity of the curve better than the previous statistics. This yields, in turn, a better estimate of the curve parameters and a further reduction of the uncertainty. The CCD algorithm iterates these two steps until convergence, i.e. until the changes of the estimate $\mathbf{m_\Phi}$ and the covariance matrix $\mathbf{\Sigma_\Phi}$ are below some given thresholds. During the iterations, the probability density of the curve in the image contracts towards a single curve estimate.

Outline of the Contracting Curve Density (CCD) algorithm

Input: image data $\mathbf{I}^*$, curve function $\mathbf{c}$, mean vector $\mathbf{m}^*_{\mathbf{\Phi}}$, and covariance matrix $\mathbf{\Sigma}^*_{\mathbf{\Phi}}$
Output: estimate $\mathbf{m}_{\mathbf{\Phi}}$ of the model parameter vector and associated covariance matrix $\mathbf{\Sigma}_{\mathbf{\Phi}}$

Initialization: $\mathbf{m}_{\mathbf{\Phi}} = \mathbf{m}^*_{\mathbf{\Phi}}$, $\mathbf{\Sigma}_{\mathbf{\Phi}} = c_1 \cdot \mathbf{\Sigma}^*_{\mathbf{\Phi}}$
repeat

1. **Learn local statistics** of the pixel values from the vicinity of the expected curve based on the current mean vector $\mathbf{m}_{\mathbf{\Phi}}$ and the current covariance matrix $\mathbf{\Sigma}_{\mathbf{\Phi}}$. The resulting local statistics characterize the two sides of the curve. This step consists of two substeps:
   (a) Determine the pixels in the vicinity of the expected image curve and assign them probabilistically to either side of the curve, based on $\mathbf{m}_{\mathbf{\Phi}}$ and $\mathbf{\Sigma}_{\mathbf{\Phi}}$.
   (b) Compute local image statistics for both curve sides. For each side use only the set of pixels assigned to that side in (a). These local statistics are obtained using local windows, i.e. weights which are adapted in size and shape to the expected curve and its uncertainty, see Figure 3.3. The resulting local statistics represent an expectation of "what the two sides of the curve look like".
2. **Refine the estimate** of the model parameter vector. This step consists of two substeps:
   (a) Update the mean vector $\mathbf{m}_{\mathbf{\Phi}}$ using a maximum a posteriori (MAP) criterion derived from the local statistics. In this step, the mean vector $\mathbf{m}_{\mathbf{\Phi}}$ is modified such that the pixels are assigned to the side of the curve they fit best according to the local statistics computed in step 1.
   (b) Update the covariance matrix $\mathbf{\Sigma}_{\mathbf{\Phi}}$ based on the Hessian of the objective function used in (a).

until changes of $\mathbf{m}_{\mathbf{\Phi}}$ and $\mathbf{\Sigma}_{\mathbf{\Phi}}$ are small enough
Post-processing: estimate the covariance matrix $\mathbf{\Sigma}_{\mathbf{\Phi}}$ from the Hessian of objective function
return mean vector $\mathbf{m}_{\mathbf{\Phi}}$ and covariance matrix $\mathbf{\Sigma}_{\mathbf{\Phi}}$

Figure 3.2: The CCD algorithm iteratively refines a Gaussian a priori density $p(\mathbf{\Phi}) = p(\mathbf{\Phi} \mid \mathbf{m}^*_{\mathbf{\Phi}}, \mathbf{\Sigma}^*_{\mathbf{\Phi}})$ of model parameters to a Gaussian approximation $p(\mathbf{\Phi} \mid \mathbf{m}_{\mathbf{\Phi}}, \mathbf{\Sigma}_{\mathbf{\Phi}})$ of the posterior density $p(\mathbf{\Phi} \mid \mathbf{I}^*)$.

Therefore, we call the algorithm *Contracting Curve Density (CCD)* algorithm. Figure 3.3 depicts the process for two iteration steps.

Without making any assumptions about the image data $\mathbf{I}^*$ and the curve functions $\mathbf{c}$, it is difficult to prove convergence or to derive the speed of convergence. However, our experiments with challenging image data show that the area of convergence is quite large and that already a small number of iterations, i.e. 5 to 20, is sufficient to reduce the initial uncertainty by more than 99%.

The CCD algorithm has some similarities to the Expectation-Maximization (EM) algorithm (Dempster, Laird, and Rubin, 1977). The EM algorithm is often used for clustering-based image segmentation, which is a subset of region-based image segmentation (Hermes, Zöller, and Buhmann, 2002; Belongie et al., 1998). The first step computes local statistics defining an expectation of the pixel values (E-step). The second step maximizes this expectation (M-step). The CCD algorithm differs mainly by: 1.) using local statistics, 2.) exploiting a curve model and optimizing model parameters rather than pixel classifications.

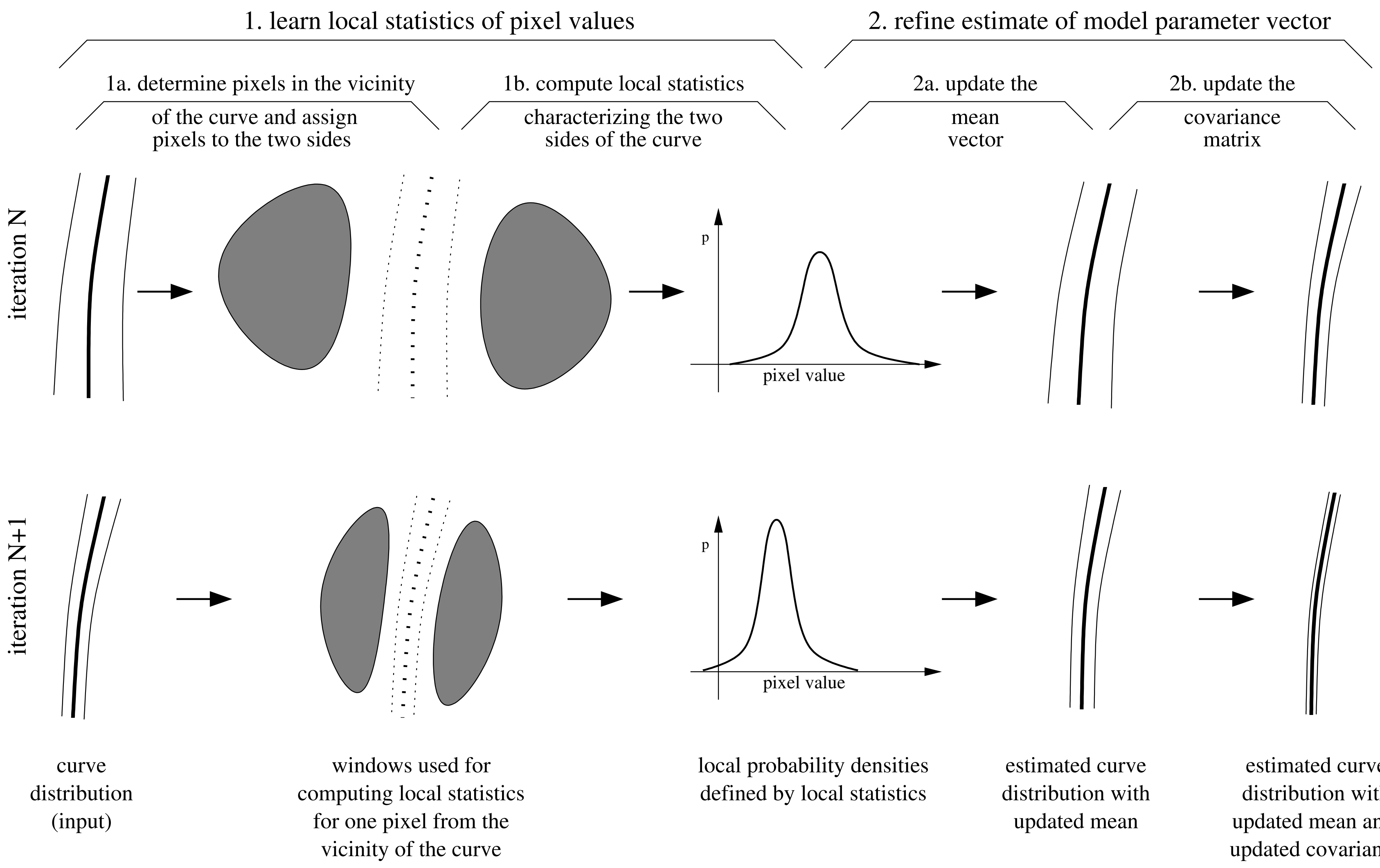
1. learn local statistics of pixel values
2. refine estimate of model parameter vector
1a. determine pixels in the vicinity of the curve and assign pixels to the two sides
1b. compute local statistics characterizing the two sides of the curve
2a. update the mean vector
2b. update the covariance matrix
iteration N
iteration N+1
p
pixel value
p
pixel value
curve distribution (input)
windows used for computing local statistics for one pixel from the vicinity of the curve
local probability densities defined by local statistics
estimated curve distribution with updated mean
estimated curve distribution with updated mean and updated covariance

Figure 3.3: In each iteration of the CCD algorithm two steps are performed: 1. learn local statistics of pixel values from the vicinity of the expected curve; and 2. refine the estimate of the model parameter vector by assigning the pixels to the side they fit best according to the local statistics. Both steps consist of two substeps.

3.2 Learning Local Statistics

Let us now describe, in detail, how the CCD algorithm learns the local statistics. This step consists of two substeps. Step 1a (section 3.2.1) determines the set of pixels in the vicinity of the expected image curve and probabilistically assigns them to either side of the curve, based on the current belief of the model parameters. Then, step 1b (section 3.2.2) computes local statistics of the pixel values for each of the two curve sides.

3.2.1 Determining the Pixels in the Vicinity of the Image Curve

The Gaussian distribution of model parameters $p(\mathbf{\Phi} \mid \mathbf{m}_\mathbf{\Phi}, \mathbf{\Sigma}_\mathbf{\Phi})$ and the model curve function $\mathbf{c}$ define a probability distribution of the curve in the image. This curve distribution probabilistically assigns pixels in the vicinity of the curve to either side of the curve. In this section, the computation of the probabilistic assignments is derived.

The assignment $\mathbf{a}_v(\mathbf{m}_\mathbf{\Phi}, \mathbf{\Sigma}_\mathbf{\Phi}) = (a_{v,1}(\mathbf{m}_\mathbf{\Phi}, \mathbf{\Sigma}_\mathbf{\Phi}), a_{v,2}(\mathbf{m}_\mathbf{\Phi}, \mathbf{\Sigma}_\mathbf{\Phi}))^T$ of a pixel v is a function of the mean $\mathbf{m}_\mathbf{\Phi}$ and the covariance $\mathbf{\Sigma}_\mathbf{\Phi}$. The first component $a_{v,1} \in [0, 1]$ describes to which extent pixel v is expected to be influenced by side 1 of the curve. The second component is the equivalent for side 2 given by $a_{v,2} = 1 - a_{v,1}$. Before we define the assignment of a pixel v for a distribution of model parameters, we first define the assignment $\tilde{a}_{v,1}(\mathbf{\Phi})$ for a single vector $\mathbf{\Phi}$ of model parameters. We model a standard charge-coupled device image sensor, which integrates the radiance function over the photosensitive element of the pixel (Baker, Nayar, and Murase, 1998). The assignment $\tilde{a}_{v,1}(\mathbf{\Phi})$ is the fraction of the photosensitive area which belongs to side 1. It is given as an integral over the photosensitive area A_v of pixel v:

$$\tilde{a}_{v,1}(\mathbf{\Phi}) \;=\; \frac{1}{|A_v|} \int_{A_v} l(\mathbf{x}, \mathbf{\Phi}) \, d\mathbf{x}, \tag{3.3}$$

where $|A_v|$ is the size of the photosensitive area and the label function $l(\mathbf{x}, \mathbf{\Phi})$ indicates on which side of the curve the point $\mathbf{x}$ lies:

$$l(\mathbf{x}, \mathbf{\Phi}) \;=\; \begin{cases} 1 & \text{if point } \mathbf{x} \text{ is on side 1 of the image curve } \mathbf{c}(\cdot, \mathbf{\Phi}) \\ 0 & \text{otherwise} \quad . \end{cases} \tag{3.4}$$

We define the probabilistic assignment $a_{v,1}(\mathbf{m}_\mathbf{\Phi}, \mathbf{\Sigma}_\mathbf{\Phi})$ induced by the Gaussian distribution $p(\mathbf{\Phi} \mid \mathbf{m}_\mathbf{\Phi}, \mathbf{\Sigma}_\mathbf{\Phi})$ of model parameters as the expectation of $\tilde{a}_{v,1}(\mathbf{\Phi})$:

$$\begin{aligned} a_{v,1}(\mathbf{m}_\mathbf{\Phi}, \mathbf{\Sigma}_\mathbf{\Phi}) &= \mathcal{E}[\tilde{a}_{v,1}(\mathbf{\Phi})] & (3.5) \\ &= \int_{I\!R^{D_\mathbf{\Phi}}} \tilde{a}_{v,1}(\mathbf{\Phi}) \cdot p(\mathbf{\Phi} \mid \mathbf{m}_\mathbf{\Phi}, \mathbf{\Sigma}_\mathbf{\Phi}) \, d\mathbf{\Phi}, & (3.6) \end{aligned}$$

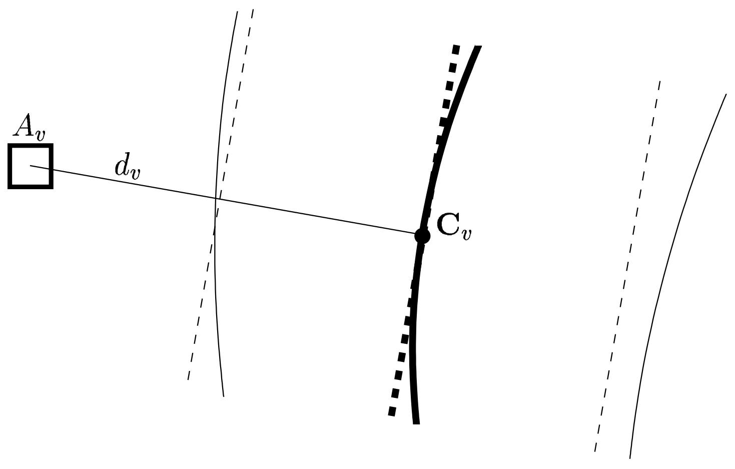

Figure 3.4: Local linear approximation (thick dashed line) of the curve function (thick solid line). The thin solid and thin dashed lines indicate the confidence interval of the curve and its approximations, respectively.

where $D_{\mathbf{\Phi}}$ denotes the dimension of the model parameter vector $\mathbf{\Phi}$. For an arbitrary curve function $\mathbf{c}$, the probabilistic assignments cannot be computed in a closed form due to the integrations in equations (3.3) and (3.6). We next derive an efficient approximation of these assignments.

Efficient Approximation of the Assignments

For each pixel v we approximate the curve function $\mathbf{c}(\omega, \mathbf{\Phi})$ in the vicinity of $(\omega_v, \mathbf{m_\Phi})$ by a function that is linear in ω and in $\mathbf{\Phi}$. The value ω_v is chosen such that $\mathbf{C}_v := c(\omega_v, \mathbf{m_\Phi})$ is the point on the 'mean' curve $\mathbf{c}(\cdot, \mathbf{m_\Phi})$ that is closest to the center of gravity of the photosensitive area A_v, see Figure 3.4. For a linear curve function $\mathbf{c}$, the point $\mathbf{c}(\omega_v, \mathbf{\Phi})$ is Gaussian distributed with mean vector $\mathbf{C}_v = c(\omega_v, \mathbf{m_\Phi})$ and covariance matrix $\mathbf{J}_v \cdot \mathbf{\Sigma_\Phi} \cdot \mathbf{J}_v^T$. The matrix $\mathbf{J}_v$ denotes the Jacobian of $\mathbf{c}$, i.e. the partial derivatives of $\mathbf{c}$ with respect to the model parameters $\mathbf{\Phi}$, in the point $(\omega_v, \mathbf{m_\Phi})$. The displacement $D_v(\mathbf{x}, \mathbf{\Phi})$, i.e. the signed distance, between a point $\mathbf{x} \in A_v$ and the curve $\mathbf{c}(\cdot, \mathbf{\Phi})$ can be approximated by

$$D_v(\mathbf{x}, \mathbf{\Phi}) \quad = \quad \mathbf{n}_v^T \cdot (\mathbf{x} - c(\omega_v, \mathbf{\Phi})), \tag{3.7}$$

where $\mathbf{n}_v^T$ is the unit normal vector to the curve at the point $\mathbf{c}(\omega_v, \mathbf{m_\Phi})$. For a linear curve function $\mathbf{c}$, the displacement $D_v(\mathbf{x}, \mathbf{\Phi})$ is Gaussian distributed, $D_v(\mathbf{x}, \mathbf{\Phi}) \sim \mathcal{N}(d_v(\mathbf{x}), \sigma_v^2)$. Its mean $d_v(\mathbf{x})$ is given by

$$d_v(\mathbf{x}) = \mathbf{n}_v^T \cdot (\mathbf{x} - \mathbf{C}_v) \tag{3.8}$$

and its variance σ_v^2 holds

$$\sigma_v^2 = \mathbf{n}_v^T \cdot \mathbf{J}_v \cdot \mathbf{\Sigma}_{\mathbf{\Phi}} \cdot \mathbf{J}_v^T \cdot \mathbf{n}_v. \tag{3.9}$$

The variance σ_v^2 describes the uncertainty of the curve along the curve normal, induced by the covariance $\mathbf{\Sigma}_{\mathbf{\Phi}}$. [1] The probability $p_{v,1}(\mathbf{x}, \mathbf{m}_{\mathbf{\Phi}}, \mathbf{\Sigma}_{\mathbf{\Phi}})$ that a point $\mathbf{x}$ lies on side 1 of the curve can be obtained by integrating the Gaussian probability density function (pdf) of the displacement $D_v(\mathbf{x}, \mathbf{\Phi})$, which yields

$$p_{v,1}(\mathbf{x}, \mathbf{m}_{\mathbf{\Phi}}, \mathbf{\Sigma}_{\mathbf{\Phi}}) = \frac{1}{2} \cdot \mathit{erf}\left(\frac{d_v(\mathbf{x})}{\sqrt{2} \cdot \sigma_v}\right) + \frac{1}{2}, \tag{3.10}$$

where $\mathit{erf}(\cdot)$ is the error function. Finally, the probabilistic assignment $a_{v,1}(\mathbf{m}_{\mathbf{\Phi}}, \mathbf{\Sigma}_{\mathbf{\Phi}})$ is obtained by integrating $p_{v,1}(\mathbf{x}, \mathbf{m}_{\mathbf{\Phi}}, \mathbf{\Sigma}_{\mathbf{\Phi}})$ over the photosensitive area A_v of pixel v:

$$a_{v,1}(\mathbf{m}_{\mathbf{\Phi}}, \mathbf{\Sigma}_{\mathbf{\Phi}}) = \frac{1}{|A_v|} \int_{A_v} p_{v,1}(\mathbf{x}, \mathbf{m}_{\mathbf{\Phi}}, \mathbf{\Sigma}_{\mathbf{\Phi}})\, d\mathbf{x}. \tag{3.11}$$

The assignment for side 2 is simply given by

$$a_{v,2}(\mathbf{m}_{\mathbf{\Phi}}, \mathbf{\Sigma}_{\mathbf{\Phi}}) = 1 - a_{v,1}(\mathbf{m}_{\mathbf{\Phi}}, \mathbf{\Sigma}_{\mathbf{\Phi}}). \tag{3.12}$$

For the integration in equation (3.11), a piecewise polynomial approximation of the error function is used. Note that the accuracy of the approximations used in this section increases as the uncertainty specified by the covariance $\mathbf{\Sigma}_{\mathbf{\Phi}}$ decreases. In step 2b of the algorithm (see Figure 3.2) the covariance $\mathbf{\Sigma}_{\mathbf{\Phi}}$ is updated, which usually decreases the uncertainty. This is the reason why the CCD algorithm achieves high sub-pixel accuracy despite the used approximations. Higher accuracies may be possible by using higher order approximations of the curve function $\mathbf{c}$.

By $\mathcal{V}_u$ we denote the set of potential edge pixels v, i.e. pixels which are not clearly assigned to either side of the curve. For these pixels $v \in \mathcal{V}_u$, the assignments must be refined. By $\mathcal{V}_s$ we denote the set of pixels, which are assigned to one side with high certainty but which are close to pixels in $\mathcal{V}_u$. From pixels in $\mathcal{V}_s$, local statistics are learned in step 1b. In step 1a, the vicinity $\mathcal{V} = \mathcal{V}_u \cup \mathcal{V}_s$ of the expected curve is determined and for all pixels $v \in \mathcal{V}$, the probabilistic assignments $\mathbf{a}_v$ are computed. Figure 3.10 row b on page 38 depicts the components $a_{v,1}$ of the assignments for different iterations. In the first iteration step, the uncertainty of the curve is higher at the right side than at the left side. Hence, the assignments are smoother at the right side.

[1] Additional inaccuracies, e.g. an inaccurate curve function $\mathbf{c}(\cdot)$ or image blurring, can be taken into account by adding an appropriate variance to the right hand side of equation (3.9).

Local Curve Coordinates

Furthermore, for all pixels $v \in \mathcal{V}$ local curve coordinates $(d_v, d_v^{=})^T$ are determined, which are better suited to describe the vicinity of the curve than pixel coordinates. The first component d_v is the displacement of the pixel's center point $\mathbf{v}$ to the mean curve according to function $d_v(\cdot)$, defined in equation (3.8):

$$d_v = d_v(\mathbf{v}). \tag{3.13}$$

The second component $d_v^{=}$ denotes the perpendicular coordinate, i.e. the position of v along the curve. All pixels in $\mathcal{V}$ are sorted according to the coordinate $d_v^{=}$, which allows for a more efficient computation in step 1b. Exploiting the fact that adjacent pixels have similar coordinates, this sorting can be done efficiently.

3.2.2 Computing Local Statistics

For the two sides separated by the curve, local statistics of the pixel values are learned from pixels that are assigned to one side of the curve with high certainty. The purpose of these statistics is to locally characterize the two sides of the curve. First, in section 3.2.2.1, we relate our statistical model to other context-sensitive statistical models used in computer vision. Then, in section 3.2.2.2, local windows (weights) describing the impact of a pixel on the local statistics are derived. Finally, in section 3.2.2.3, a fast recursive computation of the local statistics is proposed.

3.2.2.1 Context-sensitive Statistical Models

In order to decide to which side of the curve a pixel fits best, we consider the surrounding, i.e. the context of the pixel. Popular means of probabilistically modeling contextual constraints are Markov Random Fields (MRF). Some of the most frequently used MRFs are auto-normal models, also called Gaussian MRFs (Chellappa, 1985; Li, 2001). Gaussian MRFs and the related simultaneous auto-regression (SAR) models (Li, 2001) regard the pixel value as a Gaussian random variable with its expectation depending linearly on the neighboring pixels. However, in these models the variance/covariance does not directly depend on the pixel's vicinity. Homogeneous Gaussian MRFs and SAR models have a single variance/covariance per image region.

We propose a statistical model, which is related to Gaussian MRF and SAR models in the sense that it also employs Gaussian distributions that are conditioned on the pixels' vicinities. However, in our model the vicinity of a pixel does not only affect the mean vector but also the

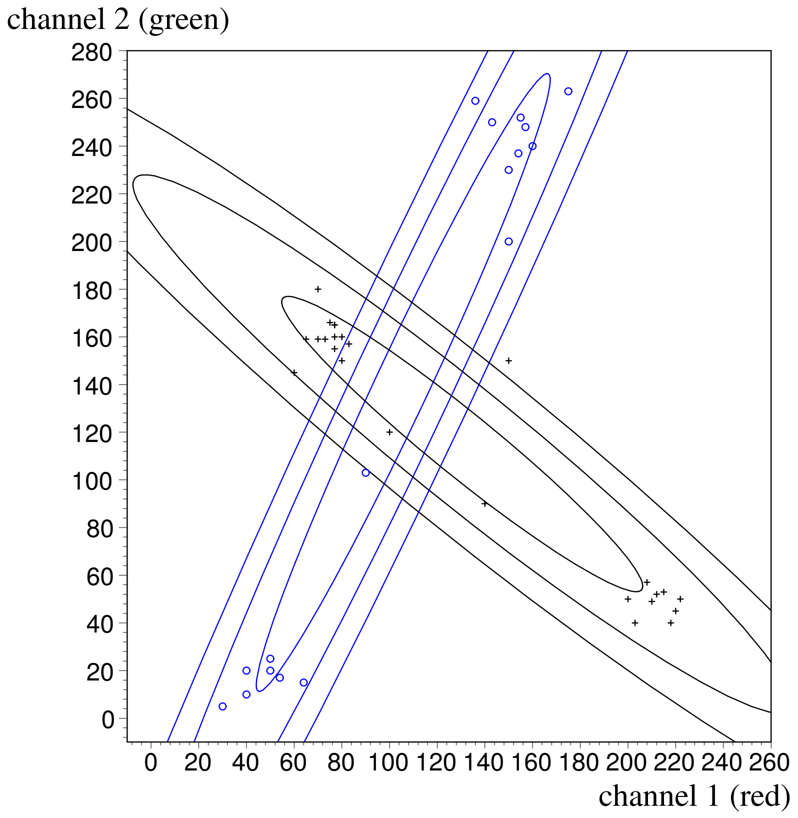

Figure 3.5: Two bimodal distributions and the confidence regions of their Gaussian approximations: The two distributions are non-Gaussian and have similar mean values. Nevertheless, a Gaussian classifier is able to accurately separate the two classes for almost all pixel values. This is due to the significantly different covariance matrixes.

covariance matrix. Our model allows both the mean vectors and the covariance matrixes of both sides of the curve to smoothly vary along the curve. For each side of the curve and for each pixel the local mean vectors and local covariance matrices define local multi-variate Gaussian approximations of the underlying distributions.[2] The local adaptation of both the mean vector and the covariance matrix is the key to the flexibility of our statistical model. Due to the local adaptation of the statistics, very often the two sides of the curve can accurately be separated even if the actual distributions are non-Gaussian. For example, often a multi-modal distribution of local pixel values spans roughly just a linear sub-space within the multi-dimensional space of possible pixel values. Such linear sub-spaces can be described accurately by a Gaussian distribution even if the actual distribution is non-Gaussian. Figure 3.5 illustrates the importance of locally adapted covariance matrices.

[2]Higher order moments of the underlying distribution may be taken into account by a pre-processing step, which maps the pixel value $\mathbf{I}^*$ to a possibly higher dimensional vector using a non-linear transformation.

Our approach is related to the approach of Ronfard (1994) who also uses local statistics. The author partitions the vicinity of the curve into stripes perpendicular to the curve and assumes constant statistics within each stripe for each side of the curve. In order to avoid the spatial discretization involved in this approach, we model the statistics as a function of the position along the curve. While Ronfard uses the same variance for all stripes, we use locally adapted covariance matrixes.[3] For each pixel, i.e. position $d_v^=$ along the curve, we employ two sets of pixels in order to compute the local statistics $\mathbf{S}_1(d_v^=)$ and $\mathbf{S}_2(d_v^=)$ corresponding to the two sides of the curve. The pixels within such a set are scaled by weights, which are described in the next section.

3.2.2.2 Weighting the Pixels in the Vicinity of the Curve

The purpose of the local statistics $\mathbf{S}_1(d_v^=)$ and $\mathbf{S}_2(d_v^=)$ is to describe whether pixel v fits better to side 1 or to side 2 of the curve. The local statistics are functions of the coordinate $d_v^=$, specifying the position of pixel v in the direction along the curve. The statistics are obtained from local windows, i.e. weights, see Figure 3.6. The weight $w_{p,s}(d_v^=)$ describes to which extent pixel p is taken into account for the computation of $\mathbf{S}_s(d_v^=)$, i.e. the local statistics for side $s \in \{1, 2\}$ at position $d_v^=$. In this section, we derive suitable weights $w_{p,s}(d_v^=)$.

First, we formulate seven partially conflicting requirements for the weights $w_{p,s}(d_v^=)$:

1. Only pixels p that are likely to belong to the desired side s should have a positive weight; all other pixels p should have a weight of zero.

2. Since the statistical dependency between two pixels decreases with the distance between the pixels, only pixels that are not too far apart from the expected curve should be taken into account.

3. In an area, in which the uncertainty of the curve is small, the weight should be higher than in an area with a high uncertainty of the curve.

4. The distance between pixel p and pixel v *along* the curve should be small. This corresponds to point 2. However, it takes the perpendicular direction into account.

5. The weights should allow for efficient computation of the local statistics.

6. The number of pixels with a non-zero weight should be sufficient in order to reliably estimate the local statistics.

[3]Moreover, the two approaches differ in the way the statistics are obtained and in the way the optimization for the curve parameters is performed.

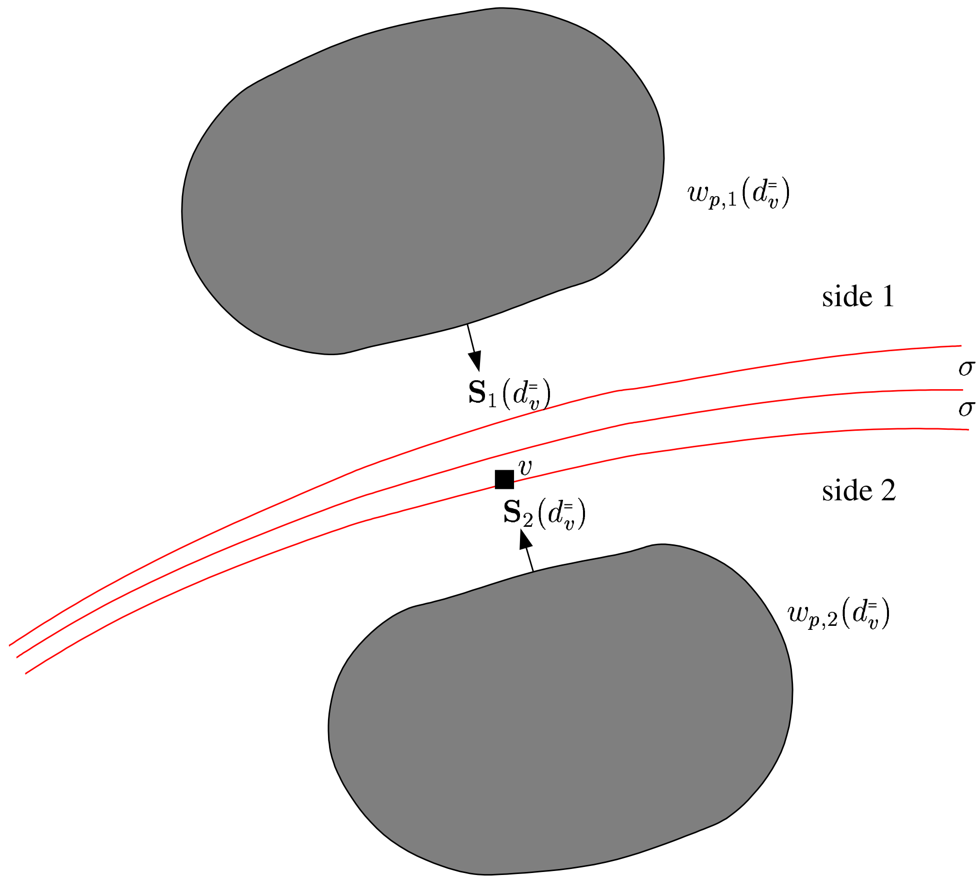

Figure 3.6: For each pixel v in the vicinity of the curve, local statistics $\mathbf{S}_1(d_v^=)$ and $\mathbf{S}_2(d_v^=)$ are computed which locally characterize the two sides of the curve.

7. For reasons of numerical stability the weights should be continuous.

Since these requirements are hard to quantify, we propose a heuristic compromise[4]. We compute the weight $w_{p,s}(d_v^=)$ as a product of two functions:

$$w_{p,s}(d_v^=) = W_s(p) \cdot W^=(|\ d_v^= - d_p^=\ |). \tag{3.14}$$

The first function, W_s, assesses the relation between pixel p and the curve. It represents a compromise between requirement 1, 2, and 3. The second function, $W^=$, takes requirement 4 into account. Requirements 5, 6, and 7 are general requirements that are important for function W_s and for function $W^=$. We first define the functions W_s and $W^=$, respectively. Then we illustrate the resulting weights.

[4]A compromise could also be learned from a set of labeled images.

Evaluating the Distance to the Mean Curve

The function $W_s(p)$, used in equation (3.14), assesses the relation between the pixel p and the current curve distribution. It mainly computes a compromise between requirements 1, 2, and 3 described above. We compute $W_s(p)$ as a product of three functions corresponding to the three requirements:

$$W_s(p) = W_A(a_{p,s}) \cdot W_B(d_p, \sigma_p) \cdot W_C(\sigma_p). \tag{3.15}$$

Function W_A: The first function $W_A(a_{p,s})$ assesses the probability that pixel p belongs to the desired side s. The quantity $a_{p,s}$ is the probabilistic side assignment for pixel p according to equations (3.11) and (3.12). The function $W_A(a_{p,s})$ is defined by

$$W_A(a_{p,s}) = \max\left(0, \left[\frac{a_{p,s} - \gamma_1}{1 - \gamma_1}\right]^{(2 \cdot E_A)}\right), \tag{3.16}$$

where $\gamma_1 \in [0, 1[$ and $E_A > 1$. The function W_A is monotonically increasing and holds $\forall a_{p,s} \in [0, \gamma_1] : W(a_{p,s}) = 0$ and $W(1) = 1$. For our experiments we use $\gamma_1 = 0.5$. That is, pixels that belong to the desired side with a confidence of 50% or less are not used for computing the local statistics. For parameter E_A we recommend $E_A = 2$ or $E_A = 3$.

Function W_B: The second function $W_B(d_p, \sigma_p)$ evaluates the proximity of pixel p to the curve. The quantity d_p denotes the expected signed distance between pixel p and the curve according to equation (3.13). The quantity d_p is evaluated relative to the uncertainty σ_p of the curve. The second parameter, σ_p, denotes the standard deviation of d_p according to equation (3.9). For $W_B(d_p, \sigma_p)$ we choose a zero mean truncated Gaussian density:

$$\begin{aligned} W_B(d_p, \sigma_p) &= C \cdot \max\left[0, \exp\left(-d_p^2/2\widehat{\sigma}_p^2\right) - \exp(-\gamma_2)\right] \quad \text{where} && (3.17) \\ \widehat{\sigma}_p &= \gamma_3 \cdot \sigma_p + \gamma_4. && (3.18) \end{aligned}$$

Here, C is a normalization constant ensuring that $W_B(d_p, \sigma_p)$ be a probability density function. The parameter $\gamma_2 > 0$ defines the truncation of the Gaussian. It is used in order to limit the number of pixels with a non-zero weight, i.e. pixels which are taken into account. The standard deviation $\widehat{\sigma}_p$ of the Gaussian is a linear function of the curve's uncertainty, i.e. σ_p. Hence, the width of the window automatically adapts to the uncertainty of the curve. The parameter $\gamma_4 > 0$ defines a lower boundary of the window's width. We recommend the following values: $\gamma_2 \in [3, 5]$, $\gamma_3 \in [4, 6]$, and $\gamma_4 \in [2, 3]$.

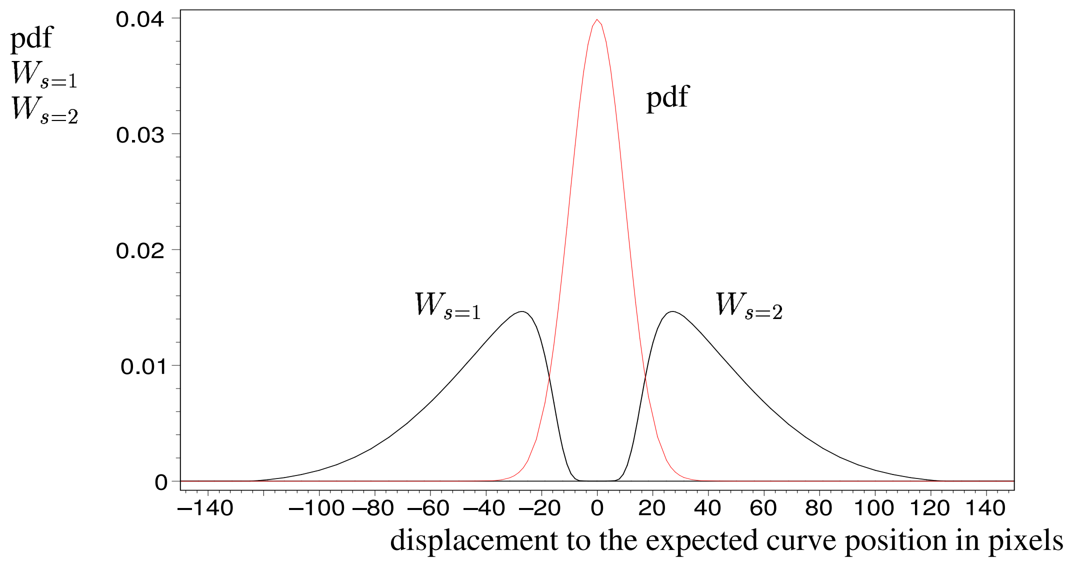

Figure 3.7: Weighting functions $W_{s=1}$, $W_{s=2}$, and probability density function (pdf) of the curve position: Only those pixels that are likely to belong to the desired side s and are close to the expected curve have a high weight.

Function W_C: The third function $W_C(\sigma_p)$ at the right hand side of equation (3.15) evaluates the uncertainty σ_p of the curve. In an area where the uncertainty is high, the weight $w_{p,s}(d_v^=)$ should be smaller than in an area where the uncertainty is small. Hence, the local statistics are propagated more from areas with high uncertainty to areas with low uncertainty than vice versa. We use the function $W_C(\sigma_p)$:

$$W_C(\sigma_p) = (\sigma_p + 1)^{-E_C} \tag{3.19}$$

where E_C is a constant in $[1, 4]$.

Figure 3.7 shows the probability density function (pdf) of the curve and the resulting weighting functions W_s for the two sides $s \in \{1, 2\}$. Only those pixels that are likely to belong to the desired side s and are close to the expected curve have a high weighting W_s.

Evaluating the Distance Along the Curve

The second function, $W^=$, in equation (3.14) assesses the distance $\mid d_v^= - d_p^= \mid$ between pixel p and pixel v along the curve (see requirement 4 on page 32). Function $W^=$ is defined as an exponentially declining function:

$$W^=(D) = \frac{\lambda}{2} \cdot \exp(-\lambda |D|) \tag{3.20}$$

where the parameter λ defines the speed of decline. Figure 3.8 illustrates the function $W^=$.

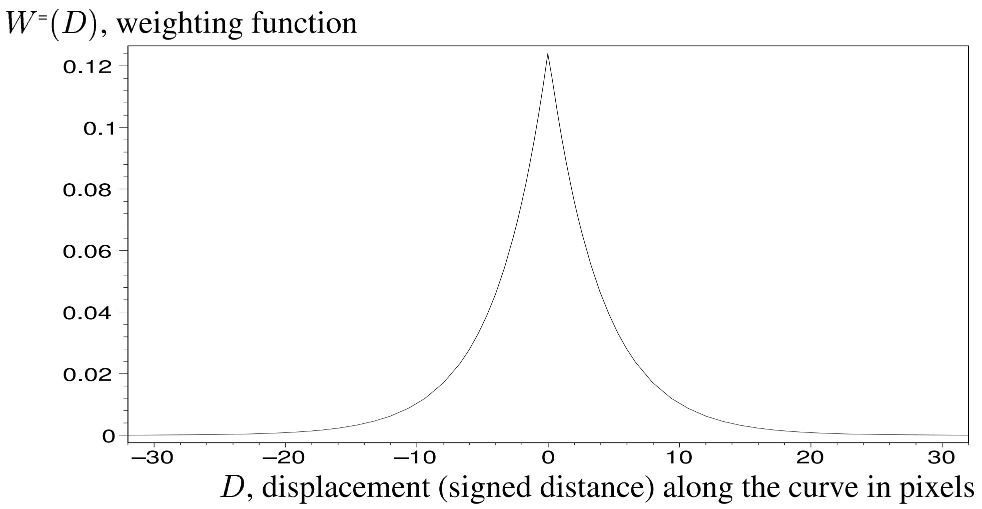

Figure 3.8: The weighting function $W^{=}(D)$ exponentially declines with the distance along the curve.

The multiplicative structure of equation (3.14), combining two independent criteria, and the exponential decline of $W^{=}(D)$ allow for a fast recursive computation of the local statistics. This will be described in section 3.2.2.3.

The Resulting Weights

Figure 3.9 depicts the resulting weights $w_{p,1}(d_v^{=})$ and $w_{p,2}(d_v^{=})$ for different pixels p and a fixed curve coordinate $d_v^{=}$. It shows that pixels p, which are too close to the expected curve, i.e. pixels which may have been assigned to the wrong side, have weights equal or close to zero. Pixels p which are too far from the expected curve or which have a large distance $\mid d_v^{=} - d_p^{=} \mid$ along the curve also have low weight. Furthermore, the size of the window adapts to the uncertainty of the curve, i.e. for a high uncertainty the window is wider than for a small uncertainty. Compare e.g. the left and the right side in Figure 3.9. Row c in Figure 3.10 depicts the weights of one side for different iterations. This illustrates how the local window sizes decrease during the progress of the iteration. (In contrast to Figure 3.9, the weights in Figure 3.10 are not depicted for a fixed position $d_v^{=}$ along the curve but for the position $d_p^{=}$ which yields the maximum weight.)

3.2.2.3 Recursive Computation of Local Statistics

Based on the weights $w_{p,s}(d_v^{=})$ derived in the previous section, we now derive the local mean vectors $\mathbf{m}_{v,s}$ and local covariance matrices $\mathbf{\Sigma}_{v,s}$ of the pixel values $\mathbf{I}^*$ for each side $s \in \{1, 2\}$ of the curve and each pixel v in the vicinity $\mathcal{V}_u$ of the curve. The local mean vectors $\mathbf{m}_{v,s}$ and

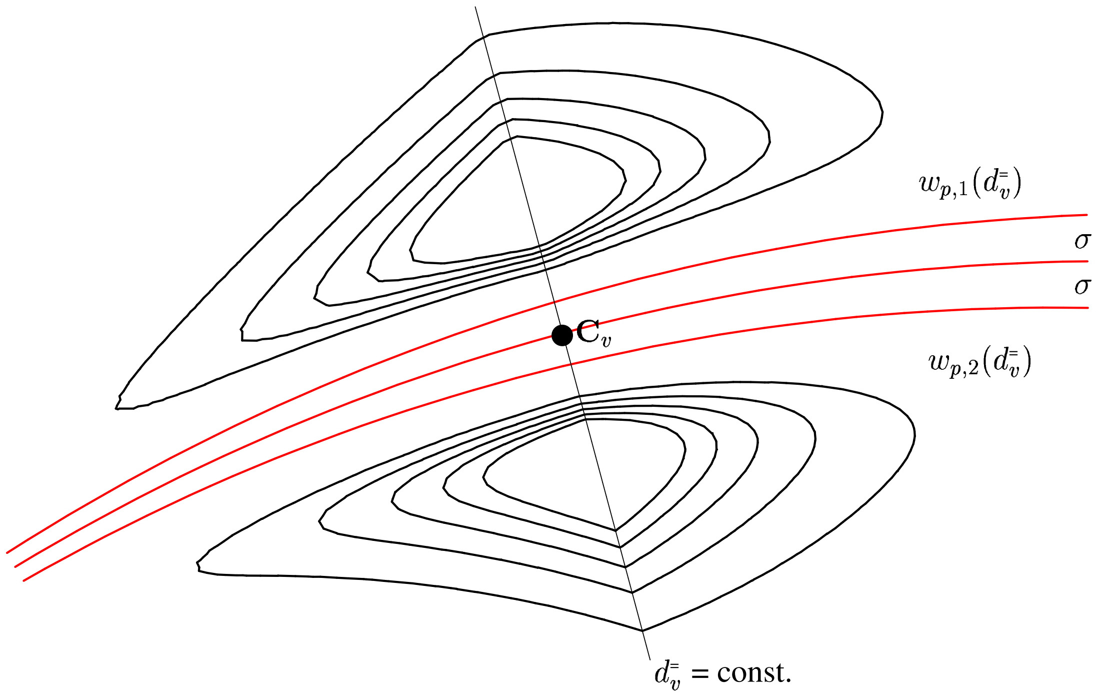

Figure 3.9: Contour plot of the windows (weights) used for computing local statistics: The bundle of the three lines describes the expected position and uncertainty (σ-interval) of the curve. For the pixels on the perpendicular line, local statistics are computed from the two depicted windows. The windows are adapted in size and shape to the expected curve and its uncertainty.

local covariance matrices $\mathbf{\Sigma}_{v,s}$ are obtained by

$$\mathbf{m}_{v,s} = \mathbf{M}_{s,1}(d_v^=)/\mathbf{M}_{s,o}(d_v^=) \tag{3.21}$$

$$\mathbf{\Sigma}_{v,s} = \mathbf{M}_{s,2}(d_v^=)/\mathbf{M}_{s,o}(d_v^=) - \mathbf{m}_{v,s}\mathbf{m}_{v,s}^T + \kappa\mathbf{1} \tag{3.22}$$

where the local weighted moments of order 0, 1, and 2 are defined as [5]

$$\mathbf{M}_{s,o}(d_v^=) = \sum_{p\in\mathcal{V}} w_{p,s}(d_v^=) \tag{3.23}$$

$$\mathbf{M}_{s,1}(d_v^=) = \sum_{p\in\mathcal{V}} w_{p,s}(d_v^=)\ \mathbf{I}_p^* \tag{3.24}$$

$$\mathbf{M}_{s,2}(d_v^=) = \sum_{p\in\mathcal{V}} w_{p,s}(d_v^=)\ \mathbf{I}_p^* \cdot \mathbf{I}_p^{*T}\ . \tag{3.25}$$

The local weights $w_{p,s}(d_v^=)$ are specified in equation (3.14) and $\mathbf{I}_p^*$ denotes the vector of pixel values of pixel p. In equation (3.22), $\kappa\mathbf{1}$ is the identity matrix $\mathbf{1}$ scaled by κ. This term is used

[5]The moments of order 0 are scalars; the moments of order 1 are vectors; and the moments of order 2 are matrices.

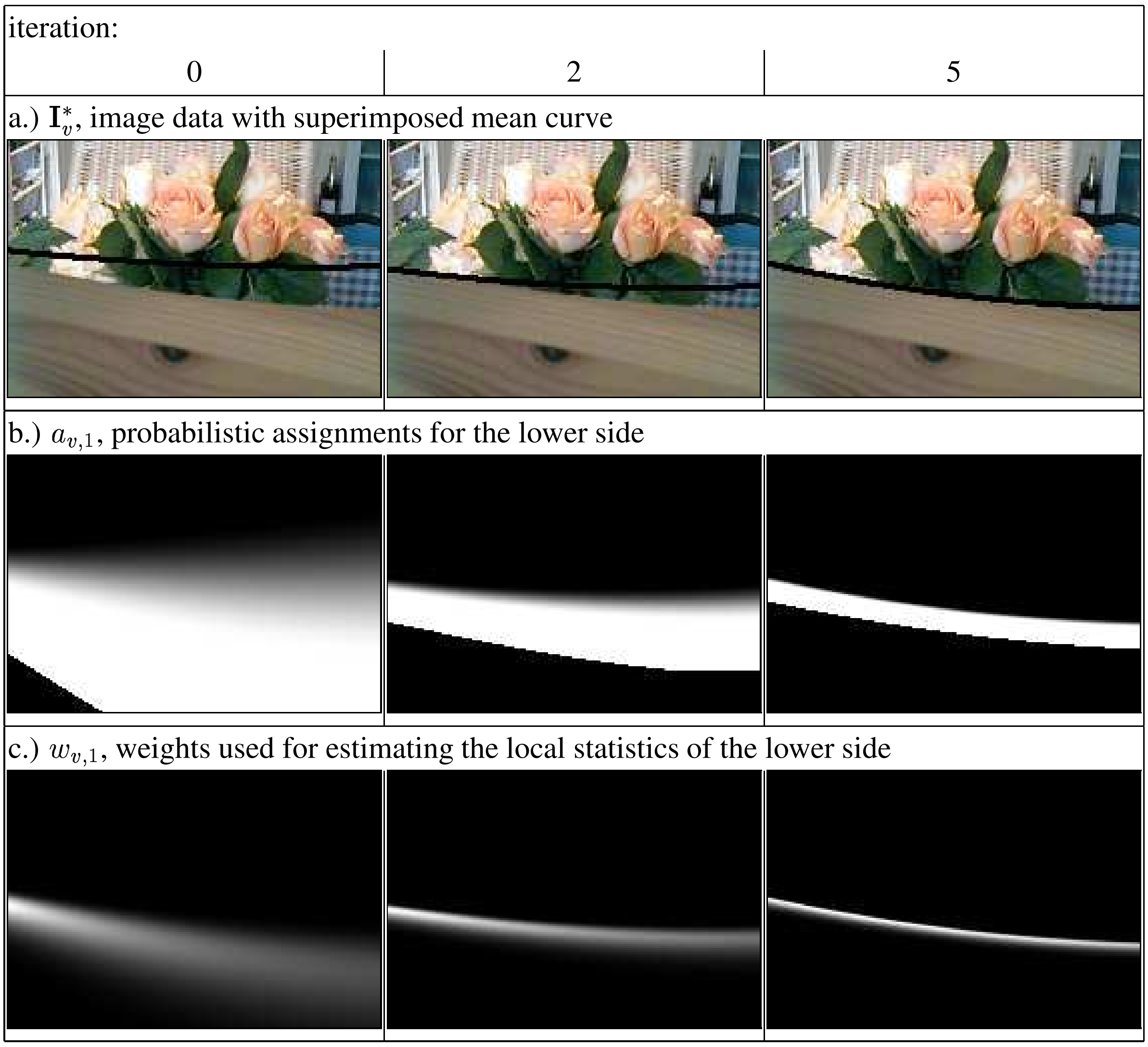
iteration:
0
2
5
a.) $\mathbf{I}_v^*$, image data with superimposed mean curve
b.) $a_{v,1}$, probabilistic assignments for the lower side
c.) $w_{v,1}$, weights used for estimating the local statistics of the lower side

Figure 3.10: Quantities of the fitting process I: The weights depend on the distance to the expected curve and the uncertainty of the curve positions. (The images in rows b and c are individually normalized such that the gray values are within [0,255].)

in order to avoid singularities, i.e. numerical problems, for degenerated distributions. In our experiments, we choose κ to be fairly small, $\kappa = 0.5$. (The pixel values are between 0 and 255.)

The time complexity of computing the local statistics $\mathbf{S}_v := (\mathbf{m}_{v,1}, \mathbf{\Sigma}_{v,1}, \mathbf{m}_{v2}, \mathbf{\Sigma}_{v,2})$ for a single pixel v is $O(N_v)$ where N_v denotes the number of pixels p with a non-zero weight $w_{p,s}(d_v^=)$. An independent computation of $\mathbf{S}_v$ for all uncertainly assigned pixels $v \in \mathcal{V}_u$ would result in a time complexity of $O(\sum_{v \in \mathcal{V}_u} N_v)$, which is too expensive. However, the special structure of the weights $w_{p,s}(d_v^=)$ defined in equation (3.14) allows for a faster simultaneous computation of the local statistics $\mathbf{S}_v$. The function $W_s(p)$ evaluates the relation between the curve and pixel p and is independent of pixel v. The function $W^{=}(|\ d_v^{=} - d_p^{=}\ |)$ defines an exponential decline along the curve. Hence, the local moments $\mathbf{M}_{s,o}(d_v^{=})$ with $o \in \{0, 1, 2\}$ defined in equations (3.23), (3.24), and (3.25) can be obtained as follows. First the expressions

$$W_s(p), \quad W_s(p) \cdot \mathbf{I}_p^*, \text{ and } \quad W_s(p) \cdot \mathbf{I}_p^* \cdot \mathbf{I}_p^{*T}$$

are computed for all pixels p in $\mathcal{V}_u$ and then these quantities are blurred along the curve using the exponential filter defined by $W^{=}(\cdot)$. This blurring can be done efficiently in a recursive manner. The resulting time complexity for the simultaneous computations of the statistics $\mathbf{S}_v$ for all $v \in \mathcal{V}_u$ is $O(|\mathcal{V}|)$ where $|\mathcal{V}|$ is the number of pixels in the vicinity $\mathcal{V}$ of the curve. Due to the choice of $W^{=}(\cdot)$, the runtime does not increase with the blurring in the direction of the curve, which allows for efficiently processing high resolution images.

3.3 Refining the Estimate of the Model Parameter Vector

In step 2 of the CCD algorithm (see Figure 3.2) the estimate of the model parameter vector is refined using the probabilistic pixel assignments $\mathbf{a}_v(\mathbf{m}_\mathbf{\Phi}, \mathbf{\Sigma}_\mathbf{\Phi})$ and the local statistics $\mathbf{S}_v$ obtained in step 1. In section 3.3.1, we detail our observation model, specifying the assumed probabilistic relation between the model parameter vector and the image data. In sections 3.3.2 and 3.3.3, we show how the mean vector and the covariance matrix of the posterior density can be updated using the observation model.

3.3.1 Observation Model

The observation model, i.e. the likelihood function, describes the range of likely image data $\mathbf{I}$ for a given vector of model parameters $\mathbf{\Phi}$. First, we derive an observation model that takes only one pixel into account. Then we extend this model to multiple pixels.

3.3.1.1 One Pixel

We model the pixel value $\mathbf{I}_v$ of pixel $v \in \mathcal{V}$ as a weighted sum of two random variables $\mathbf{I}_{v,1}$ and $\mathbf{I}_{v,2}$:

$$\mathbf{I}_v = \tilde{a}_{v,1} \cdot \mathbf{I}_{v,1} + \tilde{a}_{v,2} \cdot \mathbf{I}_{v,2} \quad \text{where} \tag{3.26}$$

$$\tilde{\mathbf{a}}_v = (\tilde{a}_{v,1}, \tilde{a}_{v,2})^T = (\tilde{a}_{v,1}, 1 - \tilde{a}_{v,1})^T \tag{3.27}$$

and $\tilde{a}_{v,1} \in [0, 1]$. The random variables $\mathbf{I}_{v,1}$ and $\mathbf{I}_{v,2}$ correspond to the two sides of the curve and are assumed to be distributed according to the statistics of the corresponding side. We approximate the distributions of $\mathbf{I}_{v,1}$ and $\mathbf{I}_{v,2}$ by two Gaussians. Their mean vectors ($\mathbf{m}_{v,1}$ and $\mathbf{m}_{v,2}$) and covariance matrices ($\mathbf{\Sigma}_{v,1}$ and $\mathbf{\Sigma}_{v,2}$) are obtained according to equations (3.21) and (3.22). The quantity $\tilde{a}_{v,1}$ specifies the fraction of the photosensitive area of pixel v, which lies at side 1 of the curve. The linear mix assumed in (3.26) corresponds to the sensor model used by Baker, Nayar, and Murase (1998). It is also used in the alpha estimation literature (Ruzon and Tomasi, 2000; Chuang et al., 2001).

Due to the linear relation in (3.26), we obtain a Gaussian probability density $p(\mathbf{I}_v \mid \mathbf{m}_v, \mathbf{\Sigma}_v)$ for the pixel value $\mathbf{I}_v$. The mean vector $\mathbf{m}_v$ and covariance $\mathbf{\Sigma}_v$ are given by

$$\mathbf{m}_v = \tilde{a}_{v,1}\mathbf{m}_{v,1} + \tilde{a}_{v,2}\mathbf{m}_{v,2} \tag{3.28}$$

$$\mathbf{\Sigma}_v = \tilde{a}_{v,1}\mathbf{\Sigma}_{v,1} + \tilde{a}_{v,2}\mathbf{\Sigma}_{v,2}. \tag{3.29}$$

To obtain an intuitive notation we define

$$p(\mathbf{I}_v \mid \tilde{\mathbf{a}}_v, \mathbf{S}_v) := p(\mathbf{I}_v \mid \mathbf{m}_v, \mathbf{\Sigma}_v). \tag{3.30}$$

The notation $p(\mathbf{I}_v \mid \tilde{\mathbf{a}}_v, \mathbf{S}_v)$ indicates that the distribution of the pixel value $\mathbf{I}_v$ depends on the assignment $\tilde{\mathbf{a}}_v = (\tilde{a}_{v,1}, 1 - \tilde{a}_{v,1})^T$ and the local statistics $\mathbf{S}_v$. Figure 3.11 depicts the conditional density $p(\mathbf{I}_v \mid \tilde{\mathbf{a}}_v, \mathbf{S}_v)$ for the case where the pixel value $\mathbf{I}_v$ is only of dimension 1. In this example the two sides of the curve have different mean values and different covariances. A cross section of this surface is illustrated in Figure 3.12. It shows the conditional density, i.e. the likelihood, for the pixel value $\mathbf{I}_v = 90$. The likelihood of the assignment $\tilde{a}_{v,1}$ is non-Gaussian and non-symmetric since the two sides of the curve have different covariances. The assignment that most likely caused the pixel value $\mathbf{I}_v = 90$ is approximately $\tilde{a}_{v,1} = 0.68$, i.e. the abscissa of the maximum in Figure 3.12. Later it will prove convenient not to optimize the likelihood but the negative log-likelihood $-\ln[p(\mathbf{I}_v \mid \tilde{\mathbf{a}}_v, \mathbf{S}_v)]$. This function is depicted in Figure 3.13 for $\mathbf{I}_v = 90$. Due to the different covariances of the two sides, the log-likelihood function penalizes deviations from the optimum to the right (towards increasing $\tilde{a}_{v,1}$) more than to the left.

3.3.1.2 Multiple Pixels

Above we defined the assumed probabilistic relation between a single pixel value $\mathbf{I}_v$ and the corresponding assignment $\tilde{\mathbf{a}}_v$. Now we derive the probabilistic relation between all pixels $\mathbf{I}_\mathcal{V}$ in the vicinity $\mathcal{V}$ of the curve and the model parameters $\mathbf{\Phi}$.

The assignments $\tilde{\mathbf{a}}_v$ can be written as a function of the model parameters $\mathbf{\Phi}$. The probability density $p(\mathbf{I}_\mathcal{V} \mid \tilde{\mathbf{a}}_\mathcal{V}(\mathbf{\Phi}), \mathbf{S}_\mathcal{V})$ of observing the image data $\mathbf{I}_\mathcal{V}$ in $\mathcal{V}$ subjected to the model

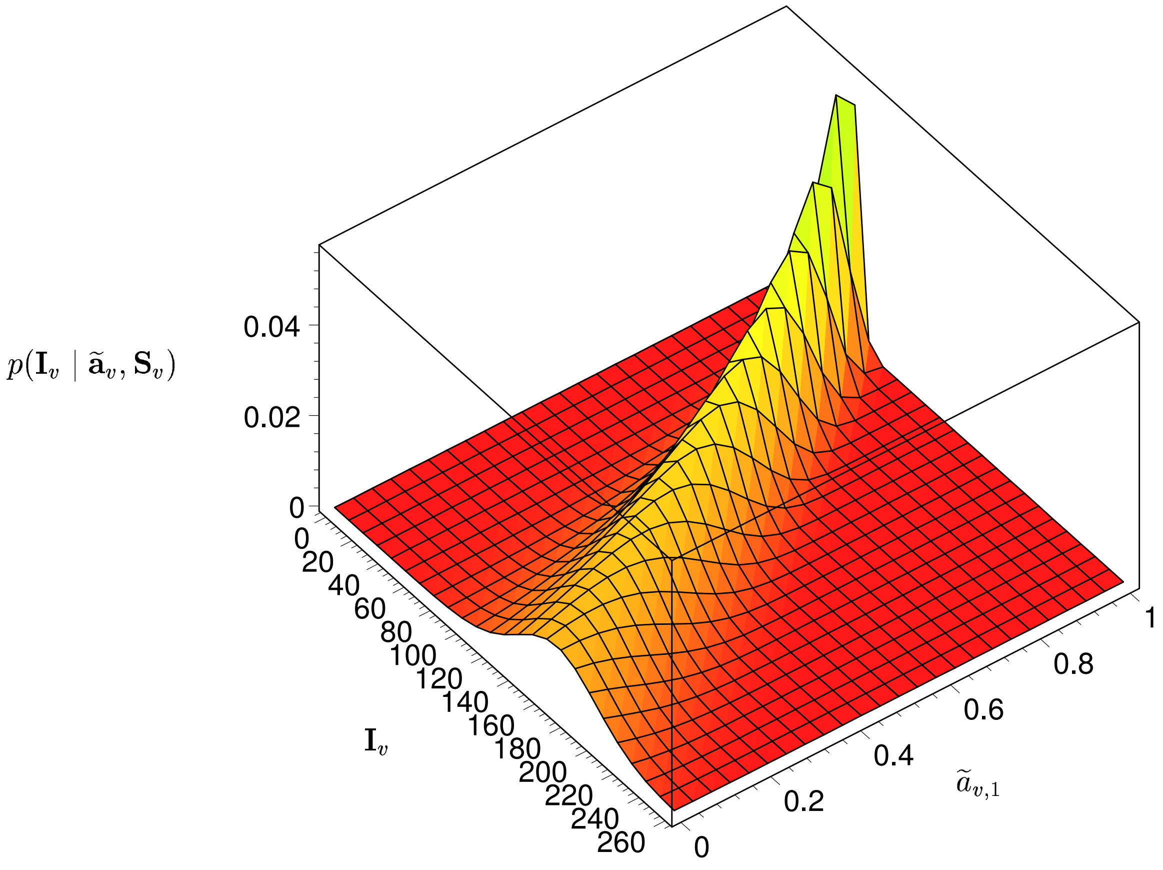

Figure 3.11: Conditional probability density function for a pixel value $\mathbf{I}_v$ of dimension one. The Gaussian distribution of the pixel value $\mathbf{I}_v$ depends on the assignment $\tilde{a}_{v,1}$.

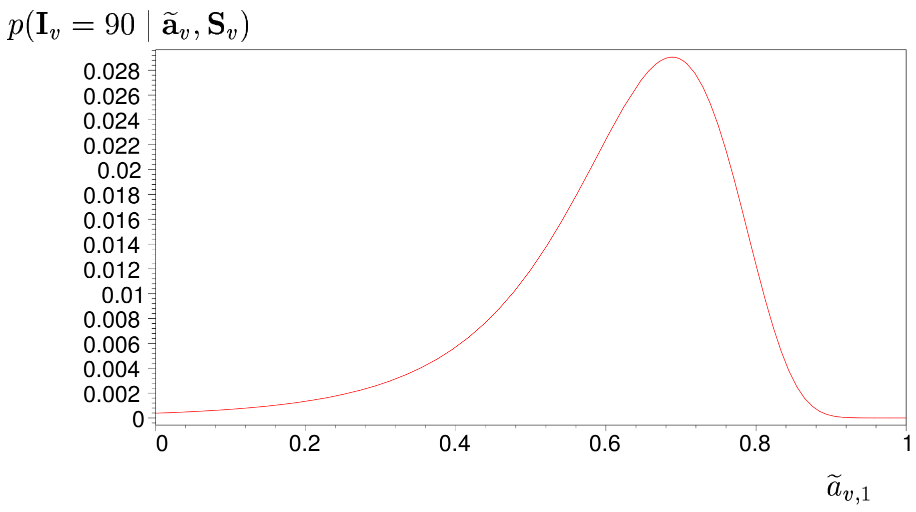

Figure 3.12: Likelihood of the assignment. The likelihood is non-Gaussian and non-symmetric since the two sides of the curve have different covariances.

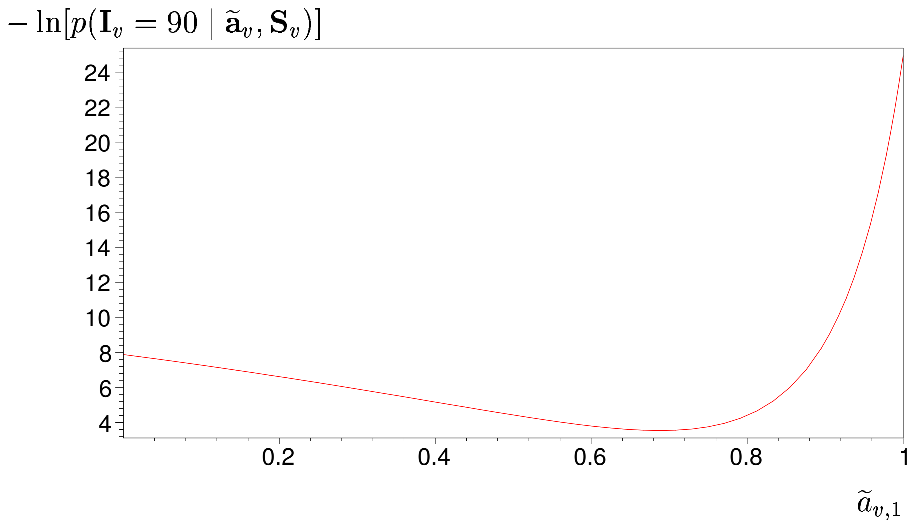

Figure 3.13: The negative log-likelihood of the assignment is not quadratic. The function penalizes deviations from the optimum to the right (increasing $\tilde{a}_{v,1}$) more than to the left.

parameters $\mathbf{\Phi}$ can be estimated by

$$p(\mathbf{I}_{\mathcal{V}} \mid \tilde{\mathbf{a}}_{\mathcal{V}}(\mathbf{\Phi}), \mathbf{S}_{\mathcal{V}}) = \prod_{v \in \mathcal{V}} p(\mathbf{I}_v \mid \tilde{\mathbf{a}}_v(\mathbf{\Phi}), \mathbf{S}_v). \tag{3.31}$$

The index v indicates quantities of a single pixel v. Analogously, the index $\mathcal{V}$ indicates quantities of all pixels v in $\mathcal{V}$. For neighboring pixels, similar windows are used in order to estimate the local statistics $\mathbf{S}_v$. Hence, in (3.31) values of pixels on the same side of the curve are modeled as statistically dependent. The intensity of the statistical dependency is defined by the degree of overlap of the windows. Equation (3.31) takes only those pixels into account that are in the vicinity $\mathcal{V}$ of the curve. Pixels outside $\mathcal{V}$ are not used.

3.3.2 Updating the Mean Vector

Let us now describe the update of the mean vector.

3.3.2.1 MAP Estimation

Using the observation density derived in equation (3.31) the MAP estimate $\widehat{\mathbf{\Phi}}$ of the model parameters $\mathbf{\Phi}$ can be written as

$$\widehat{\mathbf{\Phi}} = \arg\max_{\mathbf{\Phi}} F(\mathbf{\Phi}) \quad \text{with} \tag{3.32}$$

$$F(\mathbf{\Phi}) = p(\mathbf{I}_{\mathcal{V}} = \mathbf{I}^*_{\mathcal{V}} \mid \tilde{\mathbf{a}}_{\mathcal{V}}(\mathbf{\Phi}), \mathbf{S}_{\mathcal{V}}) \cdot p(\mathbf{\Phi} \mid \mathbf{m}^*_{\mathbf{\Phi}}, \mathbf{\Sigma}^*_{\mathbf{\Phi}}), \tag{3.33}$$

where $\mathbf{I}_{\mathcal{V}}^{*}$ denotes the sensed image data in the curve vicinity $\mathcal{V}$ and $p(\mathbf{\Phi} \mid \mathbf{m}_{\mathbf{\Phi}}^{*}, \mathbf{\Sigma}_{\mathbf{\Phi}}^{*})$ denotes the Gaussian a priori density. By applying the logarithm to the objective function, an equivalent but numerically more favorable optimization is obtained:[6]

$$\widehat{\mathbf{\Phi}} = \arg\min_{\mathbf{\Phi}} \ \widetilde{\chi}^2(\mathbf{\Phi}) \quad \text{with} \tag{3.34}$$

$$\widetilde{\chi}^2(\mathbf{\Phi}) = -2\ln[p(\mathbf{I}_{\mathcal{V}} = \mathbf{I}_{\mathcal{V}}^{*} \mid \widetilde{\mathbf{a}}_{\mathcal{V}}(\mathbf{\Phi}), \mathbf{S}_{\mathcal{V}}) \cdot p(\mathbf{\Phi} \mid \mathbf{m}_{\mathbf{\Phi}}^{*}, \mathbf{\Sigma}_{\mathbf{\Phi}}^{*})]. \tag{3.35}$$

Due to the nature of an imaging sensor, the optimization in (3.34) is not trivial. An imaging sensor performs a spatial discretization of the scene which causes a non-smooth relation between the image data $\mathbf{I}$ and the model parameters $\mathbf{\Phi}$. For most pixels v, the assignments $\widetilde{a}_{v,1}$ are equal to 1 or 0. Only for the edge pixels the partial derivatives of $\widetilde{a}_{v,1}$ for the model parameters $\mathbf{\Phi}$ are not equal to zero. The objective function $\widetilde{\chi}^2$ typically has multiple points with high or even infinite curvature, see Figure 3.14. Hence, gradient descent optimization methods such as Newton iteration yield a very small area of convergence. In the next section, we show how the area of convergence can be substantially increased.

3.3.2.2 Fitting a Blurred Model

In order to obtain a smooth objective function evaluating the fit between the image data and a single vector of model parameters, the image data are usually blurred, e.g. (Kass, Witkin, and Terzopoulos, 1988; Cremers, Schnörr, and Weickert, 2001). We take the opposite approach. We use non-blurred image data and a *blurred model*. Our objective function takes the uncertainty of the estimated model parameters into account by evaluating the fit between the non-blurred image data and a Gaussian distribution of model parameters. The advantages are as follows:

1. The capture range, i.e. local scale, is enlarged according to the uncertainty of the model parameters. This causes a twofold adaptation: (i) locally: For parts of the curve with a high uncertainty, the local scale is enlarged more than for parts with a small uncertainty. (ii) adaptation within iteration: The scale is automatically adapted to the progress of the iteration. This yields, for each pixel and each iteration step, an individual compromise between the two conflicting goals, namely a large area of convergence and a high accuracy.

2. Optimizing the fit between an image and a blurred model is usually computationally cheaper than blurring the image. Especially if the uncertainty of the initialization is small, only a small fraction of the image data is needed in order to refine the fit.

[6]Due to the logarithm, the product can be written as a sum. Hence, the partial derivatives can be obtained more easily.

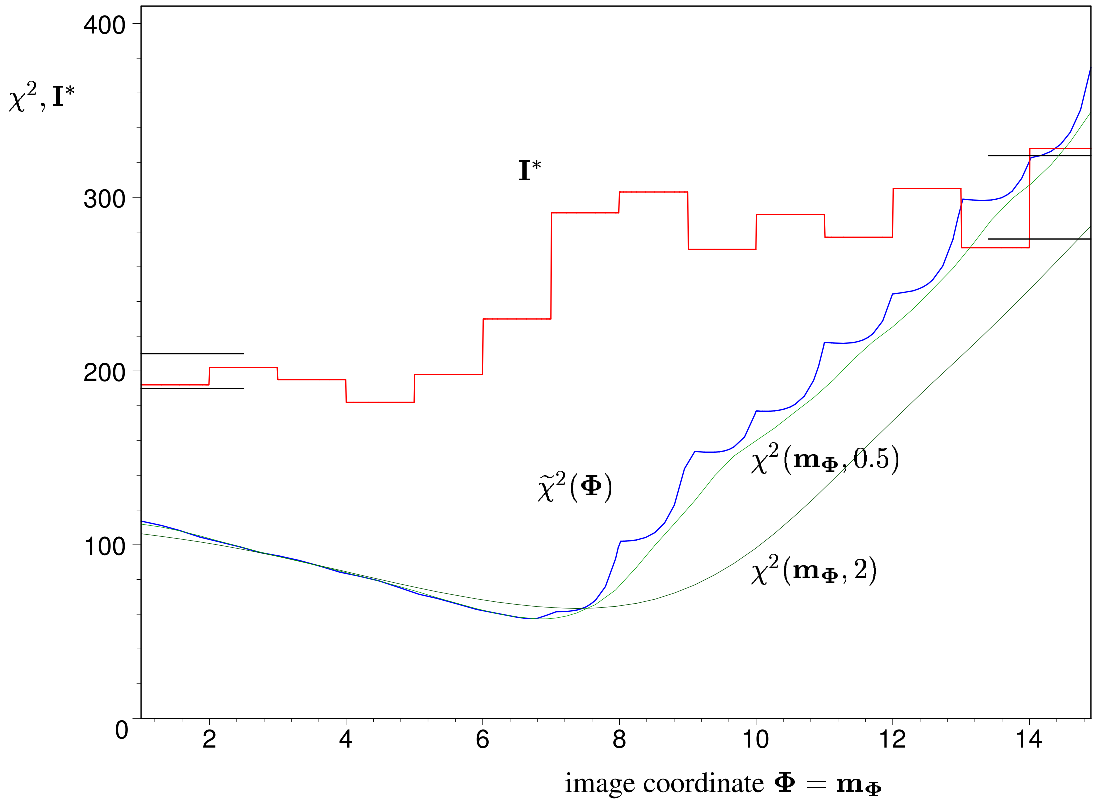

Figure 3.14: Detection of an edge in an 1-D array of gray values $\mathbf{I}^*$: the objective function $\tilde{\chi}^2(\mathbf{\Phi})$ which assesses the edge hypothesis $\mathbf{\Phi}$ is non-differentiable. The smooth approximations $\chi^2(\mathbf{m_\Phi}, \mathbf{\Sigma_\Phi})$, depicted for $\mathbf{\Sigma_\Phi} = 0.5$ and $\mathbf{\Sigma_\Phi} = 2$, are differentiable. However, they have (slightly) different global minima. The horizontal lines (left and right margins) indicate the σ-interval characterizing the distributions of the two sides.

3. No high frequency information of the image data is lost. This is particularly important in order to separate textured regions or to achieve high sub-pixel accuracy.

The discontinuities of the derivatives of $\tilde{\chi}^2$ are caused by the non-smooth assignments $\tilde{\mathbf{a}}_v(\mathbf{\Phi})$. Hence, we substitute $\tilde{\mathbf{a}}_v(\mathbf{\Phi})$ by the smooth probabilistic assignment $\mathbf{a}_v(\mathbf{m_\Phi}, \mathbf{\Sigma_\Phi})$ obtained in step 1a. While $\tilde{\mathbf{a}}_v(\mathbf{\Phi})$ is the assignment for a single vector of model parameters, $\mathbf{a}_v(\mathbf{m_\Phi}, \mathbf{\Sigma_\Phi})$ is the expectation of the assignment for a Gaussian distribution of model parameters. If the mean $\mathbf{m_\Phi}$ approaches $\mathbf{\Phi}$ and the covariance $\mathbf{\Sigma_\Phi}$ approaches the zero matrix then $\mathbf{a}_v(\mathbf{m_\Phi}, \mathbf{\Sigma_\Phi})$ approaches $\tilde{\mathbf{a}}_v(\mathbf{\Phi})$. For a non-singular covariance $\mathbf{\Sigma_\Phi}$, the function $\mathbf{a}_v(\cdot, \mathbf{\Sigma_\Phi})$ is a smooth approximation of $\tilde{\mathbf{a}}_v(\cdot)$. In each iteration, the covariance matrix is updated in step 2b and thereby the smoothing is (usually) reduced. Figure 3.14 illustrates the objective function for different uncertainties (levels of smoothing). The function $\chi^2(\cdot, 0.5)$ with little blurring better approximates the objective function $\tilde{\chi}^2(\cdot)$ than the function $\chi^2(\cdot, 2)$ with more blurring. However, $\chi^2(\cdot, 0.5)$ has a smaller area of convergence when using Newton iteration as optimization method.

We interpret the estimate $\widehat{\mathbf{\Phi}}$ of the model parameters $\mathbf{\Phi}$ as the mean $\mathbf{m_\Phi}$ of a Gaussian approximation of the posterior distribution. Therefore, in the following we denote the estimate of the model parameters by $\mathbf{m_\Phi}$. With this notation and the substitution of $\tilde{\mathbf{a}}_v(\cdot)$ by $\mathbf{a}_v(\cdot, \mathbf{\Sigma_\Phi})$ the estimate $\mathbf{m_\Phi}$ of the model parameters $\mathbf{\Phi}$ can be written as

$$\mathbf{m_\Phi} = \arg\min_{\mathbf{m_\Phi}} \chi^2(\mathbf{m_\Phi}) \quad \text{with} \tag{3.36}$$

$$\chi^2(\mathbf{m_\Phi}) = -2\ln p(\mathbf{I}_\mathcal{V} = \mathbf{I}^*_\mathcal{V} \mid \mathbf{a}_\mathcal{V}(\mathbf{m_\Phi}, \mathbf{\Sigma_\Phi}), \mathbf{S}_\mathcal{V}) - 2\ln p(\mathbf{m_\Phi} \mid \mathbf{m}^*_\mathbf{\Phi}, \mathbf{\Sigma}^*_\mathbf{\Phi}). \tag{3.37}$$

The term $-2\ln p(\mathbf{I}_\mathcal{V} = \mathbf{I}^*_\mathcal{V} \mid \mathbf{a}_\mathcal{V}(\mathbf{m_\Phi}, \mathbf{\Sigma_\Phi}), \mathbf{S}_\mathcal{V})$ evaluates the fit between the sensed image data $\mathbf{I}^*_\mathcal{V}$ and the Gaussian distribution of model parameters with mean $\mathbf{m_\Phi}$ and covariance $\mathbf{\Sigma_\Phi}$. The term $-2\ln p(\mathbf{m_\Phi} \mid \mathbf{m}^*_\mathbf{\Phi}, \mathbf{\Sigma}^*_\mathbf{\Phi})$ evaluates the fit between the estimate $\mathbf{m_\Phi}$ and the a priori density. In order to optimize $\chi^2(\mathbf{m_\Phi})$ only a single Newton iteration step is performed. Thereafter, the steps 2b and 1 of the CCD algorithm are executed, which yield new local statistics $\mathbf{S}_\mathcal{V}$ and an evaluation $-2\ln p(\mathbf{I}_\mathcal{V} = \mathbf{I}^*_\mathcal{V} \mid \mathbf{a}_\mathcal{V}(\mathbf{m_\Phi}, \mathbf{\Sigma_\Phi}), \mathbf{S}_\mathcal{V})$ to be optimized.

Figure 3.15 row d depicts the image data expected by the blurred model, i.e. the image data $\mathbf{I}_\mathcal{V}$ optimizing the blurred observation density $p(\mathbf{I}_\mathcal{V} \mid \mathbf{a}_\mathcal{V}(\mathbf{m_\Phi}, \mathbf{\Sigma_\Phi}), \mathbf{S}_\mathcal{V})$. The evaluation of a fit between the image data and the blurred model not only depends on the difference between the sensed image data (row a) and the expected image data (row d). The evaluation of a fit depends also on the covariance expected by the blurred model. Due to the high number of covariance elements, only the determinants of the covariances are illustrated in row e. The upper side of the curve is more inhomogeneous than the lower side (see row a). Hence, the expected uncertainty is higher at the upper side (see row e).

Figure 3.15 row f depicts the energy $\chi^2_v = -2\ln p(\mathbf{I}_v = \mathbf{I}^*_v \mid \mathbf{a}_v(\mathbf{m_\Phi}, \mathbf{\Sigma_\Phi}), \mathbf{S}_v)$ for each pixel v, i.e. the contribution of v to the objective function χ^2. The energy is approximately two times the squared difference between the observed pixel value $\mathbf{I}^*_v$ (row a) and the expectation according to the blurred model (row d) weighted by the expected covariances (row e).

For the estimate $\mathbf{m_\Phi}$ optimizing $\chi^2(\mathbf{m_\Phi})$, the partial derivatives of $\chi^2(\mathbf{m_\Phi})$ must be zero. For each pixel in the vicinity $\mathcal{V}$ of the curve, the partial derivative of the energy χ^2_v can be interpreted as a force. Step 2a of the CCD algorithm seeks to find the estimate $\mathbf{m_\Phi}$ that yields an equilibrium between the pixel forces. Figure 3.15 row g depicts the forces acting in the direction perpendicular to the expected curve. Pixels depicted as bright act in a direction opposite to the pixels depicted as dark. During the first iterations, the majority of the pixels forces the curve downward. In iteration 2, the curve is already aligned on the left side but not on the right side.

continued from Figure 3.10 on page 38

iteration: 0	2	5
a.) $\mathbf{I}_v^*$, image data with superimposed mean curve		
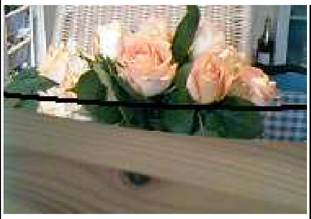	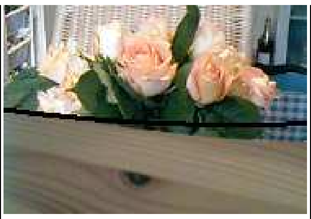	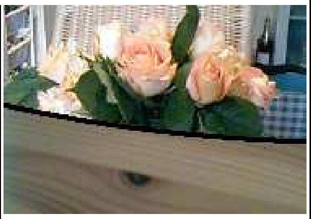
d.) $\mathbf{m}_v$, expected image according to the blurred model		
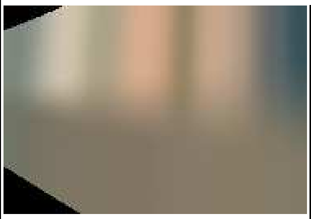	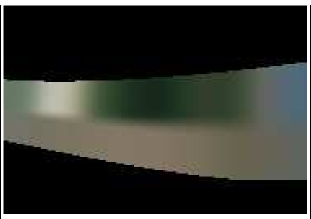	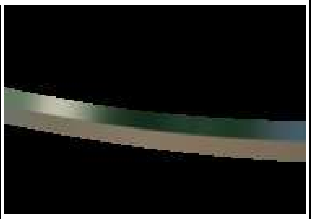
e.) $\|\mathbf{\Sigma}_v\|$, determinants of the expected covariances according to the blurred model, bright pixels indicate a high expected uncertainty		
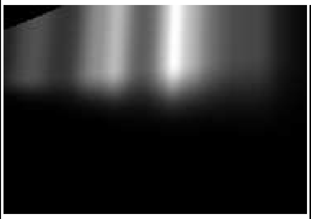	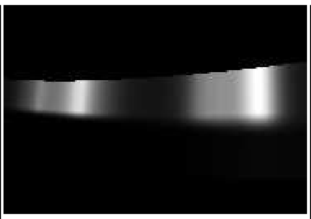	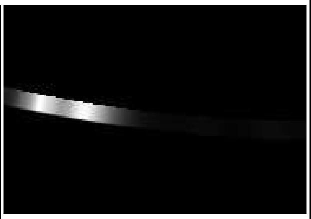
f.) energies, approximately proportional to the squared difference between row a and row d weighted by the covariance $\mathbf{\Sigma}_v$ (see row e)		
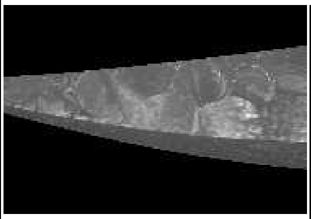	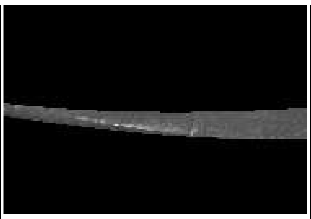	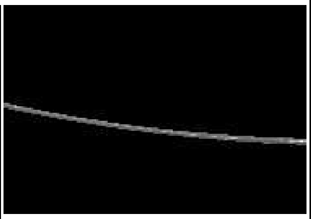
g.) forces, intensities indicate strengths and orientations of the forces (bright pixels force the curve downward, dark pixels force it upward)		
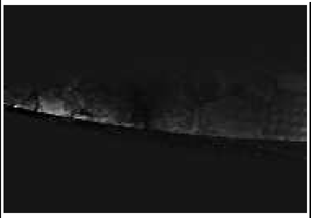	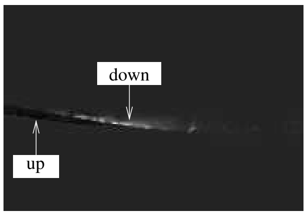	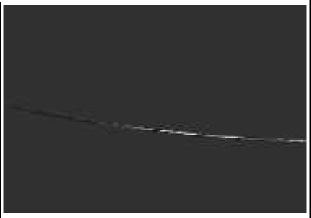

Figure 3.15: Quantities of the fitting process II: See text for description. (The images in rows e to g are individually normalized such that the gray values are within [0,255].)

On the left, the equilibrium of forces keeps the curve aligned. On the right, the curve is forced further down.

The area of pixels, which influence the position of the expected curve, depends on the uncertainty of the curve in the image. In Figure 3.15 the initial uncertainty of the curve is high on the right side and smaller on the left side. Consequently, on the right side the area of pixels affecting the curve estimate is wider than on the left side. However, pixels in the wider area exert, on average, lower forces than pixels in the narrow area. Furthermore, pixels which are close to the expected curve exert stronger forces, on average, than pixels which are further apart.

3.3.2.3 Newton Iteration Step

In a Newton iteration step, the estimate $\mathbf{m}_{\mathbf{\Phi}}$ of the model parameters is updated by minimizing the objective function $\chi^2(\mathbf{m}_{\mathbf{\Phi}})$ for $\mathbf{m}_{\mathbf{\Phi}}$. The objective function $\chi^2(\mathbf{m}_{\mathbf{\Phi}})$ consists of two parts

$$
\begin{aligned}
\chi^2(\mathbf{m}_{\mathbf{\Phi}}) &= \chi_1^2(\mathbf{m}_{\mathbf{\Phi}}) + \chi_2^2(\mathbf{m}_{\mathbf{\Phi}}) && (3.38)\\
\chi_1^2(\mathbf{m}_{\mathbf{\Phi}}) &= -2\sum_{v\in\mathcal{V}} \ln(p(\mathbf{I}_v = \mathbf{I}_v^* \mid \mathbf{a}_v(\mathbf{m}_{\mathbf{\Phi}}, \mathbf{\Sigma}_{\mathbf{\Phi}}), \mathbf{S}_v)) && (3.39)\\
\chi_2^2(\mathbf{m}_{\mathbf{\Phi}}) &= -2\ln(p(\mathbf{m}_{\mathbf{\Phi}} \mid \mathbf{m}_{\mathbf{\Phi}}^*, \mathbf{\Sigma}_{\mathbf{\Phi}}^*)), && (3.40)
\end{aligned}
$$

where $\chi_1^2(\mathbf{m}_{\mathbf{\Phi}})$ assesses the fit between the image and the estimate $\mathbf{m}_{\mathbf{\Phi}}$, and $\chi_2^2(\mathbf{m}_{\mathbf{\Phi}})$ assesses the fit between the a priori density and the estimate $\mathbf{m}_{\mathbf{\Phi}}$. The estimate $\mathbf{m}_{\mathbf{\Phi}}^{(i)}$ of iteration step i can be obtained by the update equation

$$
\mathbf{m}_{\mathbf{\Phi}}^{(i)} = \mathbf{m}_{\mathbf{\Phi}}^{(i-1)} - \left(\mathbf{H}^{(i-1)}\right)^{-1} \mathbf{J}^{(i-1)}, \qquad (3.41)
$$

where $\mathbf{m}_{\mathbf{\Phi}}^{(i-1)}$ is the estimate of iteration step $i-1$. The matrix $\mathbf{H}^{(i-1)}$ is the Hessian and $\mathbf{J}^{(i-1)}$ is the Jacobian of χ^2 in the point $\mathbf{m}_{\mathbf{\Phi}}^{(i-1)}$.

Modified Newton Iteration Step

In this section, we propose a modification of the Newton iteration step defined in equation 3.41. The modification achieves an enlarged area of convergence especially for high dimensional parameter vectors. However, in many cases the area of convergence of the original Newton iteration is sufficient. Therefore, the following modification is optional.

Equation (3.41) yields a valid update only if the Hessian $\mathbf{H}$ is positive definite, i.e. its eigenvalues are strictly positive. However, for large initial errors, the Hessian may have non-positive eigenvalues. Components of the parameter vector $\mathbf{\Phi}$ that correspond to eigenvectors of $\mathbf{H}$ with *non*-positive eigenvalues cannot be updated according to equation (3.41). We update these components based on the a priori distribution only, i.e. by minimizing $\chi_2^2(\mathbf{m_\Phi})$. According to equation (3.38), the Hessian $\mathbf{H}$ and the Jacobian $\mathbf{J}$ of $\chi^2(\mathbf{m_\Phi})$ can be written as sums

$$\begin{aligned} \mathbf{H} &= \mathbf{H}_1 + \mathbf{H}_2 && (3.42) \\ \mathbf{J} &= \mathbf{J}_1 + \mathbf{J}_2 \, , && (3.43) \end{aligned}$$

where $\mathbf{H}_1$ and $\mathbf{J}_1$ correspond to $\chi_1^2(\mathbf{m_\Phi})$; and $\mathbf{H}_2$ and $\mathbf{J}_2$ correspond to $\chi_2^2(\mathbf{m_\Phi})$. The Hessian $\mathbf{H}_2$ is given by

$$\mathbf{H}_2 = 2\,(\mathbf{\Sigma}_\mathbf{\Phi}^*)^{-1} \, , \qquad (3.44)$$

which is positive definite for any valid covariance matrix $\mathbf{\Sigma}_\mathbf{\Phi}^*$. However, $\mathbf{H}_1$ may have non-positive eigenvalues. Using eigenvalue decomposition, the matrix $\mathbf{H}_1$ can be written as

$$\mathbf{H}_1 = (\mathbf{e}_1, \ldots, \mathbf{e}_{D_\mathbf{\Phi}}) \cdot \text{diag}(e_1, \ldots, e_{D_\mathbf{\Phi}}) \cdot (\mathbf{e}_1, \ldots, \mathbf{e}_{D_\mathbf{\Phi}})^T \, , \qquad (3.45)$$

where $\mathbf{e}_j$ ($j \in \{1, \ldots, D_\mathbf{\Phi}\}$) are the eigenvectors and e_j are the eigenvalues of $\mathbf{H}_1$. We substitute in $\mathbf{H}_1$ and $\mathbf{J}_1$ the partial derivatives, which correspond to directions $\mathbf{e}_j$ of negative eigenvalues e_j, by zero. The resulting modified Hessian $\mathbf{H}_1'$ is given by

$$\begin{aligned} \mathbf{H}_1' &= (\mathbf{e}_1, \ldots, \mathbf{e}_{D_\mathbf{\Phi}}) \cdot \text{diag}(e_1', \ldots, e_{D_\mathbf{\Phi}}') \cdot (\mathbf{e}_1, \ldots, \mathbf{e}_{D_\mathbf{\Phi}})^T \quad \text{where} && (3.46) \\ e_j' &= \max(0, e_j) \, . && (3.47) \end{aligned}$$

The resulting modified Jacobian $\mathbf{J}_1'$ is given by

$$\begin{aligned} \mathbf{J}_1' &= (\mathbf{e}_1, \ldots, \mathbf{e}_{D_\mathbf{\Phi}}) \cdot \text{diag}(e_1^+, \ldots, e_{D_\mathbf{\Phi}}^+) \cdot (\mathbf{e}_1, \ldots, \mathbf{e}_{D_\mathbf{\Phi}})^T \cdot \mathbf{J}_1 \quad \text{where} && (3.48) \\ e_j^+ &= \begin{cases} 1 & \text{if } e_j > 0 \\ 0 & \text{otherwise} \, . \end{cases} && (3.49) \end{aligned}$$

We substitute $\mathbf{H}_1$ by $\mathbf{H}_1'$ in equation (3.42), and $\mathbf{J}_1$ by $\mathbf{J}_1'$ in equation (3.43). With the resulting matrixes $\mathbf{H}$ and $\mathbf{J}$, the update equation (3.41) can always be applied. Components of the parameter vector that are not improved in iteration step i are usually improved in the successive iteration steps. Our experiments presented in chapter 5 show that the CCD algorithm generally achieves a high convergence rate.

3.3.2.4 Outlier Treatment

In this section, we show how the update of the mean vector can be further improved. The observation model derived in section 3.3.1 assumes that the pixel value $\mathbf{I}_v$ of a pixel v is a linear mix of two random variables $\mathbf{I}_{v,1}$ and $\mathbf{I}_{v,2}$. Furthermore, it assumes that the two random variables are distributed according to the corresponding statistics of the two sides computed in step 1 of the CCD algorithm. Our experiments show that this observation model is appropriate even for heavily textured and cluttered scenes. However, the performance of the CCD algorithm can be further improved by reducing the impact of outliers.

We define an outlier as a pixel value $\mathbf{I}_v$ that does not fit to the observation model, i.e. it is not a linear mix of the two sides. Such outliers are local variations of the pixel values that have not been observed in the windows used for computing the local statistics. One reason for outliers are e.g. local highlights. The number of outlier pixels is usually relatively small. Nevertheless, outliers can still have a strong impact on the fitting process because they can exert very strong forces on the curve. In some cases, the outliers can not be counterbalanced by the non-outliers and thus the area of convergence is reduced substantially. Furthermore, outliers may also limit the accuracy of the final fit.

Pixels that do not fit to any of the two sides of the curve should not exert any forces on the curve; these pixels should simply be ignored. We achieve this goal by performing a weighted fit. For each pixel in the vicinity of the curve, we compute the probability of being not an outlier. This non-outlier probability is used as a weight in order to construct a weighted variant of the objective function.

This approach is related to other robust estimators commonly used in computer vision (Zhang, 1997; Huber, 1981). The basic strategy of these methods is to iteratively adapt the weights based on the distance between the measurements (in our case the sensed pixel values) and the fitted model (in our case the expected pixel values).

We formulate the problem of computing appropriate weights as a classification problem with two classes. The two classes are the outlier class $\mathcal{O}$ and the non-outlier class $\mathcal{N}$ with the a priori probabilities $p_{\mathcal{O}}$ and $p_{\mathcal{N}} = 1 - p_{\mathcal{O}}$, respectively. We assume that the classes generate pixel values $\mathbf{I}_v$ according to the conditional densities $p(\mathbf{I}_v \mid \mathcal{O})$ and $p(\mathbf{I}_v \mid \mathcal{N})$. For the non-outlier class, we employ the distribution $p(\mathbf{I}_v \mid \mathbf{a}_v, \mathbf{S}_v)$ derived in section 3.3.1:

$$p(\mathbf{I}_v \mid \mathcal{N}) = p(\mathbf{I}_v \mid \mathbf{a}_v, \mathbf{S}_v) \; . \tag{3.50}$$

In contrast to equation (3.30), we here use the probabilistic assignment $\mathbf{a}_v(\mathbf{m}_\Phi, \mathbf{\Sigma}_\Phi)$ instead of the sharp assignment $\tilde{\mathbf{a}}(\mathbf{m}_\Phi)$. For reasons of simplicity, we employ a uniform distribution for the outlier distribution $p(\mathbf{I}_v \mid \mathcal{O})$. However, one could also apply a more sophisticated distribution, e.g. a distribution that takes into account that outliers often have clipped pixel values. Such pixel values have a maximum value in one or more RGB channels.

The non-outlier probability $p(\mathcal{N} \mid \mathbf{I}_v)$ of the pixel value $\mathbf{I}_v$ can be obtained by Bayes' rule:

$$p(\mathcal{N} \mid \mathbf{I}_v) = \frac{(1 - p_{\mathcal{O}}) \cdot p(\mathbf{I}_v \mid \mathcal{N})}{p_{\mathcal{O}} \cdot p(\mathbf{I}_v \mid \mathcal{O}) + (1 - p_{\mathcal{O}}) \cdot p(\mathbf{I}_v \mid \mathcal{N})} . \tag{3.51}$$

In our experiments, we choose an a priori outlier probability of $p_{\mathcal{O}} = 0.05$. The weighted objective function $\chi^2(\mathbf{m}_{\mathbf{\Phi}})$ is obtained by including the non-outlier probability $p(\mathcal{N} \mid \mathbf{I}_v)$ in the function $\chi_1^2(\mathbf{m}_{\mathbf{\Phi}})$:

$$\begin{aligned}
\chi^2(\mathbf{m}_{\mathbf{\Phi}}) &= \chi_1^2(\mathbf{m}_{\mathbf{\Phi}}) + \chi_2^2(\mathbf{m}_{\mathbf{\Phi}}) & (3.52)\\
\chi_1^2(\mathbf{m}_{\mathbf{\Phi}}) &= -2 \sum_{v \in \mathcal{V}} \left[p(\mathcal{N} \mid \mathbf{I}_v) \cdot \ln(p(\mathbf{I}_v = \mathbf{I}_v^* \mid \mathbf{a}_v(\mathbf{m}_{\mathbf{\Phi}}, \mathbf{\Sigma}_{\mathbf{\Phi}}), \mathbf{S}_v)) \right] & (3.53)\\
\chi_2^2(\mathbf{m}_{\mathbf{\Phi}}) &= -2 \ln(p(\mathbf{m}_{\mathbf{\Phi}} \mid \mathbf{m}_{\mathbf{\Phi}}^*, \mathbf{\Sigma}_{\mathbf{\Phi}}^*)) . & (3.54)
\end{aligned}$$

Our experiments described in section 5.2.1 (page 88 variant D) show the advantages of the CCD algorithm using the outlier treatment over the CCD algorithm without outlier treatment.

3.3.3 Updating the Covariance Matrix

In step 2b, the covariance matrix $\mathbf{\Sigma}_{\mathbf{\Phi}}$ describing the uncertainty of the estimate $\mathbf{m}_{\mathbf{\Phi}}$ is updated. For the case where the relation between the model parameters and the observations is linear and the observation noise is Gaussian, the covariance matrix $\mathbf{\Sigma}_{\mathbf{\Phi}}$ of the χ^2-estimate $\mathbf{m}_{\mathbf{\Phi}}$ is given by

$$\mathbf{\Sigma}_{\mathbf{\Phi}} = \frac{2}{\mathbf{H}} , \tag{3.55}$$

where $\mathbf{H}$ denotes the Hessian of $\chi^2(\mathbf{m}_{\mathbf{\Phi}})$ in the point $\mathbf{m}_{\mathbf{\Phi}}$ minimizing $\chi^2(\mathbf{m}_{\mathbf{\Phi}})$ (Press et al., 1996). Since in our case, the relation between the model parameters and the image data is not linear, equation (3.55) can only be regarded as an estimate of the uncertainty. Another uncertainty arises due to the way the estimate $\mathbf{m}_{\mathbf{\Phi}}$ is obtained. In step 2a, only a single iteration step is performed. Hence, the resulting estimate $\mathbf{m}_{\mathbf{\Phi}}^{(i)}$ of iteration i does not necessarily minimize the objective function χ^2. Therefore, we update the covariance $\mathbf{\Sigma}_{\mathbf{\Phi}}$ by the following heuristics:

$$\mathbf{\Sigma}_{\mathbf{\Phi}}^{(i)} := c_2 \mathbf{\Sigma}_{\mathbf{\Phi}}^{(i-1)} + (1 - c_2) \frac{2}{\mathbf{H^{(i-1)}}} . \tag{3.56}$$

Here, $\mathbf{\Sigma}_{\mathbf{\Phi}}^{(i-1)}$ is the covariance computed in the last iteration step and $\frac{2}{\mathbf{H}^{(i-1)}}$ is the estimate of the covariance according to (3.55). However, $\mathbf{H}^{(i-1)}$ is the Hessian in the point $\mathbf{m}_{\mathbf{\Phi}}^{(i-1)}$, which does not necessarily maximize χ^2 exactly. The parameter $c_2 \in [0, 1[$, e.g. $c_2 = 0.25$, specifies the maximum decrease of the covariance within one iteration step. If c_2 is too high, the covariance declines slowly which leads to a high number of iterations. If c_2 is too small, the CCD algorithm may converge to a wrong solution.

At the beginning of the iteration, the covariance $\mathbf{\Sigma_\Phi}$ usually decreases roughly exponentially. However, for an overrated estimate $\mathbf{m_\Phi}$, i.e. an estimate $\mathbf{m_\Phi}$, which is not as good as specified by $\mathbf{\Sigma_\Phi}$, the curvature (Hessian) of the objective function decreases. In Figure 3.14, the curvature of the χ^2 function has its maximum close to the minimum of χ^2. This slows down the reduction of $\mathbf{\Sigma_\Phi}$ or even increases $\mathbf{\Sigma_\Phi}$ if the quality of the estimate $\mathbf{m_\Phi}$ is overrated by $\mathbf{\Sigma_\Phi}$. Hence, the chance that the iteration still converges is increased. Steps 1 and 2 of the CCD algorithm are iterated until the changes of the estimate $\mathbf{m_\Phi}$ and the associated covariance $\mathbf{\Sigma_\Phi}$ are small enough.

After the last iteration step, a post-processing step is performed, see Figure 3.2 on page 24. In this step, the covariance of the estimate $\mathbf{m}_\mathbf{\Phi}^{(i)}$ is estimated by $\mathbf{\Sigma}_\mathbf{\Phi}^{(i)} := \frac{2}{\mathbf{H}^{(i-1)}}$. Finally, the estimate $\mathbf{m}_\mathbf{\Phi}^{(i)}$ of the model parameters and the estimate $\mathbf{\Sigma}_\mathbf{\Phi}^{(i)}$ of the corresponding covariance are returned.

3.4 Summary of the Algorithm

Figure 3.16 summarizes the CCD algorithm using the notation introduced above. The algorithm represents its belief of the model parameters by the mean vector $\mathbf{m_\Phi}$ and the covariance matrix $\mathbf{\Sigma_\Phi}$ which are initialized based on the a priori density. In step 1, local statistics of the pixel values are computed from pixels in the vicinity of the curve. In step 2, the mean vector $\mathbf{m_\Phi}$ and the covariance matrix $\mathbf{\Sigma_\Phi}$ are updated using a MAP criterion. This MAP criterion is derived from the local statistics obtained in step 1. The resulting objective function $\chi^2(\mathbf{m_\Phi})$ is either defined according to equation (3.38) (without outlier treatment) or according to equation (3.52) (with outlier treatment). Step 1 and step 2 are alternately performed until the changes of $\mathbf{m_\Phi}$ and $\mathbf{\Sigma_\Phi}$ are small enough. Alternatively, for example, a predefined number of iterations can be performed. Finally, in the post-processing step, the covariance matrix $\mathbf{\Sigma_\Phi}$ is estimated using the Hessian of the last objective function.

Contracting Curve Density (CCD) algorithm

Input: image data $\mathbf{I}^*$, curve function $\mathbf{c}$, mean $\mathbf{m}^*_{\mathbf{\Phi}}$ and covariance $\mathbf{\Sigma}^*_{\mathbf{\Phi}}$

Output: estimate $\mathbf{m}_{\mathbf{\Phi}}$ of model parameters and associated covariance $\mathbf{\Sigma}_{\mathbf{\Phi}}$

```
Initialization: mean $\mathbf{m}_{\mathbf{\Phi}} = \mathbf{m}^*_{\mathbf{\Phi}}$, covariance $\mathbf{\Sigma}_{\mathbf{\Phi}} = c_1 \cdot \mathbf{\Sigma}^*_{\mathbf{\Phi}}$
repeat
    1. learn local statistics of image data from the vicinity of the curve
        (a) determine pixels $v$ in vicinity $\mathcal{V}$ of the image curve from $\mathbf{c}$, $\mathbf{m}_{\mathbf{\Phi}}$ and $\mathbf{\Sigma}_{\mathbf{\Phi}}$
            $\forall v \in \mathcal{V}$ compute probabilistic assignment $\mathbf{a}_v(\mathbf{m}_{\mathbf{\Phi}}, \mathbf{\Sigma}_{\mathbf{\Phi}})$ to the sides of the curve
        (b) $\forall v \in \mathcal{V}$ compute local statistics $\mathbf{S}_v$ of image data $\mathbf{I}^*_{\mathcal{V}}$
            which characterize the two sides of the curve
    2. refine estimate of model parameter vector
        (a) update the mean $\mathbf{m}_{\mathbf{\Phi}}$ by performing one iteration step of MAP estimation:
            $\mathbf{m}_{\mathbf{\Phi}} = \arg\min_{\mathbf{m}_{\mathbf{\Phi}}} \chi^2(\mathbf{m}_{\mathbf{\Phi}})$   with
            $\chi^2(\mathbf{m}_{\mathbf{\Phi}}) = -2\ln[p(\mathbf{I}_{\mathcal{V}} = \mathbf{I}^*_{\mathcal{V}} \mid \mathbf{a}_{\mathcal{V}}(\mathbf{m}_{\mathbf{\Phi}}, \mathbf{\Sigma}_{\mathbf{\Phi}}), \mathbf{S}_{\mathcal{V}}) \cdot$
                $\cdot\, p(\mathbf{m}_{\mathbf{\Phi}} \mid \mathbf{m}^*_{\mathbf{\Phi}}, \mathbf{\Sigma}^*_{\mathbf{\Phi}})]$
        (b) update the covariance $\mathbf{\Sigma}_{\mathbf{\Phi}}$ from the Hessian of $\chi^2(\mathbf{m}_{\mathbf{\Phi}})$
until changes of $\mathbf{m}_{\mathbf{\Phi}}$ and $\mathbf{\Sigma}_{\mathbf{\Phi}}$ are small enough
Post-processing: estimate covariance $\mathbf{\Sigma}_{\mathbf{\Phi}}$ from the Hessian of $\chi^2(\mathbf{m}_{\mathbf{\Phi}})$
return mean $\mathbf{m}_{\mathbf{\Phi}}$ and covariance $\mathbf{\Sigma}_{\mathbf{\Phi}}$
```

Figure 3.16: The CCD algorithm iteratively refines a Gaussian a priori density $p(\mathbf{\Phi}) = p(\mathbf{\Phi} \mid \mathbf{m}^*_{\mathbf{\Phi}}, \mathbf{\Sigma}^*_{\mathbf{\Phi}})$ of model parameters to a Gaussian approximation $p(\mathbf{\Phi} \mid \mathbf{m}_{\mathbf{\Phi}}, \mathbf{\Sigma}_{\mathbf{\Phi}})$ of the posterior density $p(\mathbf{\Phi} \mid \mathbf{I}^*)$.

Chapter 4

The CCD Tracker

The CCD algorithm, derived in the previous chapters, fits a parametric curve model to a *single* image. In this chapter we propose the *CCD tracker*, a method for fitting a curve model to a *sequence* of images. The image sequence could be for example, video data, i.e. a sequence of images captured at successive time-steps. It could also consist of neighboring 2-D slices of a higher-dimensional volume. Such higher-dimensional image data are often given in medical applications where, for example, magnetic resonance (MR) or computer tomography (CT) images are common.

A naive tracking algorithm can be obtained by applying the CCD algorithm, as described in the previous chapter, to each image independently. However, such a tracker would be of limited use. The CCD tracker achieves a better performance by implementing two key ideas:

1. **Focus on a small set of relevant pixels:** The CCD tracker employs a fast real-time variant of the CCD algorithm. This algorithm achieves a high speed-up mainly by focusing only on a small set of carefully chosen pixels. In each iteration step the fast variant of the CCD algorithm takes only such pixels into account that are likely to further reduce the uncertainty of the curve. Thus, the CCD tracker can cope with the large amount of data, which needs to be processed in many tracking applications.

2. **Exploit statistical dependencies between successive images:** The CCD tracker achieves an additional improvement of its performance by exploiting statistical dependencies between successive images. The CCD tracker uses two kinds of statistical dependencies:

   (a) **Coherence of motion[1]:** In general, the motion of the curve follows a particular motion pattern. For example, usually the acceleration of the curve is limited. Hence, the positions and shapes of the curve in successive images are statistically dependent.

[1]The term coherence of motion has been coined by Yuille and Grzywacz (1988).

(b) **Temporal[2] coherence of pixel values:** Typically, the pixel values, e.g. RGB values, between successive images are highly statistically dependent. For example, the same surface point of an object yields often similar pixel values in two successive images. This holds even for moving objects and for gradually changing illumination.

The CCD tracker exploits both kinds of statistical dependencies by performing two steps for each image: 1. *Propagate* knowledge about the curve motion and/or the pixel values to the next image. 2. Use the propagated knowledge for *improving* the curve fitting process.

This chapter is organized as follows. First, in section 4.1, we propose a fast or *real-time* variant of the CCD algorithm which is based on the first key idea described above. In section 4.2, we describe dynamical models that allow for exploiting the coherence of curve motion. Then, in section 4.3, we propose methods for exploiting the temporal coherence of pixel values. In section 4.4, we summarize the CCD tracker and analyze its runtime and space complexity. Finally, in section 4.5, we relate the CCD tracker to previous work.

4.1 Real-time CCD Algorithm

In many applications, e.g. in the context of mobile autonomous robots, scene analysis has to be performed with limited computational resources and within given tight time limits. Hence, often methods for curve-fitting have to be particularly efficient. To meet this requirement, we propose the *real-time* CCD (RT-CCD) algorithm, also called *fast* CCD algorithm. This variant of the CCD algorithm allows for processing even high-resolution images at frame-rate (Hanek et al., 2002a). Despite its low runtime, the RT-CCD algorithm achieves sub-pixel accuracy even for high-resolution images. Furthermore, the RT-CCD algorithm is an any-time algorithm. That is, the algorithm provides a solution at any time and continuously improves the quality of the solution. The RT-CCD algorithm is obtained by modifying the CCD algorithm of chapter 3 as follows:

1. The RT-CCD algorithm uses only a small number of carefully chosen pixels lying on specific perpendiculars to the expected image curve. In contrary, the original CCD algorithm uses all pixels in the vicinity of the curve.

2. The RT-CCD algorithm ignores the sub-pixel distances between a perpendicular and the

[2]Spatial coherence of pixel values is already used by the CCD algorithm. By *coherence of pixel values* we refer to the temporal coherence.

center points of the pixels intersected by this perpendicular. Thus, several quantities, e.g. the local statistics, need to be computed only once per perpendicular.

3. The RT-CCD algorithm approximates a pixel by a point if the local uncertainty of the curve is high, compared to the size of the pixel.

In the following we refer to the original CCD algorithm as *dense CCD algorithm.* The subsequent sections describe, in detail, the modifications to obtain the RT-CCD algorithm. Section 4.1.1 describes how the RT-CCD algorithm chooses the set of used pixels. In section 4.1.2, we show how to speed-up the probabilistic assignment of a pixel to either side of the curve. Then, in section 4.1.3, we derive an efficient method for computing the local statistics for each perpendicular. In section 4.1.4, we show how the performance of the RT-CCD algorithm can further be improved, based on a confirmation measurement evaluating the overlap between two successive solutions.

4.1.1 Choosing Pixels in the Vicinity of the Curve

Let us now describe how the RT-CCD algorithm chooses the set of pixels it takes into account. The algorithm uses only pixels lying on one of K different straight line segments $k \in [1, K]$, see Figure 4.1b. Such a line segment k is a perpendicular on the point

$$\mathbf{C}_k = \mathbf{c}(\omega_k, \mathbf{m}_\mathbf{\Phi}) \tag{4.1}$$

of the expected image curve $\mathbf{c}(\cdot, \mathbf{m}_\mathbf{\Phi})$. The scalars $\omega_k \in \{\omega_1, \ldots, \omega_K\}$ are chosen such that the corresponding curve points $\mathbf{C}_k$ are roughly equally spaced along the curve. The line segments are centered at the curve points $\mathbf{C}_k$. The lengths of the segments depend on the local uncertainties of the curve. We choose the segments to have minimal lengths but such that they reach all pixels having a non-zero weighting W_s. See equation (3.14) for the definition of the weighting function W_s.

For each perpendicular k, we use up to L (e.g. L=25) equally spaced pixels $v_{k,l}$, where $l \in [1, L]$. Since the number of considered pixels is limited (at most $K \cdot L$), the time complexity of each iteration step is independent of the image resolution. At the beginning of the iteration, the local uncertainty of the curve is high and the pixels on a perpendicular have relatively high distances. During the iteration the distances decrease, see Figure 4.1b. The RT-CCD algorithm continuously focuses on those pixels that are expected to be most relevant. The focusing enables the algorithm to be both fast and accurate even for high-resolution images.

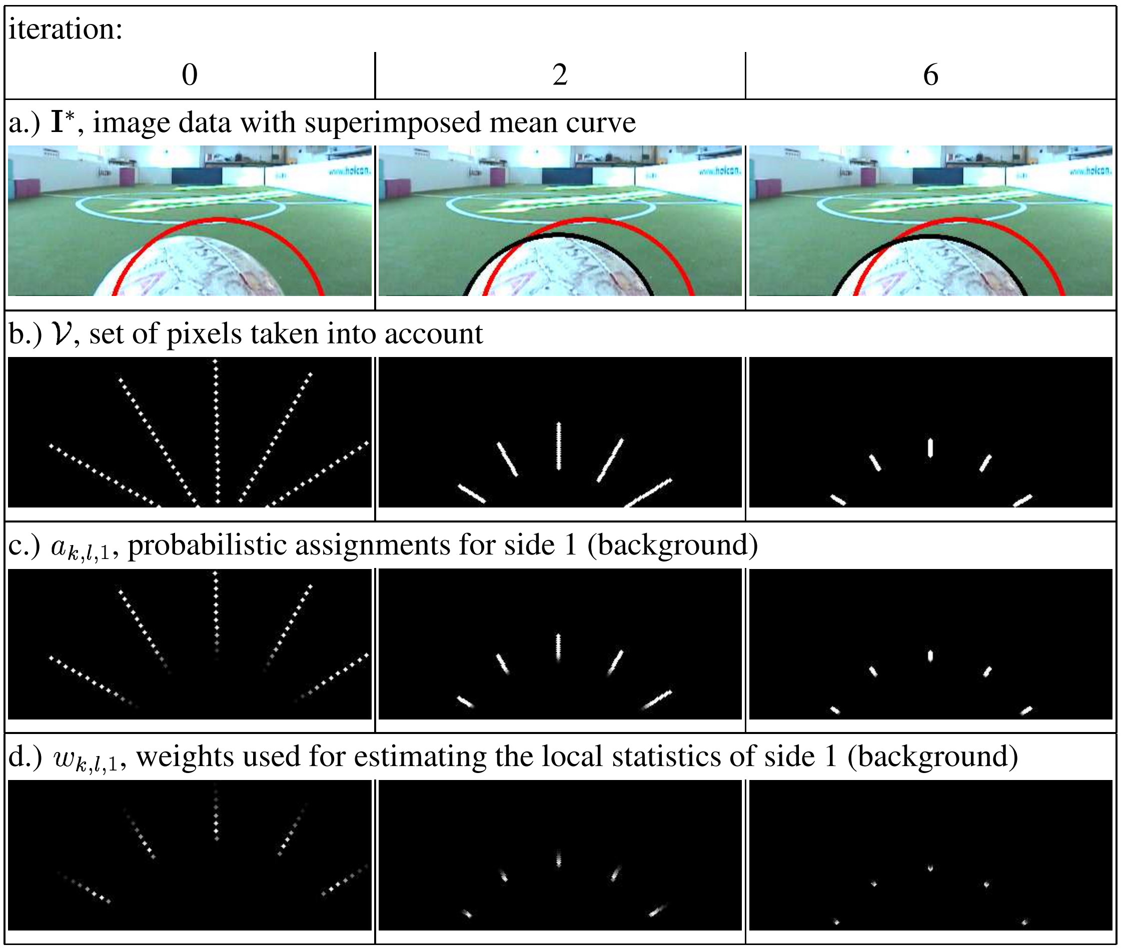
iteration:
0
2
6
a.) $\mathbf{I}^*$, image data with superimposed mean curve
b.) $\mathcal{V}$, set of pixels taken into account
c.) $a_{k,l,1}$, probabilistic assignments for side 1 (background)
d.) $w_{k,l,1}$, weights used for estimating the local statistics of side 1 (background)

Figure 4.1: Localization of a ball by an autonomous soccer robot: In each iteration step, only a small number of pixels is taken into account. However, these pixels contain the necessary information for refining the fit. (red = initial curve, black = fitted curve)

In the following, let $\mathbf{X}_{k,l}$ denote some variable $\mathbf{X}$ corresponding to pixel $v_{k,l}$. We denote the center point of pixel $v_{k,l}$ by $\mathbf{v}_{k,l}$. Quantities that correspond to a whole perpendicular k rather than to individual pixels are indexed by k.

4.1.2 Assigning Pixels to a Side of the Curve

In order to probabilistically assign a pixel to either side of the curve, the dense CCD algorithm takes the photosensitive area of the pixel into account. This requires an integration over the pixel's photosensitive area, see equation (3.11). A faster approximation can be obtained by approximating the integral by the value resulting for the pixel's center point $\mathbf{v}_{k,l}$. The RT-CCD algorithm applies this approximation if the local uncertainty of the curve is high, compared with the pixel size. If the local standard deviation σ_k defined in equation (3.9) exceeds the size of one pixel, then the probabilistic assignment $\mathbf{a}_{k,l}$ for pixel $v_{k,l}$ is obtained by

$$\begin{aligned} \mathbf{a}_{k,l} &= (a_{k,l,1}, 1 - a_{k,l,1}) \quad \text{where} & (4.2) \\ a_{k,l,1} &= \frac{1}{2} \cdot erf\left(\frac{d_{k,l}}{\sqrt{2} \cdot \sigma_k}\right) + \frac{1}{2}. & (4.3) \end{aligned}$$

Here, $d_{k,l}$ is the displacement between the pixel's center point $\mathbf{v}_{k,l}$ and the curve point $\mathbf{C}_k$ in the direction of the perpendicular:

$$d_{k,l} = \mathbf{n}_k^T \cdot (\mathbf{v}_{k,l} - \mathbf{C}_k). \tag{4.4}$$

In this equation, $\mathbf{n}_k$ denotes the unit normal vector to the curve at the point $\mathbf{C}_k$. Figure 4.1c depicts an example of the resulting probabilistic assignments to the background. During the iteration, the blurring of the probabilistic assignments decreases.

4.1.3 Recursive Computation of Local Statistics

The RT-CCD algorithm employs the same set of local statistics for all pixels belonging to the same perpendicular. The local statistics are obtained by (1) computing local statistics for each perpendicular independently; and (2) smoothing the local statistics along the curve. These two steps are detailed below.

Statistics for one Perpendicular

For each perpendicular and each side of the curve, we compute individual local statistics. These statistics take only the pixels $v_{k,l}$ of the respective perpendicular k into account. The pixels $v_{k,l}$ are scaled by weights

$$w_{k,l,s} = W_s(v_{k,l}), \tag{4.5}$$

where $s \in \{1, 2\}$ indicates the side of the curve. The weighting function W_s evaluates the distance to the curve, see equation (3.15). For each perpendicular k and each side s, the weighted statistical moments $\mathbf{m}_{k,s,o}$ of order $o \in \{0, 1, 2, \}$ are obtained by

$$\begin{aligned} \mathbf{m}_{k,s,0} &= \sum_{l \in \mathcal{V}_k} w_{k,l,s} & (4.6) \\ \mathbf{m}_{k,s,1} &= \sum_{l \in \mathcal{V}_k} w_{k,l,s}\, \mathbf{I}^*_{k,l} & (4.7) \\ \mathbf{m}_{k,s,2} &= \sum_{l \in \mathcal{V}_k} w_{k,l,s}\, \mathbf{I}^*_{k,l} \cdot {\mathbf{I}^*_{k,l}}^T & (4.8) \end{aligned}$$

where $\mathbf{I}^*_{k,l}$ is the pixel value of pixel $v_{k,l}$. The summations are performed only over the pixels $\mathcal{V}_k$ of the respective perpendicular k.

Smoothing Statistics along the Curve

In order to exploit statistical dependencies between pixels on neighboring perpendiculars, the statistical moments $\mathbf{m}_{k,s,o}$ computed individually for each perpendicular are blurred, i.e. smoothed, along the curve. We use an exponential filter since it allows for fast blurring with time complexity independent of the window size, i.e. the blurring parameter λ. By applying the same blurring along the curve as in equation (3.20), we can write the smoothed moments $\mathbf{M}_{k,s,o}$ as a weighted sum of the non-smoothed moments $\mathbf{m}_{k,s,o}$:

$$\mathbf{M}_{k,s,o} = \frac{\lambda}{2} \sum_{k'=1}^{K} \exp\left[-\lambda \cdot D(\mathbf{C}_{k'}, \mathbf{C}_k)\right] \cdot \mathbf{m}_{k',s,o} \,. \tag{4.9}$$

The distance $D(\mathbf{C}_{k'}, \mathbf{C}_k)$ is the arc length of the expected curve between point $\mathbf{C}_{k'}$ and point $\mathbf{C}_k$. The dense CCD algorithm computes this distance using all pixels along the curve between the two points. For reasons of efficiency, the RT-CCD algorithm uses just the points $\mathbf{C}_k$ defined in equation (4.1) in order to approximate the distances along the curve.

The moments $\mathbf{M}_{k,s,o}$ can be computed efficiently as follows. We split the sum defined in equation (4.9) into a lower and an upper part:

$$\begin{aligned}
\mathbf{M}_{k,s,o} &= \overrightarrow{\mathbf{M}}_{k,s,o} + \overleftarrow{\mathbf{M}}_{k,s,o} && (4.10)\\
\overrightarrow{\mathbf{M}}_{k,s,o} &= \frac{\lambda}{2} \sum_{k'=1}^{k} \exp\left[-\lambda \cdot D(\mathbf{C}_{k'}, \mathbf{C}_k)\right] \cdot \mathbf{m}_{k',s,o} && (4.11)\\
\overleftarrow{\mathbf{M}}_{k,s,o} &= \frac{\lambda}{2} \sum_{k'=k+1}^{K} \exp\left[-\lambda \cdot D(\mathbf{C}_{k'}, \mathbf{C}_k)\right] \cdot \mathbf{m}_{k',s,o} \,. && (4.12)
\end{aligned}$$

Both parts can be obtained in a fast recursive manner. The lower part $\overrightarrow{\mathbf{M}}_{k,s,o}$ is computed by[3]

$$\begin{aligned}
k = 1 : \overrightarrow{\mathbf{M}}_{k,s,o} &= \frac{\lambda}{2}\mathbf{m}_{k,s,o} && (4.13)\\
\forall k \in \{2, \ldots, K\} : \overrightarrow{\mathbf{M}}_{k,s,o} &= \exp\left[-\lambda \cdot ||\mathbf{C}_k - \mathbf{C}_{k-1}||\right] \cdot \overrightarrow{\mathbf{M}}_{k-1,s,o} + \frac{\lambda}{2}\mathbf{m}_{k,s,o} && (4.14)
\end{aligned}$$

and the upper part $\overleftarrow{\mathbf{M}}_{k,s,o}$ by

$$\begin{aligned}
k = K : \overleftarrow{\mathbf{M}}_{k,s,o} &= \mathbf{0} && (4.15)\\
\forall k \in \{1, \ldots, K-1\} : \overleftarrow{\mathbf{M}}_{k,s,o} &= \exp\left[-\lambda \cdot ||\mathbf{C}_k - \mathbf{C}_{k+1}||\right] \cdot \left[\overleftarrow{\mathbf{M}}_{k+1,s,o} + \frac{\lambda}{2}\mathbf{m}_{k+1,s,o}\right] . && (4.16)
\end{aligned}$$

In equation (4.15), $\mathbf{0}$ denotes a zero scalar, vector, or matrix, depending on the order o of the moments $\mathbf{M}_{k,s,o}$. From the local moments $\mathbf{M}_{k,s,o}$, the mean vectors $\mathbf{m}_{k,s}$ and covariance matrices $\mathbf{\Sigma}_{k,s}$ specifying the local Gaussian distributions can be obtained according to equations (3.21) and (3.22), respectively.

[3]Here, the recursions are derived for a non-closed curve. For a closed curve, similar recursions can be used.

4.1.4 Confirmation Measurement

In this section, we show how the performance of the real-time CCD algorithm can be further improved by using a confirmation measurement. Based on the confirmation measurement, the real-time CCD algorithm decides whether a result of an iteration step should be used or not.

The real-time CCD algorithm takes only a relatively small number of pixels into account. The considered set of pixels depends on the current estimate $\mathbf{m}_{\mathbf{\Phi}}$ of the model parameters. In some cases, even a very small change of the estimate $\mathbf{m}_{\mathbf{\Phi}}$ may cause a change of the considered set of pixels. This, in turn, may cause a small change of the estimate $\mathbf{m}_{\mathbf{\Phi}}$. For this reason and due to the limited machine precision, two successive estimates of the model parameters are usually not identical, even after a high number of iterations. In order to pick the most promising estimate from a sequence of estimates, we employ a confirmation measurement. It evaluates to which extent two successive Gaussian distributions agree with each other. The confirmation measurement $\mathcal{C}^{(i)}$ of iteration step i is defined by:

$$\begin{aligned}\mathcal{C}^{(i)} &= \mathcal{C}\left(\mathbf{m}_{\mathbf{\Phi}}^{(i)}, \mathbf{\Sigma}_{\mathbf{\Phi}}^{(i)}, \mathbf{m}_{\mathbf{\Phi}}^{(i-1)}, \mathbf{\Sigma}_{\mathbf{\Phi}}^{(i-1)}\right) \\ &= \int_{I\!R^{D_{\mathbf{\Phi}}}} p\left(\mathbf{x} \mid \mathbf{m}_{\mathbf{\Phi}}^{(i)}, \mathbf{\Sigma}_{\mathbf{\Phi}}^{(i)}\right) \cdot p\left(\mathbf{x} \mid \mathbf{m}_{\mathbf{\Phi}}^{(i-1)}, \mathbf{\Sigma}_{\mathbf{\Phi}}^{(i-1)}\right)\, d\mathbf{x}\,, \end{aligned} \tag{4.17}$$

where $\mathbf{m}_{\mathbf{\Phi}}^{(i)}$ and $\mathbf{m}_{\mathbf{\Phi}}^{(i-1)}$ are the mean vectors, and $\mathbf{\Sigma}_{\mathbf{\Phi}}^{(i)}$ and $\mathbf{\Sigma}_{\mathbf{\Phi}}^{(i-1)}$ are the covariance matrices of the two successive Gaussian distributions. The measurement $\mathcal{C}^{(i)}$ evaluates the degree of overlap between the two distributions. For two distributions without overlap the measurement $\mathcal{C}^{(i)}$ is zero. The measurement $\mathcal{C}^{(i)}$ also evaluates the uncertainty, i.e. the covariance matrices, of the two distributions. Thus, $\mathcal{C}^{(i)}$ is high if and only if the overlap is high and the two covariance matrices indicate a small uncertainty of the estimates. Note that the integral in equation (4.17) can be written in closed form as a Gaussian probability density:

$$\mathcal{C}^{(i)} = p\left(\mathbf{m}_{\mathbf{\Phi}}^{(i)} \mid \mathbf{m}_{\mathbf{\Phi}}^{(i-1)}, \mathbf{\Sigma}_{\mathbf{\Phi}}^{(i)} + \mathbf{\Sigma}_{\mathbf{\Phi}}^{(i-1)}\right). \tag{4.18}$$

During the first few iterations, the value $\mathcal{C}^{(i)}$ usually increases strictly monotonically since the uncertainty decreases. Then, typically after about 10 iterations, further changes of $\mathcal{C}^{(i)}$ are usually small and less predictable. The RT-CCD algorithm chooses the estimate of the iteration step i that yields the highest confirmation measurement $\mathcal{C}^{(i)}$. Based on equation (4.18), the computation of $\mathcal{C}^{(i)}$ causes no substantial increase of the runtime.

4.2 Dynamical Models of Curves in Image Sequences

In the previous section, we proposed a fast method for fitting a curve to a *single* image. Here, we show how this method can be extended for tracking a curve in a *sequence* of images[4]. A simple tracker may be obtained by applying curve-fitting to each image independently. However, the performance of such a tracker can be improved substantially by exploiting statistical dependencies between successive curves.

In this section, we describe a probabilistic dynamical model which represents a priori knowledge about typical motions of curves in image sequences. Using a dynamical model the curve motion is extrapolated. That is, the distribution of model parameters is predicted based on the previous distributions. The predicted (or propagated) distribution is used as the a priori distribution in the next image. Hence, curve tracking is accomplished by alternately performing two steps:

1. Fit the curve to the image data (using the fast RT-CCD algorithm) and
2. Propagate the distribution of the curve parameters to the next image.

For the propagation (or prediction) we employ a second-order *auto-regressive process*. Auto-regressive (AR) processes are statistical models commonly used for describing motion patterns. We briefly review the foundations of AR processes and describe how they can be used for propagating the model parameters $\mathbf{\Phi}$ of the curve. The following review of AR processes is mainly adapted from Blake and Isard (1998).

Second-order AR processes are based on the second-order Markov assumption. That is, they assume that the distribution of the model parameter vector $\mathbf{\Phi}(t)$ at time t only depends on the two most recent model parameter vectors, $\mathbf{\Phi}(t-1)$ and $\mathbf{\Phi}(t-2)$. Statistical dependencies across more than two frames are ignored. Second-order AR processes model the parameter vectors $\mathbf{\Phi}(t)$ as Gaussian random variables and assume that the relation between three successive vectors $\mathbf{\Phi}(t)$, $\mathbf{\Phi}(t-1)$, and $\mathbf{\Phi}(t-2)$ is given by

$$\mathbf{\Phi}(t) - \overline{\mathbf{\Phi}} = \mathbf{A}_1 \left[\mathbf{\Phi}(t-1) - \overline{\mathbf{\Phi}}\right] + \mathbf{A}_2 \left[\mathbf{\Phi}(t-2) - \overline{\mathbf{\Phi}}\right] + \mathbf{B}_0 \mathbf{w}(t). \tag{4.19}$$

The vector $\overline{\mathbf{\Phi}}$ specifies the mean of the random motion. The $N_{\mathbf{\Phi}} \times N_{\mathbf{\Phi}}$ matrices $\mathbf{A}_1$ and $\mathbf{A}_2$ describe the influence of $\mathbf{\Phi}(t-1)$ and $\mathbf{\Phi}(t-2)$, respectively, on $\mathbf{\Phi}(t)$. By choosing appropriate values for $\mathbf{A}_1$, $\mathbf{A}_2$, and $\overline{\mathbf{\Phi}}$ different types of deterministic motions can be described, e.g. oscillation or translation. The random component of the motion is described by the $N_{\mathbf{\Phi}} \times N_{\mathbf{\Phi}}$

[4]The images could be recorded by a single camera or by multiple cameras from possibly different viewpoints.

matrix $\mathbf{B}_0$. The vector $\mathbf{w}(t)$ consists of $N_{\mathbf{\Phi}}$ independent random $\mathcal{N}(0,1)$ variables where $\mathbf{w}(t_1)$ and $\mathbf{w}(t_2)$ are also independent for $t_1 \neq t_2$. Procedures for learning such motion models, i.e. estimating the motion parameters $\overline{\mathbf{\Phi}}$, $\mathbf{A}_1$, $\mathbf{A}_2$, and $\mathbf{B}_0$ from training sets, have been published (Blake and Isard, 1998).

The second-order AR process can be expressed more compactly by defining a *state-vector* $\mathit{\Phi}$ which consists of the model parameters $\mathbf{\Phi}$ of two successive time-steps

$$\mathit{\Phi}(t) = \begin{pmatrix} \mathbf{\Phi}(t-1) \\ \mathbf{\Phi}(t) \end{pmatrix}. \tag{4.20}$$

Based on the state vector $\mathit{\Phi}$, the second-order AR process can be written in the form of a first-order AR process:

$$\mathit{\Phi}(t) - \overline{\mathit{\Phi}}(t) = \mathbf{A}\left[\mathit{\Phi}(t-1) - \overline{\mathit{\Phi}}\right] + \mathbf{B}\mathbf{w}(t) \tag{4.21}$$

where

$$\mathbf{A} = \begin{pmatrix} \mathbf{0} & \mathbf{1} \\ \mathbf{A}_2 & \mathbf{A}_1 \end{pmatrix}, \quad \overline{\mathit{\Phi}}(t) = \begin{pmatrix} \overline{\mathbf{\Phi}} \\ \overline{\mathbf{\Phi}} \end{pmatrix}, \quad \text{and} \quad \mathbf{B} = \begin{pmatrix} \mathbf{0} \\ \mathbf{B}_0 \end{pmatrix}. \tag{4.22}$$

The a priori estimate $\widetilde{\mathbf{m}}_{\mathit{\Phi}}(t)$, i.e. the prediction of the state for frame t, is obtained from the posterior estimate $\widehat{\mathbf{m}}_{\mathit{\Phi}}(t-1)$ of the previous frame $t-1$ by

$$\widetilde{\mathbf{m}}_{\mathit{\Phi}}(t) = \mathbf{A}\left[\widehat{\mathbf{m}}_{\mathit{\Phi}}(t-1) - \overline{\mathit{\Phi}}\right] + \overline{\mathit{\Phi}}. \tag{4.23}$$

The covariance matrix $\widetilde{\mathbf{\Sigma}}_{\mathit{\Phi}}(t)$ of the prediction is obtained from the covariance matrix $\widehat{\mathbf{\Sigma}}_{\mathit{\Phi}}(t-1)$ of the previous posterior estimate by

$$\widetilde{\mathbf{\Sigma}}_{\mathit{\Phi}}(t) = \mathbf{A}\widehat{\mathbf{\Sigma}}_{\mathit{\Phi}}(t-1)\mathbf{A}^T + \mathbf{B}\mathbf{B}^T. \tag{4.24}$$

From equation (4.20) follows that the mean parameter vector $\widetilde{\mathbf{m}}_{\mathbf{\Phi}}(t)$ is the second half of the mean state vector $\widetilde{\mathbf{m}}_{\mathit{\Phi}}(t)$. Analogously, the covariance matrix $\widetilde{\mathbf{\Sigma}}_{\mathbf{\Phi}}(t)$ is the lower right submatrix of $\widetilde{\mathbf{\Sigma}}_{\mathit{\Phi}}(t)$. The mean vector $\widetilde{\mathbf{m}}_{\mathbf{\Phi}}(t)$ and the covariance matrix $\widetilde{\mathbf{\Sigma}}_{\mathbf{\Phi}}(t)$ describe the propagated (predicted) distribution of the model parameters in frame t. These parameters specify the required a priori distribution for frame t.

4.3 Temporal Coherence of Pixel Values in Image Sequences

The CCD tracker described in the previous section does not exploit statistical dependencies between pixel values of successive frames. This means, the tracker implicitly assumes that the color of an object may change completely between two successive frames. However, objects or parts of an object usually have similar pixel values in successive frames. By exploiting the *temporal coherence of pixel values* , the performance of the tracker can be further improved.

Figure 4.2 depicts an example. Due to shade, the pixels (a) directly below the bottle's contour are darker than the pixels (b) used for computing the corresponding local statistics. This leads to wrong expectations for the pixels (a) and a wrong fit of the curve. A better expectation for the pixel values (a) can be obtained by propagating the local statistics of the pixels (c) from the previous frame $t-1$ to the current frame t. For such a *temporal propagation*, we assume that the pixels in the vicinity of the curve points $\mathbf{c}(\omega_k, \mathbf{\Phi}(t))$ in frame t are distributed similarly to the pixels in the vicinity of the curve points $\mathbf{c}(\omega_k, \mathbf{\Phi}(t-1))$ in the previous frame $t-1$. Note that in some cases this assumption does not hold.[5] However, this problem is alleviated by combining spatial and temporal propagation of local statistics. This means, we propagate local statistics of the pixel values over time and merge them with the local statistics of the current frame. The merged statistics yield a likelihood function that takes both the temporal and spatial coherence of the pixel values into account.

In the next section we describe how local statistics of pixel values are accumulated over time. The resulting local statistics represent the knowledge about the pixel values obtained from all previous images. In sections 4.3.2 and 4.3.3, we propose two methods for propagating the accumulated local statistics to the current frame. Finally, in section 4.3.4, we specify how the local statistics propagated over time are merged with the new statistics obtained from the current frame.

4.3.1 Accumulating Local Statistics of Pixel Values over Time

In section 4.1, we showed how local statistical moments $\mathbf{m}_{k,s,o}$ could be obtained efficiently from a single image. We summarize the history of all past moment $\mathbf{m}_{k,s,o}(t-1), \mathbf{m}_{k,s,o}(t-2), \ldots, \mathbf{m}_{k,s,o}(1)$ by computing accumulated or smoothed moments $\widehat{\mathbf{m}}_{k,s,o}(t-1)$. By applying an exponential filter, the smoothed moments $\widehat{\mathbf{m}}_{k,s,o}(t)$ of frame t can be efficiently obtained in a recursive manner:

$$
\begin{aligned}
t = 1 : \widehat{\mathbf{m}}_{k,s,o}(t) &= \mathbf{m}_{k,s,o}(1) && (4.25)\\
\forall t > 1 : \widehat{\mathbf{m}}_{k,s,o}(t) &= c_\tau \cdot \mathbf{m}_{k,s,o}(t) + (1 - c_\tau) \cdot \widehat{\mathbf{m}}_{k,s,o}(t-1). && (4.26)
\end{aligned}
$$

[5]For example, the pixels next to the curve point $\mathbf{c}(\omega_k, \mathbf{\Phi}(t-1))$ in frame $t-1$ may not exactly correspond to the pixels next to the curve point $\mathbf{c}(\omega_k, \mathbf{\Phi}(t))$ in the current frame. Furthermore the illumination may change.

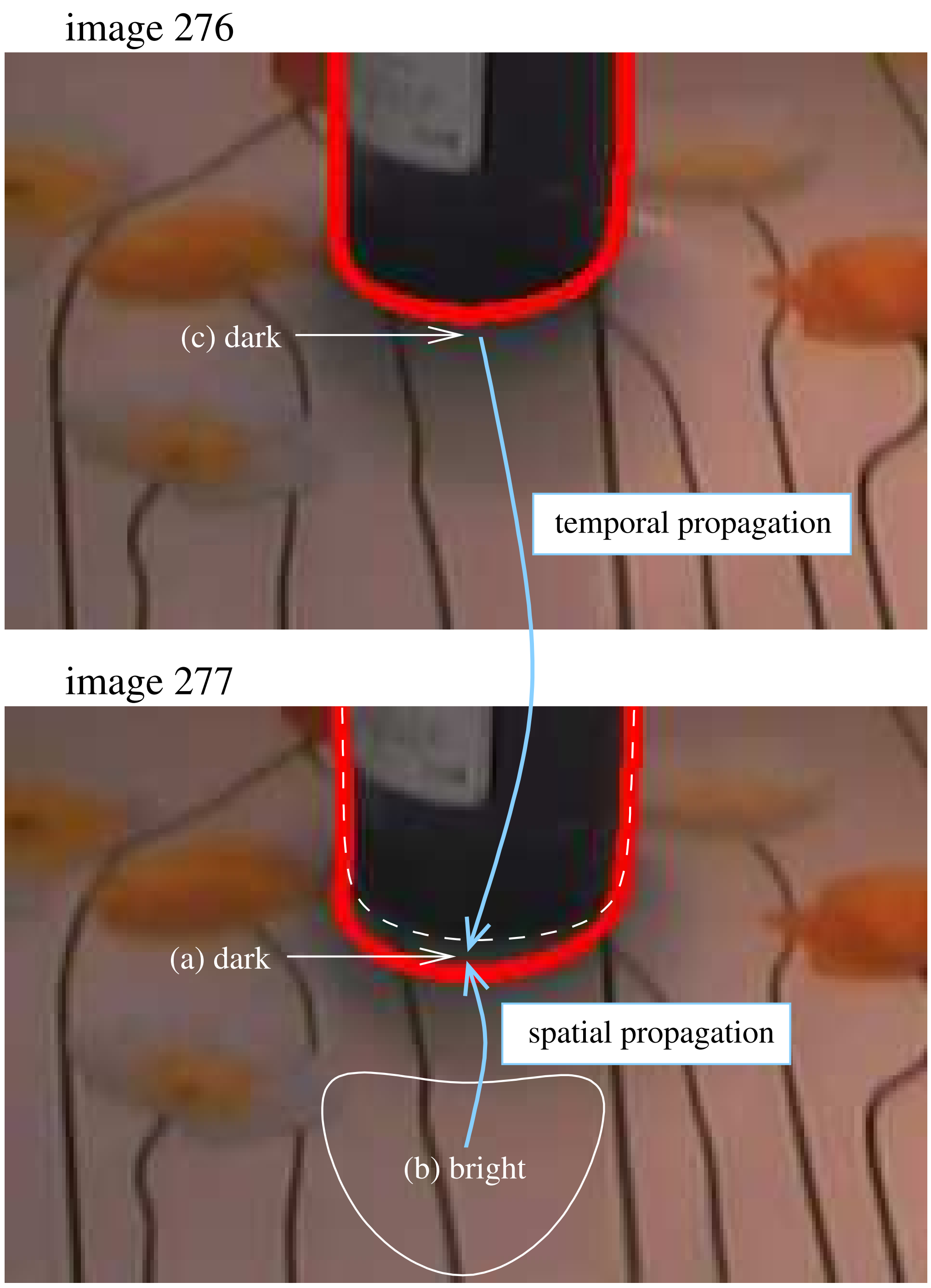

Figure 4.2: Due to the shade in image 277, the pixels (a) between the bottle's true contour (dashed line) and the estimated contour (thick solid line) are clearly darker than the pixels (b) used for computing the corresponding local statistics. Hence, the pixels (a) are assigned to the bottle region instead of the background region. Better local statistics for pixels (a) can be obtained from pixels (c) of the previous image. Therefore, we combine spatial and temporal propagation of local statistics.

The parameter $c_\tau \in]0,1[$ specifies the level of temporal smoothing (e.g. $c_\tau = \frac{1}{3}$). The moments $\mathbf{m}_{k,s,o}(t)$ at the right hand side of equations (4.25) and (4.26) are the moments obtained according to equations (4.6) to (4.8) in the iteration step yielding the highest confirmation measurement for frame t.

4.3.2 One-to-one Propagation of Local Statistics

The smoothed moments $\widehat{\mathbf{m}}_{k,s,o}(t-1)$ summarize the history of the past pixel values. In order to utilize these moments in the current frame t, they are propagated from frame $t-1$ to frame t. A straightforward propagation or prediction $\widetilde{\mathbf{m}}_{k,s,o}(t)$ is given by

$$\widetilde{\mathbf{m}}_{k,s,o}(t) = \widehat{\mathbf{m}}_{k,s,o}(t-1). \tag{4.27}$$

This prediction assumes that the local distributions of the pixel values do not substantially change from one frame to the next one. Instead of equation (4.27) other prediction methods could be applied. In particular, prediction methods taking a trend into account may be worth investigating. The advantage of equation (4.27) is that it does not require any parameters describing an expected dynamic behavior of the pixel values.

Equation (4.27) propagates the local statistical moments of each perpendicular k, independently. That is, statistical moments of perpendicular k are not propagated to perpendiculars $k' \neq k$. We call this *one-to-one propagation.* It is extremely efficient and easy to implement.

Drawback of the One-to-one Propagation

The one-to-one propagation has a drawback if the local statistics change along the curve. Figure 4.3a shows the perpendiculars for a curve that is aligned in frame $t-1$. For the perpendiculars $k < 6$, the algorithm learns that the region below the curve is black, and for the perpendiculars $k > 7$, it learns that the region below the curve is white. Figure 4.3b depicts the propagated perpendiculars and the propagated colors for frame t. Due to the uncertainty in the curve propagation process, the propagated curve points $\mathbf{c}(\omega_k, \mathbf{\Phi})$ are uncertain not only in the direction perpendicular to the curve but also along the curve. Hence, the propagated perpendiculars are usually also shifted along the curve. The short arrow in Figure 4.3b illustrates the shift of the curve point $\mathbf{c}(\omega_7, \mathbf{\Phi})$. Because of this shift, the one-to-one propagation yields wrong constraints on the pixel values for perpendiculars $k = 6$, $k = 7$, and $k = 8$. For example, the propagated color for the lower side of perpendicular $k = 7$ is white. However, at this position the correct color is black. The problem is that the pixels on perpendicular $k = 7$

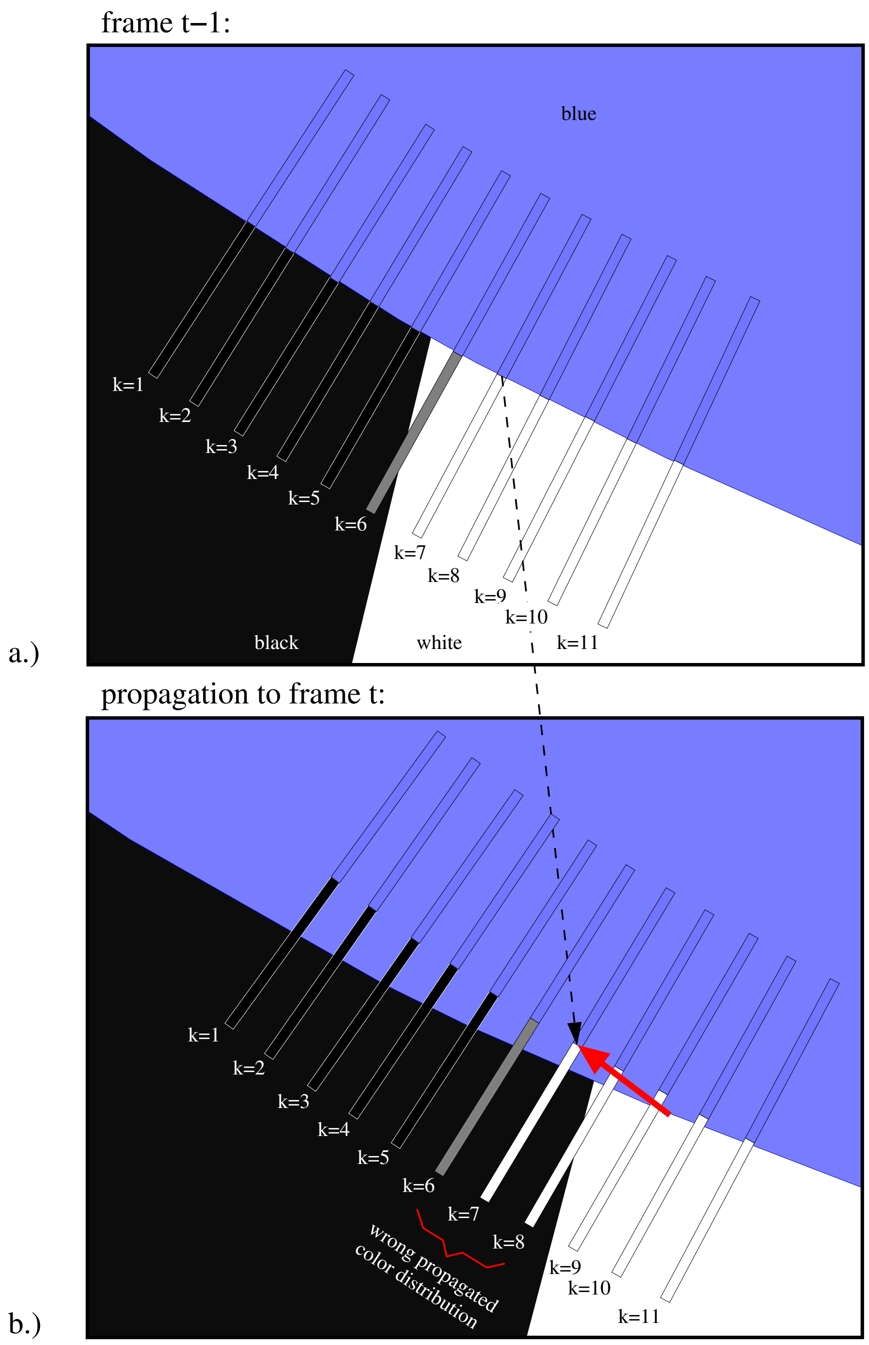

Figure 4.3: One-to-one propagation of color distributions over time: a.) For each perpendicular, color distributions are learned from the vicinity of the aligned curve in frame $t-1$. b.) Then the curve points and the associated color distributions are propagated to frame t. Due to the propagation error, the curve points are shifted along the curve (see short arrow). Hence, for perpendiculars $k = 6, 7, 8$ wrong color distributions are obtained. The lower half of perpendicular $k = 7$ is predicted to be white. However, in frame t it should be black.

in frame $t-1$ do not correspond to the pixels on perpendicular $k=7$ in frame t. In the next section, we propose another propagation method which takes the uncertainty of correspondence into account.

4.3.3 M-to-one Propagation of Local Statistics

The one-to-one propagation described above uses the statistical moments of a perpendicular k only for the same perpendicular k in the following frames. In this section, we propose an *M-to-one* approach. We propagate the statistical moments of multiple perpendiculars of frame $t-1$ to a perpendicular k in frame t and merge them according to the expected likelihood of correspondence.

Figure 4.4 illustrates the M-to-one propagation from frame $t-1$ to frame t. After propagating the curve from frame $t-1$ to frame t, the uncertainty of the propagated curve points is relatively high. The ellipse illustrates the uncertainty of the propagated curve point $\mathbf{c}(\omega_7, \mathbf{\Phi})$, the center point of perpendicular $k=7$. Due to the uncertainty, it is not clear which points in frame $t-1$ correspond to the points on perpendicular $k=7$ in frame t.[6]

Hence, we propagate the statistics of all perpendiculars in frame $t-1$ to each of the perpendiculars in frame t and merge them according to the expected likelihood of correspondence. The perpendiculars with significant influence on perpendicular $k=7$ are indicated in Figure 4.4a by thin lines. The lower halves of these perpendiculars contain either black or white pixels. Therefore, in frame t for perpendicular $k=7$ both black and white pixels are expected in the region below the curve. For perpendiculars that are relatively far away from the border between the black and white area, the expected color distributions are almost unchanged.

In contrast to Figure 4.3b, in Figure 4.4b all predicted color distributions are consistent with the actual colors in the image. However, due to the merging of multiple perpendiculars, the predicted distributions are less specific, i.e. the magnitude of the covariance is higher than for the one-to-one propagation. During the iteration process, the uncertainty of the curve is reduced step-by-step. Hence, the number of perpendiculars essentially propagated to one perpendicular decreases and the M-to-one propagation approaches the one-to-one propagation.

Locally Adapted Blurring of Propagated Statistics

The M-to-one propagation is realized efficiently by first performing the one-to-one propagation as described above, and then smoothing the resulting statistical moments $\widetilde{\mathbf{m}}_{k,s,o}$ along the

[6]In extreme cases not a single point in frame $t-1$ corresponds to any point in frame t, for example, if an object suddenly occludes the entire scene or the camera is rotating very fast.

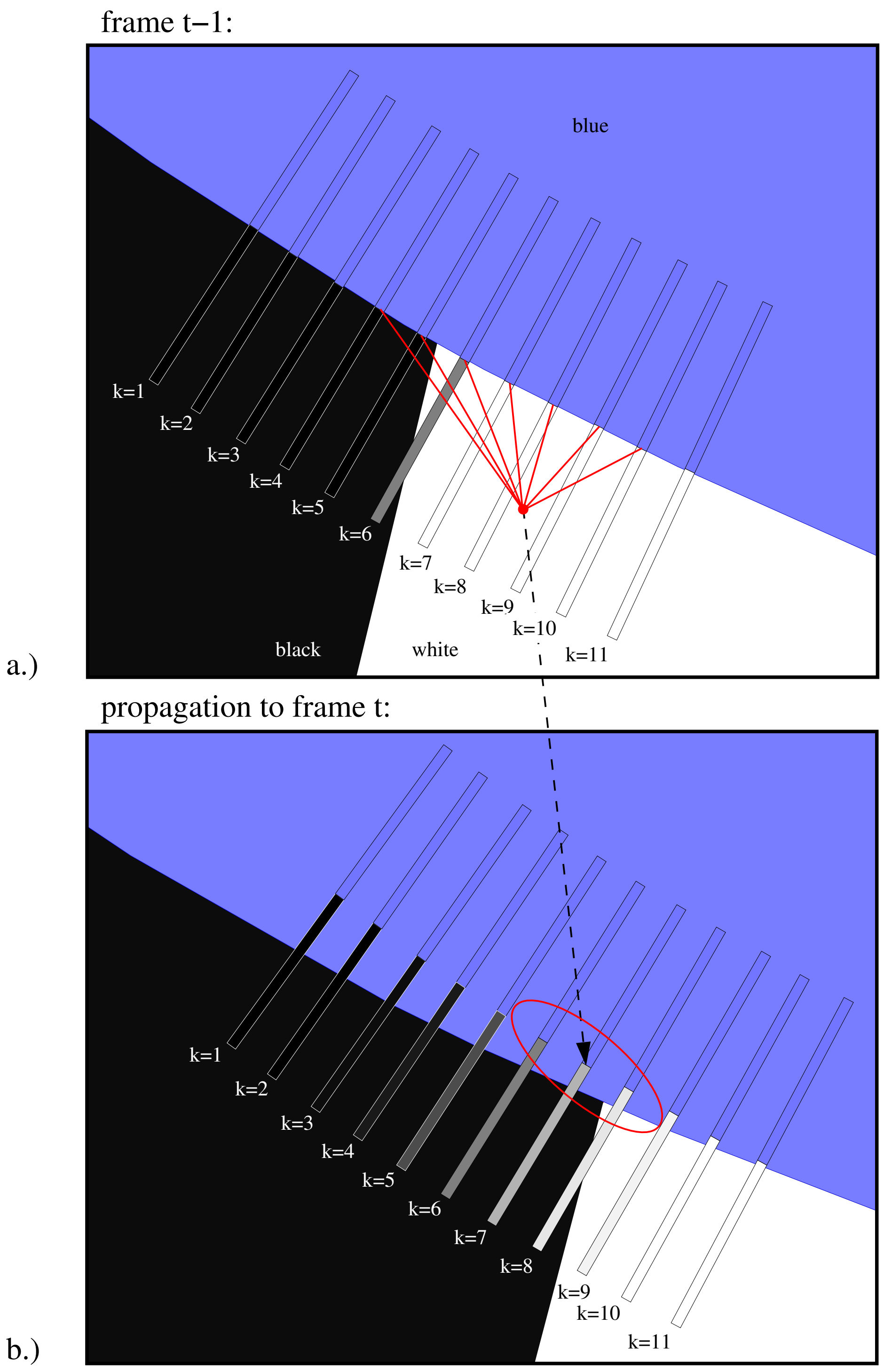

Figure 4.4: M-to-one propagation: Local statistical moments of multiple perpendiculars of frame $t-1$ are propagated to one perpendicular in frame t and merged according to the estimated likelihood of correspondence. In contrast to the one-to-one propagation, for the lower side of perpendicular $k = 7$ both black and white pixels are accepted.

curve. The first step accomplishes temporal smoothing and the second step accomplishes spatial smoothing. The two steps are depicted in Figure 4.5.

For the smoothing or blurring along the curve, locally adapted window sizes are applied which depend on the local uncertainty of the curve. We now show how the locally adapted blurring of the temporarily propagated statistical moments $\widetilde{\mathbf{m}}_{k,s,o}$ can be performed efficiently, again by employing a recursive implementation of a filter. However, this time the amount of blurring along the curve is not constant. Instead it depends on the local uncertainties of the curve points, i.e. the uncertainty in the direction along the curve. This can be taken into account as follows.

The local uncertainty, i.e. the standard deviation, $\sigma_k^{=}$ of the curve point $\mathbf{c}(\omega_k, \mathbf{\Phi})$ in the direction along the curve can be obtained analogously to equation (3.9). It is given by

$$\sigma_k^{=} \;=\; \sqrt{\mathbf{t}_k^T \cdot \mathbf{J}_k \cdot \mathbf{\Sigma_\Phi} \cdot \mathbf{J}_k^T \cdot \mathbf{t}_k}, \tag{4.28}$$

where $\mathbf{t}_k$ is the tangent vector of unit length and $\mathbf{J}_k$ denotes the Jacobian of the curve in the point $\mathbf{c}(\omega_k, \mathbf{m_\Phi})$. The average uncertainty along the curve in the interval between two points $\mathbf{c}(\omega_{k-1}, \mathbf{m_\Phi})$ and $\mathbf{c}(\omega_k, \mathbf{m_\Phi})$ can be estimated by

$$\sigma_{k-1,k}^{=} = \frac{\sigma_{k-1}^{=} + \sigma_k^{=}}{2}. \tag{4.29}$$

The uncertainty $\sigma_{k-1,k}^{=}$ could be used as the window size for smoothing the propagated statistical moments $\widetilde{\mathbf{m}}_{k,s,o}$ between perpendicular $k-1$ and perpendicular k. However, this would result in no smoothing if the uncertainty of the curve was zero. In this case, the statistical dependency between the pixel values of neighboring perpendiculars would not be exploited. Therefore, we apply a minimum window size even if the uncertainty of the curve is zero. We compute the window size $\sigma_{k-1,k}^{=}$ by

$$\sigma_{k-1,k}^{=} = \sqrt{\left(\frac{\sigma_{k-1}^{=} + \sigma_k^{=}}{2}\right)^2 + \left(\sigma_{min}^{=}\right)^2}. \tag{4.30}$$

The choice of the minimum window size $\sigma_{min}^{=}$ will be described below.

For reasons of efficiency, we smooth the statistical moments $\widetilde{\mathbf{m}}_{k,s,o}$ using an exponential filter in a manner similar to equations (4.13)-(4.16) in section 3.2.2.3. However, here we do not use a constant window size but the local window sizes $\sigma_{k-1,k}^{=}$. The local blurring parameter $\lambda_{k-1,k}$ that yields an exponential filter of window size (i.e. standard deviation) $\sigma_{k-1,k}^{=}$ holds

$$\lambda_{k-1,k} = \frac{\sqrt{2}}{\sigma_{k-1,k}^{=}}. \tag{4.31}$$

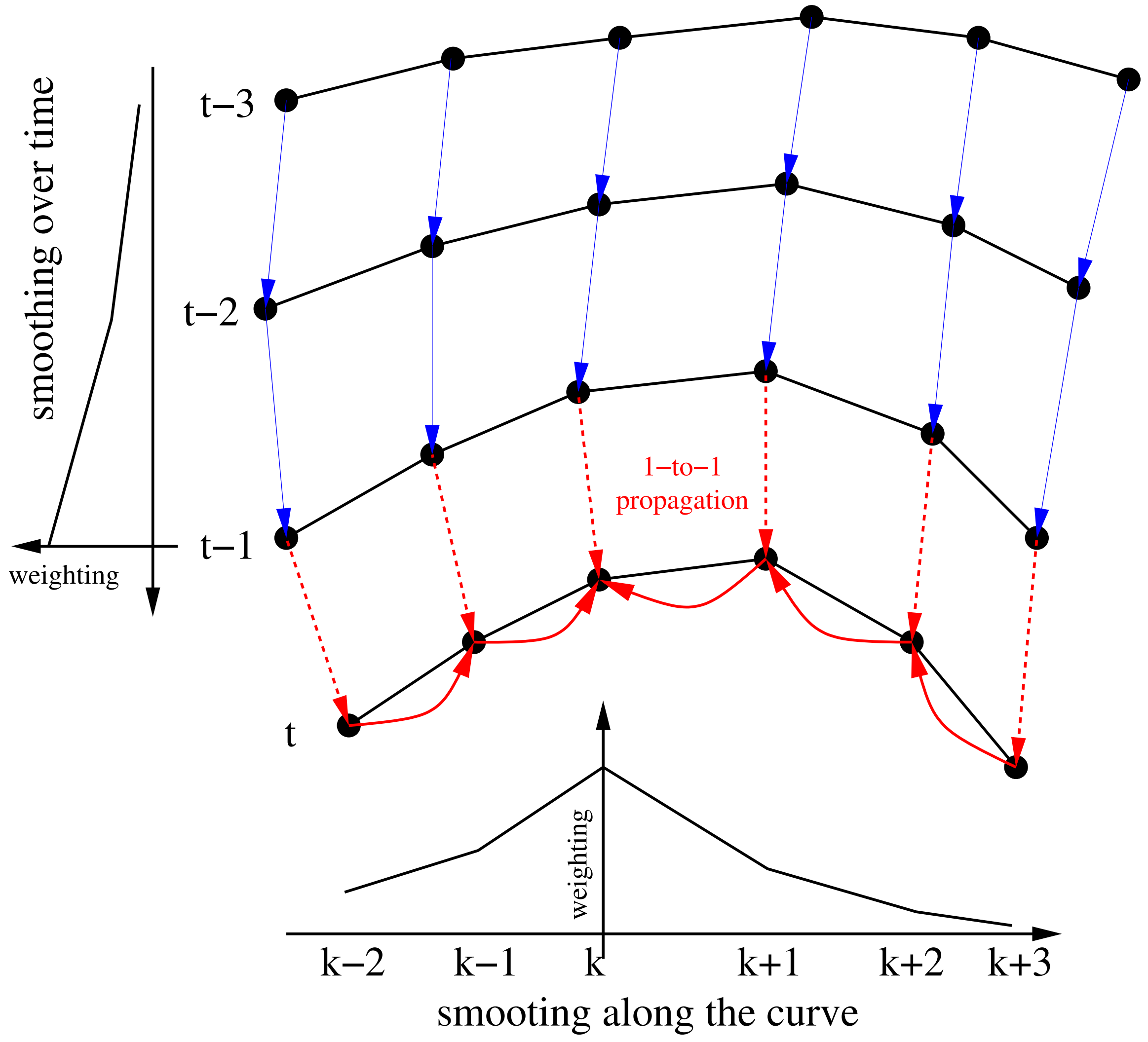

Figure 4.5: Steps of the M-to-one propagation: First, the temporarily smoothed moments are propagated from frame $t-1$ to the current frame t using the one-to-one propagation. Second, the propagated moments are smoothed along the curve based on the local uncertainty of the predicted curve. This way, the local statistics of perpendicular k at frame t get contributions from all perpendiculars of all previous frames. However, the influence decreases with increasing temporal and spatial distance.

Using this relation, we choose the minimum window size $\sigma^{=}_{min} = \frac{\sqrt{2}}{\lambda}$. The parameter λ was introduced in equation (3.20). It specifies the window size used for blurring the moments of the current frame along the curve. By choosing $\sigma^{=}_{min} = \frac{\sqrt{2}}{\lambda}$, the temporarily propagated moments are blurred at least as much as the moments of the current frame are blurred.

The moments $\widetilde{\mathbf{M}}_{k,s,o}$ obtained by smoothing the propagated moments $\widetilde{\mathbf{m}}_{k,s,o}$ along the curve can be written as a sum of two terms:

$$\widetilde{\mathbf{M}}_{k,s,o} \;=\; \overset{\rightrightarrows}{\mathbf{M}}_{k,s,o} + \overset{\leftleftarrows}{\mathbf{M}}_{k,s,o}. \tag{4.32}$$

The first term $\overset{\rightrightarrows}{\mathbf{M}}_{k,s,o}$ accumulates the moments $\widetilde{\mathbf{m}}_{k,s,o}$ in the direction of increasing indices k and the second term $\overset{\leftleftarrows}{\mathbf{M}}_{k,s,o}$ accumulates the moments $\widetilde{\mathbf{m}}_{k,s,o}$ in the opposite direction. Both terms can be efficiently computed in a recursive manner. For a non-closed curve, the first term holds

$$\begin{aligned}
k=1 : \overset{\rightrightarrows}{\mathbf{M}}_{k,s,o} \;&=\; \Lambda_k^{-1} \cdot \widetilde{\mathbf{m}}_{k,s,o} && (4.33)\\
\forall k \in \{2,\ldots,K\} : \overset{\rightrightarrows}{\mathbf{M}}_{k,s,o} \;&=\; \exp\left(-\lambda_{k-1,k} \cdot ||\mathbf{C}_k - \mathbf{C}_{k-1}||\right) \cdot \overset{\rightrightarrows}{\mathbf{M}}_{k-1,s,o} + \\
&\quad +\Lambda_k^{-1} \cdot \widetilde{\mathbf{m}}_{k,s,o} && (4.34)
\end{aligned}$$

and the second term is given by

$$\begin{aligned}
k=K : \overset{\leftleftarrows}{\mathbf{M}}_{k,s,o} \;&=\; \mathbf{0} && (4.35)\\
\forall k \in \{1,\ldots,K-1\} : \overset{\leftleftarrows}{\mathbf{M}}_{k,s,o} \;&=\; \exp\left[-\lambda_{k,k+1} \cdot ||\mathbf{C}_k - \mathbf{C}_{k+1}||\right] \cdot \\
&\quad \cdot \left[\overset{\leftleftarrows}{\mathbf{M}}_{k+1,s,o} + \Lambda_{k+1}^{-1} \cdot \widetilde{\mathbf{m}}_{k+1,s,o}\right] . && (4.36)
\end{aligned}$$

For a closed curve, minor modifications are necessary. In contrast to equations (4.13) to (4.16), local normalization variables Λ_k are necessary here. These variables depend on the local blurring parameters $\lambda_{k-1,k}$. They ensure that perpendiculars in an area with a high uncertainty of the curve do not have a higher overall influence than perpendiculars in an area with a low uncertainty. The normalization variables Λ_k are obtained by applying the above filtering scheme to a K-dimensional vector of ones. The normalization variables Λ_k are given by

$$\Lambda_k \;=\; \overrightarrow{\Lambda}_k + \overleftarrow{\Lambda}_k, \tag{4.37}$$

where $\overrightarrow{\Lambda}_k$ holds

$$\begin{aligned}
k=1 : \overrightarrow{\Lambda}_k \;&=\; 1 && (4.38)\\
\forall k \in \{2,\ldots,K\} : \overrightarrow{\Lambda}_k \;&=\; \exp\left[-\lambda_{k-1,k} \cdot ||\mathbf{C}_k - \mathbf{C}_{k-1}||\right] \cdot \overrightarrow{\Lambda}_{k-1} + 1 && (4.39)
\end{aligned}$$

and $\overleftarrow{\Lambda}_k$ equals

$$\begin{aligned}
k=K : \overleftarrow{\Lambda}_k \;&=\; 0 && (4.40)\\
\forall k \in 1,\ldots,K-1 : \overleftarrow{\Lambda}_k \;&=\; \exp\left[-\lambda_{k,k+1} \cdot ||\mathbf{C}_k - \mathbf{C}_{k+1}||\right] \cdot \left[\overleftarrow{\Lambda}_{k+1} + 1\right] . && (4.41)
\end{aligned}$$

4.3.4 Merging Propagated and New Local Statistics

We merge the local statistical moments $\widetilde{\mathbf{M}}_{k,s,o}$, propagated over time, with the new statistical moments $\mathbf{M}_{k,s,o}$ obtained from the current frame. The merged moments $\widehat{\mathbf{M}}_{k,s,o}$ are given by

$$\widehat{\mathbf{M}}_{k,s,o} = \frac{\mathbf{M}_{k,s,o}}{\mathbf{M}_{k,s,0}} + \beta_{k,s} \cdot \frac{\widetilde{\mathbf{M}}_{k,s,o}}{\widetilde{\mathbf{M}}_{k,s,0}}, \tag{4.42}$$

where $\frac{\mathbf{M}_{k,s,o}}{\mathbf{M}_{k,s,0}}$ and $\frac{\widetilde{\mathbf{M}}_{k,s,o}}{\widetilde{\mathbf{M}}_{k,s,0}}$ are the statistical moments normalized by the corresponding moments of order zero. The parameter $\beta_{k,s}$ specifies the weighting of the moments propagated over time. We use $\beta_{k,s} = 1$ for the side s of the curve belonging to the object to be tracked. Since in the background region the pixel values next to the curve usually change more heavily, we use $\beta_{k,s} = 1/3$ for the background side. Obviously, for the first frame, no prediction of the pixel values exists. Hence, for the first frame we substitute equation (4.42) by $\widehat{\mathbf{M}}_{k,s,o} = \frac{\mathbf{M}_{k,s,o}}{\mathbf{M}_{k,s,0}}$. Based on the merged moments $\widehat{\mathbf{M}}_{k,s,o}$, the local mean vectors and covariance matrices describing the local expectation of the pixel values can be obtained according to equations (3.21) and (3.22).

4.4 Summary of the Algorithm

In this section, we summarize the CCD tracker and discuss its runtime and space complexity.

The Algorithm

Figure 4.6 summarizes the CCD tracker using the M-to-one propagation described above. The input consists of the image sequence $\mathbf{I}^*(t)$, the curve function $\mathbf{c}$, the mean vector $\mathbf{m}^*_{\mathit{\Phi}}$, and the covariance matrix $\mathbf{\Sigma}^*_{\mathit{\Phi}}$. The latter two define the a priori distribution of the initial *state* vector $\mathit{\Phi}$. (We use a second-order state vector $\mathit{\Phi}$, which consists of two successive model parameter vectors $\mathbf{\Phi}$, see equation (4.20)). The CCD tracker estimates the state vector for each image. The output consists of the sequence of estimated state vectors $\widehat{\mathbf{m}}_{\mathit{\Phi}}(t)$ and the corresponding sequence of covariance matrices $\widehat{\mathbf{\Sigma}}_{\mathit{\Phi}}(t)$.

The initialization for the first image is obtained from the a priori mean vector $\mathbf{m}^*_{\mathit{\Phi}}$ and covariance matrix $\mathbf{\Sigma}^*_{\mathit{\Phi}}$ (lines 010-020). The iteration, which is performed for each image, is initialized based on the predicted *state* $\mathit{\Phi}$ (lines 060-130). In lines 060-070, those components of the predicted mean $\widetilde{\mathbf{m}}_{\mathit{\Phi}}(t)$ and covariance $\widetilde{\mathbf{\Sigma}}_{\mathit{\Phi}}(t)$ that correspond to the current image, are used for initializing the mean $\widetilde{\mathbf{m}}_{\mathbf{\Phi}}(t)$ and covariance $\widetilde{\mathbf{\Sigma}}_{\mathbf{\Phi}}(t)$ of the model parameters $\mathbf{\Phi}$.

In the loop (lines 140-350), the estimate of the model parameter vector is iteratively refined. To this end, first the pixels on the perpendiculars are determined and local statistical moments are computed from the image data (lines 160-170). Then the resulting statistical moments are blurred along the curve (line 180). These moments are merged with the temporarily propagated and blurred moments (lines 200-210). Line 220 computes the local statistics, i.e. the mean vectors and covariance matrices, of the pixel values from the merged statistical moments. For the first image $(t = 1)$ no temporarily propagated statistical moments exist. Hence, only the moments of the current image are used (line 230).

Line 240 computes the Hessian and the Jacobian of the MAP objective function, which is derived from the local statistics. Using a modified Newton iteration step, the mean vector is updated (line 250). Then, in line 260, the covariance matrix is updated based on the Hessian. At the end of the loop, the current solution is stored as the estimate of the model parameters if it achieves the highest confirmation measurement (lines 270-340).

After the iteration, the estimate of the state vector $\mathit{\Phi}$ is updated based on the estimate of the model parameter vector $\mathbf{\Phi}$ (line 360). Then the local statistical moments are accumulated (lines 370-400) and predicted over time (lines 420). Finally, in line 430, the state vector of the next image is predicted using a motion model. Then the CCD algorithm continues with the next image.

Complexity Analysis

Let us now discuss the runtime and the space complexity of the CCD tracker.

Runtime Complexity

The most expensive part in the initialization (see lines 010-130 in Figure 4.6) is the computation of the confirmation measurement $\mathcal{C}$ (line 120). This computation requires inverting a matrix of the size of the covariance matrix, i.e. a matrix of size $D_{\mathbf{\Phi}} \times D_{\mathbf{\Phi}}$, where $D_{\mathbf{\Phi}}$ is the dimension of the parameter vector $\mathbf{\Phi}$. In the general case, this takes

$$O\left(D_{\mathbf{\Phi}}^3\right)$$

time. (If the matrix is sparse, the inversion can be achieved more efficiently.)

The next steps are iterated in the loop. First, in line 160, the set of considered pixels is determined. This requires per perpendicular $D_{\mathbf{\Phi}} + 2$ evaluations of the curve function $\mathbf{c}$ or its partial derivatives. We denote the complexity of such an evaluation by O_c. Thus, the complexity of line 160 is of

$$O\left(K \cdot D_{\mathbf{\Phi}}\right) \cdot O_c,$$

Contracting Curve Density (CCD) tracker

Input: image sequence $\mathbf{I}^*(t)$
curve function $\mathbf{c}$
mean vector $\mathbf{m}^*_{\Phi}$ and covariance matrix $\mathbf{\Sigma}^*_{\Phi}$ defining a Gaussian
a priori distribution of the *state* vector Φ in the first image

Output: sequence of estimated *state* vectors $\widehat{\mathbf{m}}_{\Phi}(t)$
and corresponding covariance matrices $\widehat{\mathbf{\Sigma}}_{\Phi}(t)$

```
    // initialization for first image
010 $\widetilde{\mathbf{m}}_{\Phi}(1) = \mathbf{m}^*_{\Phi}$
020 $\widetilde{\mathbf{\Sigma}}_{\Phi}(1) = \mathbf{\Sigma}^*_{\Phi}$
030 $t = 1$
040 while ($t \leq$ #Images)
050   {
      // initialization for iteration
060   set mean vector $\widetilde{\mathbf{m}}_{\boldsymbol{\Phi}}(t)$ of parameters using subvector of the state's mean vector $\widetilde{\mathbf{m}}_{\Phi}(t)$
070   set covar. matrix $\widetilde{\mathbf{\Sigma}}_{\boldsymbol{\Phi}}(t)$ of parameters using submatrix of the state's covar. matrix $\widetilde{\mathbf{\Sigma}}_{\Phi}(t)$
080   $\mathbf{m}^{(0)}_{\boldsymbol{\Phi}}(t) = \widetilde{\mathbf{m}}_{\boldsymbol{\Phi}}(t)$
090   $\mathbf{\Sigma}^{(0)}_{\boldsymbol{\Phi}}(t) = c_1 \cdot \widetilde{\mathbf{\Sigma}}_{\boldsymbol{\Phi}}(t)$
100   $\widehat{\mathbf{m}}_{\boldsymbol{\Phi}}(t) = \widetilde{\mathbf{m}}_{\boldsymbol{\Phi}}(t)$
110   $\widehat{\mathbf{\Sigma}}_{\boldsymbol{\Phi}}(t) = \widetilde{\mathbf{\Sigma}}_{\boldsymbol{\Phi}}(t)$
120   $C_{best} = \mathcal{C}\left(\widetilde{\mathbf{m}}_{\boldsymbol{\Phi}}(t), \widetilde{\mathbf{\Sigma}}_{\boldsymbol{\Phi}}(t), \widetilde{\mathbf{m}}_{\boldsymbol{\Phi}}(t), \widetilde{\mathbf{\Sigma}}_{\boldsymbol{\Phi}}(t)\right)$
130   $i_{best} = 1$
      // perform iteration
140   for($i = 1, i \leq$ #Iterations, $i = i + 1$)
150     {
        // learn local statistics
160     determine pixels on perpendiculars of the curve c using $\mathbf{m}^{(i-1)}_{\boldsymbol{\Phi}}(t)$ and $\mathbf{\Sigma}^{(i-1)}_{\boldsymbol{\Phi}}(t)$
170     compute local stat. moments $\mathbf{m}^{(i)}_{k,s,o}(t)$ for each perpendicular using image $\mathbf{I}^*(t)$
180     blur stat. moments $\mathbf{m}^{(i)}_{k,s,o}(t)$ along the curve yielding $\mathbf{M}^{(i)}_{k,s,o}(t)$
190     if($t > 1$) {
200         blur propagated stat. moments $\widetilde{\mathbf{m}}_{k,s,o}(t)$ along the curve yielding $\widetilde{\mathbf{M}}^{(i)}_{k,s,o}(t)$
210         merge stat. moments $\mathbf{M}^{(i)}_{k,s,o}(t)$ and $\widetilde{\mathbf{M}}^{(i)}_{k,s,o}(t)$ yielding $\widehat{\mathbf{M}}^{(i)}_{k,s,o}(t)$
220         compute statistics $\mathbf{S}^{(i)}_{k,s}(t)$ (mean and covar.) from stat. moments $\widehat{\mathbf{M}}^{(i)}_{k,s,o}(t)$ }
230     else { compute statistics $\mathbf{S}^{(i)}_{k,s}(t)$ (mean and covar.) from stat. moments $\mathbf{M}^{(i)}_{k,s,o}(t)$ }
```

continued on next page

Figure 4.6: The CCD tracker

continued from previous page

```
            // update the mean vector by performing one modified Newton iteration step
            // optimizing the MAP criterion $\chi^2$
240         compute modified Hessian $\mathbf{H}^{(i-1)}(t)$ and Jacobian $\mathbf{J}^{(i-1)}(t)$ of
                  $\chi^2(\mathbf{m}_{\mathbf{\Phi}}) = -2\ln p\left(\mathbf{I}_{\mathcal{V}} = \mathbf{I}^*_{\mathcal{V}} \mid \mathbf{a}_{\mathcal{V}}\left(\mathbf{m}_{\mathbf{\Phi}}, \mathbf{\Sigma}^{(i-1)}_{\mathbf{\Phi}}(t)\right), \mathbf{S}^{(i)}_{k,s}(t)\right)$
                        $-2\ln p(\mathbf{m}_{\mathbf{\Phi}} \mid \widetilde{\mathbf{m}}_{\mathbf{\Phi}}(t), \widetilde{\mathbf{\Sigma}}_{\mathbf{\Phi}}(t))$
            in the point $\mathbf{m}_{\mathbf{\Phi}} = \mathbf{m}^{(i-1)}_{\mathbf{\Phi}}(t)$
250         update mean vector
                  $\mathbf{m}^{(i)}_{\mathbf{\Phi}}(t) = \mathbf{m}^{(i-1)}_{\mathbf{\Phi}}(t) - \left(\mathbf{H}^{(i-1)}(t)\right)^{-1} \mathbf{J}^{(i-1)}(t)$
260         update covariance matrix
                  $\mathbf{\Sigma}^{(i)}_{\mathbf{\Phi}}(t) = c_2 \mathbf{\Sigma}^{(i-1)}_{\mathbf{\Phi}}(t) + (1 - c_2)\frac{2}{\mathbf{H}^{(i-1)}(t)}$

            // store solution if confirmation measurement $\mathcal{C}$ increases
270         $C_{new} = \mathcal{C}\left(\mathbf{m}^{(i)}_{\mathbf{\Phi}}(t), \mathbf{\Sigma}^{(i)}_{\mathbf{\Phi}}(t), \mathbf{m}^{(i-1)}_{\mathbf{\Phi}}(t), \mathbf{\Sigma}^{(i-1)}_{\mathbf{\Phi}}(t)\right)$
280         if($C_{new} \geq C_{best}$)
290           {
300             $i_{best} = i$
310             $C_{best} = C_{new}$
320             $\widehat{\mathbf{m}}_{\mathbf{\Phi}}(t) = \mathbf{m}^{(i)}_{\mathbf{\Phi}}(t)$
330             $\widehat{\mathbf{\Sigma}}_{\mathbf{\Phi}}(t) = \frac{2}{\mathbf{H}^{(i-1)}(t)}$
340           }
350       }
360       set mean vector $\widehat{\mathbf{m}}_{\Phi}(t)$ and covariance matrix $\widehat{\mathbf{\Sigma}}_{\Phi}(t)$ of the state
          using mean vector $\widehat{\mathbf{m}}_{\mathbf{\Phi}}(t)$ and covariance matrix $\widehat{\mathbf{\Sigma}}_{\mathbf{\Phi}}(t)$ of the model parameters

          //accumulate statistical moments
370       if($t = 1$)
380         { $\widehat{\mathbf{m}}_{k,s,o}(t) = \mathbf{m}^{(i_{best})}_{k,s,o}(t)$ }
390       else
400         { $\widehat{\mathbf{m}}_{k,s,o}(t) = c_\tau \cdot \mathbf{m}^{(i_{best})}_{k,s,o}(t) + (1 - c_\tau) \cdot \widehat{\mathbf{m}}_{k,s,o}(t-1)$}
410       t=t+1
          // prediction for next image
420       propagate (predict) statistical moments
          $\widetilde{\mathbf{m}}_{k,s,o}(t) = \widehat{\mathbf{m}}_{k,s,o}(t-1)$
430       predict state using
          $\widehat{\mathbf{m}}_{\Phi}(t-1)$, $\widehat{\mathbf{\Sigma}}_{\Phi}(t-1)$, and a motion model (e.g. an AR process)
          yielding mean vector $\widetilde{\mathbf{m}}_{\Phi}(t)$ and covariance matrix $\widetilde{\mathbf{\Sigma}}_{\Phi}(t)$
440   }
```

where K is the number of perpendiculars. For lines 170-230, the dominating part is the computation of the statistical moments of order two. This computation runs in

$$O\left(K \cdot L \cdot D_{\mathbf{I}^*}^2\right),$$

where $D_{\mathbf{I}^*}$ is the dimension of the pixel values. Usually, the dimension $D_{\mathbf{I}^*}$ is fairly small, e.g. for RGB values $D_{\mathbf{I}^*} = 3$. The quantity L denotes the maximum number of pixels used per perpendicular. The computation of the Hessian and the Jacobian (line 240) runs in

$$O\left(K \cdot L \cdot D_{\mathbf{I}^*}^3 + K \cdot D_{\mathbf{\Phi}}^2\right).$$

Inverting the Hessian (line 250) takes

$$O\left(D_{\mathbf{\Phi}}^3\right)$$

time. For less general but practically highly relevant curve functions $\mathbf{c}$, the complexity can be further reduced. For example, in the case of snakes (Kass, Witkin, and Terzopoulos, 1988), a point on the curve depends only on a small subset of the model parameters. This yields sparse matrices allowing for an additional speed-up.

The remaining parts of the algorithm (lines 260-440) do not further increase the runtime complexity. Hence, a complete iteration step runs in

$$O\left(K \cdot D_{\mathbf{\Phi}} \cdot O_c + K \cdot L \cdot D_{\mathbf{I}^*}^3 + K \cdot D_{\mathbf{\Phi}}^2 + D_{\mathbf{\Phi}}^3\right)$$

time. The runtime for processing an image is

$$O\left(\#\text{Iterations} \cdot \left(K \cdot D_{\mathbf{\Phi}} \cdot O_c + K \cdot L \cdot D_{\mathbf{I}^*}^3 + K \cdot D_{\mathbf{\Phi}}^2 + D_{\mathbf{\Phi}}^3\right)\right),$$

where #Iterations is the number of iterations. Note that the runtime complexity does not depend on the image resolution. This allows for processing high resolution images in a limited time. Furthermore, the CCD tracker does not require any expensive computation before the iteration. For example, no feature detection or filtering of the image data is performed. Hence, the CCD tracker achieves the first updates of the model parameters without substantial latency. This is essential for many time-constrained applications, e.g. in the field of robotics.

Space Complexity

The space complexity of the CCD tracker is

$$O\left(K \cdot D_{\mathbf{I}^*}^2 + D_{\mathbf{\Phi}}^2 + |\mathbf{I}^*|\right),$$

where $O\left(K \cdot D_{\mathbf{I}^*}^2\right)$ is the space required for the statistical moments, $O\left(D_{\mathbf{\Phi}}^2\right)$ is the space for the Hessian, and $O\left(|\mathbf{I}^*|\right)$ is the size of an image. In practice, the storage requirement of the CCD tracker is relatively small and mainly depends on the image size $|\mathbf{I}^*|$.

4.5 Related Methods for Object Tracking

In this section we briefly compare the CCD tracker with related tracking methods. The CCD tracker differs most notably from other contour-based trackers by employing a novel *likelihood function* and a novel optimization method based on a *blurred curve model*. In previous chapters we discussed, in detail, the advantages of both. Here, we focus on aspects that are of particular relevance for image *sequences*.

Several methods achieve a substantial speed-up by considering only pixels on some perpendiculars (Blake and Isard, 1998; Cootes and Taylor, 2001; Pece, 2003). The CCD tracker differs from these methods by iteratively 'focusing' on the boundary. This means the CCD tracker uses a small set of equally spaced pixels on the perpendiculars and iteratively adapting the spacing to the remaining uncertainty of the curve. Thus, the accurate boundary can be found without using all pixels on the perpendicular.

The CCD tracker is related to the iterative Kalman tracker and similar iterative methods, e.g. (Bar-Shalom and Fortmann, 1988; Lowe, 1992). These methods also propagate a Gaussian distribution of the model parameters over time and then use an iterative procedure for updating the Gaussian distribution based on the observations.

Several methods use a priori knowledge about pixel values, e.g. appearance models (Cootes, Edwards, and Taylor, 1998) or others (Hanek et al., 2000). These methods learn the knowledge in an off-line stage before tracking. The CCD tracker does not need a priori knowledge about pixel values. It incrementally acquires the knowledge while tracking.

Optical flow methods exploit dependencies between pixel values of successive images, e.g. (Black, 1992; Horn and Schunck, 1981). These methods usually employ the *intensity* or *brightness constancy assumption*: They assume that a point on a surface has similar pixel values in successive images. Furthermore, many optical flow methods assume that the intensity/pixel values are spatially smooth, i.e. the spatial derivatives exist. We generalize these two assumptions as follows. We model a pixel value as a random variable. We assume that not the pixel values but their local probability distributions are spatially and temporally smooth. This has significant advantages in cases where the intensity constancy assumption is violated, for example, due to reflections or changes of illumination.

Chapter 5

Experimental Evaluation

In this chapter we provide an experimental evaluation of the CCD algorithm and the CCD tracker. We analyze the performances of both methods in terms of robustness, accuracy, and runtime. Section 5.1 defines the criteria we use to quantify the performance. Section 5.2 describes, in detail, the experimental evaluation of the CCD algorithm. Then, in section 5.3, we evaluate the CCD tracker and compare it with other state-of-the-art trackers. Finally, in section 5.4, we summarize the obtained results.

5.1 Quantifying the Performance

In section 1.1.3, we stated requirements for curve-fitting methods. We now define quantities that characterize to which extent a method meets these requirements.

Robustness: We quantify the robustness of a method by the *failure rate* it achieves for a given set of test data. We classify a result as a failure if its error E, i.e. the *distance* between the ground truth and the result, exceeds a given threshold T_E. The distance measurement and the threshold T_E will be described later individually for each experiment. The failure rate is defined as

$$\frac{\text{number of failures}}{\text{number of cases}} \cdot 100\%. \tag{5.1}$$

We say a method is robust if its failure rate is low.

Accuracy: We characterize the accuracy by the mean error and the standard deviation of the errors E. For the computation of these quantities only those cases are taken into account where the method does not fail, i.e. the resulting error E does not exceed the threshold T_E. [1]

Runtime: We characterize the computational cost by the mean and the standard deviation of the runtime. We run our methods on an off-the-shelf PC with a 500 MHz Intel Pentium III processor and operating system Windows NT. We compare the CCD tracker with several variants of the condensation tracker and the Kalman tracker (Blake and Isard, 1998), see section 5.3.1. For these methods, we use the original implementation of the Oxford Tracking Group which has been developed for SGI computers. We run the condensation tracker and the Kalman tracker on an SGI Octane with a 195 MHz IP30 processor. In order to allow for a quantitative comparison, for experiments conducted on the SGI, we provide a normalized runtime T_n defined by:

$$T_n = C_n \cdot \text{(runtime measured on SGI)}. \tag{5.2}$$

The normalization constant C_n takes the differences in the hardware into account. For the constant we use $C_n = 0.459$. This value is obtained by comparing the performances of both computers based on the Dhrystone benchmark (Weicker, 1984).

5.2 Evaluation of the CCD Algorithm

In this section, we evaluate the CCD algorithm, including the fast variant of the CCD algorithm described in section 4.1. First, in section 5.2.1, we report on results for 'semi-synthetic' images with a known ground truth. Then, in section 5.2.2, we present results for real images.

5.2.1 Results for Semi-synthetic Images

Generating Semi-synthetic Images

To obtain ground truth data, in this section, we use semi-synthetic images in order to evaluate the performance of the CCD algorithm. Figure 5.1 illustrates how a semi-synthetic image is composed of two real images. For a given curve function and a given parameter vector, i.e. the ground truth, a mask image is computed representing a perfect segmentation corresponding to the ground truth. This mask image specifies background and foreground pixels. The semi-synthetic image is obtained by taking foreground pixels from the first input image and background pixels from the second input image. Pixels which are not clearly assigned to the foreground or the background, i.e. pixels which are intersected by the curve, are obtained by

[1]Since the error E is defined as a distance, it is non-negative by definition. Hence, the mean error accumulates individual errors, i.e. individual errors do not cancel each other out.

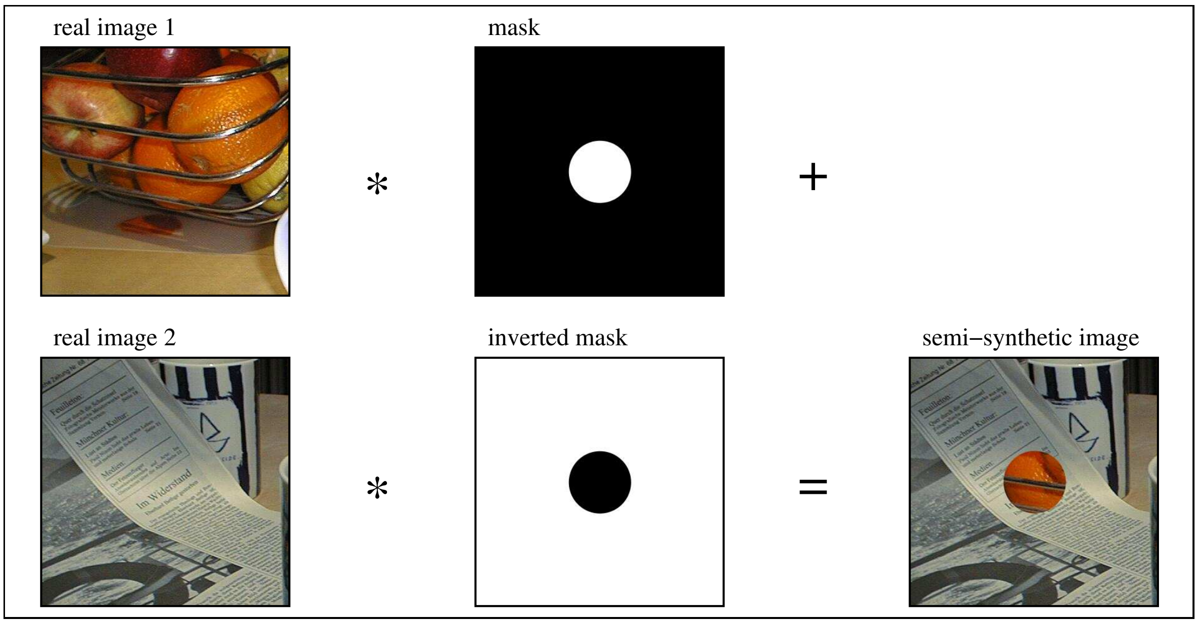

Figure 5.1: A semi-synthetic image is generated from two real images and a given vector of model parameters, i.e. the ground truth. From the ground truth a mask image is generated that specifies an ideal segmentation. For foreground pixels (white in the mask), the RGB values are taken from the first input image. For background pixels (white in the inverted mask), the RGB values are taken from the second input image.

interpolation. Resulting semi-synthetic images are depicted, for example, on pages 84 to 87 and page 106.

This procedure allows for generating a large number of images with an exact ground truth. Furthermore, it allows us to systematically vary relevant properties of the curve, e.g. the set of deformations allowed by the curve model. In section 5.3.2, we use a similar procedure for generating semi-synthetic image sequences from real image sequences.

Fast CCD Algorithm

In the first experiment we generate 90 semi-synthetic images from 10 real images depicted in Figure 5.2. For each pair of input images a semi-synthetic image is generated. Note that some of the input images, e.g. image 5 and image 6, have very similar textures. As model curve we use a circle with a radius of 50 pixels. Using the fast CCD algorithm, we fit a circle with known radius to the test images. The parameters to be estimated are the two coordinates of the circle's center point. We declare a fit as a failure if the Euclidean distance between the correct center point and the estimated center point exceeds $T_E = 1.0$ pixel.

For each of the 90 test images, we run the fast CCD algorithm with 45 different initial

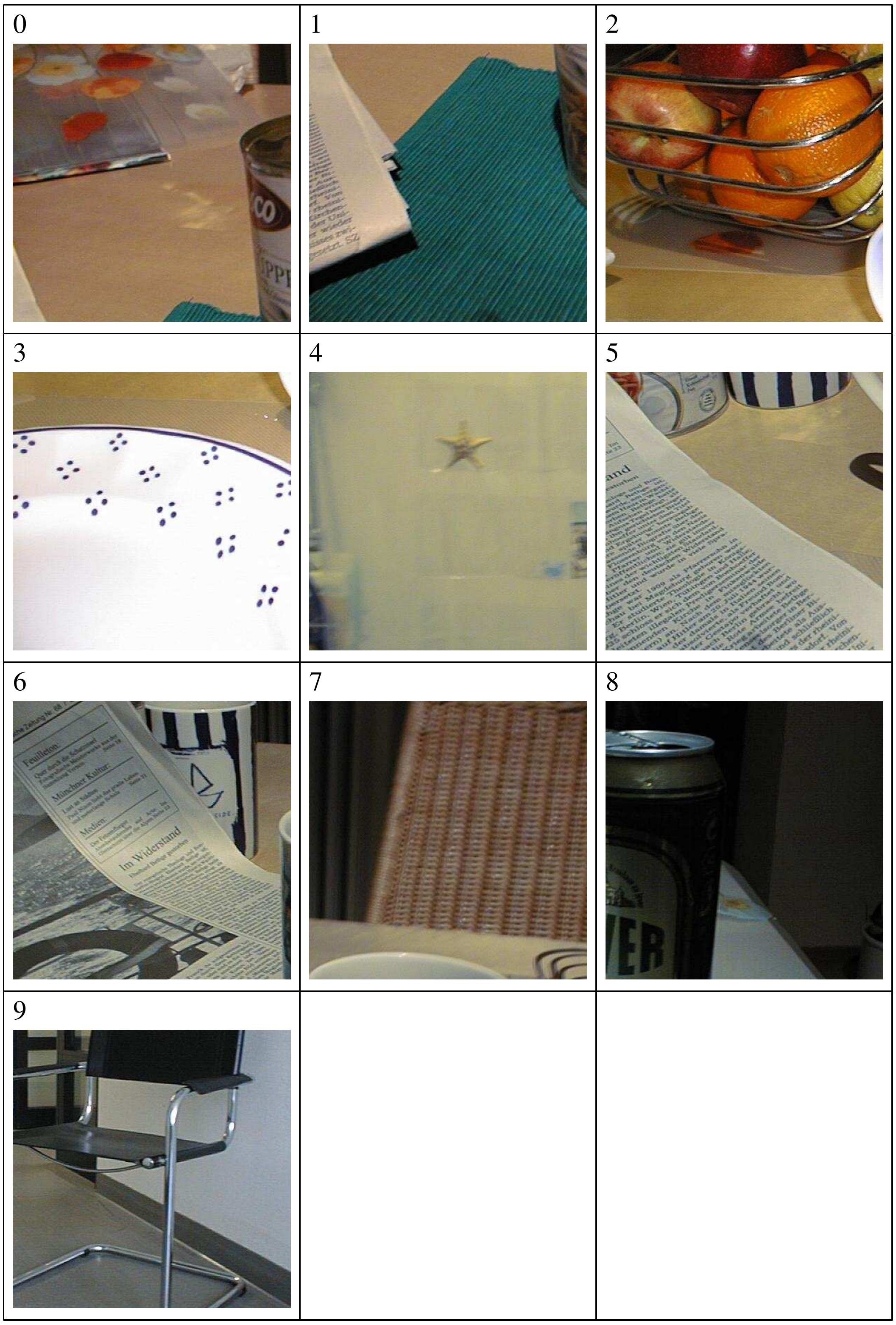

Figure 5.2: 10 real images used for generating 90 semi-synthetic images. Some images, e.g. image 5 and image 6, have very similar textures.

	variants of parameters				variants of input data		
	number of perpen-diculars $K =$	number of iterations #Itera-tions=	reduction of co-variance $c_2 =$	outlier treatment	uncertainty of prior (stand. dev. in pixels)	shape	blurred input images
A standard	15	20	$1/2$	yes	5	circle	no
B more accurate	**60**	20	$1/2$	yes	5	circle	no
C faster	15	**5**	$\mathbf{1/4}$	yes	5	circle	no
D no outlier treatment	15	20	$1/2$	**no**	5	circle	no
E prior with smaller standard deviation	15	20	$1/2$	yes	**2**	circle	no
F star shape	15	20	$1/2$	yes	5	**star**	no
G blurred images	15	20	$1/2$	yes	5	circle	**yes**

Table 5.1: Variants of parameters and input data used for evaluating the CCD algorithm: Below, we compare the variants B to G with the standard variant A.

positions of the circle. The 45 initial positions are obtained by combining 9 different magnitudes of initial error (1, 2, 5, 10, 20, 30, 40, 50, and 60 pixels) with 5 different angles of the initial error ($0 \cdot 72$, $1 \cdot 72$, $2 \cdot 72$, $3 \cdot 72$, and $4 \cdot 72$ degrees). This results in $90 \cdot 9 \cdot 5 = 4,050$ runs. We perform these $4,050$ runs for 7 different variants (A to G) of the algorithm's parameters and input data, which sums up to $28,350$ runs. Tab. 5.1 gives an overview of the 7 variants. We now discuss each variant and the corresponding performance of the fast CCD algorithm.

Variant A: Variant A is the standard variant. We compare all other variants with this variant. Table 5.2 shows the failure rate over the error of the initialization. For initial errors of up to 10 pixels, i.e. 20% of the circle's radius, variant A of the CCD algorithm converges to the correct solution in all cases. The failure rate monotonically increases with the initial error. For initial errors higher than 50 pixels, convergence to the correct solution is unlikely. In 21.23% of all runs, variant A does not converge to the correct solution.

Columns 2 and 3 in Table 5.3 summarize the error of the CCD algorithm. Variant A achieves a mean error of 0.0347 pixels, which is very accurate, given the intense texture of the images. For variant A, only 15 perpendiculars are used. The standard deviation of 0.0281 pixels indicates that errors much higher than the mean error are quite rare. Figure 5.3 depicts the histogram of the errors. In more than 96% of all cases the error is less than 0.1 pixels.

The right four columns in Table 5.3 summarize the runtime. For cases where variant A of

variant	Euclidean distance between initialization and ground truth (in pixels)									total
	1	2	5	10	20	30	40	50	60	(average)
A	0.00	0.00	0.00	0.00	4.22	14.00	35.11	56.22	81.56	21.23
B	0.00	0.00	0.00	0.00	6.67	16.22	31.56	54.89	81.11	21.16
C	0.00	0.00	0.00	2.44	28.22	58.22	82.22	93.56	99.11	40.42
D	0.00	0.00	0.00	0.22	4.67	15.56	36.67	59.33	84.89	22.37
E	0.00	0.00	0.00	3.78	38.67	65.33	99.33	100.00	100.00	45.23
F	0.00	0.00	0.22	0.44	2.89	18.22	52.44	66.66	90.00	25.65
G	0.00	0.00	0.00	0.00	3.56	13.78	35.33	55.78	83.78	21.36

Table 5.2: Failure rate (in %) over the error of the initialization. For initial errors up to 5 pixels, the CCD algorithm converges almost in all cases to the correct solution. For initial errors higher than the circle's radius (50 pixels), the CCD algorithm usually fails in accurately estimating the position of the curve.

	error in pixels		runtime in seconds (measured on a 0.5 GHz computer)			
			non-failure		failure	
variant	mean	σ	mean	σ	mean	σ
A	0.0347	0.0281	1.027	0.177	1.285	0.205
B	0.0186	0.0231	4.088	0.655	5.122	0.926
C	0.1088	0.1236	0.246	0.017	0.282	0.017
D	0.0354	0.0713	1.016	0.127	1.274	0.151
E	0.0342	0.0265	0.835	0.168	1.201	0.259
F	0.0388	0.0292	1.192	0.053	1.355	0.114
G	0.0439	0.0339	1.013	0.130	1.241	0.152

Table 5.3: Error and runtime overview: Using different variants, i.e parameterization, the CCD algorithm can be tailored to different requirements. For example, variant B is very accurate and achieves a mean error of 0.0186 pixels. Variant C is quite fast and achieves a mean runtime of 0.246 seconds (for the non-failure case). It is more than 16 times faster than variant B but also about 6 times less accurate.

the CCD algorithm converges to the right solution, the mean runtime is 1.027 seconds. In cases where the method does not converge to the right solution, the mean runtime is 1.285 seconds. In both cases, the standard deviation is less than 20% of the mean values. Hence, the runtime does not vary substantially. Both the runtime and the failure rate improve if the initial error decreases.

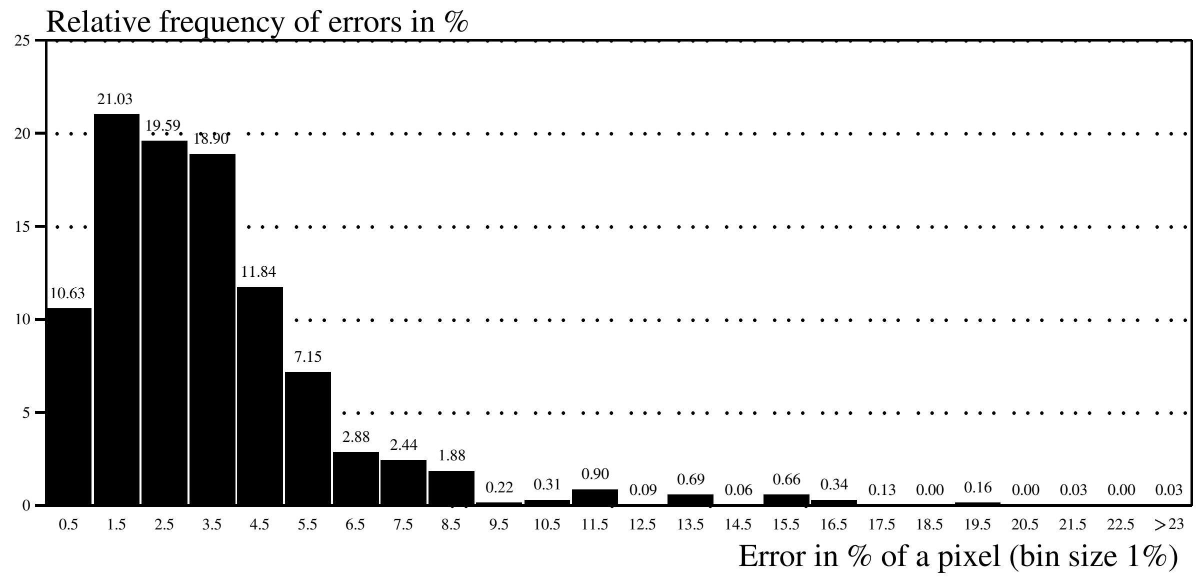

Figure 5.3: Error histogram of variant A: In more than 96% of all cases the error is less than 0.1 pixels and in more than 99.9% of all cases the error is less than 0.2 pixels.

Let us now discuss how the performance of the CCD algorithm depends on the image texture. Figures 5.4 and 5.5 depict the images yielding the highest and the lowest failure rate, respectively. Salient edges surrounding the circle lead to a clearly higher failure rate of up to 40%, see Figure 5.4. The average failure rate of variant A is 21.23%. For mainly homogeneous regions, the area of convergence is clearly larger. For such images the failure rate is less than 10%, see Figure 5.5.

Figures 5.6 and 5.7 depict the images with the highest and the lowest mean errors, respectively. In images yielding high errors, salient edges are given close to the circle, see Figure 5.6, whereas the images yielding low errors have clearly less edges close to and parallel to the circle, see Figure 5.7. We now compare variant A with the other variants.

Variant B: Variant B achieves a higher accuracy than variant A by using more perpendiculars. In variant B we use 60 perpendiculars, four times as many as in variant A. Thus, the mean error decreases by about 46% to only 0.0186 pixels, see Table 5.3. (For completeness, the error histograms of variants B to G are given in appendix A.1.) The almost two times higher accuracy requires an about 4 times higher runtime, see Table 5.3. The failure rate of variant B is 21.16% which is only slightly lower than for variant A, see Table 5.2. Due to these results, we think that an even higher accuracy and a reduced runtime could be obtained as follows. First, run the algorithm with a small number of perpendiculars and then substantially increase the number of perpendiculars in the last iteration steps.

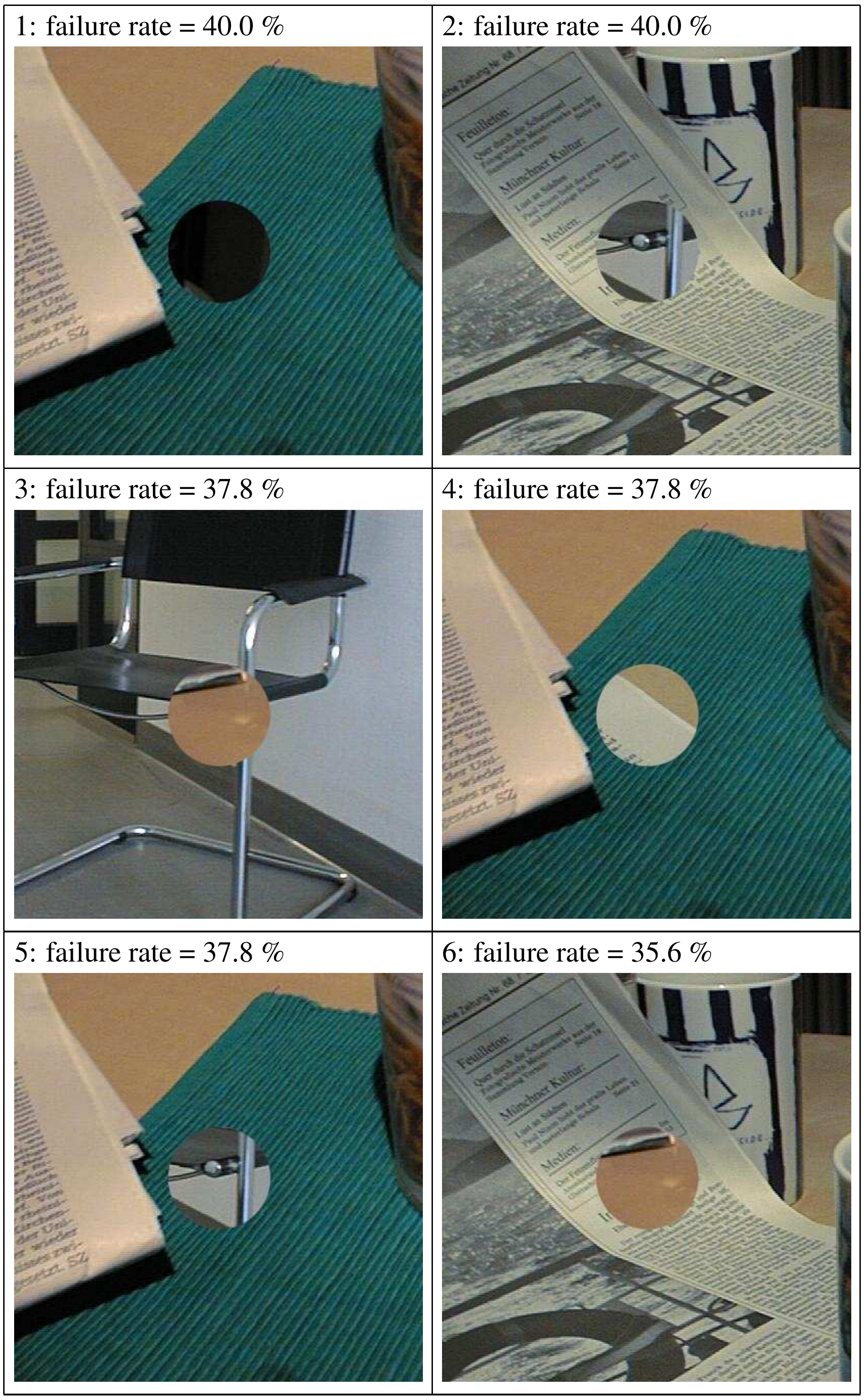

Figure 5.4: Images yielding the highest failure rate: In these images salient edges are given next to the circle's boundary.

1: failure rate = 4.4 %

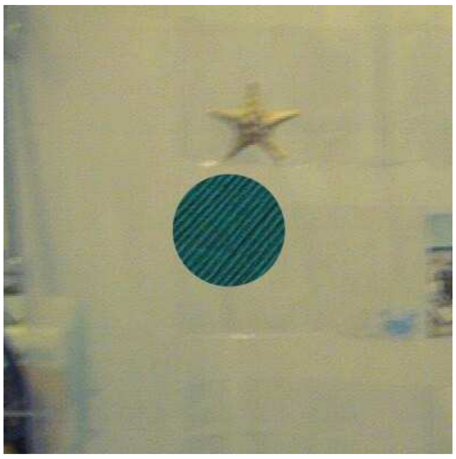

2: failure rate = 6.7 %

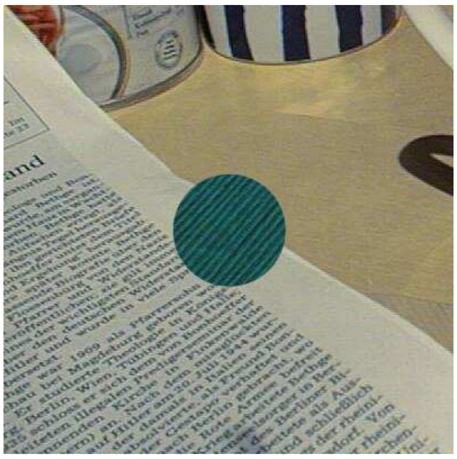

3: failure rate = 6.7 %

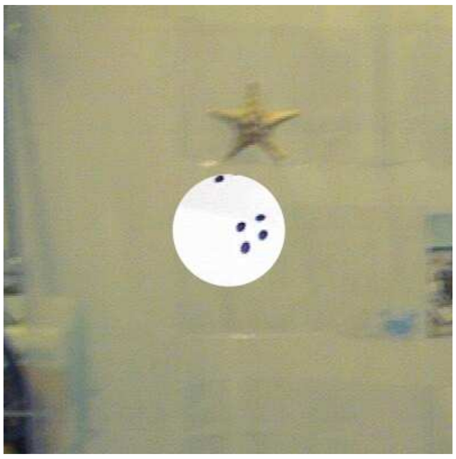

4: failure rate = 6.7 %

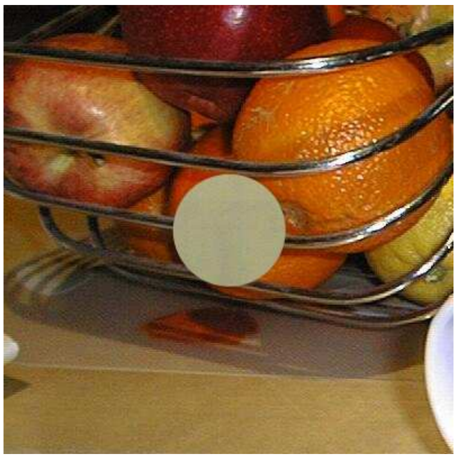

5: failure rate = 6.7 %

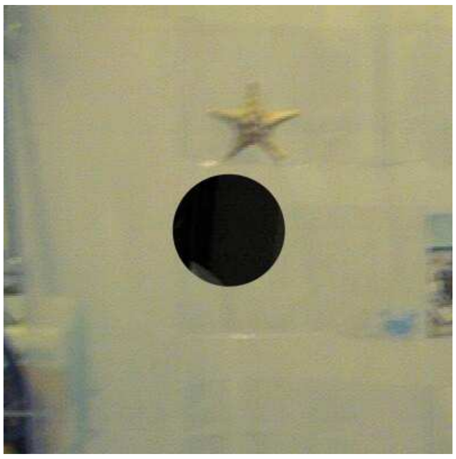

6: failure rate = 8.9 %

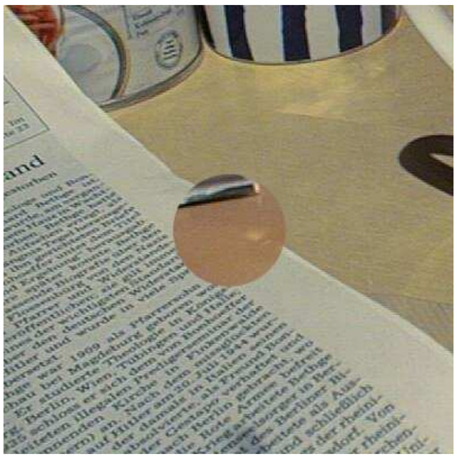

Figure 5.5: Images yielding the lowest failure rate: In these images the histograms of the two regions have little overlap.

1: mean error in pixels = 0.1523 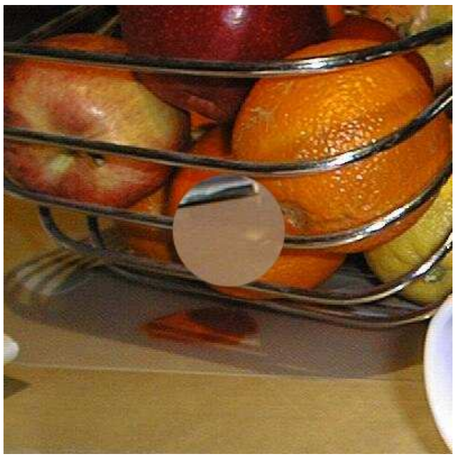	2: mean error in pixels = 0.1505 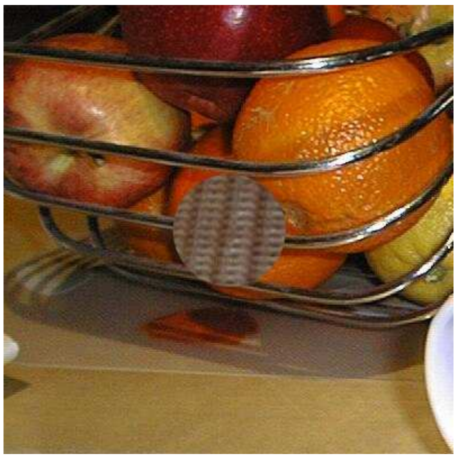
3: mean error in pixels = 0.1095 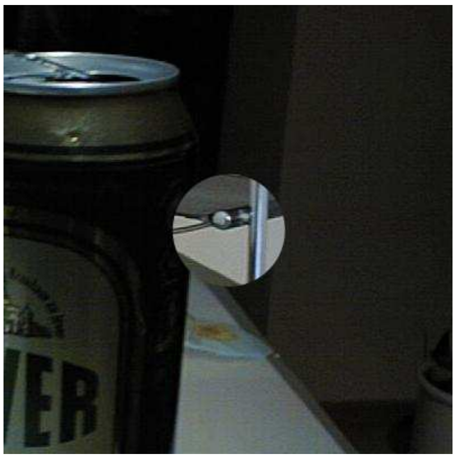	4: mean error in pixels = 0.0868 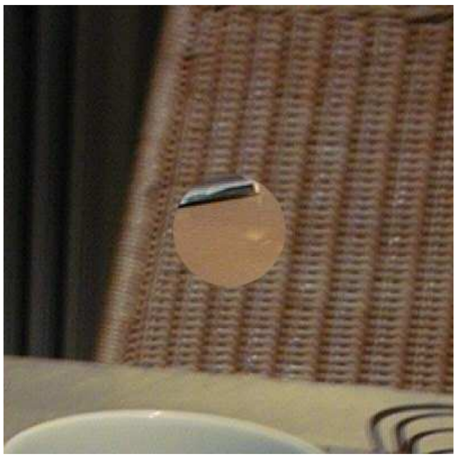
5: mean error in pixels = 0.0782 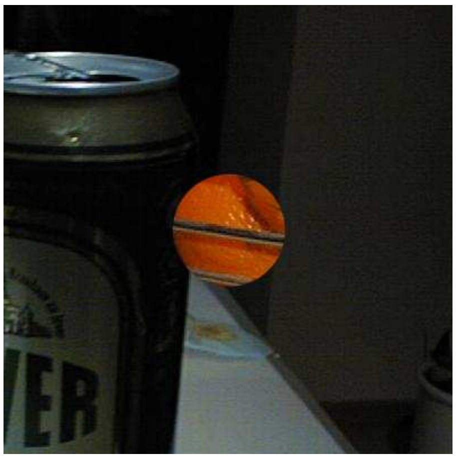	6: mean error in pixels = 0.0670 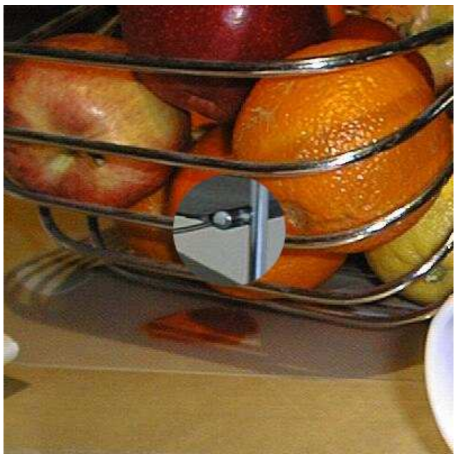

Figure 5.6: Images yielding the highest mean error: In these images strong edges are given close to the circle.

1: mean error in pixels = 0.0025	2: mean error in pixels = 0.0055
3: mean error in pixels = 0.0069 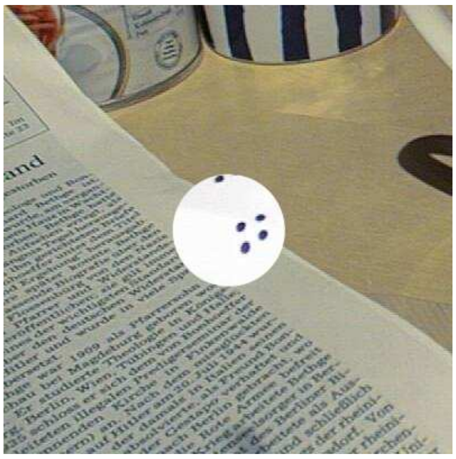	4: mean error in pixels = 0.0105
5: mean error in pixels = 0.0106 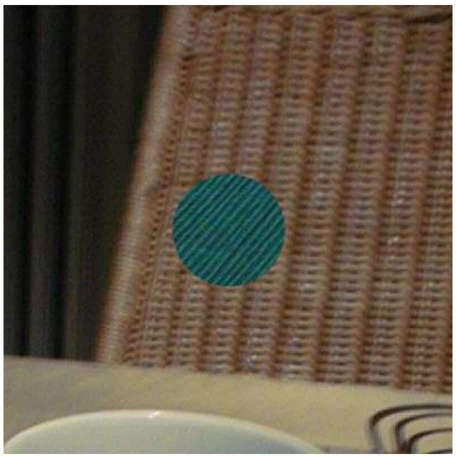	6: mean error in pixels = 0.0108 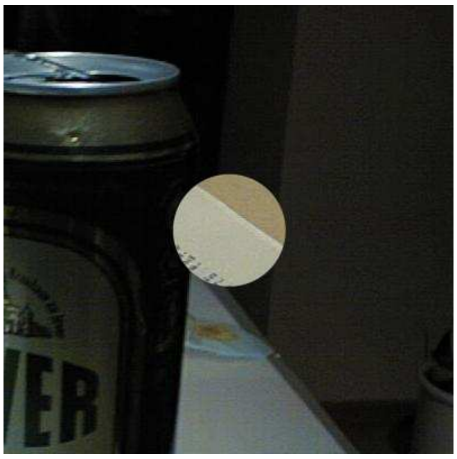

Figure 5.7: Images yielding the lowest mean error

Variant C: Variant C is a fast variant. It performs only 5 iteration steps (variant A: 20). Furthermore, variant C uses a smaller value for parameter c_2. This parameter specifies how fast the uncertainty of the curve is reduced, see equation (3.56). We choose $c_2 = 1/4$ instead of $c_2 = 1/2$ which yields an about two times faster reduction of the covariance matrix $\mathbf{\Sigma_\Phi}$. Therefore, the curve distribution does faster contract. These modifications lead to an about two times higher failure rate (Table 5.2). Nevertheless, for small initial errors (which are common in tracking applications) the failure rate is still zero. The mean error of 0.1088 pixels is about three times higher than for variant A, see Table 5.3. On a 0.5 GHz computer Variant C achieves a runtime of 0.246 seconds, which is about four times faster than variant A. On a more up-to-date computer, i.e. a 6 times faster computer, variant C can process about 24 frames per second. A higher frame rate can be achieved by performing less iteration steps. However, for heavily textured images, this usually results in a significant deterioration of the accuracy and the robustness.

Variant D: We investigate the impact of the outlier treatment described in section 3.3.2.4. In variant D we switch off the outlier treatment. This results in an increased failure rate (+1.14%) and a slightly higher mean error. However, the most significant change is the 2.54 times higher standard deviation of the error. It increases from 0.0281 to 0.0713 pixels, see Table 5.3. Without outlier treatment, relatively high errors are clearly more frequent than with outlier treatment. In most applications, a more constant quality of the estimates is preferred. For example, in tracking applications, high errors can substantially increase the risk of loosing track of the object. Therefore, we recommend the use of the outlier treatment.

Variant E: Let us now investigate the impact of the a priori uncertainty. In variant A, the initial covariance matrix is $\mathbf{\Sigma}^*_\mathbf{\Phi} = \text{diag}(5^2, 5^2)$. For variant E, we use $\mathbf{\Sigma}^*_\mathbf{\Phi} = \text{diag}(1^2, 1^2)$ representing a 5 times smaller uncertainty, i.e. standard deviation. For small initial errors, up to 5 pixels, variant E converges to the correct solution in all cases (Table 5.2). However, for initial errors clearly higher than the initial uncertainty of one pixel, the failure rate significantly increases. For initial errors of 50 pixels, variant E never converges to the correct solution. Variant E fails in 45.23% of all runs, whereas variant A fails only in 21.23%. Hence, an a priori uncertainty that substantially underestimates the initial error leads to a too small area of convergence.

Variant F: We evaluate the impact of the shape to be extracted. In variant A we employ a circle, whereas in variant F we employ a non-convex shape with higher curvature. The shape is defined by the curve function

$$\mathbf{c}(\omega, \mathbf{\Phi}) = 50(1 + 0.15\sin(5\omega)) \cdot [\cos(\omega), \sin(\omega)]^T + \mathbf{\Phi}. \tag{5.3}$$

This yields a shape somewhat similar to a star or a starfish, see Figure A.8 (page 128). For this more complex shape, the failure rate is 25.65%, i.e. 4.42% higher than for the circle. The mean error increases by 11.8% to 0.0388 pixels. Further results for this shape are given in appendix A.2.

Variant G: For variant A to F, we used semi-synthetic images which are generated according to section 5.2.1. These images are constructed using a perfectly sharp mask image. However, real imaging devices blur the image. In order to simulate this effect, in variant G we use blurred mask images. We blur the mask with an isotropic Gaussian kernel with a standard deviation of $\sigma = 0.5$ pixels. This yields semi-synthetic images with blurred edges. For the resulting images, the failure rate is only 0.13% higher than for the sharp images, i.e. variant A. The mean error increases from 0.0347 pixels to 0.0439 pixels. However, compared to the blurring this increase is relatively small and the achieved accuracy is still very high.

Dense CCD Algorithm

We now analyze the performance of the dense CCD algorithm, i.e. the CCD algorithm as described in chapter 3. We apply the dense CCD algorithm to the segmentation of a circle. Now the circle is modeled with three degrees of freedom, namely the two coordinates of the center point and the radius. Figs. 5.8 and 5.9 depict the iterations for two semi-synthetic images. In both cases, the initial error is reduced by more than 99.8% and the final error is less than 5% of a pixel.

Figure 5.10 depicts the area of convergence for the image shown in Figure 5.8. The CCD algorithm is started with a radius of 35 pixels, which is 5 pixels higher than the correct radius. A high initial covariance defining an uninformed a priori distribution is used, leading to a large area of convergence. The area of convergence has roughly the size of the image circle. On a 0.5 GHz computer, the first iteration step of Figure 5.8 takes about 4 seconds. The initial uncertainty is high and roughly 10,000 pixels are used. After about 5 iterations the runtime is reduced to less than 1 second per iteration. For 10 iterations the runtime is about 20 seconds which is much longer than for the fast CCD algorithm.

iteration: error in pixels (x, y, radius)			
0: 23.0, 10.0, -5.0	2: 8.39, 2.07, -6,71	6: .214, .012, -.272	10: -.025, .028, -.033
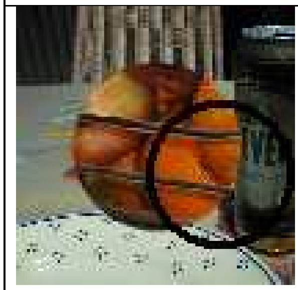	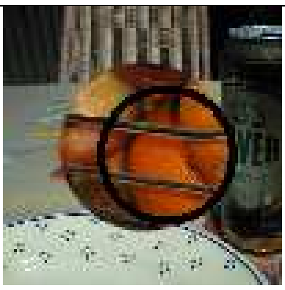	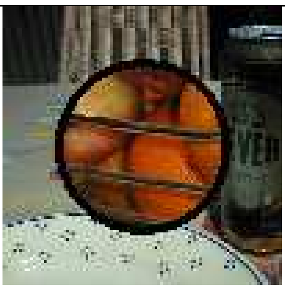	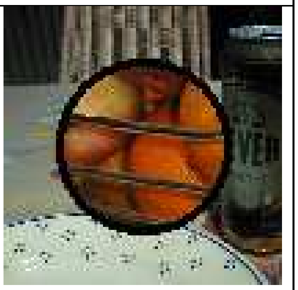

Figure 5.8: Despite the inhomogeneity of the foreground and the background the initial error is reduced by more than 99.8%.

iteration: error in pixels (x, y, radius)			
0: 35.0, 20.0, -5.5	2: 6.43, 3.74, -4.93	8: -.041, -.018, -.053	13: -.040, -.013, -.044
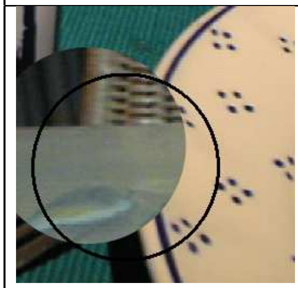	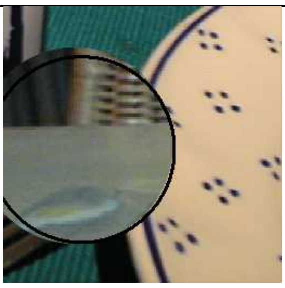	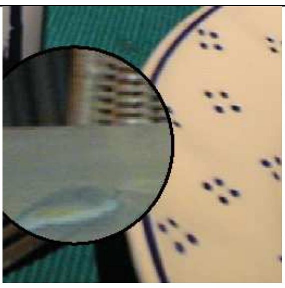	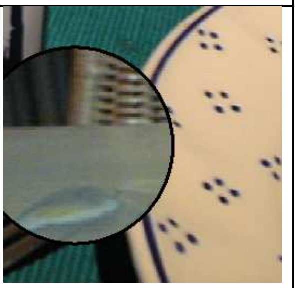

Figure 5.9: The circle is only partially visible. Nevertheless, the final error is less than 5% of a pixel.

5.2.2 Results for Real Images

We apply the CCD algorithm to different kinds of curve fitting problems using real images: (i) 3-D pose estimation of cylindrical objects, (ii) 3-D pose estimation of polyhedral objects, (iii) fitting deformable models, i.e. Point Distribution Models (Cootes et al., 1993). Details about the used curve models, i.e. the curve functions, are given in appendix B.

Cylindrical Objects

In the introductory example depicted in Figure 1.2 on page 4 we model the mug as a cylinder of known dimensions. We assume that the internal camera parameters are given. These parameters are, for example the focal length, the pixel size, and parameters, which define the radial distortion of the lens (see appendix B for details). By fitting the cylinder contour to the image,

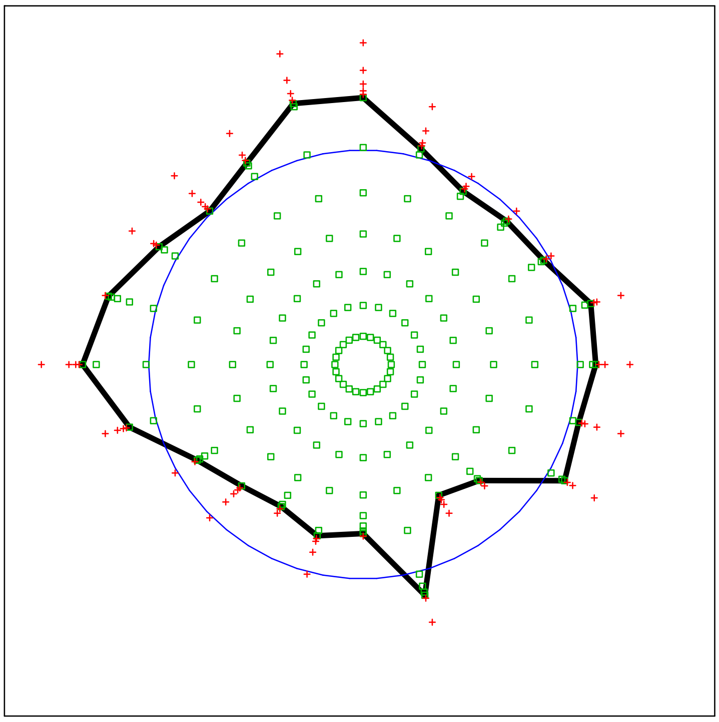

Figure 5.10: Area of convergence for the image depicted in Figure 5.8. The thick line separates all investigated converging center points (green rectangles) from the non-converging center points (red crosses). The thin blue line is the real image circle. The area of convergence has roughly the size of the real circle.

we estimate the 3-D pose of the mug with respect to the camera coordinate system. Despite the strong background clutter, the texture, and the shading, the CCD algorithm accurately estimates the mug's contour as illustrated in Figure 1.2c. Note that methods fitting the curve model not directly to the image data but to an edge map have to deal with multiple false positive and false negative errors, see Figure 2.1b on page 15. Furthermore, the edge map shows a limited accuracy, for example, in the presence of inhomogeneous regions.

Polyhedral Objects

The 6 pose parameters defining the 3-D pose of a given polyhedral object are estimated by fitting the object contour to the image data. The contour consists of radially distorted line segments. Figure 5.11a shows a tea box with flower pattern lying in a flower meadow. Both the box and the background region have multiple internal edges, see Figure 5.11b. Nevertheless, the CCD algorithm accurately estimates the contour of the tea box.

The next example shows that the CCD algorithm is not only able to exploit object contours, but it can also use internal model edges separating multiple, possibly dependent, image regions. We fit a rigid wire frame model to the image depicted in Figure 5.12a. The degrees of freedom are the 6 pose parameters. The CCD algorithm reliably estimates the pose of the box despite the partial occlusion. Again, a gradient-based edge detector (Steger, 2000) yields multiple false positive and false negative errors, see Figure 5.12b.

Deformable Models

We fit a deformable model, i.e. a Point Distribution Model (Cootes et al., 1993), with 12 degrees of freedom to the image data. Figure 5.13 depicts the results for different iteration steps. Only 4 iterations are needed in order to largely reduce the initial error. Note that the number of necessary iterations is small despite the relatively high dimension of the parameter vector. While region-based and graph-theoretic methods usually require closed region boundaries, the CCD algorithm can also deal with non-closed curves as depicted in Figure 5.13.

a.)
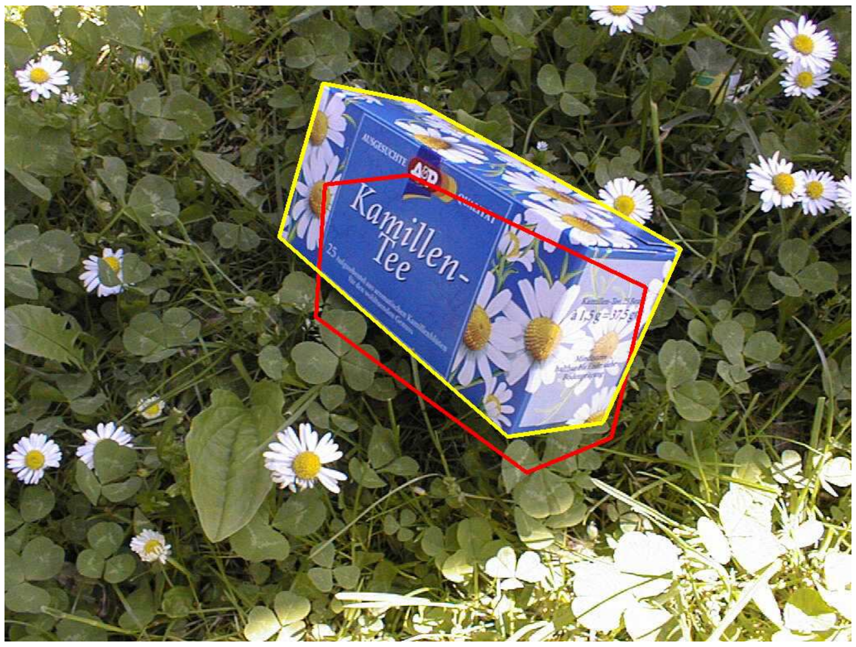

b.)
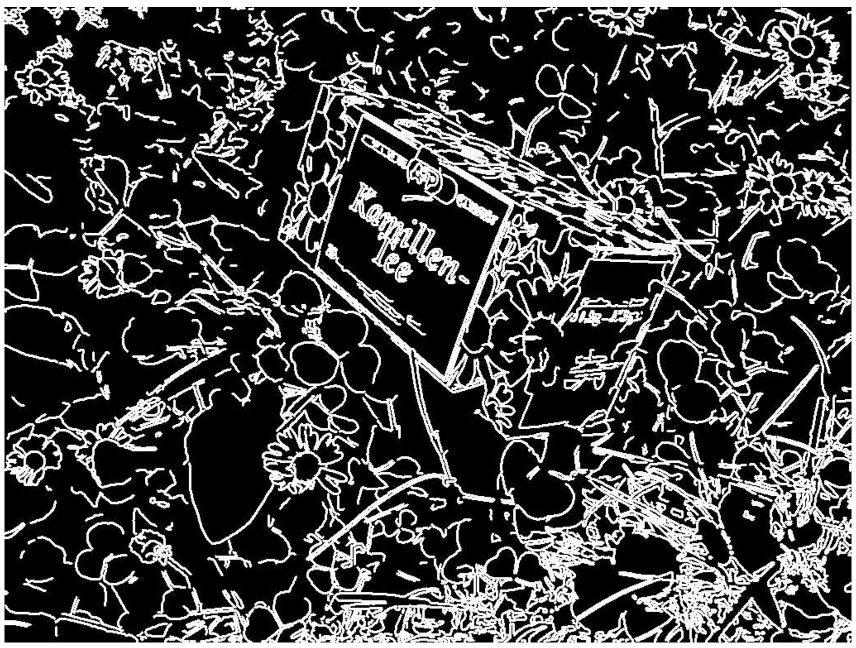

Figure 5.11: Tea box with flower pattern lying in a flower meadow: a.) Despite the inhomogeneities of the foreground and the background, the CCD algorithm accurately fits the model of the tea box to the image contour (red = initialization, yellow = estimated contour). b.) Color edges detected by a gradient-based approach (Steger, 2000): The huge majority of the detected edges does not correspond to the contour of the box. Furthermore, the result of the edge detection depends heavily on the illumination. In the bright part, bottom right, clearly more edges are detected.

a.)
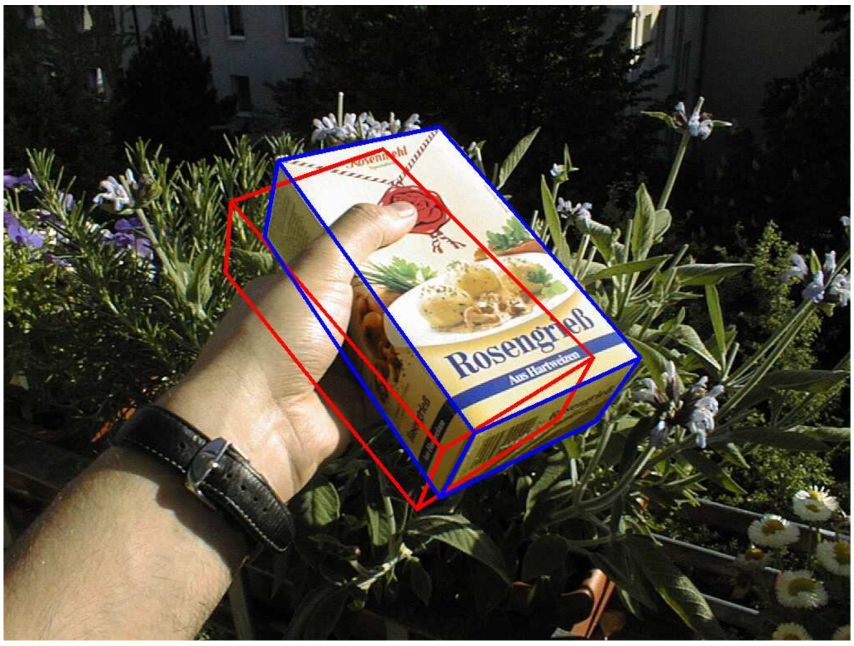

b.)
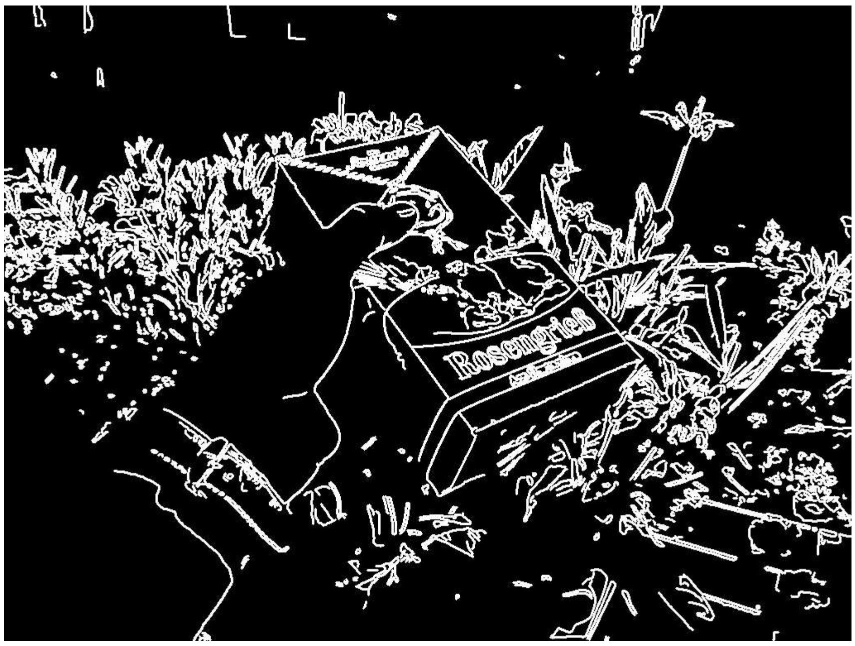

Figure 5.12: Partially occluded box in front of an inhomogeneous background: a.) Due to the directed illumination, the contrast between the background and the box heavily varies. Nevertheless, the CCD algorithm accurately fits a wire frame model to the image data (red = initialization, blue = estimate). b.) Here again a gradient-based edge detector (Steger, 2000) yields multiple false positives and false negative errors.

iteration 0 (initialization):

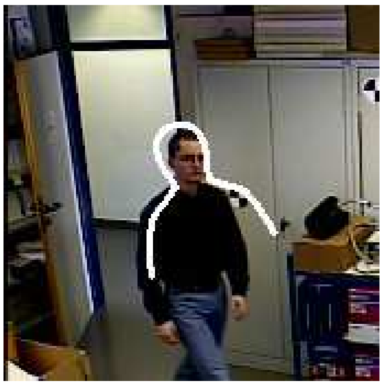

iteration 1:

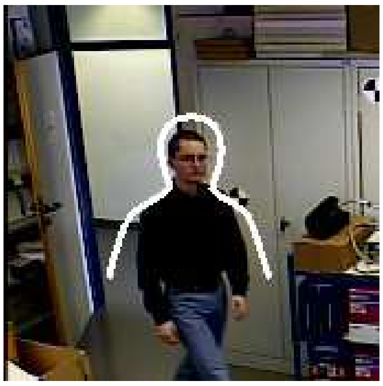

iteration 2:

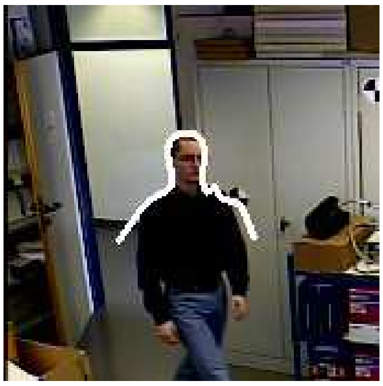

iteration 3:

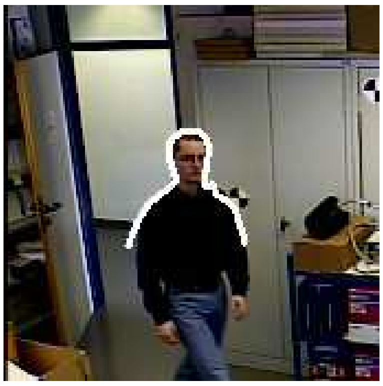

iteration 4:

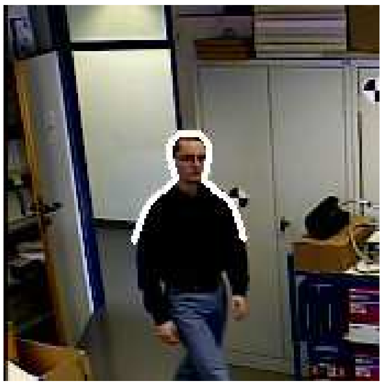

iteration 5:

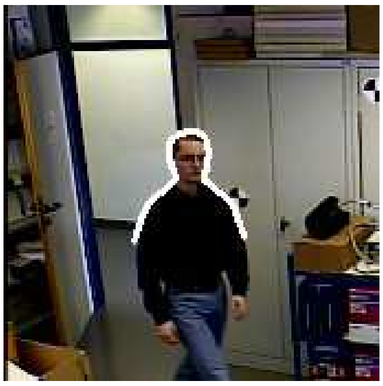

Figure 5.13: Fitting a deformable model with 12 degrees of freedom: Already after 4 iterations the initial error is largely reduced.

5.3 Evaluation of the CCD Tracker

We evaluate the CCD tracker using both semi-synthetic image sequences (section 5.3.2) and real image sequences (section 5.3.3). In both cases, we compare the performance of the CCD tracker with other well-known standard trackers.

5.3.1 Compared Trackers

We compare the CCD tracker with different variants of the condensation tracker and the Kalman tracker (Blake and Isard, 1998). Since the seminal work of Isard and Blake (1996), the condensation tracker represents the state-of-the-art in contour-based tracking.

For the comparison with the CCD tracker, we employ the original implementation of the condensation tracker developed by Michael Isard. This implementation and an implementation of the Kalman tracker are part of the Oxford Tracking Library[2]. In addition, we apply extensions of these two methods. The original methods perform edge detection on gray values. For color images, these methods first convert the color values into gray values and then perform edge detection on the gray values. We apply RGB-variants of the trackers. These variants perform edge detection directly on the RGB values. The advantage is that edges can be detected even if no significant gradient of the corresponding gray values is given. The disadvantage is that the edge detection process is more expensive, since it takes three channels into account.

We run the condensation tracker with different numbers of samples: 10, 100, 1,000, and 10,000 samples. Each of these sample sizes is applied for the RGB variant and the gray value variant. Additionally, in some cases we even use 100,000 samples for the RGB variant. Furthermore, we apply the RGB variant and the gray value variant of the Kalman tracker. All together we compare the CCD tracker with 11 different trackers in terms of robustness, accuracy, and runtime.

5.3.2 Results for Semi-synthetic Image Sequences

In this section, we use semi-synthetic image sequences to compare the CCD tracker with the other trackers. In most relevant applications, a tracker has to cope with flexible curve models having multiple degrees of freedom. A rigid object with an arbitrary 3-D pose has 6 degrees of freedom. For deformable objects, usually much more parameters are required. For example, for approximating the human body, models with more than 25 degrees of freedom are used (Aggarwal and Cai, 1999; Deutscher, Blake, and Reid, 2000; MacCormick and Isard, 2000). In

[2]The Oxford Tracking Library is available at http://www.robots.ox.ac.uk/∼vdg/Darling.html .

this section, we analyze how the performances of the CCD tracker and other trackers depend on the dimension of the parameter vector.

Generating Image Sequences

We use shape-space models (Blake and Isard, 1998) with different numbers of parameters. Appendix B.2 explains the foundations of these deformable 2-D models. We start with a model that has 15 degrees of freedom, two parameters for the 2-D translation and 13 parameters specifying deformations. Using a dynamical model as described in section 4.2, we generate a random sequence of 200 model parameter vectors defining a sequence of 200 successive shapes. We obtain sequences of less deformable shapes by substituting some or all deformation parameters by zeros. Thus, we construct sequences of shapes with 2, 3, 4, 5, 7, 10, and 15 degrees of freedom. For each of the resulting shapes, we generate an ideal mask image according to section 5.2.1. Figure 5.14 depicts some of the $7 \cdot 200 = 1,400$ mask images.

We use the resulting sequences of masks in order to merge 4 pairs (A to D) of real image sequences. Figure 5.15 depicts some images of these sequences. The merging is performed by employing the merging procedure described in section 5.2.1. This yields $7 \cdot 4 = 28$ image sequences, each with a length of 200 images which results in $28 \cdot 200 = 5,600$ images. Since we apply the CCD tracker and 11 other trackers to these image sequences, in this experiment, we obtain 64,000 individual fits.[3]

Definition of a failure: We classify a fit as a failure if the error E, i.e. the distance between the correct curve and the estimated curve, exceeds $T_E = 3$ pixels. Here, error E is defined as the maximum distance between a point on the correct curve and the corresponding point on the estimated curve, projected onto the curve normal. The error E is given by

$$E \quad = \quad \max_r \mathbf{n}_r[\mathbf{c}(\omega_r, \mathbf{\Phi}) - \mathbf{c}(\omega_r, \mathbf{m}_{\mathbf{\Phi}})], \tag{5.4}$$

where $\mathbf{\Phi}$ is the ground truth parameter vector and $\mathbf{m}_{\mathbf{\Phi}}$ is the estimated parameter vector. We evaluate the two curve functions for 200 equally spaced values ω_r. The vector $\mathbf{n}_r$ denotes the unit normal vector to the curve at the point $\mathbf{c}(\omega_r, \mathbf{\Phi})$.

Parameterization: We apply the same parameterization as in variant A, the standard variant, introduced in section 5.2.1 (see Table 5.1). However, in order to adapt the CCD tracker to

[3]Due to the very high runtime, we apply the condensation tracker with 100,000 samples only to 12 out of the 28 image sequences.

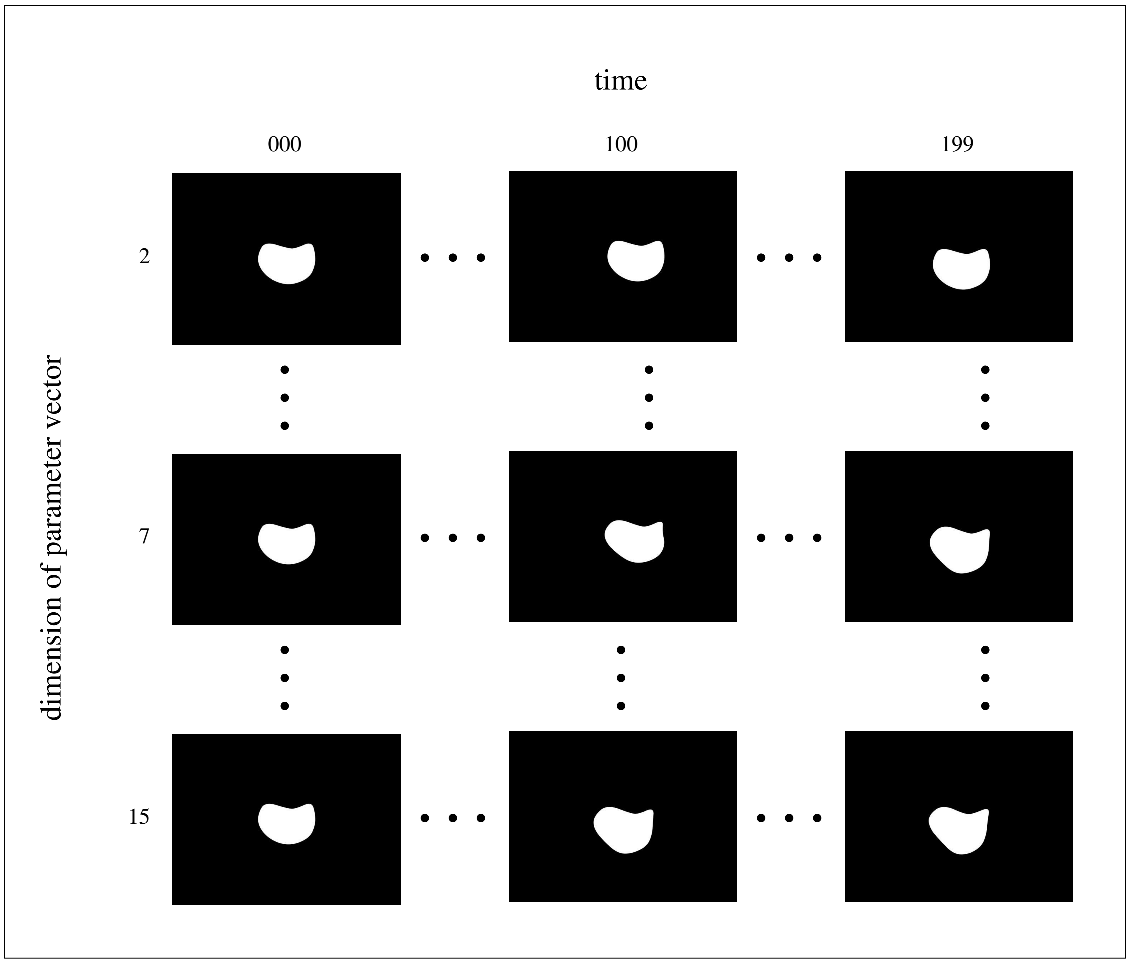

Figure 5.14: Masks used for generating semi-synthetic image sequences: The masks depend on the time, i.e. the frame number, and on the dimension of the parameter vector defining the deformations of the shape.

different degrees of freedom, i.e. different dimensions $D_{\mathbf{\Phi}}$ of the model parameter vector $\mathbf{\Phi}$, we choose the number K of perpendiculars by

$$K = 5 \cdot D_{\mathbf{\Phi}} + 5. \tag{5.5}$$

Note that more accurate or faster variants of the CCD tracker can be obtained by choosing the parameters of the tracker according to variant B or variant C (see Table 5.1).

Results

Figure 5.16 shows the failure rates over the dimension of the parameter vector. For dimensions 2 to 10 the CCD tracker achieves an almost perfect result. (Only for dimension 3, the CCD tracker fails in a single image.) For dimension 15, the CCD tracker fails in 67 images (8.38%).

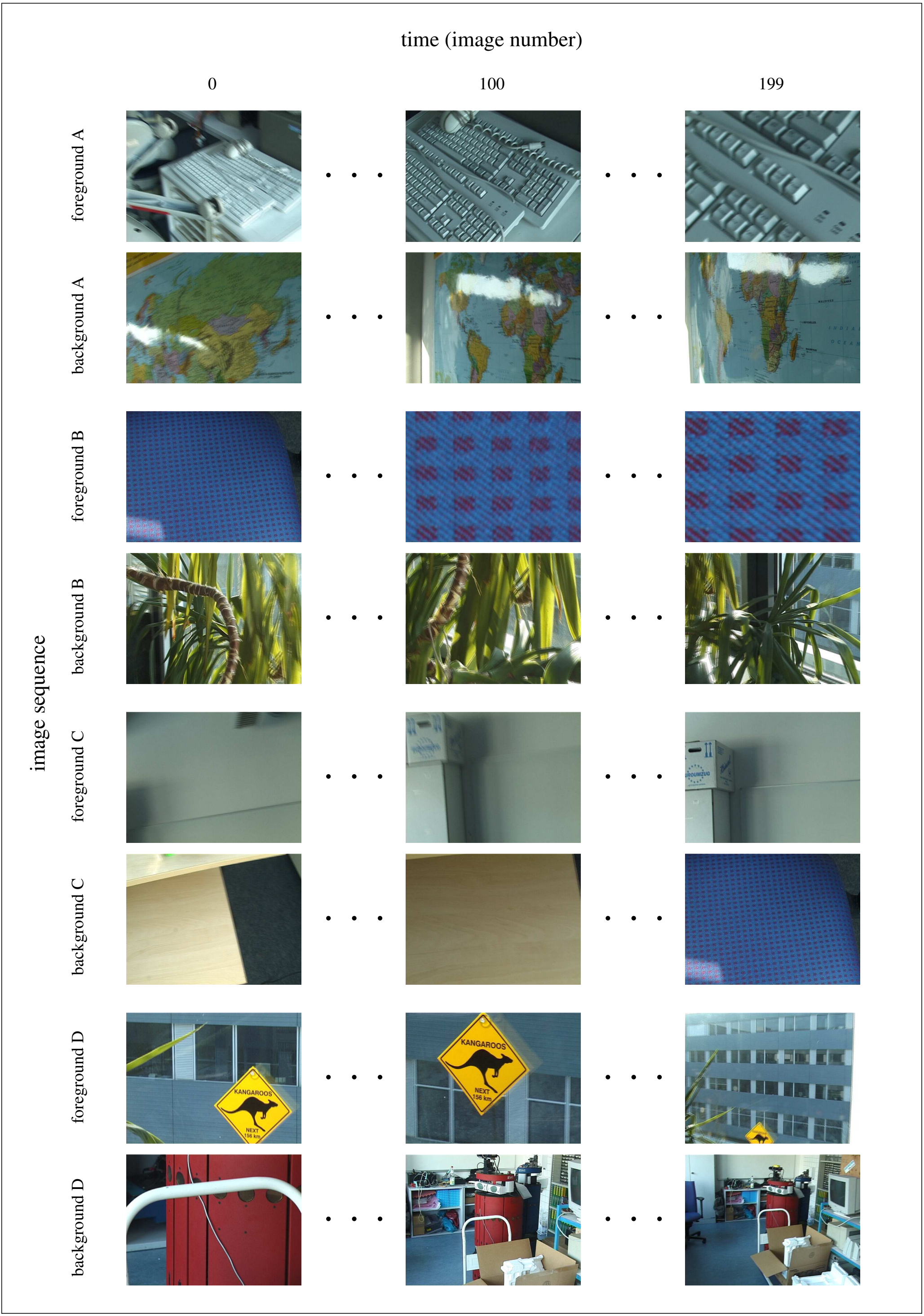

Figure 5.15: From these image sequences, we generate 28 semi-synthetic image sequences each with a length of 200 images and a resolution of 640 × 480 pixels. The images cover a variety of different textures.

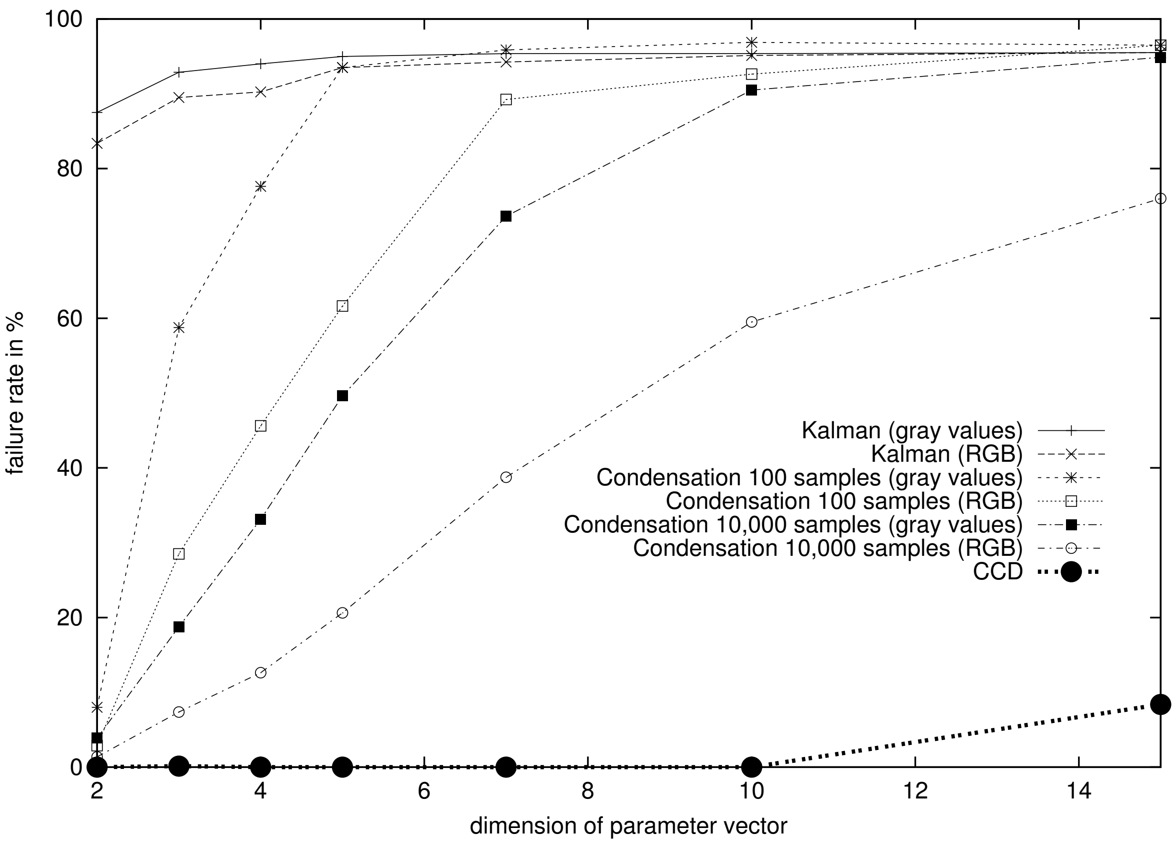

Figure 5.16: Failure rate over the dimension of the parameter vector: Up to dimension 10 the failure rate of the CCD tracker is less than 0.13%. For dimension 15, the CCD tracker fails in 8.4% of the images. The other trackers fail for all dimensions at least 9 times more often than the CCD tracker.

The other trackers yield much higher failure rates. Due to clutter and texture, the Kalman tracker fails in more than 80% of the images. The condensation tracker yields a relatively low failure rate for small dimensions (2 and 3). However, its failure rate rapidly increases with the dimension of the parameter vector. The trackers using RGB values are clearly more robust than the corresponding trackers using gray values. For all dimensions the failure rate of the CCD tracker is at least 9 times lower than the failure rate of the best compared tracker, i.e. the condensation tracker using 10,000 samples and RGB values. Table 5.4 (page 104) shows the failure rates in more detail.

Different sample sizes of the condensation tracker yield different failure rates and runtimes. For dimensions 5, 10, and 15, Figure 5.17 shows the failure rate of the condensation (RGB) trackers over the runtime. The runtime and the corresponding failure rate of the CCD tracker are illustrated in these plots by additional points. For all dimensions, the point characterizing the performance of the CCD algorithm is clearly below the curve characterizing the condensation tracker. Thus, given the same runtime, the condensation tracker achieves a much better failure rate. For dimension 5, the CCD tracker achieves a failure rate of 0.0%. The condensation tracker with the same runtime fails in about 20% of the images. For dimensions 10 and 15, the differences between the condensation tracker and the CCD tracker are even larger. Even with a 3 to 7 times higher runtime, the condensation tracker does not achieve a significant reduction of the failure rate.

Figure 5.18 depicts the error of the CCD tracker and the condensation tracker (RGB, 10,000 samples) over the dimension of the parameter vector. For both trackers, the mean error monotonically increases with the dimension of the parameter vector. The CCD tracker achieves high sub-pixel accuracy. Up to dimension 7, the mean error of the CCD tracker is not higher than 0.080 pixels. For dimension 15, the mean error is 0.158 pixels. This is a very high accuracy, given the heavy texture of the images. The condensation tracker is about 12 to 22 times less accurate.

Table 5.4 shows the failure rate, the mean error, and the standard deviation of the error for different trackers and different dimensions of the parameter vector. For all dimensions, the CCD tracker clearly outperforms all other trackers in terms of robustness and accuracy.

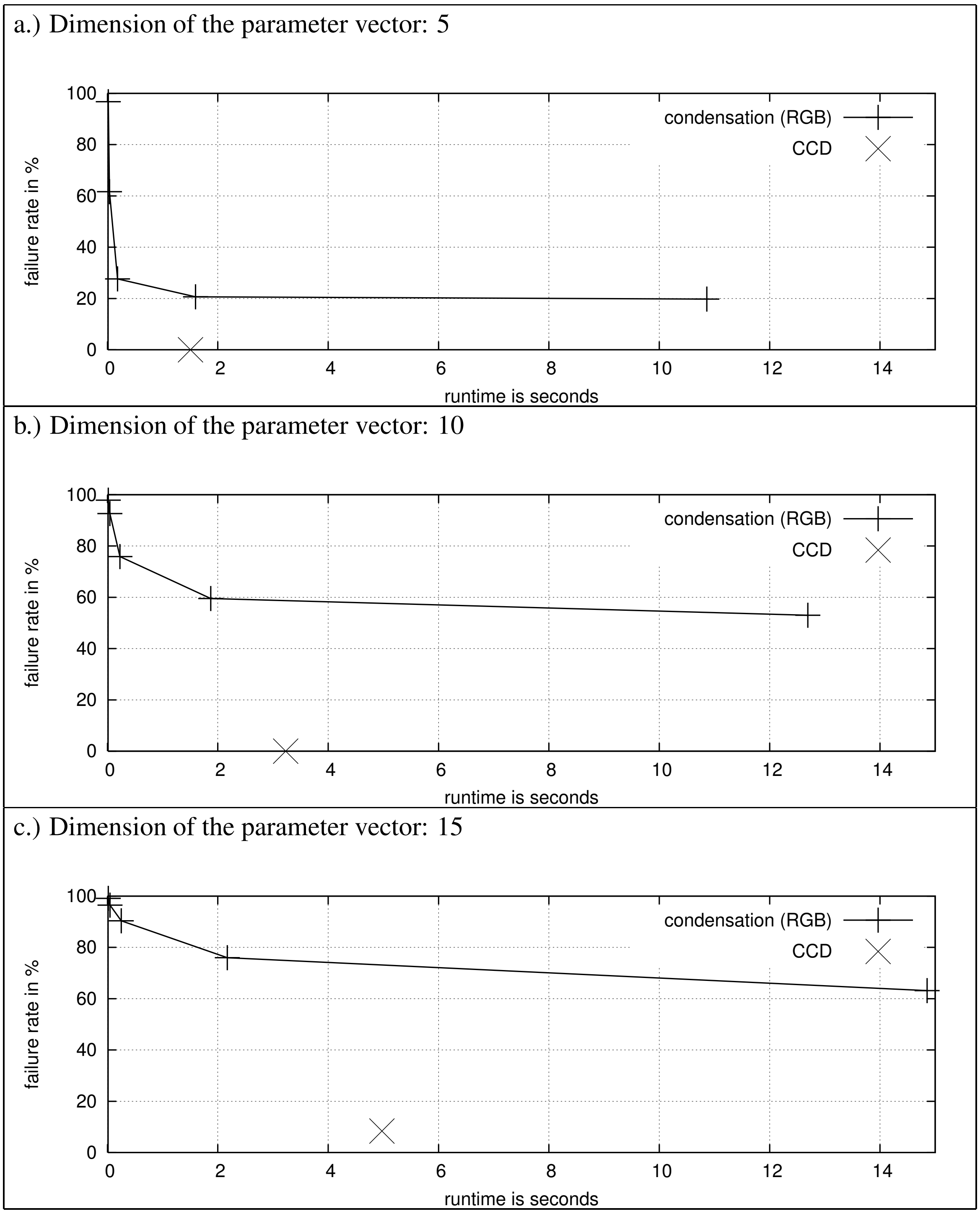

Figure 5.17: Failure rate over runtime for different dimensions of parameter vector: Given the same runtime, the CCD tracker achieves a much lower failure rate than the condensation tracker. Even with a 3-7 times higher runtime, the failure rate of the condensation tracker still clearly exceeds the failure rate of the CCD tracker.

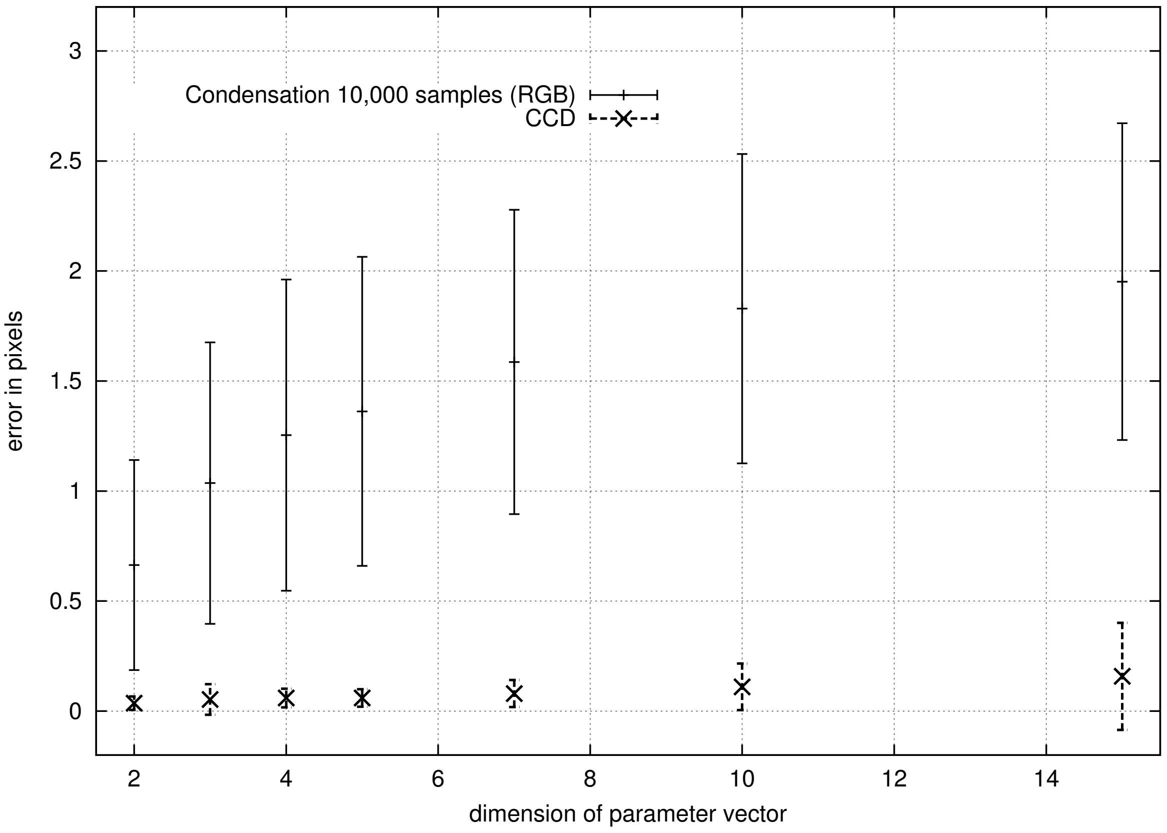

Figure 5.18: Error over dimension of parameter vector: The CCD tracker achieves sub-pixel accuracy. Its average error is less than 0.1 pixels up to dimension 7. For all dimensions, the average error of the condensation tracker is more than 10 times higher.

	dimension of parameter vector						
tracker	2	3	4	5	7	10	15
CCD	00.00	00.13	00.00	00.00	00.00	00.00	08.38
	0.036	0.053	0.059	0.060	0.080	0.110	0.158
	0.030	0.069	0.042	0.040	0.061	0.106	0.243
Condensation 10,000 samples (RGB)	01.38	07.38	12.63	20.63	38.75	59.50	76.00
	0.664	1.036	1.254	1.362	1.587	1.829	1.956
	0.478	0.640	0.707	0.702	0.691	0.703	0.720
Condensation 10,000 samples (gray values)	03.88	18.75	33.13	49.63	73.63	90.50	94.88
	0.949	1.410	1.595	1.653	1.896	1.836	1.454
	0.612	0.717	0.710	0.720	0.754	0.842	0.836
Condensation 1,000 samples (RGB)	01.13	09.13	19.63	27.63	53.25	75.88	90.38
	0.707	1.118	1.304	1.542	1.889	2.013	2.034
	0.516	0.667	0.669	0.711	0.679	0.705	0.765
Condensation 1,000 samples (gray values)	04.88	25.38	40.75	64.88	87.13	93.25	96.13
	0.975	1.425	1.705	1.719	1.895	1.770	1.583
	0.623	0.713	0.710	0.731	0.761	0.805	0.769
Condensation 100 samples (RGB)	02.88	28.50	45.63	61.63	89.25	92.63	96.50
	0.849	1.380	1.719	1.824	1.923	2.088	1.972
	0.584	0.723	0.691	0.683	0.621	0.734	0.809
Condensation 100 samples (gray values)	08.00	58.75	77.63	93.50	95.88	96.88	96.50
	1.119	1.641	1.880	1.694	1.518	1.836	2.004
	0.657	0.705	0.707	0.867	0.748	0.816	0.815
Condensation 10 samples (RGB)	62.25	87.38	93.63	96.75	97.13	97.88	98.63
	1.261	1.732	1.883	1.479	1.807	1.737	1.955
	0.722	0.752	0.673	0.737	0.870	0.779	0.786
Condensation 10 samples (gray values)	86.38	94.63	94.63	98.13	98.13	98.00	99.13
	1.366	1.774	2.005	1.510	1.687	1.863	1.531
	0.729	0.730	0.659	0.765	0.836	0.795	0.824
Kalman (RGB)	83.38	89.50	90.25	93.50	94.25	95.13	95.50
	1.600	1.640	1.797	1.807	1.758	2.026	1.812
	0.686	0.713	0.729	0.713	0.717	0.789	0.788
Kalman (gray values)	87.50	92.88	94.00	95.00	95.38	95.38	95.50
	1.684	1.679	1.657	1.626	1.763	1.864	1.825
	0.747	0.791	0.764	0.752	0.712	0.755	0.750

Table 5.4: Performance of different trackers over the dimension of the parameter vector. Each cell contains: a) the failure rate in %, b) the mean error in pixels, c) the standard deviation of the error in pixels. The CCD tracker is more than 9 times better in terms of robustness (failure rate) and in terms of accuracy (mean error) than the second best tracker, the condensation tracker with 10,000 samples using RGB values. The performance of the condensation tracker quickly declines with an increasing dimension of the parameter vector.

Sequences A to D

Let us now briefly discuss the four image sequences (A to D) resulting for the most flexible shape, i.e. the shape with 15 degrees of freedom. In sequence A, both image regions are heavily textured. Figure 5.19 (pages 106-107) compares the results of the condensation tracker (RGB, 10,000 samples) and the CCD tracker. The CCD tracker is clearly more robust especially for those images where the two regions have poor contrast.

In sequence B, the background region shows very dark and very bright pixels, see Figure 5.20 on pages 108-109. The condensation tracker fails particularly often in images where salient edges are given that are parallel and close to the correct curve (e.g. images 030 and 130). The CCD tracker reliably works also in these cases.

In sequence C, the background and the foreground are mainly homogeneous. However, in several images the RGB values of the background and the foreground are very similar, see Figure 5.21 on pages 110-111. The CCD tracker copes better with the poor contrast and localizes the curve with more accuracy than the condensation tracker.

For image sequence D, the CCD tracker accurately tracks the curve for all dimensions up to and including dimension 10. However, for dimension 15, the CCD tracker looses track of the curve, see Figure 5.22. Starting in image 134 the error significantly increases. The magnification depicted in Figure 5.23 on page 115 shows the reason for this failure. Since the foreground and the background region have locally the same pixel values, the CCD algorithm fails to accurately estimate the region boundary. The CCD algorithm converges to a wrong salient edge nearby. In the remainder of the image sequence, the CCD tracker does not find the correct boundary anymore.

condensation 10,000 samples (RGB)		CCD
error in pixels: 00.34	image: 000	error in pixels: 00.04
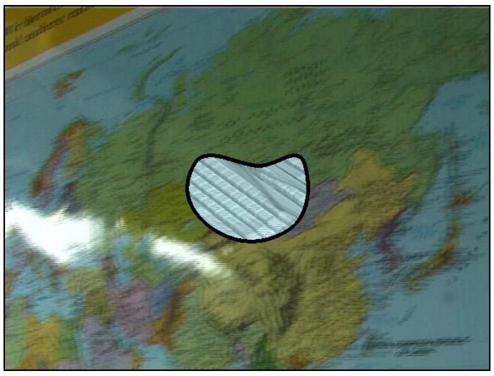		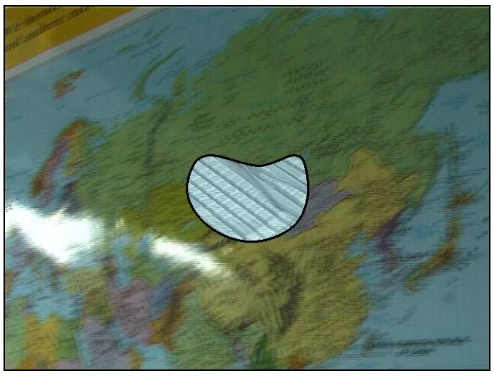
error in pixels: 36.53	image: 030	error in pixels: 00.72
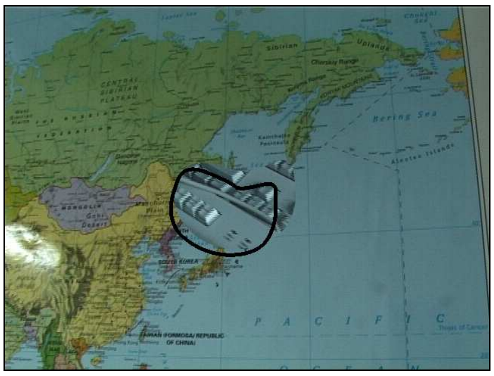		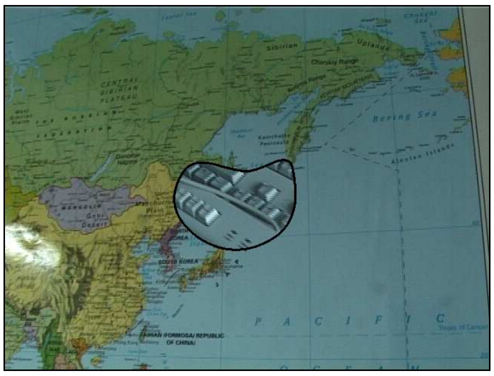
error in pixels: 05.25	image: 050	error in pixels: 00.06
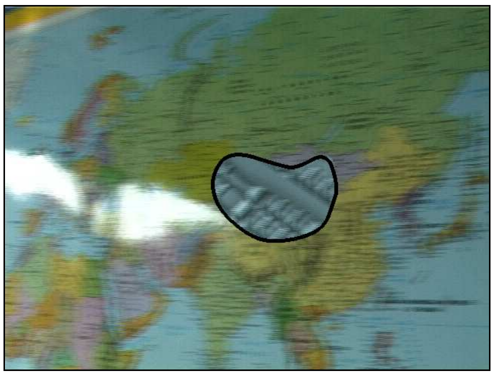		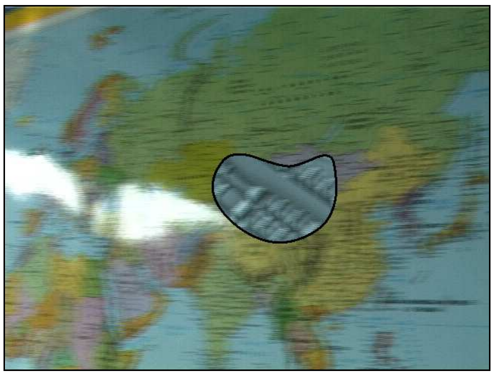

continued on next page

Figure 5.19: Image sequence A (15 dimensions): The CCD tracker accurately tracks the shape even if the contrast between the two regions is poor (e.g. images 030 and 150).

continued from previous page

condensation 10,000 samples (RGB)	CCD
error in pixels: 24.07 image: 100	error in pixels: 00.09
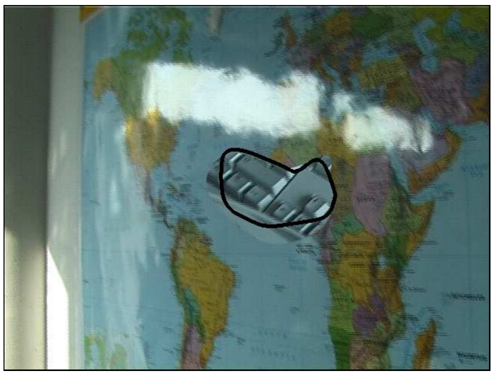	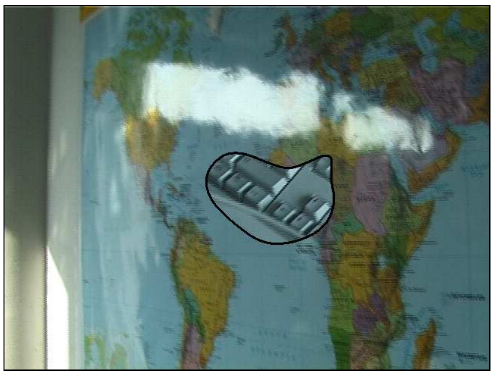
error in pixels: 41.27 image: 150	error in pixels: 00.52
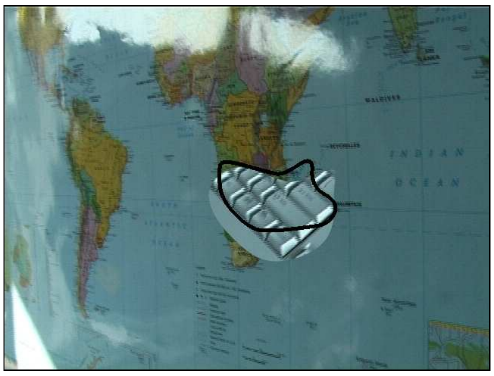	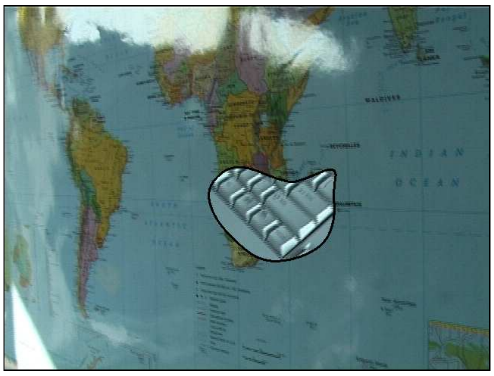
error in pixels: 21.49 image: 199	error in pixels: 00.18
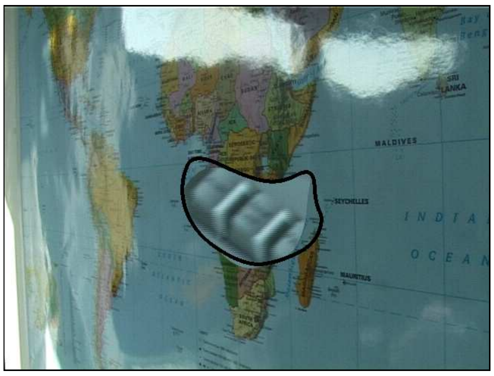	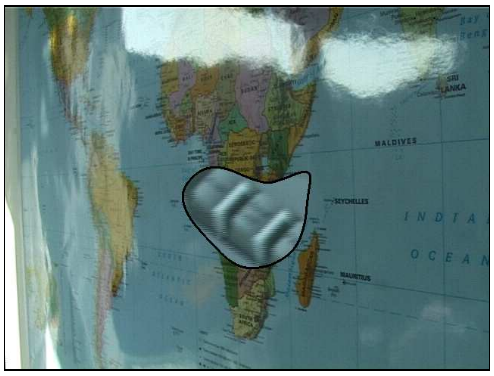

condensation 10,000 samples (RGB)		CCD
error in pixels: 00.43	image: 000	error in pixels: 00.05
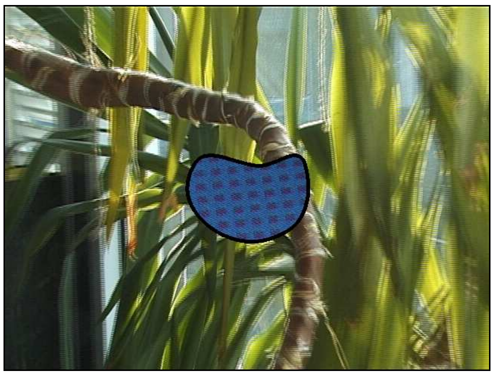		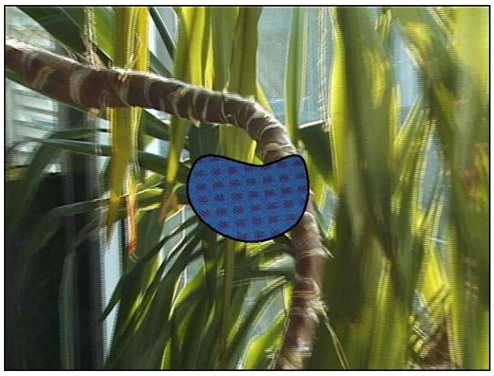
error in pixels: 12.19	image: 030	error in pixels: 00.15
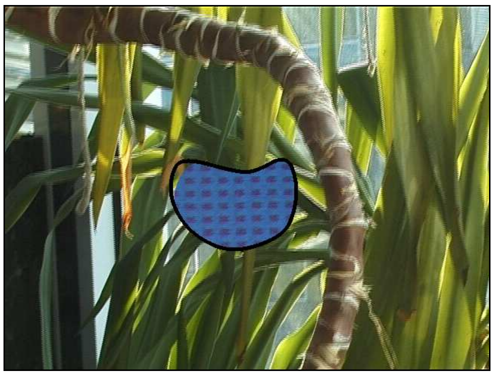		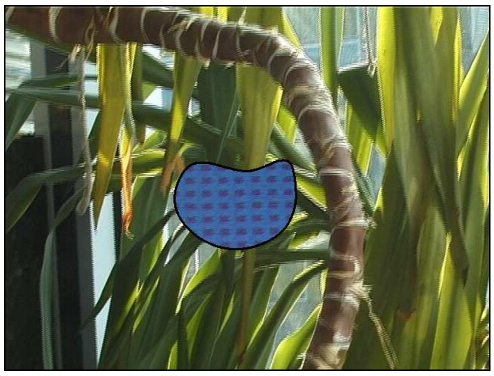
error in pixels: 18.13	image: 070	error in pixels: 00.07
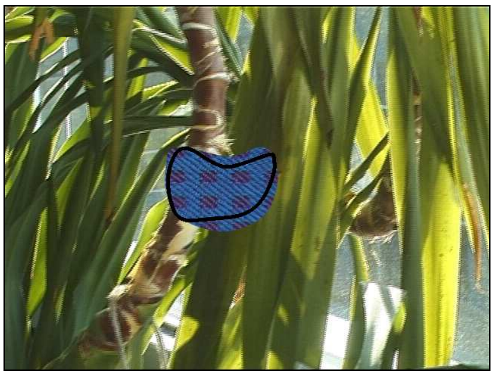		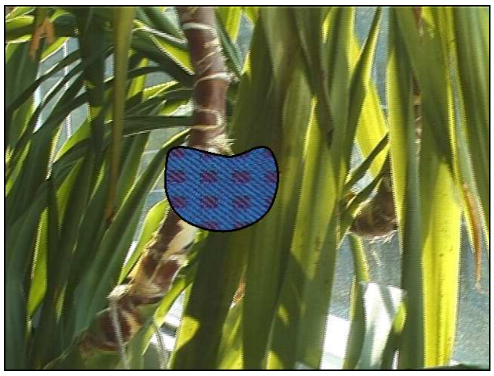

continued on next page

Figure 5.20: Image sequence B (15 dimensions): The CCD tracker is robust against strong edges next to the shape to be tracked (e.g. images 030 and 130).

continued from previous page

condensation 10,000 samples (RGB)	CCD
error in pixels: 26.56 image: 130	error in pixels: 00.07
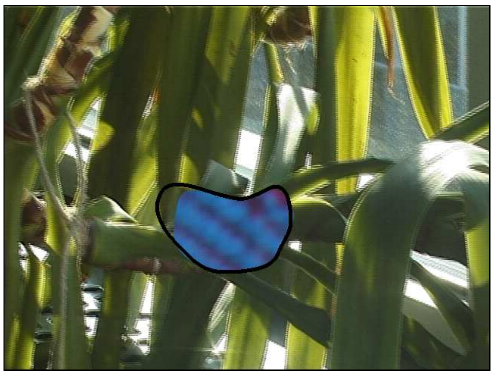	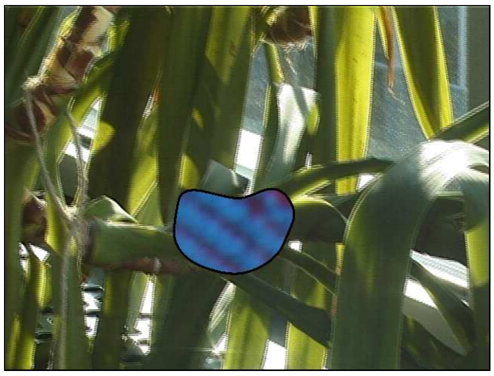
error in pixels: 02.71 image: 170	error in pixels: 00.05
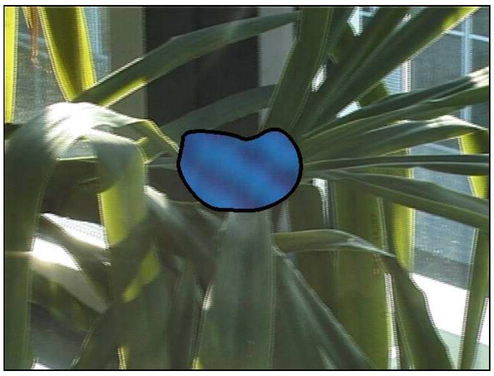	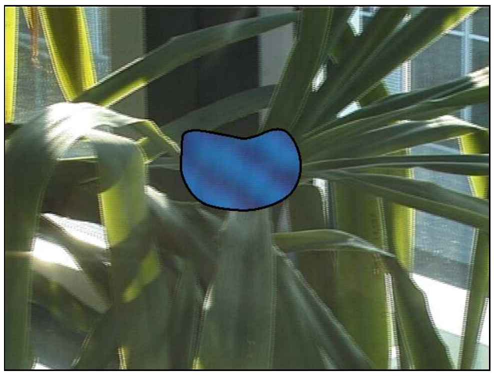
error in pixels: 02.88 image: 199	error in pixels: 00.08
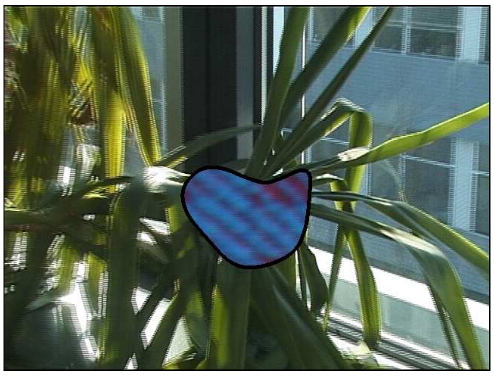	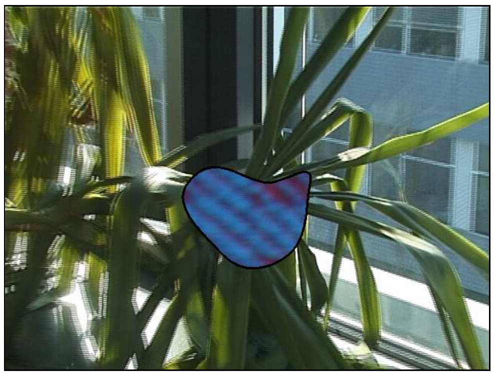

condensation 10,000 samples (RGB)	CCD
error in pixels: 00.38 image: 000	error in pixels: 00.06
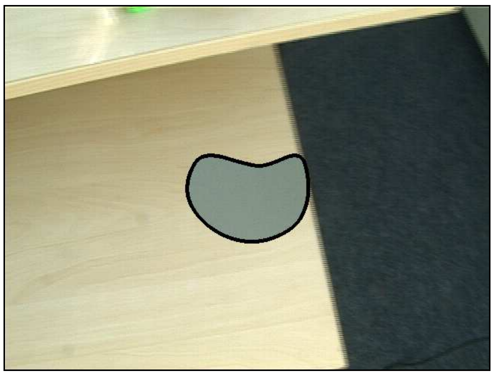	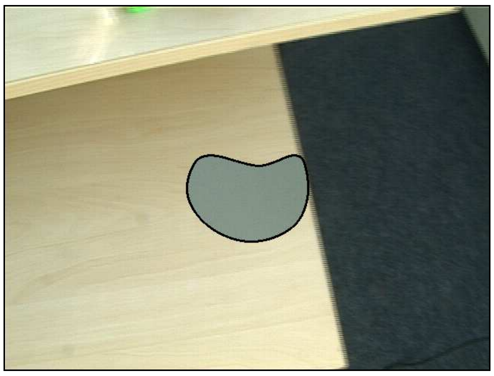
error in pixels: 07.34 image: 080	error in pixels: 00.02
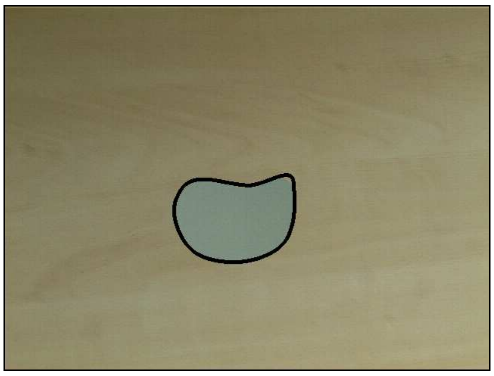	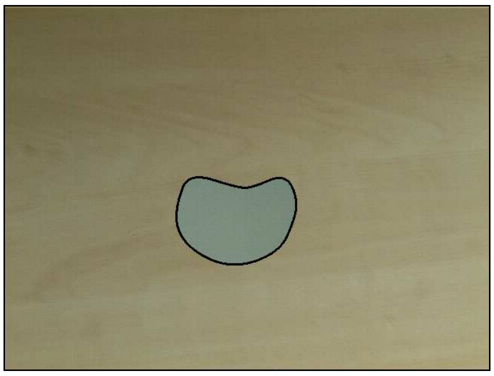
error in pixels: 08.15 image: 090	error in pixels: 00.03
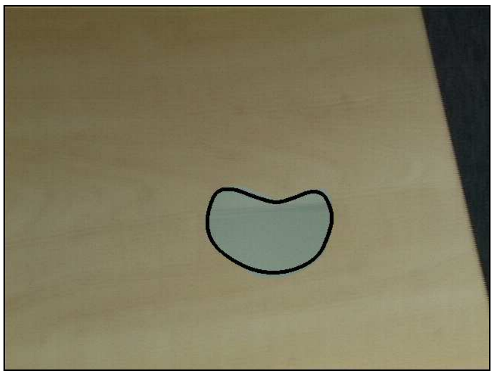	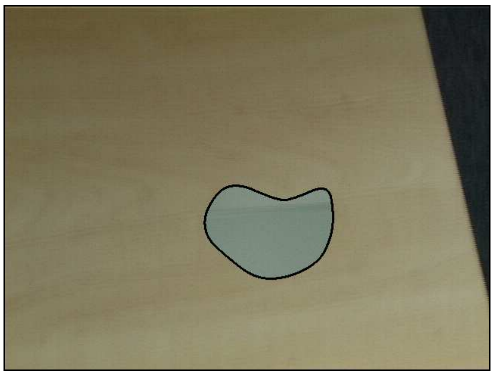

continued on next page

Figure 5.21: Image sequence C (15 dimensions): This sequence has little clutter. However, in some images the contrast is very poor. Again, the CCD tracker is clearly more accurate than the condensation tracker.

continued from previous page

condensation 10,000 samples (RGB)	CCD
error in pixels: 09.17 image: 120	error in pixels: 00.10
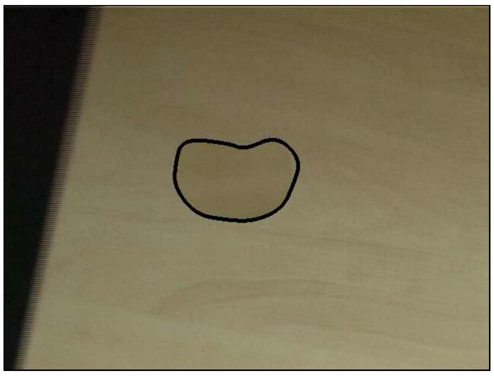	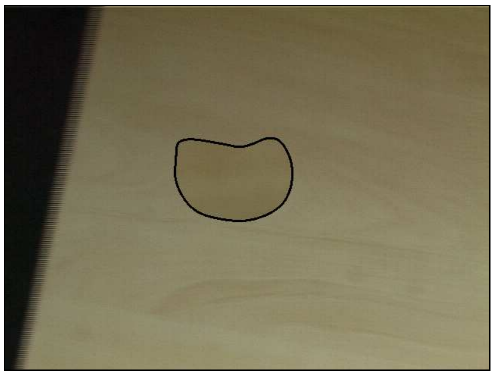
error in pixels: 05.59 image: 160	error in pixels: 00.05
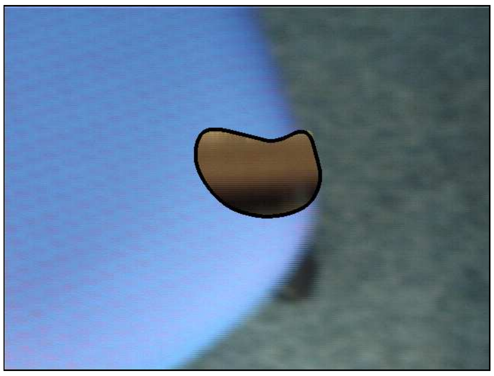	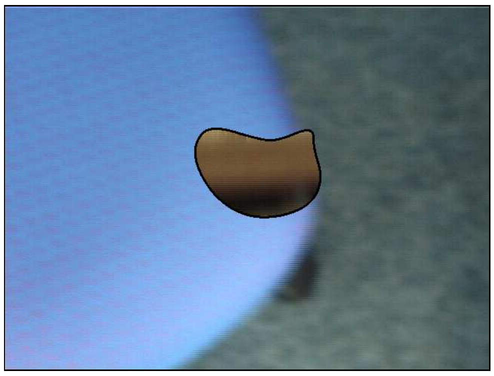
error in pixels: 06.93 image: 199	error in pixels: 00.12
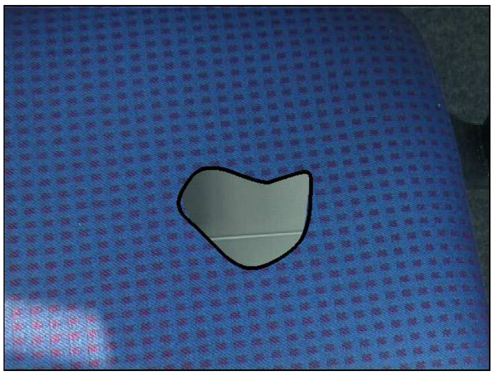	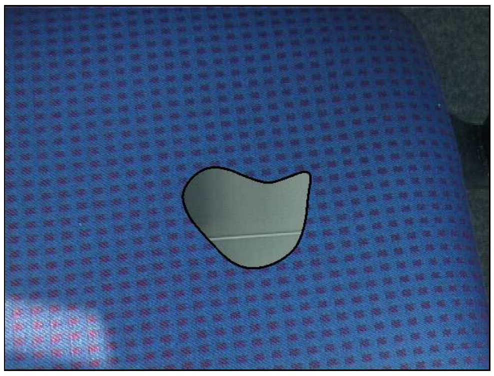

condensation 10,000 samples (RGB)	CCD
error in pixels: 00.34 image: 000	error in pixels: 00.03
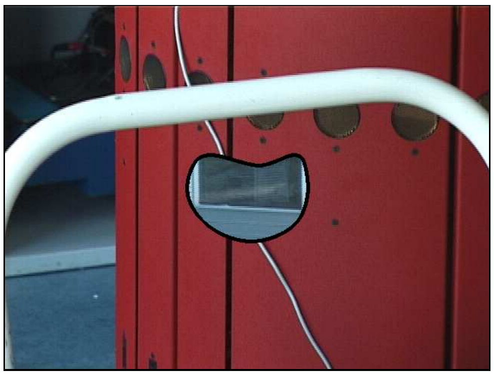	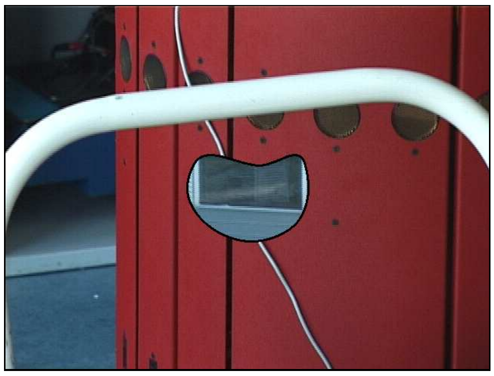
error in pixels: 15.02 image: 030	error in pixels: 00.12
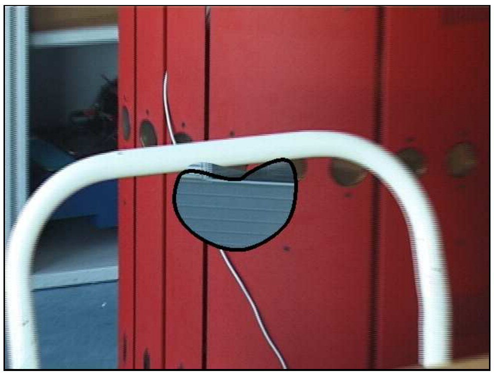	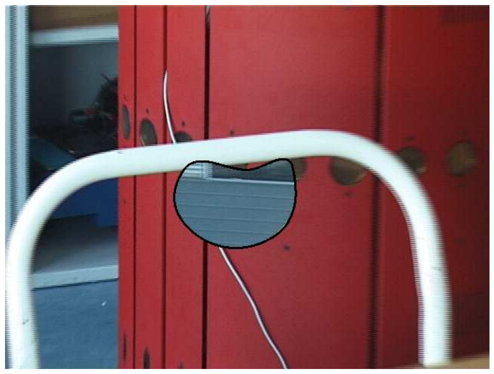
error in pixels: 14.34 image: 090	error in pixels: 00.11
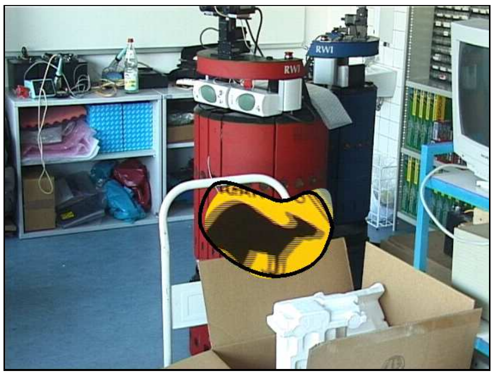	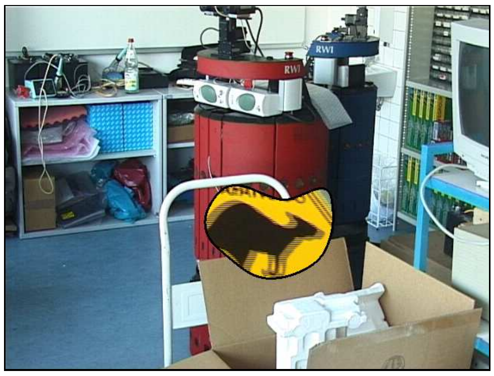

continued on next page

Figure 5.22: Image sequence D (15 dimensions): This is the only sequence out of the 28 image sequences where the CCD tracker fails in keeping track of the shape. Starting in image 134 the error significantly increases. The magnification depicted in Figure 5.23 shows the reason for this failure. In the remainder of the image sequence, the CCD tracker does not recover from this failure.

continued from previous page

condensation 10,000 samples (RGB)	CCD
error in pixels: 07.23 image: 120	error in pixels: 00.10
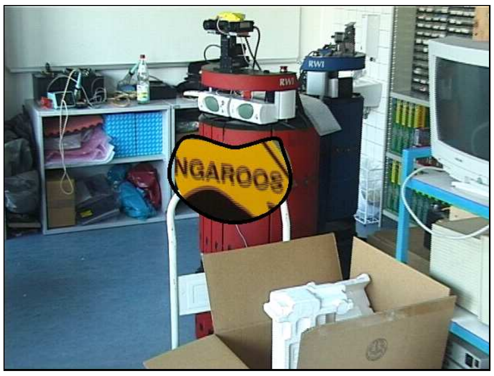	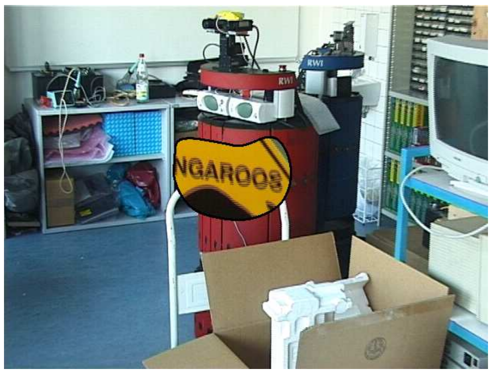
error in pixels: 18.24 image: 133	error in pixels: 0.44
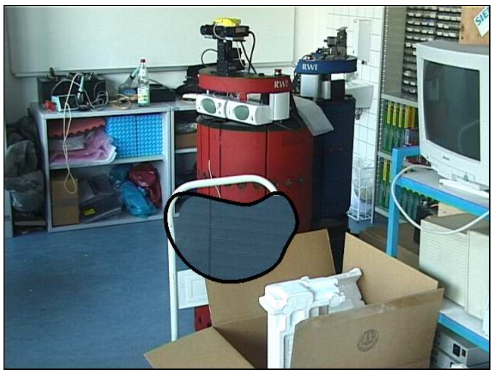	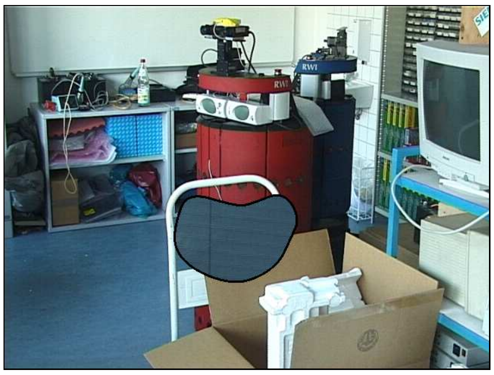
error in pixels: 22.26 image: 134	error in pixels: 03.22
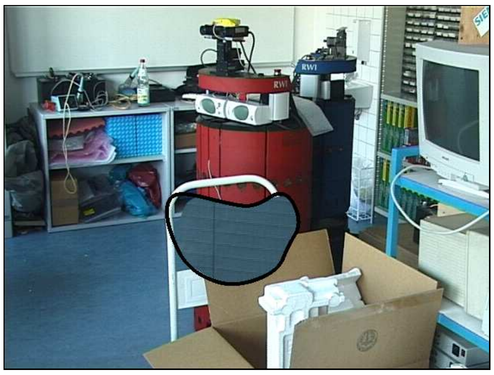	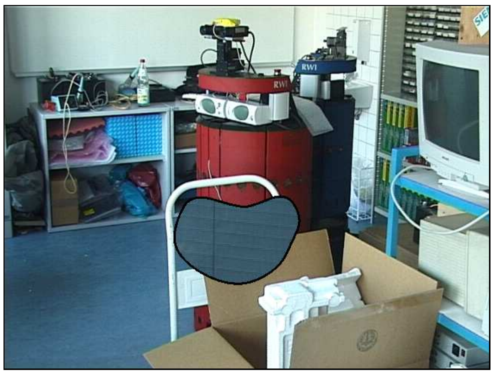

continued on next page

continued from previous page

condensation 10,000 samples (RGB)	CCD
error in pixels: 26.25 image: 135	error in pixels: 07.07
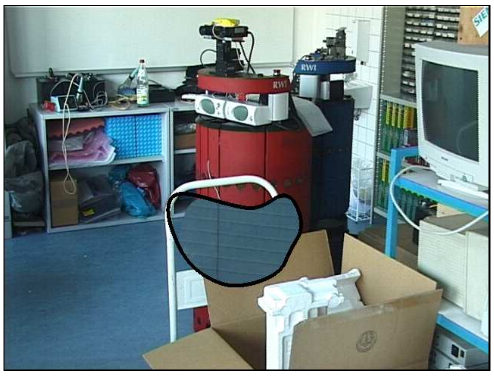	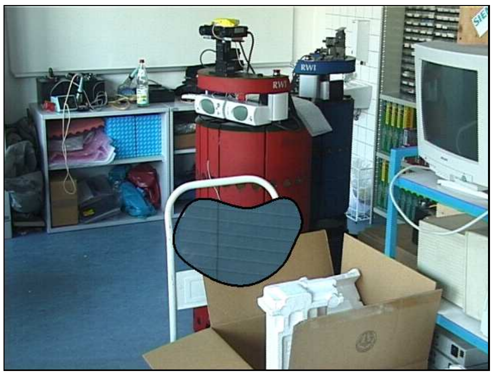
error in pixels: 31.47 image: 136	error in pixels: 13.20
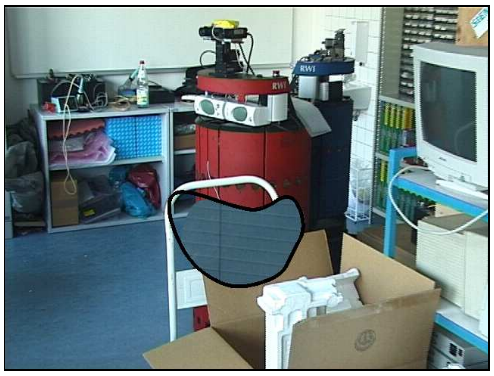	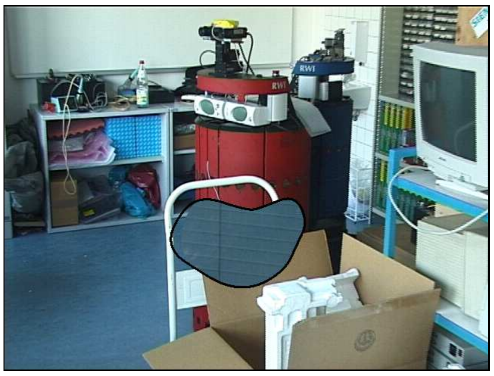
error in pixels: 41.96 image: 140	error in pixels: 29.25
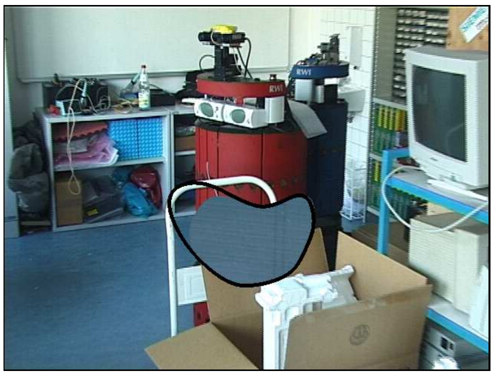	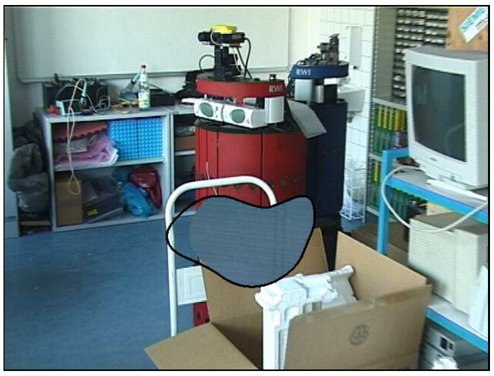

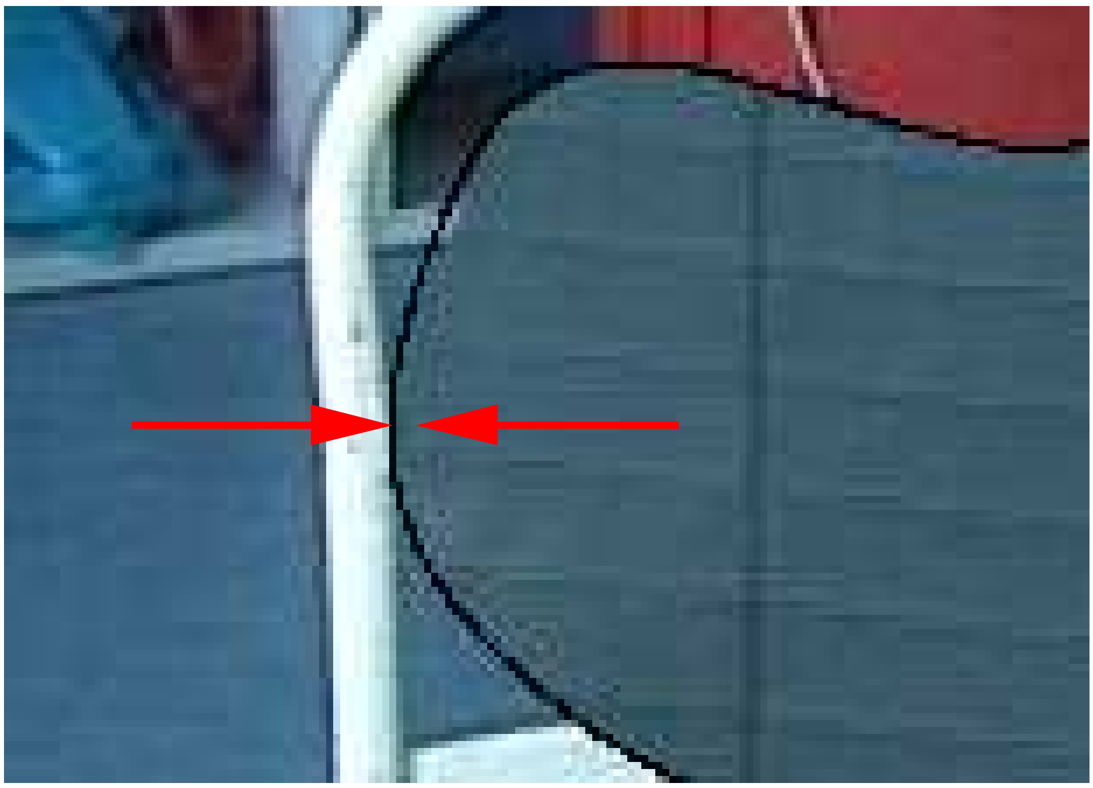

Figure 5.23: Failure of the CCD tracker: The pixels between the arrows belong to the background region. However, their color values fit better to the adjacent foreground region. Hence, the CCD tracker assigns these pixels to the wrong side of the curve. The algorithm converges to the next salient boundary, the edge of the white region. Due to the small error of about 3 pixels, this wrong solution still complies with the motion model.

5.3.3 Results for Real Image Sequences

In this section we evaluate the CCD tracker using real images. In order to obtain a quantitative evaluation of the CCD tracker, at least a rough ground truth is required. For a small number of images, such a ground truth can be provided manually. However, for image sequences consisting of more than hundred images this is hardly feasible. Therefore, we proceed as follows.

We record a non-moving object, a bottle, with a static camera. During recording, we continuously change the background and the illumination of the bottle. Then, for the first image, we manually specify the correct contour of the bottle. Since both the bottle and the camera are fixed, this contour describes the location of the bottle in the entire image sequence. In order to obtain a moving contour, we use rectangular sub-images with changing offsets, i.e. we shift the original images. The offset of the sub-images are random numbers obtained by a 2-D motion model using an AR process according to section 4.2. This yields a sequence of images with a moving contour and a given ground truth. However, the contour does not deform. An arbitrary motion would result in a deforming contour. Therefore, we fit a curve model to the image sequences that also allows for deformations.

As in section 5.3.2, we describe the contour by a shape-space model. We use a *planar affine shape-space*, which has six degrees of freedom, two translation parameters and four parameters defining the deformation (including size and orientation). Appendix B.2 (page 138) gives a description of planar affine shape-spaces. Additionally, we apply curve models with less degrees of freedom. By reducing the number of possible deformations, we obtain less flexible curve models with 2, 3, 4, and 5 degrees of freedom.

Figure 5.24 shows the failure rate of different trackers over the dimension of the parameter vector. The CCD tracker is clearly more robust than the other trackers. For more than three degrees of freedom, the CCD algorithm achieves a 5 to 77 times lower failure rate than the best compared tracker, the condensation tracker with 10,000 samples using RGB values.

Figure 5.25 shows the fitting result for the curve model with 6 degrees of freedom. The first and the third columns contain the results of the condensation tracker (10,000 samples, RGB). The second and fourth columns contain the results of the CCD tracker. The CCD tracker reliably tracks the contour of the bottle despite the heavy changes of the illumination. The condensation tracker is frequently distracted by other edges and finally yields a collapsed contour. Figure 5.26 depicts two images for which the CCD tracker yields exceptionally large errors. Even in these images, the CCD tracker roughly finds the contour of the bottle.

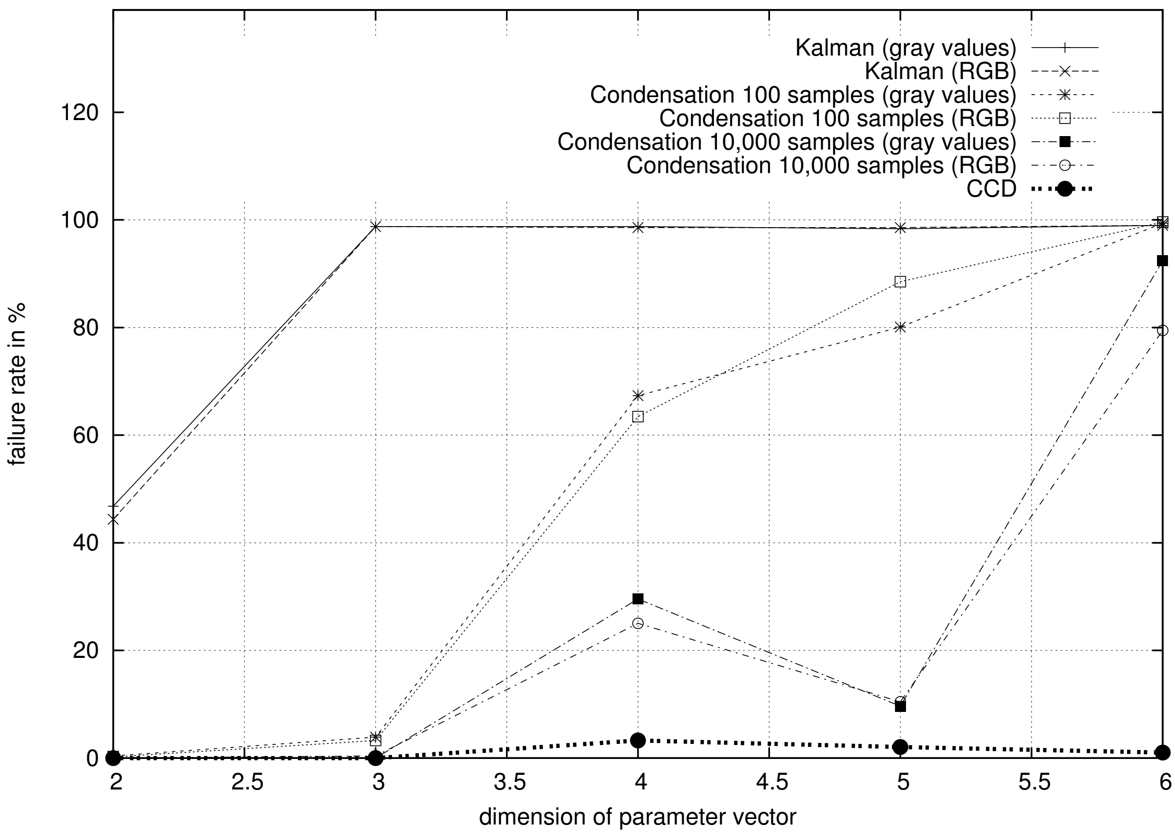

Figure 5.24: Failure rate over the dimension of the parameter vector (bottle sequence): the CCD tracker is clearly more robust than the other trackers. For dimension 4 to 6, the CCD tracker achieves a 5 to 77 times lower failure rate than the best compared tracker.

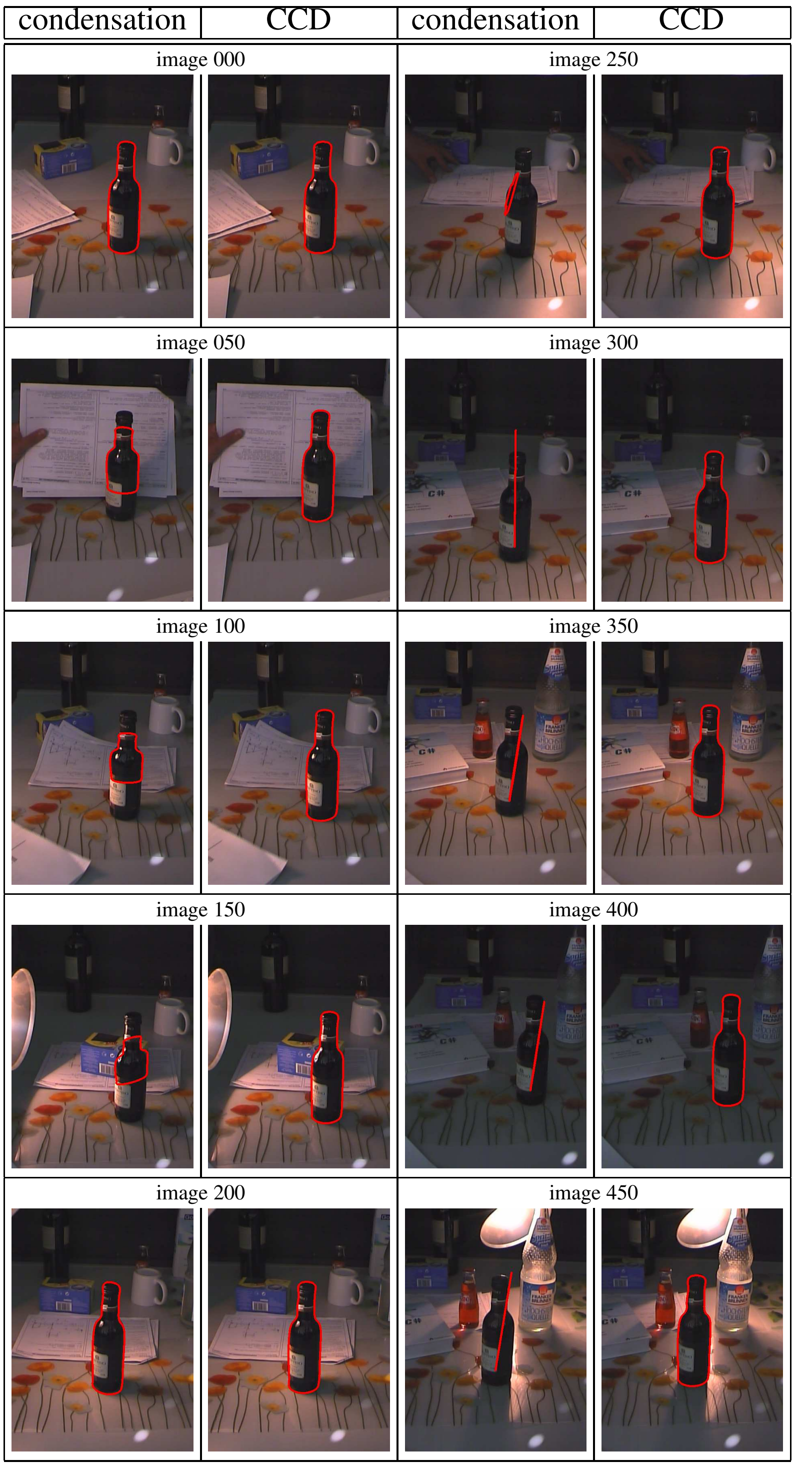

Figure 5.25: Bottle sequence: The background of the bottle and the illumination are constantly changing. Nevertheless, the CCD tracker successfully tracks the contour of the bottle. The condensation tracker converges to wrong edges.

condensation	CCD
image 277	
error: 190.8 pixels	error: 10.2 pixels
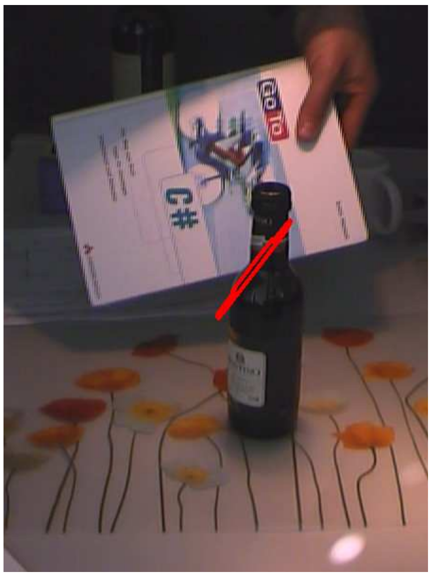	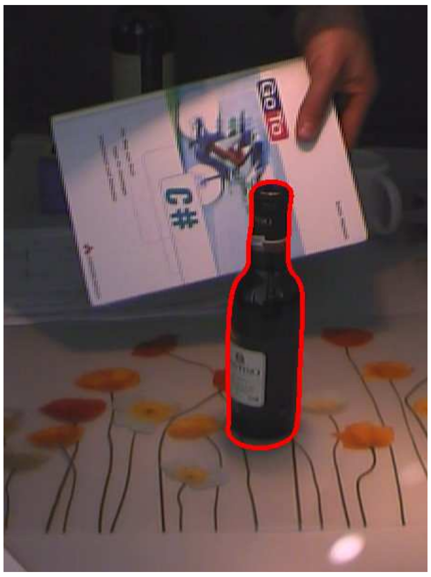
image 222	
error: 5.3 pixels	error: 6.2 pixels
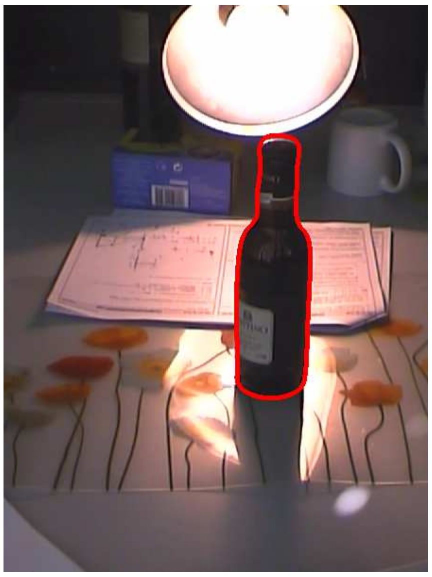	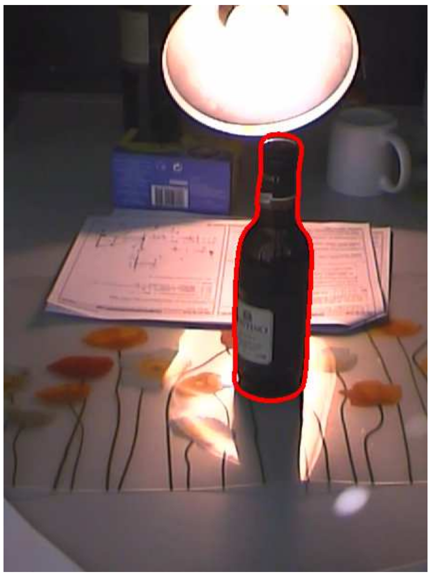

Figure 5.26: For these images, the CCD tracker (right column) yields exceptionally large errors. In image 277, the CCD tracker has difficulties finding the bottom of the bottle due to the shadow and the resulting poor contrast. In image 222, the CCD tracker does not accurately find the lid of the bottle. The tracker converges to the much stronger edge caused by the lamp. In both images, the condensation tracker (left column) has similar or even greater difficulties.

5.4 Summary of the Results

In order to evaluate the CCD algorithm, we performed more than 28,000 individual fits, using different curve models and images, i.e. real and semi-synthetic images. Our experiments show that the CCD algorithm is very robust. For moderate initial errors, the approach converges to the correct solution in 99.8 - 100% of the cases, even in the presence of challenging texture. The CCD algorithm achieves a high level of accuracy; the mean error is 0.0186-0.1088 pixels, depending on the parameterization. Furthermore, the method can process up to 24 images per second on a standard PC if the curve has a small number of parameters. The CCD algorithm allows for a reliable 3-D pose estimation, despite partial occlusion, heavy texture, and poor contrast.

We compared the CCD tracker with other state-of-the-art trackers. For this comparison more than 30 different image sequences and more than 65,000 individual fits were used. Our experiments show that the CCD tracker is clearly more robust than the condensation and the Kalman tracker. The condensation tracker fails in all experiments at least 5 times (often 20 times) more often than the CCD tracker. Furthermore, the CCD tracker is 12 to 22 times more accurate. The runtimes of the trackers depend on the parameterization of the algorithms and on the degrees of freedom of the curve. For a curve with 15 degrees of freedom, the runtime of the CCD tracker is about 5 seconds per image on a 0.5 GHz computer. Given the same runtime, the condensation tracker performs clearly worse in terms of robustness and accuracy. While the CCD tracker is much better at accurately keeping track of the curve, the condensation tracker is better at finding already lost curves.

The CCD tracker and the condensation tracker show different capabilities to take advantage of the continuously increasing computing power. Given a longer runtime, the CCD tracker achieves a substantial improvement in accuracy and robustness. However, the accuracy and the robustness of the condensation tracker increase only very slowly with the number of samples, i.e. with the length of the runtime. Hence, given the rapidly increasing computing power of modern machines, the performance of the CCD tracker improves faster than the performance of the condensation tracker.

Chapter 6

Conclusion

In this thesis, we propose two novel methods for fitting parametric curve models to images: the *Contracting Curve Density (CCD) algorithm* and the *CCD tracker*. The CCD algorithm fits a model curve to a *single* image and the CCD tracker fits a model curve to a *sequence* of images.

The CCD algorithm contributes to the state-of-the-art in two important ways. First, for the assessment of a fit between the curve model and the image data, the CCD algorithm employs a novel *likelihood function* that can cope with highly inhomogeneous image regions. This capability is achieved by formulating the likelihood function in terms of local image statistics that are iteratively learned from the vicinity of the expected curve. The local statistics provide locally adapted criteria for separating adjacent image regions. This replaces often used predefined fixed criteria, relying on homogeneous image regions or specific edge properties, such as a particular edge profile or an image gradient exceeding a preset threshold. The second key contribution is a *blurred curve model*. This is an efficient means for iteratively optimizing the posterior density over possible model parameters. Blurred curve models enable the algorithm to trade-off two conflicting objectives, namely a large area of convergence and a high level of accuracy.

The CCD tracker employs a fast real-time variant of the CCD algorithm. The method yields for each iteration step a runtime complexity that is independent of the image resolution. Hence, it achieves a low runtime even for high-resolution images. The CCD tracker extends the real-time CCD algorithm by exploiting two kinds of statistical dependencies between successive images: dependency between successive shapes and dependency between successive pixel values. By exploiting both kinds of statistical dependencies between successive images, the robustness of the tracking algorithm is substantially increased. We showed how this improvement can be achieved without significantly increasing the runtime.

We applied our methods to several image segmentation, 3-D pose estimation, and object tracking problems. Our experimental analysis demonstrates that the CCD algorithm and the CCD tracker are capable of achieving high sub-pixel accuracy and robustness even in the presence of heavy texture, shading, clutter, partial occlusion, poor contrast, and severe changes of illumination. The mean error of the CCD algorithm is between 0.0186 and 0.1088 pixels, depending on the parameterization of the algorithm. A comparison with different variants of the state-of-the-art condensation tracker and the Kalman tracker shows that the CCD tracker clearly outperforms these trackers. The CCD tracker achieved an at least 5 times (usually more than 20 times) lower failure rate and a 12 to 22 times lower mean error. Furthermore, in non-trivial cases, the CCD tracker proved to be computationally cheaper than the condensation tracker.

Appendix A

Further Results for the Fast CCD Algorithm

In section 5.2.1 we described an experimental evaluation of the fast CCD algorithm using semi-synthetic images. Here, we present further results of these experiments. First, in section A.1, we compare the error histogram of the variant A with the error histograms of variants B-G. Then, in section A.2, we depict the images for which variant F, the variant fitting the star shape, performs exceptionally well or badly.

A.1 Error Histograms

Let us now briefly compare the error histogram of variant A with the error histograms of variants B-G. A detailed description of the different variants is given in section 5.2.1. Figures A.1 and A.2 illustrate, respectively, the error histograms of variant A, i.e. the standard variant, and variant B, i.e. the more accurate variant using four times as many perpendiculars. Variant B achieves a clearly higher accuracy. Only in less than 0.3% of all cases the error of variant B exceeds 0.1 pixels. This is more than 10 times less frequent than for variant A. For variant C, the faster variant, the histogram is relatively flat, see Figure A.3. Errors larger than 0.2 pixels are more than 200 times more likely than for variant A. Figure A.4 shows that variant D, the variant without outlier treatment, yields more often relatively large errors than variant A. Therefore, we recommend to use the outlier treatment proposed in section 3.3.2.4.

The last three variants (E-G) do not correspond to different parameters of the CCD algorithm but to different input data. In variant E the a priori distribution represents a smaller initial uncertainty. The resulting error histogram is depicted in Figure A.5. It is similar to the error histogram of variant A. (However, the areas of convergence differ substantially.) Figure A.6 depicts the error histogram for variant F. In this variant the shape to be extracted is not a circle

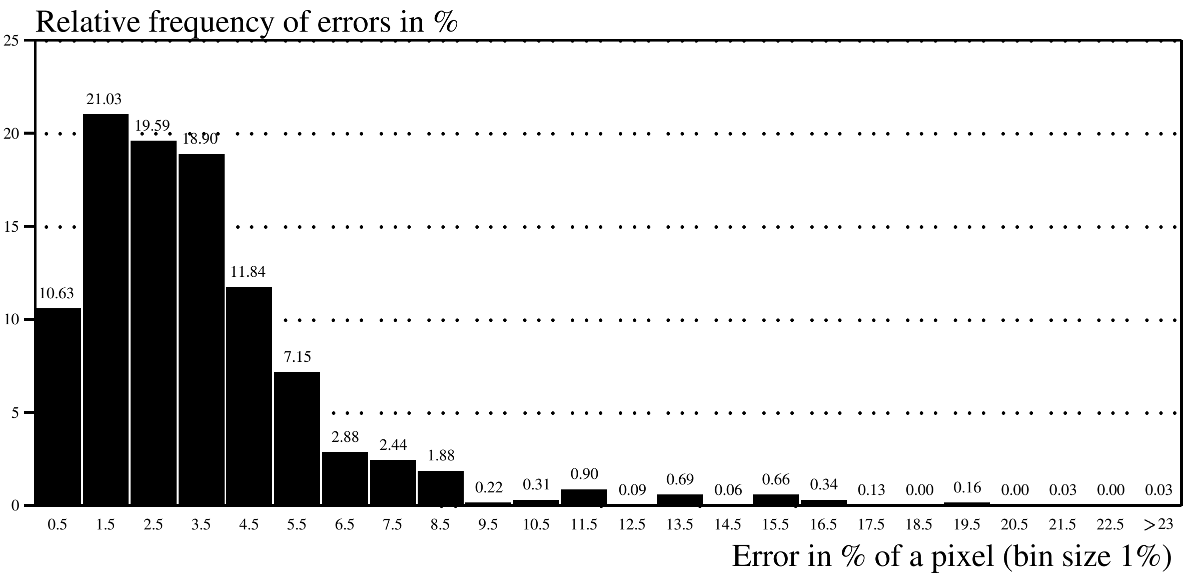

Figure A.1: Error histogram of variant A: For variant A, i.e.the standard variant, in more than 96% of all cases the error is less than 0.1 pixels and in more than 99.9% of all cases the error is less than 0.2 pixels. The mean error is 0.0347 pixels and the standard deviation is 0.0281 pixels.

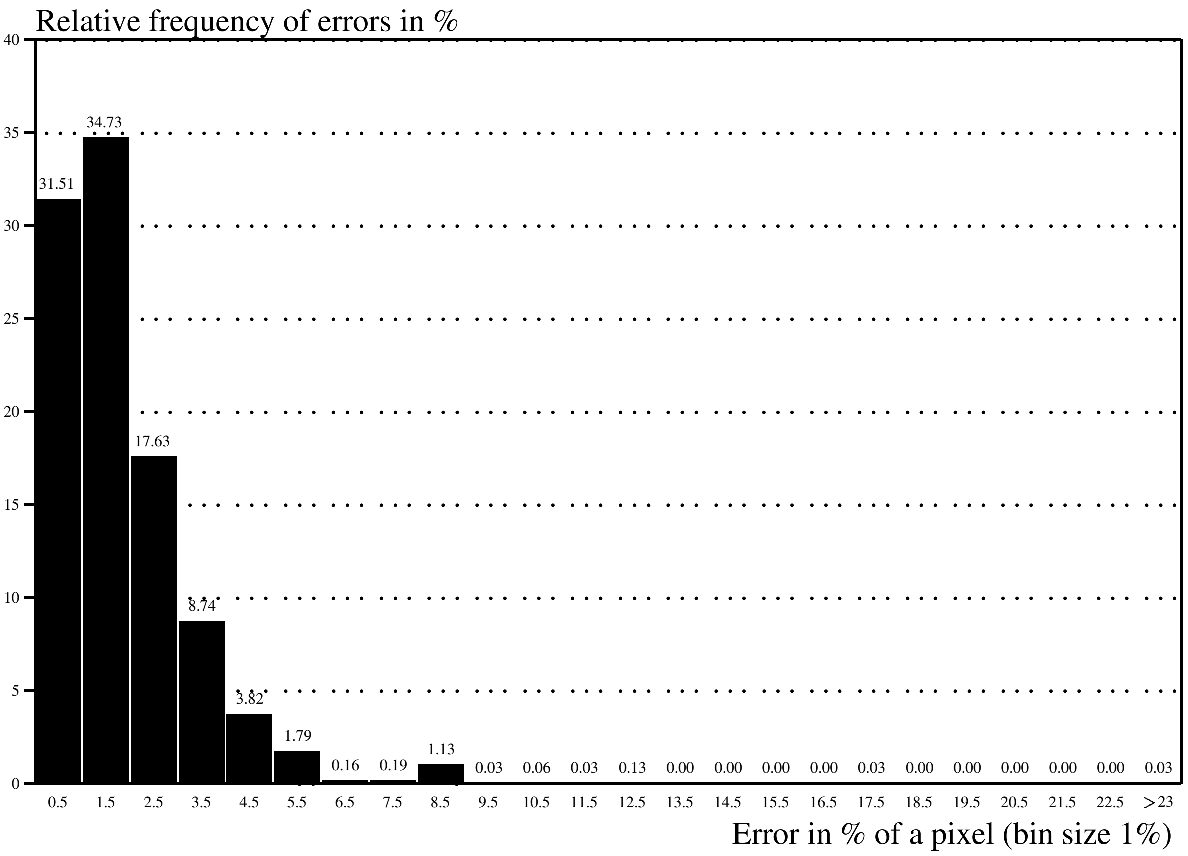

Figure A.2: Error histogram of variant B: For variant B, the more accurate variant, errors exceeding 0.1 pixels are more than 10 times less likely than for variant A. The mean error of variant B is 0.0186 pixels and the standard deviation is 0.0231 pixels.

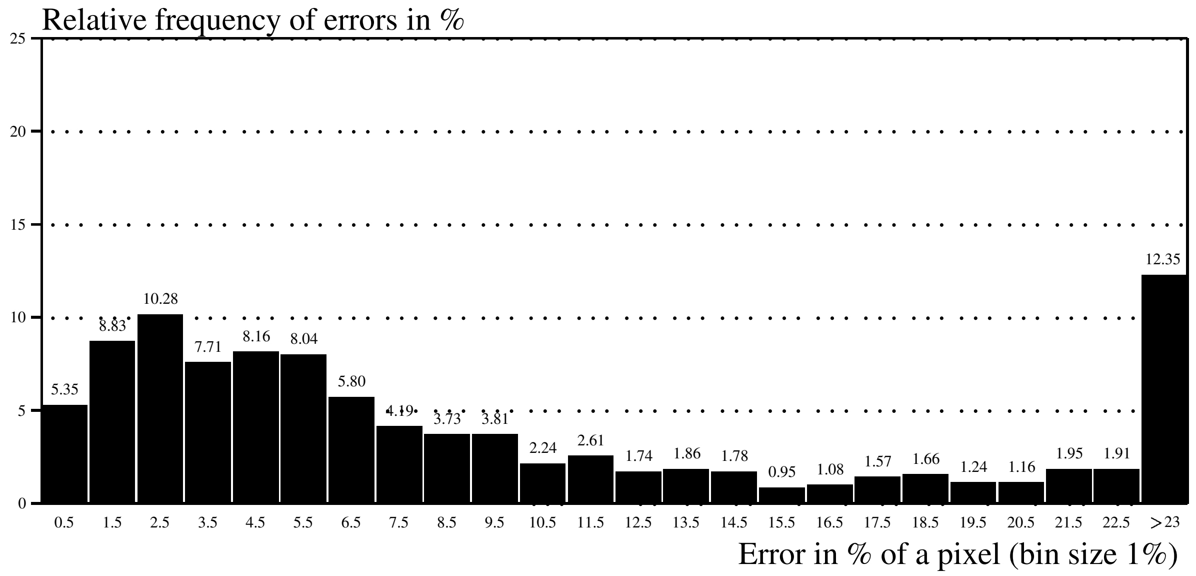

Figure A.3: Error histogram of variant C: For variant C, the faster variant, relatively large errors are clearly more likely than for variant A. For example, errors exceeding 0.2 pixels are more than 200 times more likely than for variant A. The mean error of variant C is 0.1088 pixels and the standard deviation is 0.1236 pixels.

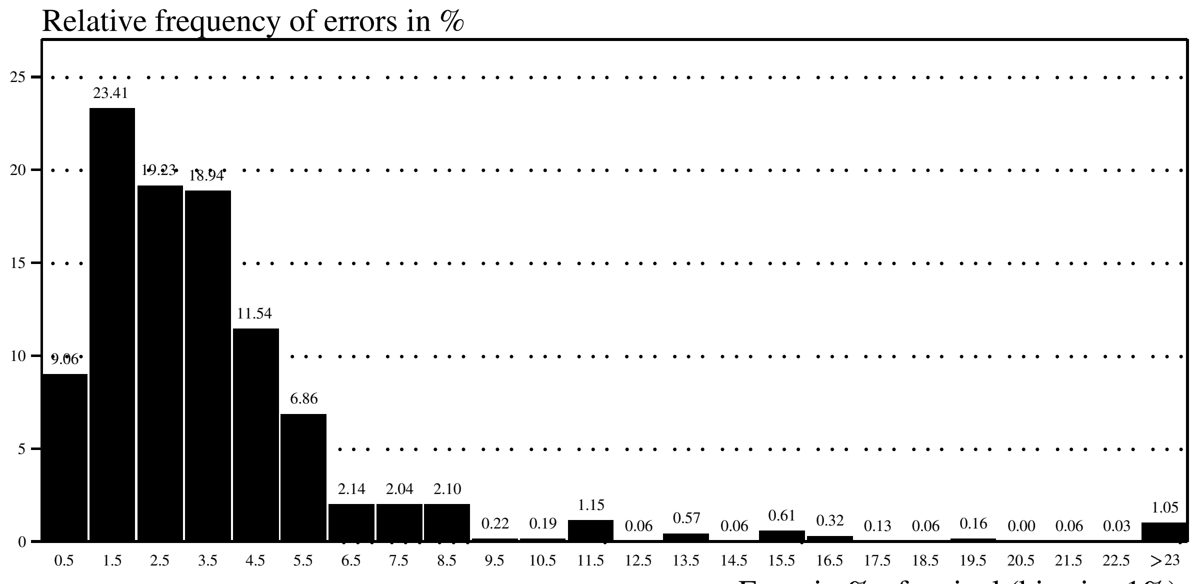

Figure A.4: Error histogram of variant D: In variant D the outlier treatment is switched off. Without outlier treatment, errors larger than 0.2 pixels are about 20 times more likely than with outlier treatment. The mean error of variant D is 0.0354 pixels, only slightly higher than for variant A (0.0347 pixels). However, the standard deviation of 0.0713 pixels is more than 2.5 times higher than those of variant A.

but a star-like shape. (The shape will be depicted in section A.2.) Despite the differences in shape, the errors in variant F and variant A are quite similarly distributed. In variant G the input images are not perfectly sharp but blurred. Figure A.7 depicts the resulting error histogram.

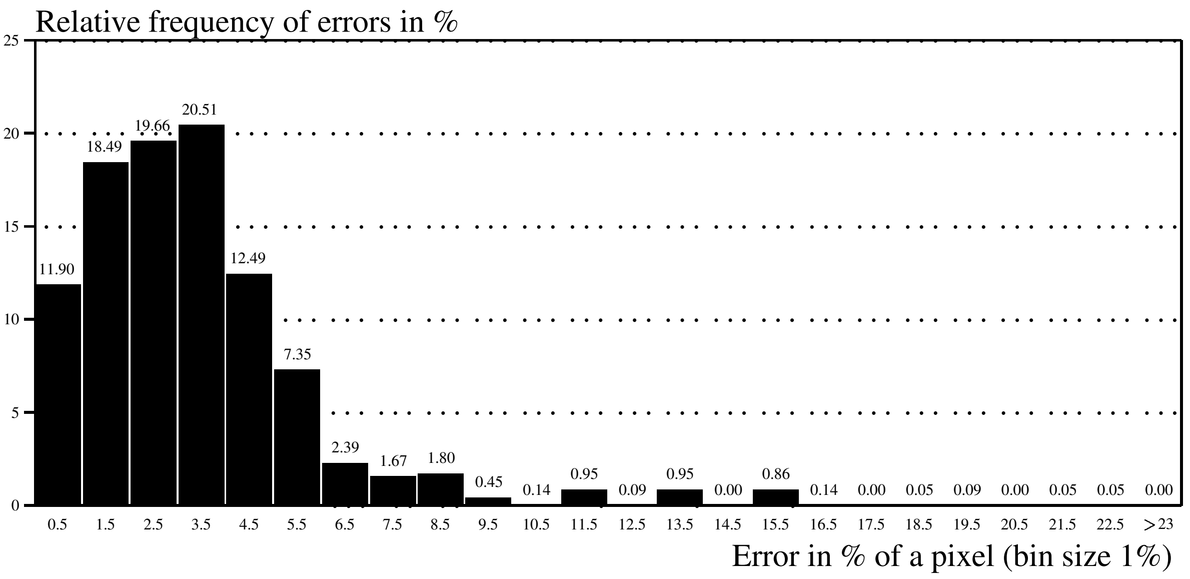

Figure A.5: Error histogram of variant E: For variant E, the variant with a lower initial uncertainty, the error is similarly distributed as for variant A. The mean error of variant E is 0.0342 pixels and the standard deviation is 0.0265 pixels.

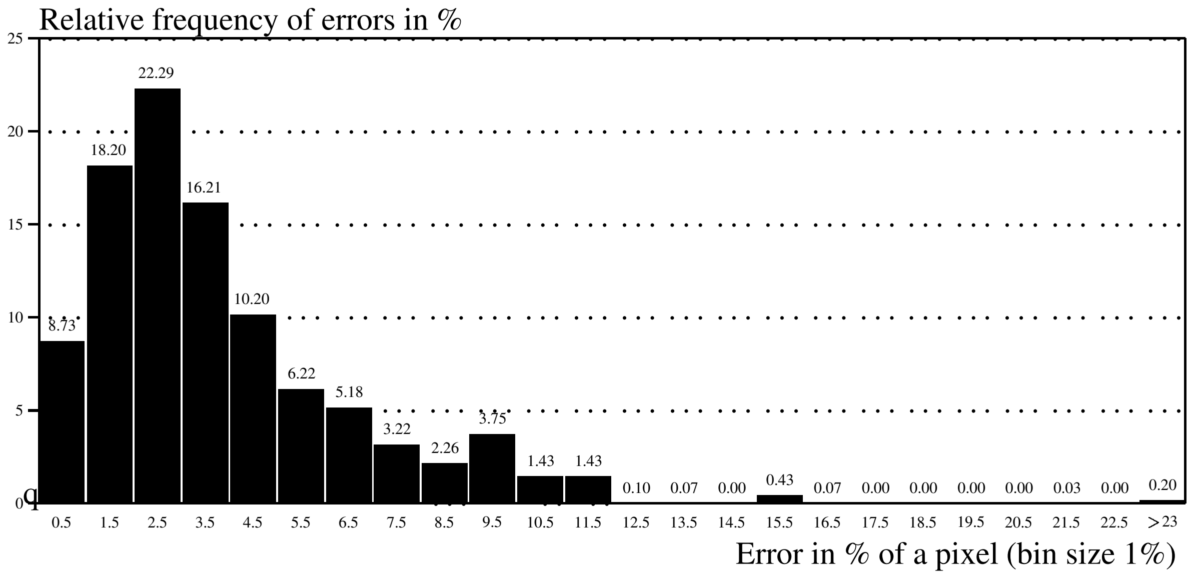

Figure A.6: Error histogram of variant F: In variant F the shape to be extracted has a much higher curvature than in variant A. Nevertheless, the error histograms are relatively similar. The mean error of variant F is 0.0388 pixels and the standard deviation is 0.0292 pixels.

Due to the blurring, very small errors (< 0.01 pixels) are clearly less likely and errors larger than 0.2 pixels are more likely.

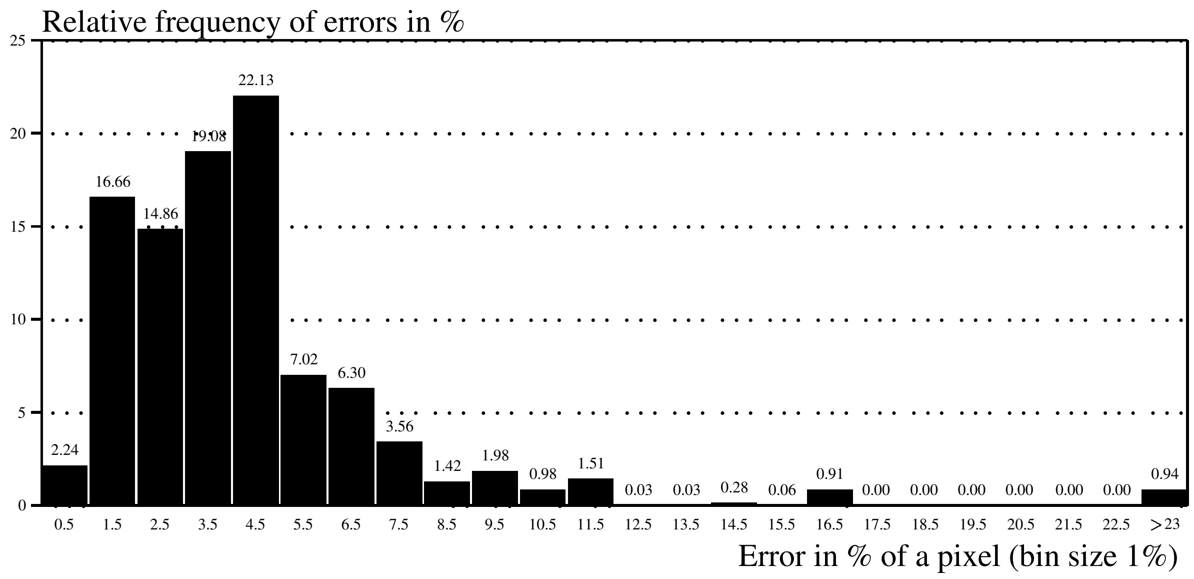

Figure A.7: Error histogram of variant G: For variant G the mask image is blurred using a Gaussian kernel of window size 0.5 pixels. This simulates the blurring caused by an imaging device. Due to the blurring, the mean error increases from 0.0347 pixels to 0.0439 pixels. This is a quite small increase compared to the window size of 0.5 pixels. The standard deviation of the error increases from 0.0281 pixels to 0.0339 pixels.

A.2 Star Shape

This section shows the images for which variant F of the CCD algorithm performs exceptionally well or badly. The following images correspond to the images depicted on pages 84 to 87. However, not the circle but the star-like shape defined by equation (5.3) is used here. Figures A.8 and A.9 depict the images yielding the highest and the lowest failure rate, respectively. For images where the local distributions have much overlap, the failure rate is about three times higher than for images, where the local distributions have little overlap. Figures A.10 and A.11 depict the images yielding the highest and the lowest mean error, respectively.

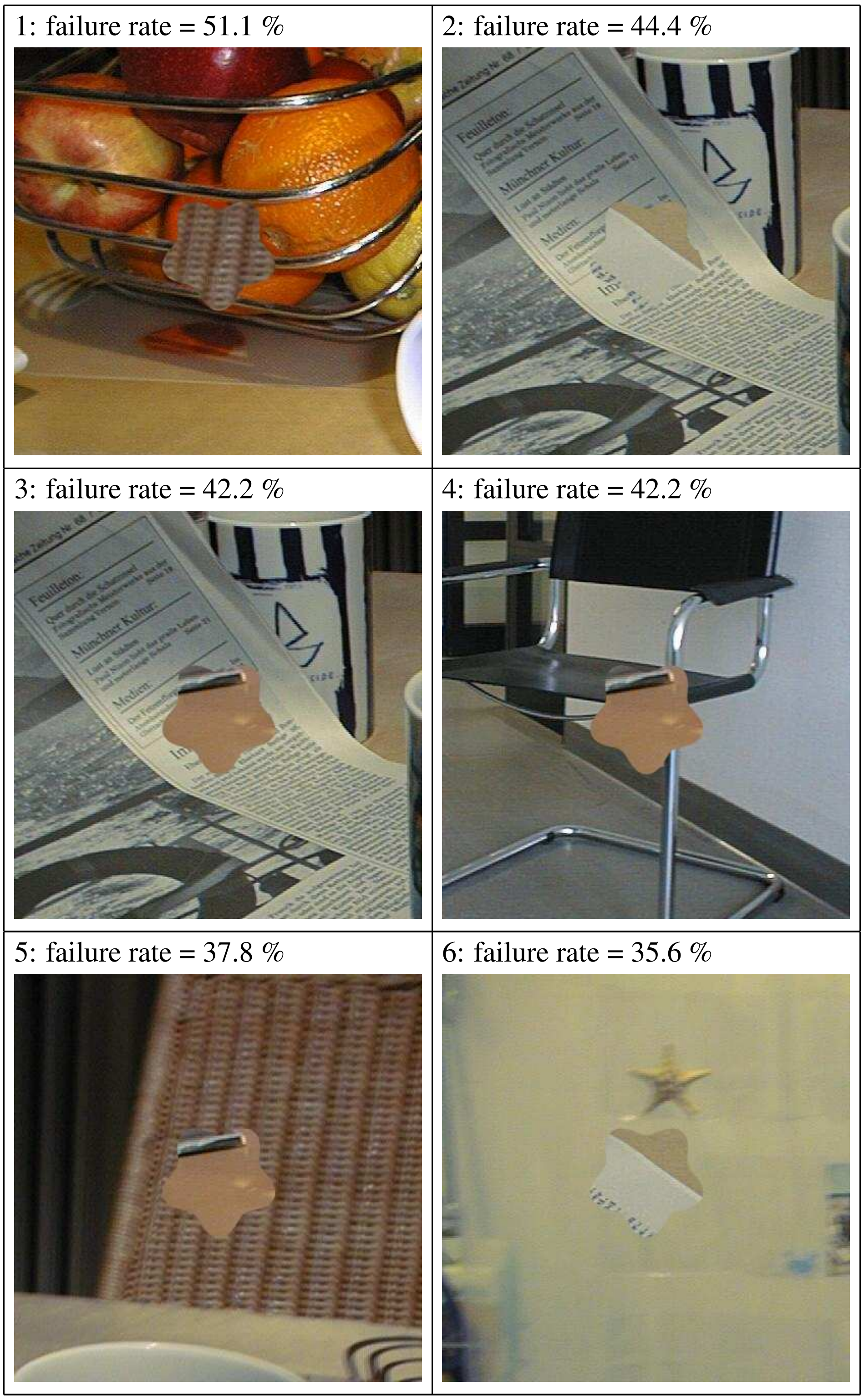

Figure A.8: Images yielding the highest failure rate: In these images, salient edges are given next to the region boundary, or the histograms of the two regions have a significant overlap.

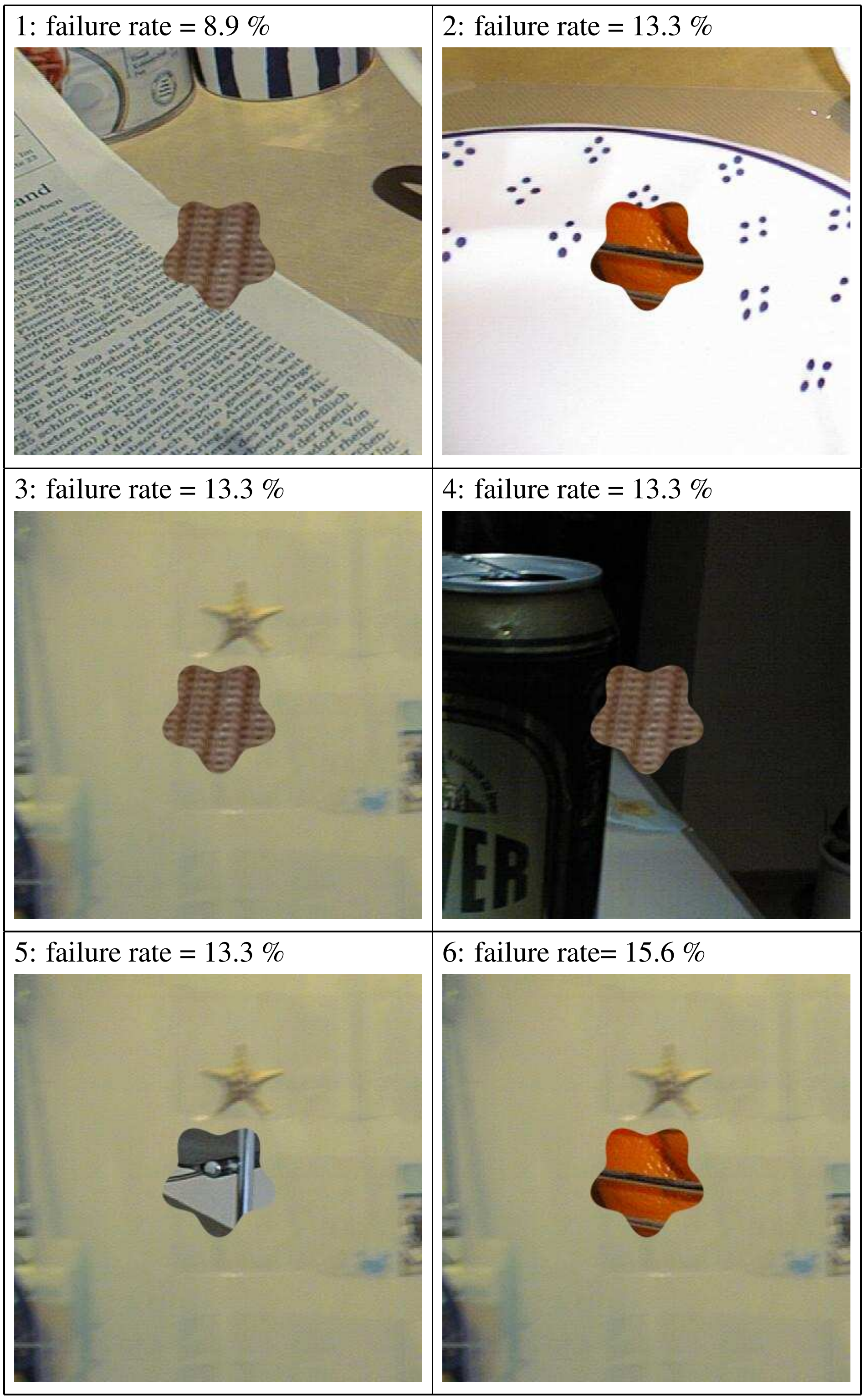

Figure A.9: Images yielding the lowest failure rate: In these images the histograms of the two regions have little overlap.

1: mean error in pixels = 0.1116 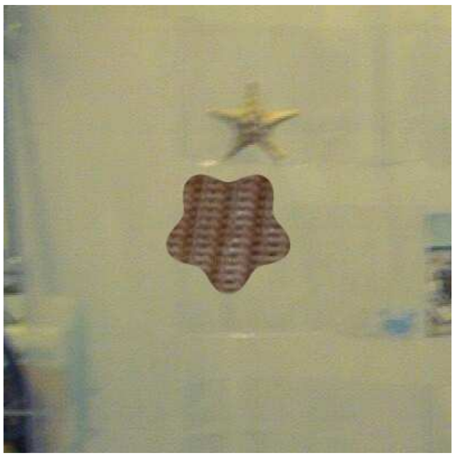	2: mean error in pixels = 0.1092 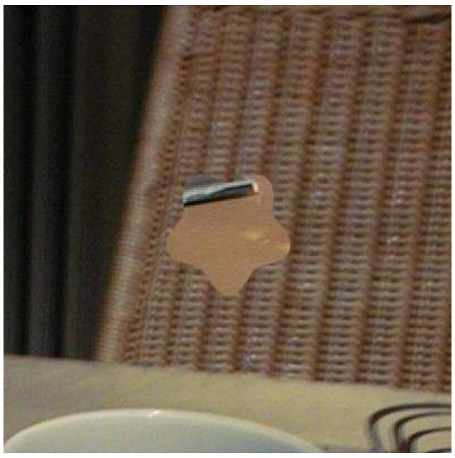
3: mean error in pixels = 0.1091 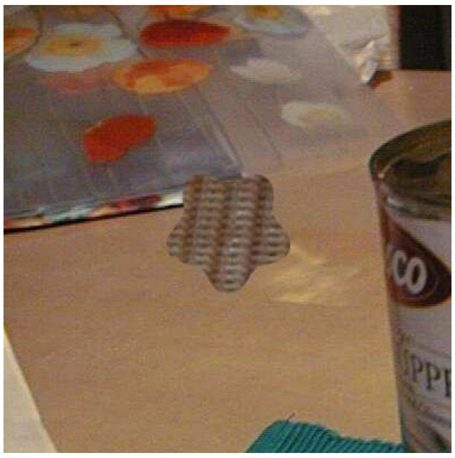	4: mean error in pixels = 0.0915 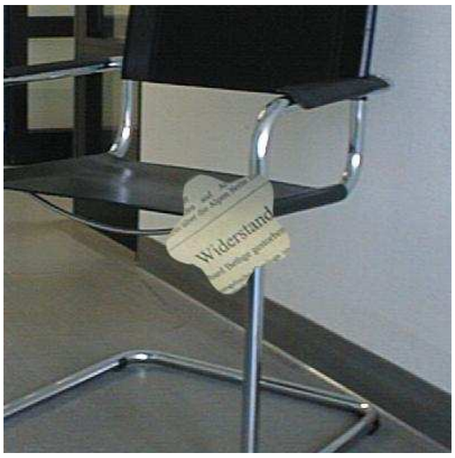
5: mean error in pixels = 0.0905 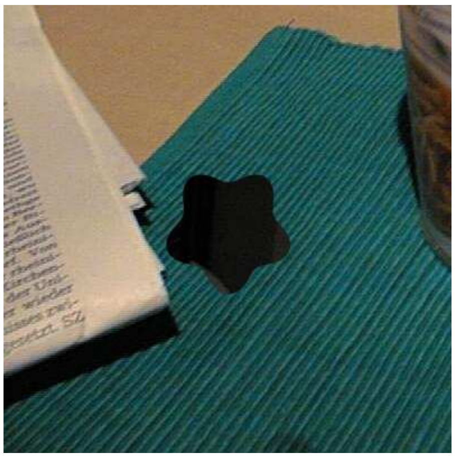	6: mean error in pixels = 0.0883 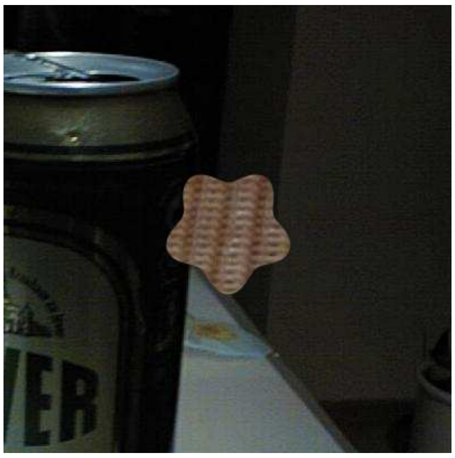

Figure A.10: Images yielding the highest mean error.

1: mean error in pixels = 0.0054

2: mean error in pixels = 0.0093

3: mean error in pixels = 0.0099

4: mean error in pixels = 0.0117

5: mean error in pixels = 0.0135

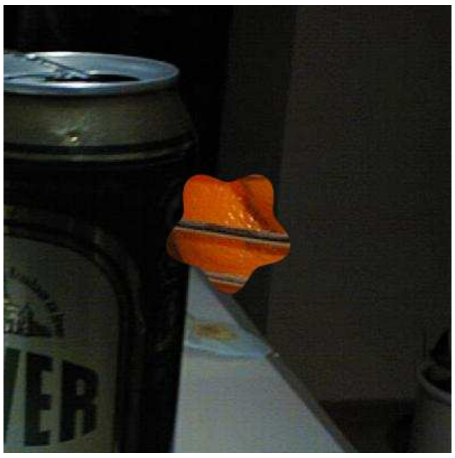

6: mean error in pixels = 0.0139

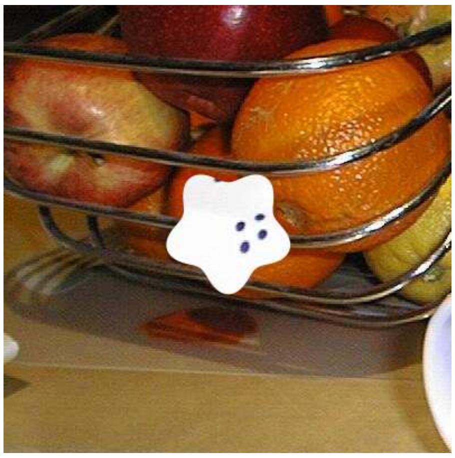

Figure A.11: Images yielding the lowest mean error.

Appendix B

Parametric Curve Models

In this appendix we describe classes of parametric curve models, i.e. curve functions $\mathbf{c}(\omega, \mathbf{\Phi})$, which we employ in our experiments. First, in section B.1, we define image curves as perspective projections of rigid 3-D models. Then, in section B.2, we specify image curves by deformable 2-D models.

B.1 Rigid 3-D Models

In several experiments we estimate the 3-D pose $\mathbf{\Phi}$ of a rigid object by fitting a rigid 3-D model to the image data. For example, the box in Figure 5.11 (page 93) is described by a wire frame model consisting of multiple 3-D line segments. For each of the line segments a different curve function $\mathbf{c}$ is used. The curve function is obtained by two steps. First, a point on the 3-D line segment is computed, and then the 3-D point is projected onto the image. Let us start with the projection. For this step we use a pinhole camera model.

Pinhole Camera Model

Here, we describe the relation between a point on the 3-D curve given in object coordinate $\mathbf{P}_O$ and its corresponding projection given in pixel coordinates $\mathbf{c}$. For this projection, we apply the *pinhole camera model* , e.g. (Niemann, 1990; Faugeras, 1993). The relation is established in four steps: First, the object coordinates are transformed into camera coordinates. Second, the 3-D camera coordinates are projected onto the image plane. Third, radial distortions caused by the lens are modeled. Finally, the radially distorted coordinates are converted into pixel coordinates.

Rigid Transformation

The object coordinates $\mathbf{P}_O$ are transformed into camera coordinates $\mathbf{P}_C$ using the rigid transformation

$$\mathbf{P}_C = \mathbf{R} \cdot (\mathbf{P}_O - \mathbf{T}). \tag{B.1}$$

The vector $\mathbf{T} = (T_x, T_y, T_z)^T$ specifies the location of the camera, i.e. the position of the optical center, in object coordinates. The 3×3 rotation matrix $\mathbf{R}$ describes the rotation between the object and the camera coordinate system. A 3×3 rotation matrix has only three degrees of freedom. Several compact representations of a rotation have been proposed, see e.g. (Faugeras, 1993; Shoemake, 1994). We represent a rotation by three Euler angles $(r_x, r_y, r_z)^T$. The rotation matrix $\mathbf{R}$ can be written as the product of three individual rotations:

$$\mathbf{R} = \mathbf{R}_x(r_x) \cdot \mathbf{R}_y(r_y) \cdot \mathbf{R}_z(r_z). \tag{B.2}$$

Each of the matrixes $\mathbf{R}_x(r_x)$, $\mathbf{R}_y(r_y)$, and $\mathbf{R}_z(r_z)$ defines a rotation about one axis. The three Euler-angels $(r_x, r_y, r_z)^T$ specify the angle of the respective rotation. The three rotation matrixes are given by

$$\mathbf{R}_x(r_x) = \begin{pmatrix} 1 & 0 & 0 \\ 0 & \cos(r_x) & -\sin(r_x) \\ 0 & \sin(r_x) & \cos(r_x) \end{pmatrix} \tag{B.3}$$

$$\mathbf{R}_y(r_y) = \begin{pmatrix} \cos(r_y) & 0 & \sin(r_y) \\ 0 & 1 & 0 \\ -\sin(r_y) & 0 & \cos(r_y) \end{pmatrix} \tag{B.4}$$

$$\mathbf{R}_z(r_z) = \begin{pmatrix} \cos(r_z) & -\sin(r_z) & 0 \\ \sin(r_z) & \cos(r_z) & 0 \\ 0 & 0 & 1 \end{pmatrix}. \tag{B.5}$$

A rigid transformation is compactly represented by the parameter vector $\mathbf{\Phi}$

$$\mathbf{\Phi} = (T_x, T_y, T_z, r_x, r_y, r_z)^T, \tag{B.6}$$

which consists of the three elements of the translation vector and the three Euler-angles.

Perspective Projection

The relation between a 3-D point with camera coordinate $\mathbf{P}_C = (c_x, c_y, c_z)^T$ and its perspective projection $\mathbf{u}$ onto the image plane is given by

$$\mathbf{u} = \begin{pmatrix} u_x \\ u_y \end{pmatrix} = \frac{f}{c_z} \begin{pmatrix} c_x \\ c_y \end{pmatrix}, \tag{B.7}$$

where f is the focal length of the camera. Due to occlusion, the projection $\mathbf{u}$ may not be visible in the image. To deal with the problem of occlusion, for general objects, additional machinery is needed, which is beyond the scope of this dissertation. In our experiments we use convex objects that allow for an efficient solution to the occlusion problem.

Radial Distortions

The lens of the camera may cause *radial distortions* of the image. The relation between the undistorted coordinates $\mathbf{u} = (u_x, u_y)^T$ and the corresponding distorted image coordinates $\mathbf{v} = (v_x, v_y)^T$ can be approximated by

$$\mathbf{v} = \begin{pmatrix} v_x \\ v_y \end{pmatrix} = \frac{2}{1 + \sqrt{1 - 4\kappa(u_x^2 + u_y^2)}} \begin{pmatrix} u_x \\ u_y \end{pmatrix}, \tag{B.8}$$

where the distortion parameter κ describes the shape and intensity of the radial distortions. Some authors use two or even more parameters in order to describe the radial distortions, e.g. (Niemann, 1990).

Transformation into Pixel Coordinates

The pixel coordinates $\mathbf{c}$ are obtained from the radially distorted image coordinates $\mathbf{v} = (v_x, v_y)^T$ by

$$\mathbf{c} = \begin{pmatrix} v_x/S_x + C_x \\ v_y/S_y + C_y \end{pmatrix}, \tag{B.9}$$

where the step sizes S_x and S_y represent the size of the pixels. The point $(C_x, C_y)^T$ specifies the intersection between the optical axis of the camera and the image plane.

Equations (B.1) to (B.9) define the relation between a 3-D point (given in object coordinates $\mathbf{P}_O$) and its projection onto the image plane (given in pixel coordinates $\mathbf{c}$). By proj we denote the resulting projection function which holds

$$\mathbf{c} = \text{proj}(\mathbf{P}_O, \mathbf{\Phi}). \tag{B.10}$$

Projecting Polyhedral Objects

Based on the projection function, 2-D projections of polyhedral wire frame models can by obtained. The points **P** on a straight model line segment are defined by

$$\mathbf{P}(\omega) = \mathbf{P}_1 \cdot (1-\omega) + \mathbf{P}_2 \cdot \omega, \tag{B.11}$$

with $\omega \in [0,1]$. The points $\mathbf{P}_1$ and $\mathbf{P}_2$ are the end points of the line segment given in object coordinates. The curve function $\mathbf{c}(\omega, \mathbf{\Phi})$ corresponding to the 3-D line segment is given by

$$\mathbf{c}(\omega, \mathbf{\Phi}) = \text{proj}(\mathbf{P}(\omega), \mathbf{\Phi}). \tag{B.12}$$

Projecting Cylinders and Spheres

We model the mug depicted in Figure 1.2 as a cylinder and the ball depicted in Figure 4.1 as a sphere. For these object a slightly different procedure is required, since the occluding edges do not correspond to 3-D model curves but rather to surfaces. The contour of the sphere corresponds to a 3-D circle of tangent points. The tangents are defined by the optical center of the camera and the sphere. We first determine the 3-D circle of tangent points using the pose parameters. Then we project the 3-D circle onto the image, see (Hanek et al., 2002b) for more details. For the cylinder we use a similar approach. The computation of occluding lines of a cylinder has been addressed in (Hanek, Navab, and Appel, 1999).

B.2 Deformable 2-D Models

In this section, we describe a class of deformable 2-D models called *shape-space models*. This representation of curves is used by Blake and Isard (1998). We apply this representation in order to compare the CCD tracker with the condensation and the Kalman tracker, see section 5.3. The following review of shape-space models is adapted from Blake and Isard (1998).

Shape-space models define parametric curves $\mathbf{c}(\omega) = (x(\omega), y(\omega))^T$ as a pair of two parametric B-spline functions, one for the x-coordinate and one for the y-coordinate.

B-spline Functions

A B-spline function $x(\omega)$ is constructed as a weighted sum of N_B *basis functions* $B_n(\omega)$, $n \in \{0, ..., N_B - 1\}$:

$$x(\omega) = \sum_{n=0}^{N_B-1} x_n B_n(\omega), \tag{B.13}$$

where x_n are the weights applied to the respective basis function $B_n(\omega)$. This can be written compactly in matrix notation as

$$x(\omega) = \mathbf{B}(\omega)^T \mathbf{Q}^x, \tag{B.14}$$

where the vector $\mathbf{Q}^x$ is composed of the weights x_n

$$\mathbf{Q}^x = (x_0, x_1, ..., x_{N_B - 1})^T \tag{B.15}$$

and $\mathbf{B}(\omega)$ is a vector of basis functions

$$\mathbf{B}(\omega) = (B_0(\omega), B_1(\omega), ..., B_{N_B-1}(\omega))^T. \tag{B.16}$$

We use quadratic basis functions as described in (Blake and Isard, 1998).

Spline Curve

A spline curve $\mathbf{c}(\omega)$ is defined as a pair of two spline functions

$$\mathbf{c}(\omega) = (x(\omega), y(\omega))^T. \tag{B.17}$$

The spline functions $x(\omega)$ and $y(\omega)$ denote the pixel coordinates of the curve point $\mathbf{c}(\omega)$. A curve point $\mathbf{c}(\omega)$ can be expressed compactly in matrix notation:

$$\mathbf{c}(\omega) = \mathbf{U}(\omega)\mathbf{Q}. \tag{B.18}$$

The *spline-vector* $\mathbf{Q}$ consists of the weights of the two spline functions, first the weights of the x-coordinate, then the weights of the y-coordinate:

$$\mathbf{Q} = (\mathbf{Q}^x, \mathbf{Q}^y)^T. \tag{B.19}$$

The matrix $\mathbf{U}(\omega)$ contains twice the basis functions $\mathbf{B}(\omega)$, once for each coordinate:

$$\mathbf{U}(\omega) = \begin{pmatrix} \mathbf{B}(\omega)^T & \mathbf{0} \\ \mathbf{0} & \mathbf{B}(\omega)^T \end{pmatrix}. \tag{B.20}$$

Definition of Shape-space Models

A shape-space is a linear mapping of the curve parameters $\mathbf{\Phi}$ to a spline-vector $\mathbf{Q}$:

$$\mathbf{Q} = \mathbf{W}\mathbf{\Phi} + \mathbf{Q}_0. \tag{B.21}$$

In the context of shape-space models, the vector of curve parameters $\mathbf{\Phi}$ is called *shape-space vector* and the $N_Q \times D_{\mathbf{\Phi}}$ matrix $\mathbf{W}$ is called *shape-matrix*. The vector $\mathbf{Q}_0$ is a *template vector* defining a standard or template curve. The shape matrix $\mathbf{W}$ and the shape-space vector $\mathbf{\Phi}$ define *linear* variations of the template. Usually, the dimension N_Q of the shape-space vector $\mathbf{\Phi}$ is clearly smaller than the dimension of the spline-vector $\mathbf{Q}$. Hence, the shape-space vector $\mathbf{\Phi}$ represents the curve in a more compact manner than the spline-vector $\mathbf{Q}$ does.

Based on the desired variations different shape matrixes $\mathbf{W}$ are used. The planar affine shape-space, which is used in Figure 5.25, has six degrees of freedom. It is given by the shape-matrix

$$\mathbf{W} = \begin{pmatrix} \mathbf{1} & \mathbf{0} & \mathbf{Q}_0^x & \mathbf{0} & \mathbf{0} & \mathbf{Q}_0^y \\ \mathbf{0} & \mathbf{1} & \mathbf{0} & \mathbf{Q}_0^y & \mathbf{Q}_0^x & \mathbf{0} \end{pmatrix}, \tag{B.22}$$

where the vector $\mathbf{0}$ consists of N_B zeros and the vector $\mathbf{1}$ consists of N_B ones. The vectors $\mathbf{Q}_0^x$ and $\mathbf{Q}_0^y$ contain the x-coordinates and the y-coordinates, respectively, of the template vector $\mathbf{Q}_0$. The shape matrix $\mathbf{W}$ allows for translation (horizontal and vertical), scaling (horizontal, vertical, and diagonal), and rotation of the template.

Note that the shape-space, i.e. the shape-matrix $\mathbf{W}$ and the template vector $\mathbf{Q}_0$, can also be learned from characteristic training images using principle component analysis (Blake and Isard, 1998). The resulting model is similar to a Point Distribution Model (PDM) proposed by Cootes et al. (1993). The curve model used in Figure 5.13 is based on such a PDM.

Appendix C

Remarks on the Implementation

The CCD algorithm and the CCD tracker are implemented in C++ on an off-the-shelf PC running Windows NT. Our implementation is optimized for versatility and not for speed. We apply the library LEDA (http://www.mpi-sb.mpg.de/LEDA/leda.html) which uses double precision. By using a less general implementation and single precision, presumably a substantial speed-up can be achieved.

Glossary of Notation

SYMBOL	MEANING	see page
$\widehat{x}$	an *estimate* of the quantity x	
$\widetilde{x}$	a *prediction* of the quantity x	
^{T}	superscript denoting vector / matrix transpose	
*	superscript denoting input data	7,21
$\mathbf{\Phi}$	model parameter vector to be estimated	7,22
$\mathbf{m_\Phi}$	mean vector of $\mathbf{\Phi}$	22
$\mathbf{\Sigma_\Phi}$	covariance matrix of $\mathbf{\Phi}$	22
$\mathit{\Phi}$	state-vector, a pair of two successive parameter vectors	61
$\mathbf{m}_{\mathit{\Phi}}$	mean vector of $\mathit{\Phi}$	61
$\mathbf{\Sigma}_{\mathit{\Phi}}$	covariance matrix of $\mathit{\Phi}$	61
$\mathbf{I}^*$	pixel values (image data)	21
$\mathbf{c}$	curve function	22
ω	parameter specifying a point on the image curve	22
$\mathbf{a}_v$	probabilistic assignment of pixel v to one side of the curve	27
A_v	photosensitive area of pixel v	27
$D_{\mathbf{\Phi}}$	dimension of the model parameter vector $\mathbf{\Phi}$	27
$D_{\mathbf{I}^*}$	dimension of the pixel value (number of channels of the image)	75
σ_v^2	variance of the curve point next to pixel v	29
$\mathbf{n}_v$	unit normal vector to the curve at the curve point closest to pixel v	28
v	a pixel in the vicinity of the image curve $\mathbf{c}$	27
$\mathcal{V}$	set of pixels in the vicinity of the image curve $\mathbf{c}$	29
$\mathbf{S}$	local statistics (mean vector and covariance matrix) of the pixel values	32
s	side of the curve, $(s \in \{1, 2\})$	32
w	weight of a pixel used for computing local image statistics $\mathbf{S}$	32

continued on next page

SYMBOL	**MEANING**	**see page**
d	displacement to the expected curve	30
$d^{=}$	position along the expected curve	30
χ^2	objective function be be optimized	43
$\mathbf{J}$	Jacobian matrix of the curve or the objective function	28,47
$\mathbf{H}$	Hessian matrix of the objective function	47
(i)	number of the iteration	47
$\mathbf{C}_k$	intersection between perpendicular k and the mean curve	55
k	perpendicular on the curve	55
l	index indicating a pixel on a perpendicular k	55
L	maximum number of pixels per perpendicular	55
K	number of perpendiculars	55
$\mathbf{M}$	local statistical moments of the pixel values obtained from one image	37
$\mathbf{m}$	moments of the pixel values for one perpendicular	57
$\widehat{\mathbf{m}}$	moments $\mathbf{m}$ accumulated over time	62
$\widetilde{\mathbf{m}}$	moments $\widehat{\mathbf{m}}$ predicted (propagated) over time	64
$\widetilde{\mathbf{M}}$	predicted moments $\widetilde{\mathbf{m}}$ smoothed along the curve	69
$\widehat{\mathbf{M}}$	moments combining predicted moments and moments of the latest image	71
o	order of the moments, $(o \in \{1, 2, 3\})$	39
t	time	60
W_s	function evaluating the relation between a pixel and the curve	33
$W^{=}$	function evaluating the distance along the curve	33
λ	parameter specifying the window size for blurring along the curve	35, 68
$\mathbf{A}$	deterministic coefficient matrix in discrete dynamical model	60
$\mathbf{B}$	stochastic coefficient matrix in discrete dynamical model	60
$\mathbf{w}(t)$	motion noise of frame t	60

Bibliography

Aggarwal, J.K. and Q. Cai (1999). Human motion analysis: A review. *Computer Vision and Image Understanding* 73(3): 428–440.

Aider, O. A., P. Hoppenot, and E. Colle (2002). A Model to Image Straight Line Matching Method for Vision-Based Indoor Mobile Robot Self-Location. In *Proc. of the IEEE/RSJ Int. Conf. on Intelligent Robots and Systems*, Lausanne, pp. 460–465.

Amini, A.A., T.E. Weymouth, and R.C. Jain (1990). Using dynamic programming for solving variational problems in vision. *IEEE Transactions on Pattern Analysis and Machine Intelligence* 12(9): 855–867.

Azarbayejani, A., T. Starner, B. Horowitz, and A.P. Pentland (1993). Visually controlled graphics. *IEEE Transactions on Pattern Analysis and Machine Intelligence* 15(6): 602–605.

Baker, S., S.K. Nayar, and H. Murase (1998). Parametric feature detection. *International Journal of Computer Vision* 27(1): 27–50.

Ballard, D. H. (1981). Generalizing the hough transform to detect arbitrary shapes. *Pattern Recognition* 13(2): 111–122.

Bar-Shalom, Y. and T. Fortmann (1988). Tracking and data association. Academic Press.

Beck, J. V. and K. J. Arnold (1977). *Parameter Estimation in Engineering and Science*. John Wiley and Sons, New York.

Belongie, S., C. Carson, H. Greenspan, and J. Malik (1998). Color- and texture-based image segmentation using the expectation-maximization algorithm and its application to content-based image retrieval. In *Proc. of the IEEE Int. Conf. on Computer Vision*, pp. 675–682.

Bennett, J. and A. Khotanzad (1998). Multispectral random field models for synthesis and analysis of color images. *IEEE Transactions on Pattern Analysis and Machine Intelligence* 20(3): 327–332.

Bertero, M., T. Poggio, and V. Torre (1988). Ill-posed problems in early vision. *Proceedings of the IEEE* 76(8): 869–889.

Black, M.J. (1992). Robust Incremental Optical Flow. Phd thesis, Yale University.

Blake, Andrew and Michael Isard (1998). *Active Contours*. Springer-Verlag, Berlin Heidelberg New York.

Boddy, M. and T. Dean (1994). Decision-theoretic deliberation scheduling for problem solving in time-constrained environments. *Artificial Intelligence* 67(2): 245–286.

Bongiovanni, G., P. Crescenzi, and C. Guerra (1995). Parallel simulated annealing for shape detection. *Computer Vision and Image Understanding* 61(1): 60–69.

Bouman, C. and K. Sauer (1993). A generalized gaussian image model for edge-preserving map estimation. *IEEE Transactions on Image Processing* 2(3): 296–310.

Canny, J. (1986). A computational approach to edge detection. *IEEE Transactions on Pattern Analysis and Machine Intelligence* 8(6): 679–698.

Chakraborty, A. and J.S. Duncan (1999). Game-theoretic integration for image segmentation. *IEEE Transactions on Pattern Analysis and Machine Intelligence* 21(1): 12–30.

Chellappa, R. (1985). Two-dimensional discrete gauss markovian random field models for image processing. *Progress in Pattern Recognition* 2: 79–112.

Chesnaud, C., P. Refregier, and V. Boulet (1999). Statistical region snake-based segmentation adapted to different physical noise models. *IEEE Transactions on Pattern Analysis and Machine Intelligence* 21(11): 1145–1157.

Chuang, Y.Y., B. Curless, D.H. Salesin, and R. Szeliski (2001). A bayesian approach to digital matting. In *Proc. of the IEEE Conf. Computer Vision and Pattern Recognition*, pp. II:264–271.

Clausi, D.A. and M.E. Jernigan (2000). Designing gabor filters for optimal texture separability. *Pattern Recognition* 33(11): 1835–1849.

Cootes, T. F., G. J. Edwards, and C. J. Taylor (1998). Active appearance models. In *Proc. of the European Conf. on Computer Vision*, pp. 484–498.

Cootes, T.F., G.J. Edwards, and C.J. Taylor (2001). Active appearance models. *IEEE Transactions on Pattern Analysis and Machine Intelligence* 23(6): 681–684.

Cootes, T.F., A. Hill, C.J. Taylor, and J. Haslam (1994). The use of active shape models for locating structure in medical images. *Image and Vision Computing* 12(6): 355–365.

Cootes, T.F. and C.J. Taylor (2001). On representing edge structure for model matching. In *Proc. of the IEEE Conf. Computer Vision and Pattern Recognition*, pp. I:1114–1119.

Cootes, T.F., C.J. Taylor, A. Lanitis, D.H. Cooper, and J. Graham (1993). Building and using flexible models incorporating grey-level information. In *Proc. of the IEEE Int. Conf. on Computer Vision*, pp. 242–246.

Coughlan, J., A.L. Yuille, C. English, and D. Snow (1998). Efficient optimization of a deformable template using dynamic programming. In *Proc. of the IEEE Conf. Computer Vision and Pattern Recognition*, pp. 747–752.

Cox, I.J., Y. Zhong, and S.B. Rao (1996). Ratio regions: A technique for image segmentation. In *Proc. of the IEEE Int. Conf. on Pattern Recognition*, pp. B: 557–564.

Cremers, D., C. Schnörr, and J. Weickert (2001). Diffusion-snakes: Combining statistical shape knowledge and image information in a variational framework. In *Variational and Level Set Methods in Computer Vision*, pp. 137–144.

Davidson, C. and A. Blake (1998). Error-tolerant visual planning of planar grasp. In *Proc. of the IEEE Int. Conf. on Computer Vision*, pp. 911–916.

Dempster, A.P., N.M. Laird, and D.B. Rubin (1977). Maximum likelihood from incomplete data via the EM algorithm. *J. R. Statist. Soc. B* 39: 1–38.

Deutscher, J., A. Blake, and I.D. Reid (2000). Articulated body motion capture by annealed particle filtering. In *Proc. of the IEEE Conf. Computer Vision and Pattern Recognition*, pp. II: 126–133.

Dierckx, P. (1993). *Curve and Surface Fitting with Splines*. Oxford University Press, Oxford New York Tokyo.

Dubuisson-Jolly, M.P. and A. Gupta (2001). Tracking deformable templates using a shortest path algorithm. *Computer Vision and Image Understanding* 81(1): 26–45.

Faugeras, O.D. (1993). Three-dimensional computer vision: A geometric viewpoint. *MIT Press* p. 302.

Felzenszwalb, P.F. and D.P. Huttenlocher (1998). Image segmentation using local variation. In *Proc. of the IEEE Conf. Computer Vision and Pattern Recognition*, pp. 98–104.

Fitzgibbon, A. W., M. Pilu, and R. B. Fisher (1999). Direct least square fitting of ellipses. *IEEE Transactions on Pattern Analysis and Machine Intelligence* 21(5): 476–480.

Geiger, D., A. Gupta, L.A. Costa, and J. Vlontzos (1995). Dynamic-programming for detecting, tracking, and matching deformable contours. *IEEE Transactions on Pattern Analysis and Machine Intelligence* 17(3): 294–302.

Geman, S. and D. Geman (1984). Stochastic relaxation, gibbs distributions, and the bayesian restoration of images. *IEEE Transactions on Pattern Analysis and Machine Intelligence* 6(6): 721–741.

Hadamard, J. (1902). Sur les problèmes aux dérivées partielles et leur signification physique. *Princeton University Bulletin* 13: 49–52.

Hanek, R. (2001a). Model-Based Image Segmentation Using Local Self-Adapting Separation Criteria. In Radig, B. and S. Florczyk, editors, *23. DAGM Symposium*, LNCS 2191, pp. 1–8, Munich, Germany. Springer.

Hanek, R. (2001b). The Contracting Curve Density Algorithm and its Application to Model-based Image Segmentation. In *Proc. of the IEEE Conf. Computer Vision and Pattern Recognition*, pp. I:797–804.

Hanek, R. and M. Beetz (2004). The contracting curve density algorithm: Fitting parametric curve models to images using local self-adapting separation criteria. *International Journal of Computer Vision* 59(3): 233–258.

Hanek, R., N. Navab, and M. Appel (1999). Yet another method for pose estimation: A probabilistic approach using points, lines, and cylinders. In *Proc. of the IEEE Conf. Computer Vision and Pattern Recognition*, pp. II:544–550.

Hanek, R. and T. Schmitt (2000). Vision-Based Localization and Data Fusion in a System of Cooperating Mobile Robots. In *Proc. of the IEEE/RSJ Int. Conf. on Intelligent Robots and Systems*, pp. 1199–1204.

Hanek, R., T. Schmitt, S. Buck, and M. Beetz (2002a). Fast Image-based Object Localization in Natural Scenes. In *Proc. of the IEEE/RSJ Int. Conf. on Intelligent Robots and Systems*, Lausanne, pp. 116–122.

Hanek, R., T. Schmitt, S. Buck, and M. Beetz (2002b). Towards RoboCup without Color Labeling. In *RoboCup International Symposium*, Fukuoka, Japan, pp. 179–194. Springer.

Hanek, R., T. Schmitt, M. Klupsch, and Buck S. (2000). From Multiple Images to a Consistent View. In *RoboCup International Symposium*, Melbourne, Australia, pp. 288–296. Springer.

Hansen, C. (2002). Modellgetriebene Verfolgung formvariabler Objekte in Videobildfolgen. Dissertation, Technische Universität München.

Harris., C. (1992). Tracking with rigid models. In Blake, A. and A. Yuille, editors, *Active Vision*, pp. 59–73. MIT Press.

Herlin, I. L. and N. Ayache (1992). Feature extraction and analysis methods for sequences of ultrasound images. *Image and Vision Computing* 10(10): 673–682.

Hermes, L., T. Zöller, and J.M. Buhmann (2002). Parametric distributional clustering for image segmentation. In *Proc. of the European Conf. on Computer Vision*, Vol. 3, pp. 577–591.

Horn, B.K.P. and B.G. Schunck (1981). Determining optical flow. *Artificial Intelligence* 17: 185–203.

Hough, P. V. (1962). Method and means for recognizing complex patterns. U.S. Patent 3069654.

Huang, P. S. (2001). Automatic gait recognition via statistical approaches for extended template features. *IEEE Transactions on Systems, Man, and Cybernetics, Part B:Cybernetics* 31(5): 818–824.

Huber, P. (1981). *Robust Statistics*. John Wiley and Sons, New York.

Isard, M. and A. Blake (1996). Contour tracking by stochastic propagation of conditional density. In *Proc. of the European Conf. on Computer Vision*, pp. I:343–356.

Jones, T.D. and P. Plassmann (2000). An active contour model for measuring the area of leg ulcers. *IEEE Transactions on Medical Imaging* 19(12): 1202–1210.

Jones, T.N. and D.N. Metaxas (1998). Image segmentation based on the integration of pixel affinity and deformable models. In *Proc. of the IEEE Conf. Computer Vision and Pattern Recognition*, pp. 330–337.

Kass, M., A.P. Witkin, and D. Terzopoulos (1988). Snakes: Active contour models. *International Journal of Computer Vision* 1(4): 321–331.

Koller, D., K. Daniilidis, and H.H. Nagel (1993). Model-based object tracking in monocular image sequences of road traffic scenes. *International Journal of Computer Vision* 10(3): 257–281.

Kollnig, H. and H.H. Nagel (1995). 3d pose estimation by fitting image gradients directly to polyhedral models. In *Proc. of the IEEE Int. Conf. on Computer Vision*, pp. 569–574.

Konishi, S., A.L. Yuille, J.M. Coughlan, and S.C. Zhu (2003). Statistical edge detection: learning and evaluating edge cues. *IEEE Transactions on Pattern Analysis and Machine Intelligence* 25(1): 57–74.

Lanser, S. (1997). Modellbasierte Lokalisation gestützt auf monokulare Videobilder. Dissertation, Technische Universität München.

Li, P., T. Zhang, and A.E.C. Pece (2003). Visual contour tracking based on particle filters. *Image and Vision Computing* 21(1): 111–123.

Li, S.Z. (2001). *Markov Random Field Modeling in Image Analysis*. Springer-Verlag, Berlin Heidelberg New York.

Lindeberg, T. (1998). Feature detection with automatic scale selection. *International Journal of Computer Vision* 30(2): 79–116.

Lowe, David G. (1991). Fitting parameterized 3-d models to images. *IEEE Transactions on Pattern Analysis and Machine Intelligence* 13(5): 441–450.

Lowe, D.G. (1987). Three-dimensional object recognition from single two-dimensional images. *Artificial Intelligence* 31: 355–395.

Lowe, D.G. (1992). Robust model-based motion tracking through the integration of search and estimation. *International Journal of Computer Vision* 8(2): 113–122.

Luo, H., Q. Lu, R.S. Acharya, and R. Gaborski (2000). Robust snake model. In *Proc. of the IEEE Conf. Computer Vision and Pattern Recognition*, pp. I:452–457.

Luong, Q. T. (1993). Color in computer vision. In Chen C. H., Pau L. F., Wang P. S. P., editor, *Handbook of Pattern Recognition and Computer Vision*, pp. 311–368. World Scientific.

MacCormick, J.P. and M. Isard (2000). Partitioned sampling, articulated objects, and interface-quality hand tracking. In *Proc. of the European Conf. on Computer Vision*, pp. II: 3–19.

Malik, J., S. Belongie, J. Shi, and T. Leung (1999). Textons, contours and regions: Cue integration in image segmentation. In *Proc. of the IEEE Int. Conf. on Computer Vision*, pp. 918–925.

Manduchi, R. (1999). Bayesian fusion of color and texture segmentations. In *Proc. of the IEEE Int. Conf. on Computer Vision*, pp. 956–962.

McInerney, T. and D. Terzopoulos (1996). Deformable models in medical image analysis: a survey. *Medical Image Analysis* 1(2): 91–108.

Mirmehdi, M. and M. Petrou (2000). Segmentation of color textures. *IEEE Transactions on Pattern Analysis and Machine Intelligence* 22(2): 142–159.

Mortensen, E.N. and W.A. Barrett (1998). Interactive segmentation with intelligent scissors. *Graphical Models and Image Processing* 60(5): 349–384.

Nalwa, V.S. and T.O. Binford (1986). On detecting edges. *IEEE Transactions on Pattern Analysis and Machine Intelligence* 8(6): 699–714.

Niemann, H. (1990). *Pattern Analysis and Understanding*. Springer, Heidelberg.

Panjwani, D.K. and G. Healey (1995). Markov random-field models for unsupervised segmentation of textured color images. *IEEE Transactions on Pattern Analysis and Machine Intelligence* 17(10): 939–954.

Paragios, N. and R. Deriche (2000). Coupled geodesic active regions for image segmentation: A level set approach. In *Proc. of the European Conf. on Computer Vision*, pp. 224–240.

Pece, A. E. C. (2003). The Kalman-EM contour tracker. In *Proc. 3rd workshop on Statistical and Computational Theories of Vision:SCTV 2003*.

Pece, A.E.C. and A.D. Worrall (2002). Tracking with the EM contour algorithm. In *Proc. of the European Conf. on Computer Vision*, pp. I: 3–17.

Phong, T.Q., R. Horaud, A. Yassine, and P.D. Tao (1995). Object pose from 2-d to 3-d point and line correspondences. *International Journal of Computer Vision* 15: 225–243.

Portilla, J. and E.P. Simoncelli (2000). A parametric texture model based on joint statistics of complex wavelet coefficients. *International Journal of Computer Vision* 40(1): 49–70.

Press, W. H., S. A. Teukolsky, W. T. Vetterling, and B. P. Flannery (1996). *Numerical Recipes in C.* Cambridge University Press, Cambridge.

Rimon, E. and A. Blake (1996). Caging 2d bodies by 1-parameter two-fingered gripping systems. In *Proc. of the IEEE Int. Conf. on Robotics and Automation*, pp. 1458–1464.

Robert, L. (1996). Camera calibration without feature extraction. *Computer Vision and Image Understanding* 63(2): 314–325.

Ronfard, R. (1994). Region-based strategies for active contour models. *International Journal of Computer Vision* 13(2): 229–251.

Ruzon, M.A. and C. Tomasi (2000). Alpha estimation in natural images. In *Proc. of the IEEE Conf. Computer Vision and Pattern Recognition*, pp. I:18–25.

Ruzon, M.A. and C. Tomasi (2001). Edge, junction, and corner detection using color distributions. *IEEE Transactions on Pattern Analysis and Machine Intelligence* 23(11): 1281–1295.

Schmitt, T., R. Hanek, M. Beetz, S. Buck, and B. Radig (2002). Cooperative probabilistic state estimation for vision-based autonomous mobile robots. *IEEE Transactions on Robotics and Automation* 18(5): 670–684.

Sclaroff, S. and L. Liu (2001). Deformable shape detection and description via model-based region grouping. *IEEE Transactions on Pattern Analysis and Machine Intelligence* 23(5): 475–489.

Shi, J. and J. Malik (2000). Normalized cuts and image segmentation. *IEEE Transactions on Pattern Analysis and Machine Intelligence* 22(8): 888–905.

Shoemake, Ken (1994). Euler angle conversion. In Heckbert, Paul, editor, *Graphics Gems IV*, pp. 222–229. Academic Press, Boston.

Siebel, N. T. (2003). Design and Implementation of People Tracking Algorithms for Visual Surveillance Applications. Phd thesis, Department of Computer Science, The University of Reading.

Steger, C. (2000). Subpixel-precise extraction of lines and edges. *International Archives of Photogrammetry and Remote Sensing* XXXIII, part B3: 141–156.

Storvik, G. (1994). A bayesian-approach to dynamic contours through stochastic sampling and simulated annealing. *IEEE Transactions on Pattern Analysis and Machine Intelligence* 16(10): 976–986.

Sullivan, G.D. (1992). Visual interpretation of known objects in constrained scenes. *Phil. Trans. Roy. Soc.* B-337: 361–370.

Sullivan, Steve and Jean Ponce (1998). Automatic model construction and pose estimation from photographs using triangular splines. *IEEE Transactions on Pattern Analysis and Machine Intelligence* 20(10): 1091–1096.

Thirion, B., B. Bascle, V. Ramesh, and N. Navab (2000). Fusion of color, shading and boundary information for factory pipe segmentation. In *Proc. of the IEEE Conf. Computer Vision and Pattern Recognition*, pp. II:349–356.

Ulrich, M., C. Steger, A. Baumgartner, and H. Ebner (2001). Real-time object recognition using a modified generalized Hough transform. In Seyfert, Eckhardt, editor, *Photogrammetrie — Fernerkundung — Geoinformation: Geodaten schaffen Verbindungen*, 21. Wissenschaftlich-Technische Jahrestagung der DGPF, pp. 571–578, Berlin. DGPF.

Weicker, R. (1984). A synthetic systems programming benchmark. *Communications of the ACM* 27(10): 1013–1030.

Werman, M. and D. Keren (2001). A bayesian method for fitting parametric and nonparametric models to noisy data. *IEEE Transactions on Pattern Analysis and Machine Intelligence* 23(5): 528–534.

Wu, Z. and R. Leahy (1993). An optimal graph theoretic approach to data clustering: Theory and its application to image segmentation. *IEEE Transactions on Pattern Analysis and Machine Intelligence* 15(11): 1101–1113.

Xu, C.Y. and J.L. Prince (1998). Snakes, shapes, and gradient vector flow. *IEEE Transactions on Image Processing* 7(3): 359–369.

Yezzi, Jr., A., S. Kichenassamy, A. Kumar, P. Olver, and A. Tannenbaum (1997). A geometric snake model for segmentation of medical imagery. *IEEE Transactions on Medical Imaging* 16(2): 199–209.

Yuille, A. and N. Grzywacz (1988). A computational theory for the perception of coherent visual motion. *Nature* 333, 6168: 71–74.

Yuille, A.L., D.S. Cohen, and P.W. Hallinan (1992). Feature extraction from faces using deformable templates. *International Journal of Computer Vision* 8(2): 99–111.

Zhang, Z. (1997). Parameter estimation techniques: A tutorial with application to conic fitting. *International Journal of Image and Vision Computing* 15(1): 59–76.

Zhong, Y., A.K. Jain, and M.P. Dubuisson-Jolly (2000). Object tracking using deformable templates. *IEEE Transactions on Pattern Analysis and Machine Intelligence* 22(5): 544–549.

Zhu, S.C. and A. Yuille (1996). Region competition: Unifying snakes, region growing, and Bayes/MDL for multiband image segmentation. *IEEE Transactions on Pattern Analysis and Machine Intelligence* 18(9): 884–900.

Zöller, T., L. Hermes, and J. M. Buhmann (2002). Combined color and texture segmentation by parametric distributional clustering. In *Proc. of the IEEE Int. Conf. on Pattern Recognition*, Vol. 2, pp. 627–630.

Index